



# **Mechanistic Investigation of Developmental Copper Chemotherapeutics**

---

**Creina Slator B.Sc. (Hons)**

A thesis submitted in partial fulfilment for the degree of Ph.D.

Supervisor: Dr. Andrew Kellett

Secondary supervisor: Dr. Niall Barron

School of Chemical Sciences

Dublin City University

January 2017





## **Declaration**

I hereby certify that this material, which I now submit for assessment on the programme of study leading to the award of Doctor of Philosophy (PhD) is entirely of my own work, and that I have exercised reasonable care to ensure that the work is original and, does not to the best of my knowledge breach any law of copyright, and has not been taken from the work of others save and to the extent that such work has been cited and acknowledged within the text of my work.

Signature:\_\_\_\_\_ ID number: 58505063 Date:\_\_\_\_\_



## Acknowledgements

I would like to extend my profound gratitude to my supervisor Dr. Andrew Kellett. While being hugely supportive throughout the project, you have offered a wealth of knowledge and advice while also respecting my opinions and decisions. This allowed the project, and I, to evolve in such a way I could have never foreseen and broadened my knowledge beyond measure. You have gone above and beyond the call of an academic supervisor and have been a great mentor.

I also would like to thank my co-supervisor, Dr. Niall Barron. He gave invaluable advice, guidance and training, particularly at the start of the project. Without this, the progression of the work would have been immensely more difficult.

I would like to thank all the staff in the School of Chemical Sciences, NICB and NRF. They keep all the centres going like well-oiled machines and are an invaluable resource. They happily and readily gave advice and support, and great impromptu chats in the hallways.

I would also like thank the Kellett research group for their support throughout the years. To Zara, Andreea, Tadhg, Sean, Nicolo, Teresa, Natasha, Joey and Ziga, for the laughter and chats in the office. To Tadhg, your solution to every problem ‘Ah sure, it’ll be grand!’ made failed experiments and late nights in the lab all the more bearable. Zara, we have quite literally worked side-by-side throughout this whole process, I am glad to have gone through this experience with you (and as a result, I am far more organised). Also to the ‘biologists’ of the NICB, who happily accepted the ‘chemists’ into their domain. Thank you for all the advice over the years and nerdy chats (I’m looking at you Paul) that made the hours of sample prep fly by.

I would also like to thank my DCU pals and personal shrinks, Suzanne and Aisling. From our undergraduate degrees to finally obtaining our PhDs, it has been an amazing journey with you both. Our little lunch dates were welcome respite away from the lab and you always knew exactly what to say or do at stressful times. To include my non-DCU friends, Joanna, Megan, Aoife and the girls, I cannot thank you all enough for your support and friendship.

To my better half, Steve, you never once complained about my complete lack of work-life balance and have always supported me. From the late night lifts, never moaning about my laptop constantly being at hand or you waiting for an indefinite period of time while I ‘just pop into the lab for 10 minutes’ on a Saturday, I you have always been patient and understanding.

And finally to my parents, Monica and David, and my brother, Robert. I could not have done this without your understanding, encouragement and unconditional love. When times were stressful especially at the end, you always offered any help that you could give. I cannot thank you enough for all that you have done.



## Research Output

### Publications

A. Kellett, A. Prisecaru, C. Slator, Z. Molphy and M. McCann. Metal-Based Antimicrobial Protease Inhibitors. *Current Medicinal Chemistry*, 2013, 20, 3134-3151.

Z. Molphy, A. Prisecaru, C. Slator, N. Barron, M. McCann, J. Colleran, D. Chandran, N. Gathergood, and A. Kellett. Copper Phenanthrene Oxidative Chemical Nucleases. *Inorganic Chemistry*. 2014, 53, 5392–5404.

Z. Molphy, C. Slator, C. Chatgililoglu and A. Kellett. DNA Oxidation Profiles of Copper Phenanthrene Chemical Nucleases. *Frontiers in Chemistry*. 2015, Volume 3, Article 28

C. Slator, N. Barron, O. Howe and A. Kellett. [Cu(*o*-phthalate)(phenanthroline)] Exhibits Unique NCI-60 Chemotherapeutic Action with Superoxide-Mediated Mitochondrial and Genomic DNA Targeting Effects. *ACS Chemical Biology*, 2016, 11 (1), 159–171.

A. Kellett, Z. Molphy, C. Slator, V. McKee, and N.P. Farrell. Molecular Methods for Probing Cytotoxic Metallodrug-DNA Interactions. *Current Medicinal Chemistry*, Accepted.

C. Slator, Z. Molphy, V. McKee, A. Kellett. *Di-Mn<sup>2+</sup> bis-1,10-phenanthroline octanedioate* induces superoxide-mediated autophagic cell death. Accepted to *Redox Biology*, 2016.

### Scientific Talks

‘Flow Cytometry Analysis of Di-Nuclear Copper Complexes with Potent in vitro Anticancer Properties’ at 6th Meeting of the Irish Institute of Metal-Based Drugs, 1<sup>st</sup> November 2014, Royal College of Surgeons, Dublin.

‘Di-Nuclear Copper(II) Complexes as Antitumour Therapeutic Leads’ at MCB2014; ‘Joining forces in pharmaceutical analysis and medicinal chemistry’ Conference, August 25<sup>th</sup> - 26<sup>th</sup>, 2014, Groningen

‘Mechanistic investigation into unique chemotherapeutic action of [Cu(*o*-phthalate)(1,10-phenanthroline)]’ at First Inaugural Chemistry Day on June 19<sup>th</sup> 2015, Dublin City University.

‘DNA Oxidation Profiles of Copper Phenanthrene Chemical Nucleases’ at COST Action CM1201 Inter-WG (WG2/WG4) Meeting, 24<sup>th</sup> July 2015, Carton House, Kildare.

‘Mechanistic Investigation of Developmental Copper Chemotherapeutics’ at 68<sup>th</sup> Irish University Chemistry Research Colloquium 2016, 23<sup>rd</sup>-24<sup>th</sup> June 2016, University College Cork.

## Posters

Metal-Based Antimicrobial Protease Inhibitors. Livia Viganor Silva, Creina Slator, Zara Molphy, Malachy McCann, Andr. Luis Souza dos Santos, Andrew Kellett. 65th Irish Universities Chemistry Research Colloquium, 27<sup>th</sup> - 28<sup>th</sup> June 2013, Trinity College Dublin.

DNA Oxidation Profiles of Copper Phenanthrene Chemical Nucleases. Zara Molphy, Creina Slator, Chrysostomos Chatgililoglu and Andrew Kellett. 13<sup>th</sup> International Symposium on Applied Bioinorganic Chemistry, ISABC13, June 12<sup>th</sup>-15<sup>th</sup> 2015, NUI Galway.

[Cu(*o*-phthalate)(phenanthroline)] Exhibits Unique Superoxide-Mediated NCI-60 Chemotherapeutic Action through Genomic DNA Damage and Mitochondrial Dysfunction. Creina Slator, Niall Barron, and Andrew Kellett. 1<sup>st</sup> Medicinal Chemistry Ireland Conference, 1<sup>st</sup> July 2016, Trinity College Dublin.

## Awards

Awarded Faculty of Science and Health Distinguished Scholar Studentship in 2012.

Awarded Irish Research Council Scholarship GOIPG/2014/1182 in 2014 for the project title 'Copper Metallo-Nuclease as Novel Cancer Chemotherapeutics'.

Awarded best poster prize at 1<sup>st</sup> Medicinal Chemistry Ireland Conference, 1<sup>st</sup> July 2016, Trinity College Dublin.

## Aims of Research

Comprehending the underpinning mode of cytotoxic action of novel chemotherapeutic agents is paramount to the progression of therapeutic leads. Given the current state of metallodrug research, this level of understanding is critical to further improve molecular design for enhanced targeting, potency, affinity, efficiency and selectivity within cancer cells for subsequent advancement towards clinical approval. The main objective of my PhD was to establish methodologies and techniques for the development of  $\text{Cu}^{2+}$  and  $\text{Mn}^{2+}$  chemotherapeutic agents. On the basis of previous publications reporting a promising series of *mono*- and *di*-nuclear copper complexes, founded upon artificial chemical nucleases, *in vitro* DNA binding and degradation properties were identified. Furthermore, general toxic activity against a range of human cancerous cell lines and liberation of general reactive oxygen species were examined. Although preliminary DNA interactions and cellular toxicities were investigated, no detailed mechanistic analysis was conducted to determine the intracellular mode of cytotoxic action. The foremost efforts of my PhD were to establish cell culture methods and techniques within the National Institute for Cellular Biotechnology to study developmental agents and identify complex efficacy and targeting properties through detailed analysis of mechanistic pathways and modes of induced cell death. This was achieved by founding protocols for flow cytometry, epifluorescence and confocal microscopy, in combination with a range of biomolecular procedures.

# Thesis Outline

## Chapter 1

This chapter gives an overview of biomolecular methodologies to probe metallodrug-DNA interactions used in the discovery of novel agents that specifically target nucleic acids. This review includes background information on DNA structure and categories of binding modes and motifs. Furthermore, this chapter highlights approaches used in the detection of binding interfaces and those used to identify intracellular genotoxicity. Such experimental investigations are categorised based upon electrophoretic, fluorescence and absorbance-based techniques, as well as mass spectrometry, NMR and cell culture procedures. Relevant examples of  $\text{Cu}^{2+}$  complexes developed within the Kellett group, mononuclear and polynuclear  $\text{Pt}^{2+}$  complexes from collaborator, Professor Nicholas P. Farrell's group, are reviewed and examined throughout.

## Chapter 2

This chapter describes the effects of a novel  $\text{Cu}^{2+}$  phenanthrene series with fused diimines *N, N'*-ligands and their oxidative nuclease activity and redox cycling properties. Intercalative binding through the minor groove was found to direct DNA cleavage processes, mediated *via* the generation of hydroxyl radicals and subsequent formation of oxidative DNA lesion including 8-oxo-dG. The extent of nuclease activity and resulting implications on DNA replication processes is also reported.

## Chapter 3

This chapter describes the mechanistic investigations into the mode of cytotoxic action of a *mono*-Cu complex with *di*-carboxylate *O, O'*-ligand, *o*-phthalate. The unique activity of this complex is highlighted through broad-spectrum cytotoxicity within the National Cancer Institute (NCI) cancer cell lines screen. The mode of cell death is outlined and attributed to proficient generation of the superoxide anions, instigating a cascade of deleterious radical species, and thus inducing internal activation of the apoptotic pathway.

## Chapter 4

This chapter describes *di*-nuclear  $\text{Cu}^{2+}$  complexes based on the *bis*-1,10-phenanthroline chemo-type, bridged with *di*-carboxylate moieties of varying rigidity, and the mechanistic activation of apoptosis from intrinsic, mitochondrial origin. In-depth analysis of NCI-60 results through the use of the COMPARE algorithm endorsed experimental design and rationale for subsequent investigations into genotoxicity and further identification of cell death pathways. Both complexes reported within this work possess dual-targeting properties towards genomic DNA and the mitochondria. Superior liberation of superoxide and singlet oxygen induce extensive mitochondrial depolarisation, and subsequent induction of intrinsic apoptotic cell death.



## Chapter 5

This body of work outlines an alternative mechanism of cell death upon substitution of the metal centre from  $\text{Cu}^{2+}$  to  $\text{Mn}^{2+}$  within the octanedioate–phenanthroline scaffold. DNA interaction and genotoxicity studies identified an intercalative binding mode that does not directly induce DNA damage. Biomolecule degradation is instead explained as a downstream effect of autophagic induction. The *di*- $\text{Mn}^{2+}$  complex activation of this self-digestion pathway is mediated by superoxide generation and in turn, activates intrinsic apoptosis.

## Thesis publications

Chapter	Title	Publication Status*	Authors	Contribution
1	Molecular Methods for Probing Cytotoxic Metallodrug-DNA Interactions	<i>Curr. Med. Chem.</i> Accepted.	Kellett, A., Molphy, Z., <u>Slator, C.</u> , McKee, V., and Farrell, N. P.	Co-author of review with significant written input into the following sections: introduction, <i>in vitro</i> and <i>in cellulo</i> methods.
2	DNA Oxidation Profiles of Copper Phenanthrene Chemical Nucleases	<i>Front. Chem.</i> 2015, <b>3</b> , 28.	Molphy, Z., <u>Slator, C.</u> , Chatgililoglu, C., and Kellett, A	Co-author of manuscript. Designed and executed scavenger experiments. Conducted 8-oxo-dG experiments in partnership with Molphy.
3	[Cu(o-phthalate) (phenanthroline)] Exhibits Unique Superoxide-Mediated NCI-60 Chemotherapeutic Action through Genomic DNA Damage and Mitochondrial Dysfunction	<i>ACS Chem. Biol.</i> 2016, <b>11</b> , 159-171.	<u>Slator, C.</u> , Barron, N., Howe, O., and Kellett, A	Manuscript primary author. Primary contributor to experimental design and execution.
4	Dual Targeting <i>Di</i> -Copper Complexes Promote NCI-60 Chemotherapy by Intracellular Superoxide and Singlet Oxygen Production	Manuscript submitted.	<u>Slator, C.</u> , Molphy, Z., Kellett, A.	Manuscript primary author. Primary contributor to experimental design and execution.
5	<i>Di</i> -Mn <sup>2+</sup> bis-1,10-phenanthroline octanedioate induces superoxide-mediated autophagic cell death.	<i>Redox Biol.</i> Accepted.	<u>Slator, C.</u> , Molphy, Z., McKee, V., Kellett, A.	Manuscript primary author. Primary contributor to experimental design and execution.

\* For example, ‘published’/ ‘in press’/ ‘accepted’/ ‘returned for revision’/ ‘submitted’

**Signed:**

-----  
Candidate

-----  
Principal Supervisor

-----  
Secondary Supervisor

-----  
Date

# Table of Contents

<b>ACKNOWLEDGEMENTS.....</b>	<b>I</b>
<b>RESEARCH OUTPUT.....</b>	<b>III</b>
<b>PUBLICATIONS.....</b>	<b>III</b>
<b>SCIENTIFIC TALKS.....</b>	<b>III</b>
<b>POSTERS.....</b>	<b>IV</b>
<b>AWARDS.....</b>	<b>IV</b>
<b>AIMS OF RESEARCH .....</b>	<b>V</b>
<b>THESIS OUTLINE.....</b>	<b>VI</b>
<b>CHAPTER 1.....</b>	<b>VI</b>
<b>CHAPTER 2.....</b>	<b>VI</b>
<b>CHAPTER 3.....</b>	<b>VI</b>
<b>CHAPTER 4.....</b>	<b>VI</b>
<b>CHAPTER 5.....</b>	<b>VII</b>
<b>THESIS PUBLICATIONS.....</b>	<b>VIII</b>
<b>TABLE OF FIGURES .....</b>	<b>XIV</b>
<b>TABLE OF SCHEMES.....</b>	<b>XX</b>
<b>TABLE OF TABLES .....</b>	<b>XX</b>
<b>ABBREVIATIONS.....</b>	<b>XXII</b>
<b>UNITS OF MEASUREMENT .....</b>	<b>XXIII</b>
<b>THESIS ABSTRACT .....</b>	<b>XXV</b>
<b>CHAPTER 1</b>	
<b>MOLECULAR METHODS FOR PROBING CYTOTOXIC METALLODRUG-DNA</b>	
<b>INTERACTIONS.....</b>	<b>1</b>
<b>1.1 ABSTRACT .....</b>	<b>2</b>
<b>1.2 INTRODUCTION .....</b>	<b>3</b>
1.2.1 NUCLEIC ACID STRUCTURE .....	3
1.2.2 NUCLEIC ACIDS AS METALLODRUG TARGETS .....	5
1.2.2.1 Covalent interactions by platinum(II) chemotherapeutics .....	5
1.2.2.2 Non-covalent interactions .....	8
1.2.2.2.1 Metallointercalation and metalloinsertion .....	8
1.2.2.2.2 Non-covalent binding by polynuclear platinum complexes (PCCs) .....	11
<b>1.3 ELECTROPHORETIC-BASED TECHNIQUES .....</b>	<b>12</b>
1.3.1 DNA DAMAGE DETECTION .....	12
1.3.2 ANTIOXIDANT TRAPS FOR OXIDATIVE CLEAVAGE DETECTION.....	13
1.3.3 INTERCALATION: TOPOISOMERASE I AND II INHIBITION .....	14
1.3.4 DNA UNWINDING AND BENDING .....	15

1.3.5	ALKYLATION ASSAYS WITH MELPHALAN .....	16
1.3.6	ON-CHIP MICROFLUIDIC ANALYSIS .....	16
1.3.7	NON-COVALENT RECOGNITION ELEMENTS .....	17
<b>1.4</b>	<b>FLUORESCENCE AND ABSORBANCE BASED TECHNIQUES.....</b>	<b>18</b>
1.4.1	INDIRECT FLUOROMETRIC ASSAYS.....	18
1.4.2	COMPETITIVE FLUORESCENT DISPLACEMENT .....	19
1.4.3	COMPETITIVE FLUORESCENCE QUENCHING .....	19
<b>1.5</b>	<b>ABSORBANCE BASED TECHNIQUES.....</b>	<b>19</b>
1.5.1	OVERVIEW.....	19
1.5.2	THERMAL MELTING .....	20
1.5.3	CIRCULAR DICHROISM SPECTROSCOPY .....	21
1.5.4	ELISA DETECTION OF 8-OXO-DG LESION FORMATION .....	22
<b>1.6</b>	<b>VISCOSITY .....</b>	<b>23</b>
<b>1.7</b>	<b>MASS SPECTROMETRY .....</b>	<b>24</b>
<b>1.8</b>	<b>NMR SPECTROSCOPY.....</b>	<b>25</b>
<b>1.9</b>	<b>IN CELLULO GENOTOXICITY.....</b>	<b>27</b>
1.9.1	INTRACELLULAR ROS DAMAGE.....	27
1.9.2	INTRACELLULAR ROS SCAVENGERS .....	27
1.9.3	CONFOCAL MICROSCOPY: DETECTION OF DNA FRAGMENTATION AND CONDENSATION .....	28
1.9.4	IMMUNODETECTION OF DOUBLE STRAND BREAKS (DSBs) WITH $\gamma$ H2AX .....	28
1.9.5	COMET ASSAY: NEUTRAL AND ALKALINE .....	29
<b>1.10</b>	<b>CONCLUSION.....</b>	<b>30</b>
<b>1.11</b>	<b>REFERENCES.....</b>	<b>31</b>

## CHAPTER 2

<b>DNA OXIDATION PROFILES OF COPPER PHENANTHRENE CHEMICAL NUCLEASES.....</b>		<b>41</b>
<b>2.1</b>	<b>ABSTRACT .....</b>	<b>42</b>
<b>2.2</b>	<b>INTRODUCTION.....</b>	<b>43</b>
<b>2.3</b>	<b>MATERIALS AND METHODS .....</b>	<b>45</b>
2.3.1	PREPARATION OF THE COMPLEXES .....	45
2.3.2	DNA CLEAVAGE STUDIES.....	46
2.3.2.1	DNA cleavage in the presence of added reductant.....	46
2.3.2.2	DNA cleavage in the presence of non-covalently bound recognition elements .....	46
2.3.2.3	DNA oxidation with ROS scavengers and stabilisers .....	46
2.3.3	HT QUANTITATION OF 8-OXO-DG .....	47
2.3.4	PCR INHIBITION STUDIES.....	47
<b>2.4</b>	<b>RESULTS AND DISCUSSION .....</b>	<b>47</b>
2.4.1	DNA CLEAVAGE IN THE PRESENCE OF NON-COVALENTLY BOUND RECOGNITION ELEMENTS .....	47
2.4.2	DNA OXIDATION WITH ROS SCAVENGERS AND STABILISERS. ....	49
2.4.3	QUANTITATION OF 8-OXO-DG.....	51
2.4.4	PCR INHIBITION STUDIES.....	51
<b>2.5</b>	<b>CONCLUSIONS.....</b>	<b>53</b>
<b>2.6</b>	<b>SUPPORTING MATERIAL .....</b>	<b>54</b>
<b>2.7</b>	<b>REFERENCES.....</b>	<b>54</b>

## CHAPTER 3

<b>[CU(<i>O</i>-PHTHALATE)(PHENANTHROLINE)] EXHIBITS UNIQUE SUPEROXIDE-MEDIATED NCI-60 CHEMOTHERAPEUTIC ACTION THROUGH GENOMIC DNA DAMAGE AND MITOCHONDRIAL DYSFUNCTION .....</b>	<b>57</b>
<b>3.1 ABSTRACT .....</b>	<b>58</b>

<b>3.2 INTRODUCTION .....</b>	<b>59</b>
<b>3.3 MATERIALS AND METHODS .....</b>	<b>61</b>
3.3.1 MATERIALS AND REAGENTS.....	61
3.3.2 PREPARATION OF CU-PH.....	61
3.3.3 NCI-60 ANALYSIS.....	61
3.3.4 DNA INTERACTION STUDIES.....	61
3.3.4.1 DNA binding analysis .....	61
3.3.4.2 Nuclease activity in the presence of ROS scavengers .....	62
3.3.5 <i>EX CELLULO</i> INVESTIGATIONS .....	62
3.3.5.1 Cell culture.....	62
3.3.5.2 Viability profile in the presence of ROS Antioxidants.....	63
3.3.5.3 Nexin® assay.....	63
Mitochondrial membrane potential .....	63
3.3.5.4 Caspase 8 FAM and 9 SR, Caspase 3/7 FAM.....	63
3.3.5.5 Confocal analysis.....	64
3.3.6 STATISTICAL ANALYSIS .....	64
<b>3.4 RESULTS AND DISCUSSION .....</b>	<b>65</b>
3.4.1 NCI-60 ANALYSIS.....	65
3.3.2 BASE SPECIFIC DNA BINDING INTERACTIONS.....	67
3.4.3 IN VITRO AND INTRACELLULAR DNA OXIDATION WITH ROS SCAVENGERS .....	68
3.4.4 APOPTOTIC DETECTION THROUGH ANNEXIN V AND CASPASES.....	70
3.4.5 MITOCHONDRIAL DEPOLARIZATION.....	73
3.4.6 CONFOCAL MICROSCOPY .....	75
<b>2.5 CONCLUSION.....</b>	<b>77</b>
<b>3.6 SUPPORTING MATERIAL.....</b>	<b>78</b>

## CHAPTER 4

<b>DUAL TARGETING DI-COPPER COMPLEXES PROMOTE NCI-60 CHEMOTHERAPY BY INTRACELLULAR SUPEROXIDE AND SINGLET OXYGEN PRODUCTION.....</b>	<b>85</b>
<b>4.1 ABSTRACT .....</b>	<b>86</b>
<b>4.2 INTRODUCTION .....</b>	<b>87</b>
<b>4.3 METHODS.....</b>	<b>90</b>
4.3.1 MATERIALS AND REAGENTS .....	90
4.3.2 PREPARATION OF COMPLEXES.....	90
4.3.3 NCI-60 ANALYSIS.....	90
4.3.4 TOPOISOMERASE INHIBITION .....	91
4.3.5 DNA BINDING.....	91
4.3.6 CIRCULAR DICHROISM SPECTROMETRY .....	91
4.3.7 CELL CULTURE .....	92
4.3.8 CELLULAR VIABILITY .....	92
4.3.9 CELL CYCLE ANALYSIS.....	92
4.3.10 IMMUNODECTION OF DSBs.....	92
4.3.11 DNA DEGRADATION WITH COMET ASSAY.....	93
4.3.12 NEXIN® ASSAY .....	93
4.3.13 CASPASE 8 FAM AND 9 SR, CASPASE 3/7 FAM.....	93
4.3.14 CONFOCAL MICROSCOPY.....	94
4.3.15 MITOCHONDRIAL MEMBRANE POTENTIAL.....	94
4.3.16 MITOCHONDRIAL SUPEROXIDE (MITOSOX) DETECTION .....	94
4.3.17 STATISTICAL ANALYSIS .....	94
<b>4.4 RESULTS AND DISCUSSION .....</b>	<b>96</b>
4.4.1 NCI-60 ANALYSIS.....	96
4.4.2 MECHANISTIC BINDING AND DNA INTERACTIONS.....	99

4.4.2.1 DNA binding affinities.....	99
4.4.2.2 Topoisomerase I (Top I) mediated relaxation .....	99
4.4.2.3 Circular dichroism (CD) analysis .....	99
4.4.2.4 Cell cycle analysis .....	100
4.4.2.5 Immunodetection of $\gamma$ H2AX.....	101
4.4.2.6 Comet Assay .....	102
4.4.3 DETECTION OF APOPTOSIS.....	102
4.4.3.1 Apoptotic induction .....	102
4.4.3.2 Caspase 3/7, 8 and 9 activation.....	103
4.4.3.3 Confocal Imaging.....	103
4.4.4 INVESTIGATIONS OF MITOCHONDRIAL DYSFUNCTION .....	104
4.4.4.1 Mitochondrial Membrane Potential ( $\Delta\Psi_m$ ) .....	104
4.4.4.2 Mitochondrial superoxide production .....	105
4.4.4.3 Intracellular radical production.....	106
<b>4.5 CONCLUSION .....</b>	<b>108</b>
<b>4.6 SUPPORTING INFORMATION .....</b>	<b>111</b>
<b>4.7 REFERENCES.....</b>	<b>111</b>

## CHAPTER 5

### **BIS-MN<sup>2+</sup> BIS-1,10-PHENANTHROLINE OCTANEDIOATE INDUCES AUTOPHAGIC DI CELL DEATH VIA ROS-MEDIATED DNA DAMAGE..... 119**

<b>5.1 ABSTRACT .....</b>	<b>120</b>
<b>5.2 INTRODUCTION.....</b>	<b>121</b>
<b>5.3 MATERIALS AND METHODS .....</b>	<b>123</b>
5.3.1 MATERIALS AND REAGENTS.....	123
5.3.2.1 Circular dichroism spectrometry. ....	123
5.3.2.2 Viscosity.....	123
5.3.2.2 Topoisomerase I mediated relaxation.....	124
5.3.3 <i>IN CELLULO</i> STUDIES.....	124
5.3.3.1 Cell culture.....	124
5.3.3.2 Viability.....	124
5.3.3.3 Nexin® assay.....	125
5.3.3.4 MITOCHONDRIAL MEMBRANE POTENTIAL.....	125
5.3.3.5 Caspase 8 FAM and 9 SR, Caspase 3/7 FAM.....	125
5.3.3.6 Cell cycle analysis. ....	125
5.3.3.7 Immunodetection of $\gamma$ H2AX. ....	126
5.3.3.8 DNA degradation with COMET assay.....	126
5.3.4 ACQUISITION OF CONFOCAL IMAGES. ....	126
5.3.4.1 Cell morphology. ....	126
5.3.4.2 Autophagic detection with LC3. ....	127
5.3.4.3 Autophagic detection with MDC.....	127
5.4.5 STATISTICAL ANALYSIS. ....	127
<b>5.4 RESULTS AND DISCUSSION.....</b>	<b>128</b>
5.4.1 PREPARATION OF MN-ODA .....	128
5.4.2 <i>IN VITRO</i> DRUG-DNA INTERACTIONS REVEAL INTERCALATION AT THE MINOR GROOV .....	128
5.4.2.1 Topoisomerase I mediated relaxation .....	128
5.4.2.2 Circular Dichroism studies .....	129
5.4.3 GENOTOXICITY STUDIES IMPLY INDIRECT DNA DAMAGE .....	130
5.4.3.1 COMET analysis.....	130
5.4.3.2 Cell Cycle Analysis.....	131
5.4.3.3 Immunodetection of $\gamma$ H2AX.....	131

5.4.4 MN-ODA STIMULATES MILD CASPASE 9 RELEASE BUT DOES NOT TRIGGER EARLY OR LATE-STAGE APOPTOSIS IN SKOV3 CELLS.....	132
5.4.4.1 Annexin V .....	132
5.4.4.2 Caspase activation .....	133
5.4.4.3 Mitochondrial depolarisation.....	133
5.4.5 MN-ODA STIMULATES AUTOPHAGY PRIOR TO APOPTOSIS.....	134
5.4.6 CELL MORPHOLOGY REVEALS MN-ODA-PROMOTED APOPTOSIS.....	135
5.4.7 INITIATION OF AUTOPHAGY IS SUPEROXIDE-DEPENDENT.....	136
<b>5.5 CONCLUSIONS.....</b>	<b>138</b>
<b>5.6 SUPPORTING MATERIAL.....</b>	<b>139</b>
<b>5.7 REFERENCES.....</b>	<b>139</b>
 <b>CONCLUSION AND FUTURE PERSPECTIVES.....</b>	 <b>145</b>
 <b>APPENDICES A-D</b>	
<b>APPENDIX A .....</b>	<b>147</b>
S2.1 CORRESPONDING NUCLEASE ACTIVITY FOR 8-OXO-DG CONDITIONS .....	147
S2.2 DNA CLEAVAGE OPTIMISATION (HIGH CONCENTRATION RANGE WITH ADDED REDUCTANT) FOR PCR AMPLIFICATION STUDIES.....	147
S2.3 DNA CLEAVAGE OPTIMISATION (HIGH CONCENTRATION RANGE WITHOUT ADDED REDUCTANT) FOR PCR AMPLIFICATION STUDIES .....	148
S2.4 PCR PRIMER DESIGN .....	148
S2.5 PCR AMPLIFICATION STUDIES WITHOUT REDUCTANT (HIGH CONCENTRATION RANGE) .....	149
S2.6 PCR AMPLIFICATION STUDIES WITH REDUCTANT (LOW CONCENTRATION RANGE) .....	149
<b>APPENDIX B .....</b>	<b>150</b>
S3.1 NCI-60 NUMERICAL VALUES FOR GI <sub>50</sub> , TGI, LC <sub>50</sub> .....	150
<b>APPENDIX C .....</b>	<b>151</b>
S1. MOLECULAR STRUCTURES OF CU-ODA AND CU-TERPH. ....	151
S2. NCI-60 HUMAN TUMOUR DRUG SCREEN.....	151
S3. PREFERENTIAL DNA BINDING .....	154
S4. TOPOISOMERASE I RELAXATION .....	155
S5. INDIVIDUAL CHANNEL OF CONFOCAL IMAGES .....	156
S6. MITOCHONDRIAL DEPOLARISATION SCATTER PLOTS .....	157
<b>APPENDIX D .....</b>	<b>158</b>
S1. TOPOISOMERASE I MEDIATED RELAXATION OF ETHIDIUM BROMIDE. ....	158
S2. VISCOSITY PROFILE OF MN-ODA SALMON TESTES DNA.....	158
S3. VIABILITY PROFILES OF MN-ODA AND POSITIVE CONTROLS.....	158

## Table of Figures

Figure 1. 1A. Summary of structural differences between A-, B- and Z-DNA; <sup>13</sup> B. conformational preferences of the 2' -deoxyribose rings of DNA and C. X-ray structures of A-, B- and Z-DNA from PDB files 1VJ4, 1BNA and 2DCG, respectively.....	4
Figure 1. 2 Molecular structures of, A. globally approved Pt(II) complexes cisplatin, carboplatin and oxaliplatin and B. those approved in single markets lobaplatn, nedaplatin and heptaplatin, C. polynuclear platinum complexes (PPCs) [ <i>trans</i> PtCl(NH <sub>3</sub> ) <sub>2</sub> ] <sub>2</sub> -μ- <i>trans</i> -Pt(NH <sub>3</sub> ) <sub>2</sub> (NH <sub>2</sub> (CH <sub>2</sub> ) <sub>6</sub> NH <sub>2</sub> ) <sub>2</sub> ] <sup>4+</sup> (Triplatin, BBR3464), [ <i>trans</i> -Pt(NH <sub>3</sub> ) <sub>2</sub> (NH <sub>2</sub> (CH <sub>2</sub> ) <sub>6</sub> NH <sub>2</sub> ) <sub>2</sub> ] <sup>6+</sup> (AH44), and [ <i>trans</i> Pt(NH <sub>3</sub> ) <sub>2</sub> (NH <sub>2</sub> (CH <sub>2</sub> ) <sub>6</sub> NH <sub>3</sub> ) <sub>2</sub> ]-μ-( <i>trans</i> -Pt(NH <sub>3</sub> ) <sub>2</sub> (NH <sub>2</sub> (CH <sub>2</sub> ) <sub>6</sub> NH <sub>2</sub> ) <sub>2</sub> )] <sup>8+</sup> (TriplatinNC). .....	5
Figure 1. 3 Pathways of cisplatin cytotoxicity (blue arrows) and resistance (orange arrows). i) membrane-bound influx proteins (copper transport influx pump CTR1, efflux pump ATP7A/B and glutathione adducts efflux pump GS-X) and high mobility group proteins (HMG). ii) Pt-adducts in order of occurrence: 1,2-intrastrand G-G (60-65%) and A-G (20%) and 1,3 interstrand G-G (2%). Cisplatin is incorporated into the cell through CTR1 (A). Under-expression of CTR1 results in decreased cellular accumulation of cisplatin (B). Activation through hydrolysis (C), facilitating DNA platination and distortion (D) with no, or little, inhibition of enzymatic repair activity through HMG (D) resulting induced apoptotic cell death. Acquired resistance can occur from enhanced DNA repair mechanisms and Pt adduct excision (E). Other resistance factors such as inactivation through thiol-rich reductants (F), GSH as example) and GS-Pt (and GS-Pt-SG) adduction elimination through GS-X pump (G). Accelerated efflux of cisplatin through overexpression of copper transporters, ATP7A/B (H). Membrane recognition and intracellular accumulation of polynuclear Pt complexes through heparan sulphate proteoglycans (HSPG) (I). .....	7
Figure 1. 4 Molecular structures of platinum(II), Rh(III) and Ru(II) intercalating and insertion complexes. ....	8
Figure 1. 5 Intercalation and insertion. A. D-a-[Rh{(R,R)-Me <sub>2</sub> trien}phi] <sup>3+</sup> intercalated into 5'-G(5[U)TGCAAC-3' with additional stabilisation by H-bonds from the ancillary ligand (PDB 454d), black lines indicate hydrogen bonds <sup>57</sup> and, B. D-[Rh(bpy) <sub>2</sub> (chrysi)] <sup>3+</sup> inserted into (5'-CGGAAATTCCCG-3'), displacing a mismatched AC pair (PDB 2O1I). <sup>67</sup> .....	9
Figure 1. 6 TriplatinNC bound to Dickerson-Drew dodecamer (B-DNA) through backbone tracking A. and groove spanning and, B. interactions. <sup>75</sup> N-H·····O=P hydrogen bonds shown as dashed blue lines. ....	11
Figure 1. 7 Molecular structures of selected metal complexes discussed in this review. ....	14
Figure 1. 8 A. Cleavage profile of Cu-Ph in the presence of radical-specific antioxidants and trapping agents. Table insert with scavengers <sup>a</sup> utilised in nuclease studies and intracellular antioxidants <sup>b</sup> . Electrophoretic gels of topoisomerase relaxation assay for intercalating agents, B. EtBr and C. known topoisomerase poison doxorubicin, Doxo (unpublished results). .....	15
Figure 1. 9 Minor groove binding competition assay using polynuclear platinum complexes. ....	16
Figure 1. 10 A. Molecules with fluorescent DNA binding properties; DAPI, Doxo (doxorubicin), PI (propidium iodide), EtBr (ethidium bromide) and Hoechst 33258 and B. non-covalent DNA recognition elements; MG (methyl green, major groove binder), Net (netropsin, minor groove binder) and cobalt(III) hexammine ([Co(NH <sub>3</sub> ) <sub>6</sub> ] <sup>3+</sup> , electrostatic agent). ....	18
Figure 1. 11 A. Determination of molar extinction coefficients for double stranded DNA and extinction coefficients and B. λ <sub>max</sub> values for synthetic polymers of varying GC content. ....	20



Figure 1. 12 A. B $\rightarrow$ Z NaCl titration of alternating co-polymer poly[d(G-C) <sub>2</sub> ] with increasing amounts of salt (unpublished results) and, B. and wavelengths of interest for CD DNA studies. ....	22
Figure 1. 13 Relative viscosity values of organic and inorganic compounds bound to duplex stDNA. ....	24
Figure 1. 14 ESI-MS/MS of free (top) and PPC (either TriplatinNC or AH44) adducted (bottom) 5'-d(TCTCCCAGCGTGCGCCAT) at 100 and 120V of collisional energy, respectively. <sup>40</sup> Fragmentation of the glycosidic bonds is prevalent throughout the free, with the region of enhanced stability in red. The associated fragment ions ( $w_8^{2-}$ , $w_9^{2-}$ , and $a_9$ - $a_{12}$ using standard McLuckey nomenclature <sup>136,137</sup> ) are absent in the adduct indicating the area of PPC binding. ....	25
Figure 1. 15 { <sup>1</sup> H, <sup>15</sup> N} HSQC NMR of TriplatinNC (left) and Dickerson-Drew Duplex (DDD, right). Satellites from <sup>1</sup> J( <sup>15</sup> N- <sup>195</sup> Pt) are clearly visible. Adapted with permission from Qu <i>et al.</i> <sup>145</sup> .....	26
Figure 1. 16 A. Nuclear condensation observed in colorectal cancer cells, HTC116 when treated with TriplatinNC. B. Induction of double strand break detected <i>via</i> $\gamma$ H2AX foci (green) and nuclear counterstain (red) in ovarian cancer cells SKOV3. C. COMET assay evaluation of BBR3610 and DACH analogue interstrand crosslinks in irradiated HCT116 cells. Images reproduced with permission from original publications. <sup>86,154,160</sup> .....	29
Figure 2. 1 Lane 1-4 (A-D) DNA cleavage reactions with 250 nM, 500 nM, 1.0 $\mu$ M and 2.5 $\mu$ M test complex (A: Cu-Phen, B: Cu-DPQ-Phen, C: Cu-DPPZ-Phen and D: Cu-Terph), 400 ng superhelical pUC19 and 1 mM added Na-L-ascorbate incubated at 37 °C for 30 minutes. Lanes 5-16 (A-D) DNA cleavage reactions in the presence of recognition elements, methyl green (MG), netropsin (Net) and [Co(NH <sub>3</sub> ) <sub>6</sub> ]Cl <sub>3</sub> (Co(III)), where 400 ng pUC19 was initially pre-treated with 8 $\mu$ M of respective non-covalent binding control at 37 °C for 45 minutes and then with 250 nM, 500 nM, 1 $\mu$ M and 2.5 $\mu$ M test complex in the presence of 1 mM added Na-L-ascorbate at 37 °C for 30 minutes. ....	49
Figure 2. 2 DNA cleavage reactions in the presence of ROS scavengers. 400 ng of SC pUC19 was incubated for for 30 min at 37 °C with 250 nM, 500 nM, 1 $\mu$ M and 2.5 $\mu$ M of test complex (A: Cu-Phen, B: Cu-DPQ-Phen, C: Cu-DPPZ-Phen and D: Cu-Terph) in the presence of 1 mM added Na-L-ascorbate for 30 minutes. Lanes 1-4 metal complex only, lanes 5-8: complex + 10 mM NaN <sub>3</sub> , lanes 9-12: complex + 10 mM KI, lanes 13-16: complex + 10% DMSO, and lanes 17-20: complex + 77% D <sub>2</sub> O.....	50
Figure 2. 3 Structure and quantification of 8-oxo-dG. Graph represents level of generated 8-oxo-dG as nM (left axis) and ng/mL (right axis). 3000 ng of SC pUC19 with 10 and 20 $\mu$ M of test complexes Cu-Phen, Cu-DPQ-Phen, Cu-DPPZ-Phen and Cu-Terph with 1 mM Na-L-ascorbate were incubated at 37 °C for 30 minutes and followed by ELISA protocol. ....	51
Figure 2. 4 Illustration of steps involved in a successful PCR reaction (denaturation, primer annealing, primer extension and template amplification), B. the impact of a bound metal complex as physical block of the primer extension step, C. inhibition of DNA amplification in the PCR cycle through the oxidative damage of template strand. ....	52
Figure 2. 5 400 ng pUC19 DNA was initially exposed to 2.5, 5, 10, 20, 30, 40 and 50 $\mu$ M of each test complex in the presence of 1 mM added reductant at 37 °C for 30 minutes. 20 ng of damaged DNA template was removed and PCR reaction was carried out with each varying GC content primer set at optimum annealing temperatures and analysed using gel electrophoresis. Fig. A Lane 1: 35% GC control, lane 2-8 35% GC + Cu-Phen, lane 9-15 35%	

GC + Cu-DPQ-Phen and lane 15-21: 35% GC + Cu-Terph. Fig. B 50% GC and Fig. C 63% GC respectively. All sequences generated were 120 base pairs..... 53

- Figure 3. 1 Heat map data representing  $LC_{50}$  concentrations of Cu-Ph across the NCI 60 human cancer cell line panel. Concentration ranges from most cytotoxic (1 – 5  $\mu$ M shown in black) to least cytotoxic (>100  $\mu$ M shown in light blue). ..... 66
- Figure 3. 2 Molecular structure of Cantharidin (NSC S61805), antineoplastic-353527 (NSC S353527), the active form of prodrug tamoxifen, 4-hydroxy-tamoxifen (NSC S180973), Mitotane (NSC S38721), and 7-*O*-methylnogalarol (NSC S102815). ..... 67
- Figure 3. 3 Competitive fluorescence binding of netropsin, actinomycin D, and Cu-Ph to ethidium bromide (12.6  $\mu$ M) saturated solutions of calf thymus DNA, *Micrococcus lysodeikticus* DNA (ML-DNA), poly[d(A-T)<sub>2</sub>], and poly[d(G-C)<sub>2</sub>] polynucleotides (10  $\mu$ M). ..... 68
- Figure 3. 4 DNA cleavage reactions in the presences of ROS-specific scavengers. 400 ng of SC pUC19 was incubated for 1 h at 37°C with complex concentrations of 0.5, 1, 2.5 and 5  $\mu$ M in the presence of 25 mM NaCl, 0.5 mM L-Asc in 80 mM HEPES. Lane 1: DNA only, Lanes 2-5: 0.5, 1, 2.5, 5  $\mu$ M Cu-Ph, Lanes 6-9: + 10 % DMSO, Lanes 10-13: + 10 mM tiron, Lane 14-17: + 10 mM KI, Lanes 18-21: + 10mM NaN<sub>3</sub>. ..... 69
- Figure 3. 5 A. Viability profile of Cu-Ph in SKOV3 cells in the presence of intracellular scavengers. Cells were treated with 1 mM of tiron (Tir), D-mannitol (Mann) and pyruvate (Pyr) for 1 h prior to Cu-Ph addition (3  $\mu$ M) and incubated for 24 h. B. Scavengers utilized within this study where <sup>a</sup>ROS scavengers present in *in vitro* DNA oxidation experiment and <sup>b</sup> scavengers used in intracellular work. C. Molecular structure of tiron (TH<sub>2</sub>) and D-mannitol. D. Reaction equations of radical species and their respective scavengers. Not significant (ns)  $p > 0.05$ ,  $**P \leq 0.01$ ,  $***P \leq 0.0001$ . ..... 70
- Figure 3. 6 Nexin Assay scatter plots; population represented in quadrants for viable cells (lower left), mid (lower right) and late stages of apoptosis (upper right). Graph depicting mid-apoptosis show positive for annexin V only, population for late apoptosis are positive for annexin V and 7-AAD. Not significant (ns)  $p > 0.05$ ,  $*p \leq 0.05$ ,  $**P \leq 0.01$ ,  $***P \leq 0.001$ . 71
- Figure 3. 7 Caspase 3/7, 8 and 9 activation after 24 h incubation with drug. Not significant (ns)  $p > 0.05$ ,  $*p \leq 0.05$ ,  $**P \leq 0.01$ ,  $***P \leq 0.001$ . ..... 72
- Figure 3. 8 Mitochondrial depolarization scatter plots for Doxo, CCCP and Cu-Ph where polarized mitochondria are shown in purple, to depolarized mitochondria in pink and blue (Y axis = JC-1 orange, X axis = JC-1 green) The molecular structure of indicative mitochondrial dye JC-1 (5,5',6,6'-tetrachloro-1,1',3,3'-tetraethylbenzimidazolocarbo-cyanine iodide) also shown. Graph represents population percentages of depolarized mitochondria for Doxo, CCCP and Cu-Ph. Not significant (ns)  $p > 0.05$ ,  $*p \leq 0.05$ ,  $**P \leq 0.01$ ,  $***P \leq 0.001$ . ..... 75
- Figure 3. 9 40X confocal images of SKOV3 cells treated with Cu-Ph (3  $\mu$ M), CCCP (75  $\mu$ M) and Doxo (1  $\mu$ M). The nucleus is stained with DAPI (blue), cytoskeleton with Alexa Flour 488-Phalloidin and mitochondria with MitoTracker Deep Red. ..... 76

Figure 4. 1 A. Structure of the B-DNA Dickerson-Drew dodecamer (DDD) d[CGCGAATTTCGCG]<sub>2</sub> positioned from the minor groove (PDB entry 1BNA). DNA backbone (connecting P positions), gray60; colour code for DNA bases: guanine, orange; cytosine, light orange; adenine, slate; thymine, density (cartoon mode, bases shown as spheres). B. Inset structure of the AATT minor groove tract with accessible C1' deoxyribose hydrogens shown (H, white) along with Watson-Crick H-bonding pairs (yellow dashes). Colour code for DNA bases: adenine, slate; thymine, density (shown as sticks). Figure A and B generated by PyMOL Molecular Graphics System, Version 1.5.0.4 Schrödinger, LLC. C.

Cu <sup>+</sup> mediated electron transfer reactions: a cascade of reactive oxygen species (ROS) proceeds from molecular oxygen undergoing 1-electron reduction to superoxide, followed then by dismutation to hydrogen peroxide (and oxygen - not shown), and finally Fenton-like reduction to the hydroxyl radical. D. Structures of the major groove binder doxorubicin, and minor groove targeting compounds neocarzinostatin and [Cu(1,10-phenanthroline) <sub>2</sub> ] <sup>+</sup> .....	89
Figure 4. 2A. Molecular structure of <i>di</i> -nuclear copper complexes [ {Cu(phen) <sub>2</sub> } <sub>2</sub> (μ-oda)] <sup>2+</sup> (Cu-Oda) and B. [ {Cu(phen) <sub>2</sub> } <sub>2</sub> (μ-terph)] <sup>2+</sup> (Cu-Terph). C. Heat map representation of LC <sub>50</sub> concentrations calculated from 5-dose cytotoxicity screen across the NCI-60 human cancer cell line panel. Concentration ranges from most cytotoxic (0.1 – 0.5 μM shown in navy) through to least cytotoxic (>100 μM shown in brown). D. Pearson correlation coefficients of LC <sub>50</sub> profiles generated from the NCI DTP COMPARE algorithm, where standard agents and market drugs are grouped according to their mode of cytotoxic action.....	98
Figure 4. 3A. Topoisomerase I unwinding across concentration range 0.10 - 400 μM for Cu-Oda and Cu-Terph. B. CD spectra of Cu-Oda with stDNA and alternating co-polymers poly[d(A•T <sub>2</sub> )] and poly[d(G•C <sub>2</sub> )] at 1 - 7.5% loading ratios. C. Cell cycle phase fractionations for Cu-Oda and Cu-Terph incubated for 24 h at 0.5, 1.0 and 2.0 μM. D. Double strand breaks (DSBs) induced by Cu-Oda and Cu-Terph, detected by immunostaining of γH2AX with median intensity fluorescence (MFI) presented for <i>di</i> -Cu <sup>2+</sup> complexes and Dox. Nonsignificant (ns) <i>p</i> > 0.05; * <i>p</i> ≤ 0.05; ** <i>p</i> ≤ 0.01; *** <i>p</i> ≤ 0.001.....	100
Figure 4. 4. DNA damage detected through the alkaline comet assay, A. Tail moments and DNA content of control and 1.0 μM Cu-Oda, Cu-Terph and Dox, B. Mean tail moment of >80 comets analysed, C. Typical comet images acquired for SKOV3 non-treated cells, and those treated with Cu-Oda, Cu-Terph and Dox.....	102
Figure 4. 5A. SKOV3 cells are treated over 24 h with varying concentration of Cu-Oda and Cu-Terph (0.5 - 2.0 μM) and control agent Dox (1.0 μM). A. Populations of early apoptotic cells exhibiting positive staining for Annexin V only. B. Late apoptotic population detected through positive staining for Annexin V and 7-AAD. C. Detection of caspase 3/7 in the absences of 7-AAD positive staining indicative of mid-apoptotic activation. D. Detection of late apoptotic release of caspase 3/7 through the detection of 7-AAD positive cells. E. Population of caspase 8 (extrinsic pathway) F. Activation of caspase 9 (intrinsic pathway). G. 100× magnification of SKOV3 cells treated with Dox (1.0 μM), CCCP (75 μM) and dinuclear copper complexes, Cu-Oda and Cu-Terph (1.0 μM). The nucleus is stained with DAPI, F-actin with Alexa Flour 488-Phalloidin and mitochondria with MitoTracker Deep Red. Scale bar indicates 10 μm. Individual channels are shown in Figure S4. Nonsignificant (ns) <i>p</i> > 0.05; * <i>p</i> ≤ 0.05; ** <i>p</i> ≤ 0.01; *** <i>p</i> ≤ 0.001. ....	104
Figure 4. 6 SKOV3 cells were treated with Cu-Oda, Cu-Terph and positive controls Dox and CCCP at indicated concentrations for 24 h. A. Population of depolarised mitochondria through the detection of potential-sensitive shift in JC-1 emission. Hypsochromic shifts, evident in scatter plot, demonstrates drug-induced depolarisation (Figure S5). B. Detection of MitoSOX red population indicative of superoxide-selective fluorescence activation. The molecular structures of dyes employed are given (top right). C. Viability results of Cu-Oda, Cu-Terph and Dox at 1.0 μM in the absence and presence of 1 mM ROS specific scavengers (Table 4.1 insert). Nonsignificant (ns) <i>p</i> > 0.05; * <i>p</i> ≤ 0.05; ** <i>p</i> ≤ 0.01; *** <i>p</i> ≤ 0.001. ....	106
Figure 4. 7 Proposed mechanism of action for <i>di</i> -copper(II) agents Cu-Oda and Cu-Terph. Complexes are incorporated into the cell through copper transport protein (Ctr1). <i>Di</i> -Cu <sup>2+</sup> complexes take one of two pathways i.) nuclear localisation and intercalative binding at the minor groove of duplex DNA (anionic); ii.) mitochondrial accumulation due to MMP (ΔΨ <sub>m</sub> ),	

facilitated by the cationic complex charge and lipophilicity of phenanthroline groups. Intracellular generation of superoxide ( $O_2^{\cdot-}$ ) and singlet oxygen ( $^1O_2$ ), detected through radical specific antioxidants, induce significant DNA degradation through the formation of double strand breaks (DSBs) when quantified by  $\gamma$ H2AX and comet. Enhanced levels of superoxide within the mitochondrial (MitoSOX) causes collapse transmembrane potential measured through the extent of mitochondrial depolarisation (JC-1). This results in the release of cytochrome *c* and activation of the intrinsic pathway through apoptosome formation and activation of initiator caspase 9 and executioner caspase 3 or 7. Apoptosis was quantitatively measured through Annexin V and visualised by confocal microscopy..... 108

- Figure 5. 1A. The cation  $[Mn_2(\eta^1\eta^1\mu_2\text{-oda})(phen)_4(H_2O)_2]^{2+}$ , B. Anion  $[Mn_2(\eta^1\eta^1\mu_2\text{-oda})(phen)_4(\eta^1\text{-oda})_2]^{2-}$ , and C. Hydrogen bonded chains. Hydrogen atoms omitted for clarity, hydrogen bonds indicated by black dashed lines. Redrawn from coordinates taken from reference.<sup>27</sup> Colour key: C (grey), O (red), N (blue) and Mn (purple). ..... 128
- Figure 5. 2 A. Release of topological tension of supercoiled plasmid DNA by Mn-Oda and, B. Dox. C. CD profile of Mn-Oda with stDNA and alternating co-polymers poly[d(A-T)<sub>2</sub>] and poly[d(G-C)<sub>2</sub>] under drug loadings of 1.0 – 2.5% (respective *r* values of 0.010 – 0.025). .... 130
- Figure 5. 3 SKOV3 cells were treated with 1.0  $\mu$ M Mn-Oda and Dox for 24 h and subsequently studied in the following assays. A. Comet assay analysis where the frequency of tail moment (A.U.). B. Examples of typical COMET shapes are represented below respective legends. C. Cell cycle histograms and, D. Cell cycle phase (G0/G1, S and G2/M) distributions. E. Immunodetection of  $\gamma$ H2AX positive cells. Not significant  $p > 0.05$ , \*  $p \leq 0.05$ , \*\* $p \leq 0.01$ , \*\*\* $p \leq 0.001$ . ..... 132
- Figure 5. 4 Apoptotic investigation of Mn-Oda, A. Early and B. late apoptosis measured with the translocation of Annexin V substrate. C. Detection of caspase 3/7 in mid and D. late populations. E. Activation of initiator caspase 8 and F. caspase 9. G. Extent of mitochondrial depolarisation detected through bathochromic shift of JC-1 emission upon formation of J-aggregates. Not significant  $p > 0.05$ , \*  $p \leq 0.05$ , \*\* $p \leq 0.01$ , \*\*\* $p \leq 0.001$ . ..... 134
- Figure 5. 5 Confocal images of SKOV3 100X treated with Mn-Oda, Rapa or SAHA to examine, A. MDC staining of acidic vacuoles (blue). White lines indicate cross sections for fluorescence quantification profiles (see figure 6B). B. Immunofluorescent staining of LC3 (red) and DAPI (blue) control. C. Morphological changes in cellular structure. Nuclei were stained with DAPI (blue), F-actin with Alexa Fluor 488 conjugated to phalloidin (green) and mitochondrial with MitoTracker deep red (red). All scale bars (control, bottom right) are 10  $\mu$ m. .... 135
- Figure 5. 6 A. Schematic of autophagy pathway.<sup>15,20,50</sup> Due to the number of autophagy-related genes (ATGs) and the complexity of their role in the autophagy pathway, the family is represented by ‘ATG’ (purple) for simplicity, i. Initiation begins with the formation of isolation membrane known as a phagophore, engulfing cytoplasmic material, ii. Cytosolic LC3-I is converted to the membrane-associated form LC3-II, through phosphatidylethanolamine (PE) lipidation and incorporated into autophagosomal double-membrane, iii. Docking and fusion of lysosome or late endosomes results in the formation of iv. autophagolysosome. Maturation and catabolic degradation results in recycling and restoration of nutrient stores. Autophagic inducers employed are Rapa and SAHA (purple pathway). Autophagic inhibitors are 3-methyladenine (3-MA),  $NH_4Cl$  and chloroquine (CQ) (orange pathway) while antioxidants utilised are tiron, mannitol (man), histidine (his) and sodium pyruvate (Py) (teal pathway). Induction was probed through immunodetection of LC3 with fluoregenicly conjugated secondary antibody and monodansylcadaverine (MDC), B.

Intensity profiles (indicated in Figure 5C) were analysed using Image J on raw images in 8-bit format with no further modification. C. Differential viability percentages in the presence of radical scavengers and autophagy inhibitors pre-treated at 1 mM (with the exception of CQ, 10 $\mu$ M) 2 h prior to drug addition. Mn-Oda, SAHA and Rapa were treated at respective concentrations, 1 $\mu$ M, 100 $\mu$ M and 50 $\mu$ M, over 24 h. ....	137
Figure S2. 1 DNA cleavage reactions with 10 and 20 $\mu$ M test complex, 3000 ng superhelical pUC19 and 1 mM added Na-L-Ascorbate incubated at 37 °C for 30 minutes. Lane 1: pUC19 only, lane 2,3: 10 and 20 $\mu$ M Bis-Phen, lane 4,5: 10 and 20 $\mu$ M Cu-DPQ-Phen, lane 6,7: 10 and 20 $\mu$ M Cu-DPPZ-Phen, lane 8-9: 10 and 20 $\mu$ M Cu-Terph. ....	147
Figure S2. 2 DNA cleavage reactions with 2.5, 5, 10, 20, 30, 40 and 50 $\mu$ M test complex, 400 ng superhelical pUC19 and 1 mM added Na-L-Ascorbate incubated at 37 °C for 30 minutes. Lane 1: pUC19 only, lane 2-8: Bis-Phen and lane 9-15: Cu-DPQ-Phen, lane 16-22: Cu-DPPZ-Phen and lane 23-29: Cu-Terph. ....	147
Figure S2. 3 DNA cleavage reactions with 2.5, 5, 10, 20, 30, 40 and 50 $\mu$ M test complex, 400 ng superhelical pUC19 without added Na-L-Ascorbate incubated at 37 °C for 30 minutes. Lane 1: pUC19 only, lane 2-8: Bis-Phen and lane 9-15: Cu-DPQ-Phen, lane 16-22: Cu-DPPZ-Phen and lane 23-29: Cu-Terph. ....	148
Figure S2. 4 400 ng pUC19 DNA was initially exposed to 2.5, 5, 10, 20, 30, 40 and 50 $\mu$ M of each test complex in the absence of added reductant at 37 °C for 30 minutes. 20 ng of complex exposed DNA template was removed from the reaction and PCR reaction was carried out as previously described with each varying G·C content primer set at optimum annealing temperatures and analysed using gel electrophoresis. Fig. A Lane 1: 35% G·C control, lane 2-8 35% G·C + Cu-Phen, lane 9-15: 35% G·C + Cu-DPQ-Phen and lane 16-22: 35% G·C + Cu-Terph. (B) 50% G·C and (C) 63% G·C respectively. All sequences generated were 120 base pairs. ....	149
Figure S2. 5 400 ng pUC19 DNA was initially exposed to 250 nM, 500 nM, 1 $\mu$ M and 2.5 $\mu$ M of each test complex in the presence of 1 mM added reductant at 37 °C for 30 minutes. 20 ng of complex exposed DNA template was removed from the reaction and PCR reaction was carried out as previously described with each varying G·C content primer set at optimum annealing temperatures and analysed using gel electrophoresis. Fig. A Lane 1: 35% G·C control, lane 2-5 35% G·C + Cu-Phen, lane 6-9 35% G·C + Cu-DPQ-Phen and lane 10-13: 35% G·C + Cu-Terph. (B) 50% G·C and (C) 63% G·C respectively. All sequences generated were 120 base pairs. ....	149
Figure S4. 1 Molecular structure of $[\{Cu(phen)_2\}_2(\mu-oda)]^{2+}$ (Cu-Oda, where oda = octanedioate) and $[\{Cu(phen)_2\}_2(\mu-terph)]^{2+}$ (Cu-Terph, where terph = terephthalate).....	151
Figure S4. 2 Heat map of GI <sub>50</sub> concentration ranging from less than 0.1 $\mu$ M (grey) to 5 $\mu$ M (light blue) for Cu-Terph and Cu-Oda.....	153
Figure S4. 3 Competitive fluorescence binding of Cu-Oda and Cu-Terph to ethidium bromide (12.6 $\mu$ M) saturated solutions of calf thymus DNA, <i>Micrococcus lysodeikticus</i> DNA (ML-DNA), poly[d(A·T) <sub>2</sub> ], and poly[d(G·C) <sub>2</sub> ] polynucleotides (10 $\mu$ M) in 40 mM NaCl after 1 h incubation (final volume of 100 $\mu$ l). ....	154
Figure S4. 4 Topoisomerase I unwinding across concentration range 0.01 – 400 $\mu$ M for Dox and ethidium bromide. ....	155

Figure S4. 5 100× confocal images of SKOV3 cells treated with Cu-Oda and Cu-Terph (1 $\mu$ M), CCCP (75 $\mu$ M) and Doxo (1 $\mu$ M). The nucleus is stained with DAPI (blue), cytoskeleton with Alexa Flour 488-Phalloidin and mitochondria with MitoTracker Deep Red. ....	157
Figure S4. 6 Mitochondrial depolarisation scatter plots where polarised mitochondria are shown in purple, to depolarised mitochondria in pink and blue. A) cells only, B) 1.0 $\mu$ M Dox, C) 75 $\mu$ M CCCP, D – F) 0.5, 1.0, 2.0 $\mu$ M Cu-Oda and G – I) 0.5, 1.0, 2.0 $\mu$ M Cu-Terph. ....	157
Figure S5. 1 Topoisomerase I-induced DNA relaxation in the presence of ethidium bromide .....	158
Figure S5. 2 Viscosity properties ( $\eta / \eta_0$ ) of Mn-Oda at drug-DNA ratios (r) 0.01 – 0.20. ....	158
Figure S5. 3 Viability profile after 24 h exposure to Mn-Oda (1 $\mu$ M), Dox (1 $\mu$ M), CCCP (75 $\mu$ M), SAHA (100 $\mu$ M) and Rapa (50 $\mu$ M). Not significant $p > 0.05$ and *** $p \leq 0.001$ . ....	158

## Table of Schemes

Scheme 2. 1 Molecule structures of the copper(II) complex cations examined in this study. ....	44
Scheme 3. 1 Molecular structures of the Cu(II) complex [Cu(ph)(phen)] (Cu-Ph) and clinical antitumor agent doxorubicin (Doxo), carbonyl cyanide m-chlorophenyl hydrazine (CCCP), casiopeínas [Cu(4,4'-dimethyl-2,2'-bipyridine)(acetylacetonate)(H <sub>2</sub> O)](NO <sub>3</sub> ) (Cas III-ia) and [Cu(4,7-dimethyl-1,10-phenanthroline)(glycine)(H <sub>2</sub> O)](NO <sub>3</sub> ) (Cas II-gly). ....	63

## Table of Tables

Table 1. 1 Helical unwinding and bending angles for established platinum complexes. ....	16
Table 1. 2 Influence of standard agents and selected copper phenazine complexes on the thermal melting of synthetic alternating copolymers. <sup>85</sup> .....	21
Table 2. 1 Summary of DNA binding properties of tested complexes toward calf thymus DNA (ctDNA) along with synthetic nucleic acid polymers poly[d(A-T) <sub>2</sub> ] and poly[d(G-C) <sub>2</sub> ]. ....	45
Table 2. 2 Scavengers and stabilisers utilised within this study. ....	50
Table 3. 1 Pearson's correlation coefficients ( $r$ ) generated from the NCI DTP COMPARE algorithm. ....	66
Table 3. 2 Apparent binding constants ( $K_{app}$ ) of Cu-Ph, actinomycin D and netropsin. $K_{app} = K_e \times (12.6 / C_{50})$ where $K_e = 9.5 \times 10^6$ M/bp and $C_{50}$ = concentration that causes 50% reduction in EtBr fluorescence. ....	68
Table 4. 1 Radical scavenging specificity of antioxidants utilised within viability study. ....	106
Table S3. 1 NCI-60 results. Concentrations required for 50 % growth inhibition ( $GI_{50}$ ), total growth inhibition (TGI) and 50 % lethal concentrations ( $LC_{50}$ ) were extracted from concentration-response curves by linear interpolation for the following cancers types: <sup>38</sup> leukemia (Leuk), non-Small Cell Lung (NSCL), colon, central nervous system, (CNS), melanoma (Mel), ovarian (Ov), prostate (Pros) and breast. ....	150
Table S4. 1 NCI-60 $GI_{50}^a$ , $LC_{50}^b$ and $TGI^c$ concentrations (molar, M) .....	151
Table S4. 2 Pearson correlation coefficients ( $r$ ) of $GI_{50}$ concentrations generated from the NCI DTP COMPARE algorithm. Criteria threshold $> 0.2$ for Cu-Oda or Cu-Terph. ....	153

Table S4. 3 Apparent binding constants ( $K_{\text{app}}$ ) of dinuclear $\text{Cu}^{2+}$ complexes, actinomycin D (Act D) and netropsin. Fluorescent profiles of Cu-Oda and Cu-Terph ethidium bromide displacement are shown in Figure S2.....	154
---	-----

## Abbreviations

A	Adenine
C	Cytosine
Caspase	Cysteine-dependent aspartate-specific proteases
CAT	Catalase
CCCP	Carbonyl cyanide <i>m</i> -chlorophenyl hydrazine
CD	Circular Dichroism spectroscopy
ctDNA	Calf thymus DNA
CTR1	Copper uptake transport protein
Cu/Zn-SOD	Copper and Zinc superoxide dismutase
DDD	Dickerson Drew dodecamer
DMSO	Dimethylsulfoxide
DNA	Deoxyribose nucleic acid
DSBs	Double stranded breaks
dsDNA	Double stranded DNA
Dox	Doxorubicin
DPPN	Benzol-dipyridol[3,2- <i>a</i> :2' 3'- <i>c</i> ]phenazine
DPPZ	Dipyridol[3,2- <i>a</i> :2',3'- <i>c</i> ]phenazine
DPQ	Dipyrido[3,2- <i>d</i> :2',3'- <i>f</i> ]quinoxaline
D <sub>2</sub> O	Deuterated water
EtBr	Ethidium bromide
Et <sup>+</sup>	Ethidium cation
EtOH	Ethanol
G	Guanine
H <sub>2</sub> O <sub>2</sub>	Hydrogen peroxide
IC <sub>50</sub>	half maximal inhibitory concentration
IR	Infrared spectroscopy
<i>K</i> <sub>app</sub>	Apparent binding constant
LC-3	Microtubule associated protein 1 light weight chain 3
lcDNA	Linear DNA
MDC	Monodansylcadaverine
ML-DNA	<i>Micrococcus luteus</i> DNA
ocDNA	Open circular DNA
<sup>1</sup> O <sub>2</sub>	Singlet oxygen
•OH	Hydroxyl radical
O <sub>2</sub>	Molecular oxygen



$O_2^{\bullet -}$	Superoxide radical
$^1O_2$	Singlet oxygen
Oda	Octanedioate
PCR	Polymerase chain reaction
Poly[(A-T) <sub>2</sub> ]	Poly(deoxyadenylic-thymidylic) acid sodium salt
Poly[(G-C) <sub>2</sub> ]	Poly(deoxyguanylic-deoxycytidylic) acid sodium salt
Phen	1,10-Phenanthroline
Phen-Dione	1,10-Phenanthroline-5,6-dione
Rapa	Rapamycin
RNA	Ribonucleic acid
ROS	Reactive oxygen species
rpm	rotations per minute
SAHA	Suberoylanilide hydroxamic acid
SKOV3	Human ovarian carcinoma cell line
SOD	Superoxide dismutase
SODm	Superoxide dismutase mimetic
SSBs	Single strand breaks
ssDNA	Single stranded DNA
stDNA	Salmon testes DNA
T	Thymine
Terph	Terephthalate
T <sub>M</sub>	Thermal melting
Topo	Topoisomerase
γH2AX	Phosphorylated H2AX histone

## Units of Measurement

Å	Angstrom
bp	Base pair
cm	Centimetre
cm <sup>-1</sup>	Reciprocal wavelength
cP	Centipoise
C <sub>50</sub>	Concentration required to reduce 50% fluorescence
°C	Degrees Celsius
ΔT <sub>M</sub>	Difference in thermal melting
EC <sub>50</sub>	Concentration causing half-maxima response
ε <sub>max</sub>	Molar absorption coefficient
g	Gram

GI <sub>50</sub>	Concentration causing 50% growth inhibition
h	Hour
Hz	Hertz
IC <sub>50</sub>	Concentration causing 50% inhibition
$K_{app}$	Apparent binding constant on DNA
$K_{cat}$	Apparent catalytic rate constant
L	Litre
LC <sub>50</sub>	Concentration causing 50% lethality
M	Molar
MHz	Megahertz
mol	Mole
mmol	Millimole
mg	Milligram
min	Minute
mL	Millilitre
mM	Millimolar
ng	Nanogram
$Q$	Fluorescence quenching
$R$	Pearson correlation coefficient
s	Second
T <sub>M</sub>	Thermal Melting
TGI	Total growth inhibition concentration
V	Volt
v/v	Volume per volume
U	Enzyme units
μL	Microlitre
μM	Micromolar

# Creina Slator

## Mechanistic Investigation of Developmental Copper Chemotherapeutics

### Thesis Abstract

The quest for new metal-based anticancer agents, alternative to clinically established chemotherapeutics, has been motivated by deficiencies observed in current treatment regimes. Coupled with the approach of sophisticated and targeted drug design, there is a clear need for comprehending the underlying biomolecular and cellular responses of new developmental therapeutics. Reported herein is a detailed analysis of redox active developmental metallodrugs containing 1,10-phenanthroline (Phen) ligands and their action as novel cytotoxins of human cancers.

This body of research describes mechanistic investigations into the oxidative nuclease activity and redox-targeting properties of new  $\text{Cu}^{2+}$  and  $\text{Mn}^{2+}$  phenanthroline chemo-types. A number of the  $\text{Cu}^{2+}$  complexes have been developed and examined, in collaboration with the National Cancer Institute, USA, for their ability to induce cytotoxicity within a wide variety of cancer cells. To uncover these properties, a range of molecular biology and biophysical techniques were employed including, flow cytometry, confocal microscopy, electrophoresis, and immunohistochemistry.

Replacing auxiliary 1,10-phenanthroline with phenazine-type ( $N,N'$ ) ligands in mononuclear systems,  $[\text{Cu}(N,N')(\text{Phen})]^{2+}$ , was found to enhance intercalation and oxidative DNA scission *in vitro*. Alternatively, incorporation of dicarboxylates ( $O,O'$ ) has shown to increase redox potential and stability, thereby targeting both mitochondrial and genomic DNA in human ovarian cancer cells, SKOV3. Increased nuclearity and varying rigidity was explored in dinuclear chemo-types ( $[\text{Cu}_2(O,O')(\text{Phen})_4]^{2+}$ ) through the addition of aliphatic and aromatic bridging dicarboxylate ligands. In combination with NCI-60 analysis, the dinuclear complexes were shown to enhance both geno- and cyto-toxic effects when compared to the mononuclear analogue, leading to an apoptotic mode of cellular death; activated through intrinsic mitochondrial machinery. Finally, exchange of the metal centre in the form of *di-manganese*<sup>2+</sup> complex significantly influenced the mode of programmed cell death, activating autophagic catabolism and self-digestion.



# **Chapter 1**

## **Molecular Methods for Probing Cytotoxic Metallodrug-DNA Interactions**

---

This work was submitted to *Current Medicinal Chemistry* for the special issue “Throwing light on recent advances on metallodrugs: from deemed poisons to a striking hope for the future” and was accepted for publication.

Andrew Kellett<sup>\*</sup>, Zara Molphy, Creina Slator, Vickie McKee, and Nicolas P. Farrell.

Within this work, I have written complete sections with significant contribution to the overall manuscript preparation and specifically towards the following sections: nucleic acids as drug targets, electrophoretic techniques and *in cellulo* genotoxicity.

## 1.1 Abstract

The binding of small molecule metallodrugs to discrete regions on nucleic acids is an important area of medicinal inorganic chemistry and the nature of these binding interactions allied with sequence and helical isoform selectivity form the backbone of modern metallodrug-DNA drug research. In this review we describe a range of molecular methods currently employed within our laboratories to explore covalent and non-covalent nucleic acid interactions of novel metallodrugs. At the outset, an introduction to DNA from a structural biological perspective is provided along with descriptions of covalent (short- and long-range platination) and non-covalent (intercalation, insertion, and phosphate clamping) metallodrug interactions. Molecular methods for probing these binding interactions are then organized between: i.) electrophoretic based techniques; ii.) fluorescence and absorbance based techniques; iii.) viscosity; iv.) mass spectrometry; v.) NMR spectroscopy; and vi.) in cellulo genotoxicity. In each method discussed, we provide an overview of the technique and its application toward the elucidation of new metallodrug-DNA interactions by copper(II) and platinum(II) complexes developed by our groups. As such, structure-activity factors in metal complex design become apparent and the consequences of unique binding and/or oxidation reactions at the nucleic acid interface often give rise to unique cytotoxic profiles that are subsequently followed using intracellular methods. Accordingly, a combination of molecular methods is often required to elucidate the nature of new metallodrug-DNA interactions and, from a drug discovery perspective, it is of particular relevance to identify whether metallodrug-DNA binding activity is conserved intracellularly, and is therefore applicable to cytotoxic action.

## 1.2 Introduction

### 1.2.1 Nucleic acid structure

Nucleic acids provide an intriguing molecular target for candidate antitumoral metallodrugs. Given their electron dense phosphate backbones, heterocyclic and exocyclic heteroatoms found within nucleobase structures, and intricate secondary and tertiary structures adopted upon Watson-Crick base pairing under action of ubiquitous enzymes, nucleic acids have a rich history of binding metal ions and discrete complexes.<sup>1-4</sup> From a medicinal chemistry perspective, therefore, the ability to probe metal complex coordination to DNA and RNA provides us with a powerful tool for developing new architectures to selectively target oligonucleotides. Furthermore, given the essentiality of the DNA double-helix for the storage of genetic information and in mediating faithful cell replication, the interruption of processes essential to biogenesis at this primary juncture provides an important basis for metallodrug discovery.<sup>5,6</sup> Accordingly, the structure of the DNA double helix, in particular its predominant B-DNA form, is an important consideration for bioinorganic chemists. B-DNA comprises a right-handed double helix containing two antiparallel sugar-phosphate chains. The heteroaromatic bases found in the centre of the helix engage in hydrogen bonding to effectively bind the helical chains together and are supported by flanking van der Waals base contacts that result in their perpendicular orientation to the helical axis. These nucleobases obey Chargaff's rules being found in 1:1 ratio between specific purine-pyrimidine molecules (adenine (A) : thymine (T) and guanine : cytosine (C)).<sup>7</sup> Since the edges of the base pairs from where glycosidic bonds extend and their opposite edges differ in size, unequal grooves called the minor and major groove, respectively, are found (**Figure 1.1C**). These grooves are structurally distinct with the minor being narrow and the major being wide by comparison.<sup>8,9</sup> In B-DNA the 2'-deoxyribose ring exists in the C2'-*endo* twist conformation, in contrast to the C3'-*endo* twist conformation of both A and Z-form DNA (**Figure 1.1B and C**).<sup>10</sup> Structural characteristics can be exploited for molecular recognition as the major groove (10.5 Å) is wider than the minor groove (4.8 Å) though their depths are identical. Between the base pairs of B-DNA there is an axial rise of 3.4 Å (0.34 nm) and a 34.5° twist angle associated with every residue rotation while the width of the helix diameter is 20 Å (**Figure 1.1A**). A-DNA is the dehydrated form of B-DNA and is a more rigid and compacted structure consisting of 11 base pairs per helical turn with a distance of 2.25 Å between the bases.<sup>11</sup> Z-DNA is formed during the transcription process *in-vivo* due to the torsional strains generated as negative supercoils are created by RNA polymerase moving along the sequence of the DNA double helix. A radical difference exists between Z- and classical B-DNA as the helical sense flips from right- to left-handed DNA and this conformational change is due to bases alternating between the *syn*- and *anti*-conformation. Z-DNA is elongated and narrow, with a diameter of 18 Å and is composed of only one single narrow groove analogous to that of the minor

groove of B-DNA; resulting in a zigzag arrangement of the backbone (hence Z-DNA) (**Figure 1.1C**).<sup>12</sup>

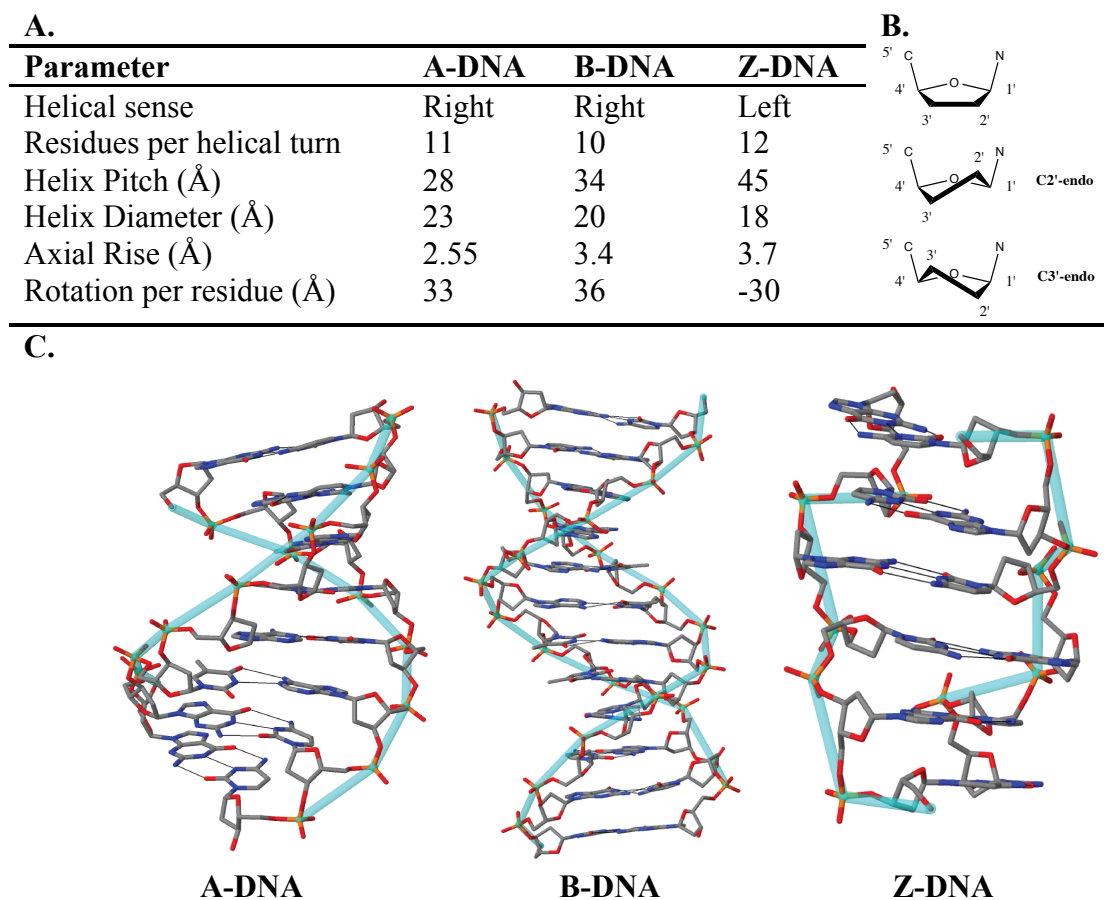


**Figure 1.** 1A. Summary of structural differences between A-, B- and Z-DNA,<sup>13</sup> **B.** conformational preferences of the 2'-deoxyribose rings of DNA and **C.** X-ray structures of A-, B- and Z-DNA from PDB files 1VJ4, 1BNA and 2DCG, respectively.

Since great effort has been expended in recent years to determine how novel metallodrug molecules interact with nucleic acids, a number of complementary molecular methods have been developed to probe these reversible and non-reversible interactions. Additionally, in the absence of high resolution structural data including X-ray diffraction and NMR studies, the mode of binding can be inferred indirectly from molecular biological and biophysical solution studies. A wealth of information regarding the binding mode and sequence specificity of these interactions can therefore be determined and in this review we provide an overview of selected molecular methods to identify metallodrug-DNA interactions with particular emphasis on copper<sup>2+</sup> and platinum<sup>2+</sup> complexes developed within our laboratories within the past 25 years. A review of polynuclear Pt<sup>2+</sup> (Triplatin) binding by X-ray diffraction was recently reported by Komeda *et al.* and, as such, is not discussed here.<sup>14</sup> Furthermore, while much elegant work has been conducted on Z-DNA, G-quadruplex and other non-canonical structures (including their targeting by selected metal complexes),<sup>15-19</sup> it is beyond the scope of this work.



## 1.2.2 Nucleic acids as metallodrug targets

### 1.2.2.1 Covalent interactions by platinum(II) chemotherapeutics

Platinum-based drugs are currently used alone or in combination with other therapies for over half of cancer treatments<sup>20</sup> and over 23 platinum complexes have entered into clinical trials since 1970.<sup>21</sup> The era of platinum-based anticancer agents began with the serendipitous discovery of the antitumoral effects of cisplatin (**Figure 1.2A**) by Rosenberg<sup>6</sup> and was the first transition metal-based agent approved by the FDA for chemotherapeutic treatment in 1978.<sup>22</sup> Subsequent generations of platinum research led to the development of carboplatin and oxaliplatin, both of which are globally used in clinical treatment,<sup>20</sup> whilst other complexes—nedaplatin, lobaplatin and heptaplatin—have gained approval for use within individual markets (**Figure 1.2B**).<sup>21</sup> The restricted use of cisplatin stems from dose-limiting effects due to metabolic degradation and accelerated uptake in rapidly dividing cells; associated side-effects include nephrotoxicity, ototoxicity, myelosuppression (due to rapid rejuvenation of bone marrow), gastrointestinal tract toxicity and nausea.<sup>21</sup>

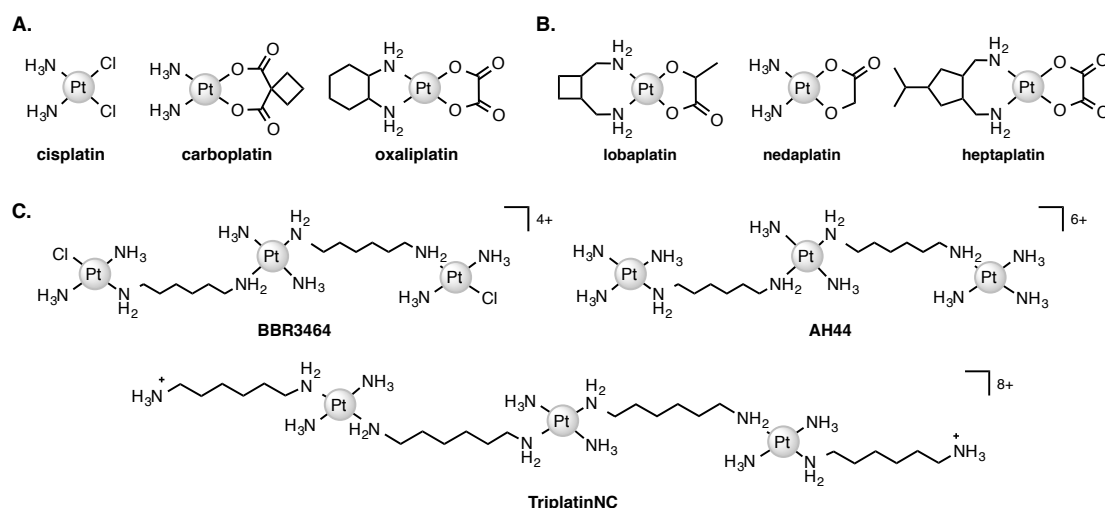


**Figure 1. 2** Molecular structures of, **A.** globally approved Pt(II) complexes cisplatin, carboplatin and oxaliplatin and **B.** those approved in single markets lobaplatin, nedaplatin and heptaplatin, **C.** polynuclear platinum complexes (PPCs)  $[\{transPtCl(NH_3)_2\}_2-\mu-\{trans-Pt(NH_3)_2(NH_2(CH_2)_6NH_2)_2\}]^{4+}$  (Triplatin, BBR3464),  $[\{Pt(NH_3)_3\}_2-\mu-\{trans-Pt(NH_3)_2(NH_2(CH_2)_6NH_2)_2\}]^{6+}$  (AH44), and  $[\{transPt(NH_3)_2(NH_2(CH_2)_6NH_3)\}_2-\mu-(trans-Pt(NH_3)_2(NH_2(CH_2)_6NH_2)_2)]^{8+}$  (TriplatinNC).

Cisplatin exists in the blood stream in its neutral form due to the innately high concentration of chloride ions (~100 mM) found therein.<sup>23</sup> The drug enters the cell *via* active or passive diffusion and is subsequently activated by aquation in a stepwise exchange of the labile chloride ligands to water or hydroxyl ions. This conversion is largely due to the compartmentalised nature of the cell where a decreased concentration range of chloride ions exists (2-30 mM).<sup>20,24,25</sup> Accordingly, Pt(II) drugs containing chloride ions require hydrolysis prior to DNA platination,<sup>26</sup> a reaction that

involves direct coordination of the platinum metal centre with electron rich sites on the nucleobase (**Figure 1.3C**). The rate of hydrolysis of the chloride ligands can depend on surrounding environment concentration,<sup>24,25</sup> pH and electronic and steric effects of the non-leaving groups (i.e. am(m)ine ligands).<sup>20</sup> The subsequent formation of mono-functional or bi-functional adducts with DNA *via* platination is often considered akin to DNA alkylation. Mono-functional adducts arise from single coordination to either negatively charged oxygen atoms on the sugar phosphate backbone<sup>27</sup> or suitable donor atoms in the heterocyclic base.<sup>22</sup> Bi-functional adducts, however, are formed when platinum chelates DNA *via* two coordination sites on the pyridine and imidazole-like nitrogen atoms in the heterocyclic bases thus forming a crosslink between two bases of DNA yielding intrastrand (most common) or interstrand adducts (**Figure 1.3ii**).<sup>28</sup> Cisplatin preferentially binds to N7 of guanine and adenine and typically results in 1,2-GG/AG intrastrand crosslinks with structural distortion through helical unwinding by 13°, and helical bending of 30 - 40° towards the major groove.<sup>29,30</sup> The structurally modified DNA strand is then recognised by repair enzymes<sup>31</sup> with excess excision of Pt-DNA adducts linked to the induction of apoptotic cell death (**Figure 3D**).<sup>32</sup> Alternatively, bi-functional cross linking can occur to a lesser extent between DNA-Pt-protein through donor atoms on the axillary chains of protein termini.<sup>33</sup>

Ineligible or discontinued treatment of platinum-based therapies can occur from intrinsic or acquired resistance proceeding sub-lethal continuous exposure to the drug.<sup>21</sup> Furthermore, as carboplatin shares cross-resistance with cisplatin (both drugs are effective against the same population of solid epithelial tumours) limiting the efficacy of platinum drugs currently available in clinical treatment.<sup>20</sup> A culmination of various parameters is responsible for platinum resistance: *i.*) decreased cellular accumulation due to differential rates of cellular influx and efflux (**Figure 1.3A and H**); *ii.*) detoxification by elevated levels of intra- and extracellular reductants such as thiol-rich reductants glutathione (GSH) (**Figure 1.3F and G**), *L*-cysteine,<sup>34</sup> ascorbic acid<sup>35</sup> and metallothionein (MET),<sup>36</sup> *iii.*) enhanced repair mechanisms and/or tolerance to platinated DNA adducts,<sup>20,28</sup> and *iv.*) full or partial bypass of 1,2-GG/AG or 1,3-GTG intrastrand crosslinks achieved by specialized polymerases in the replication process.<sup>37</sup>

BBR3464 (**Figure 1.2C**) was the first multi-nuclear platinum complex to enter clinical trials capable of bi-functional DNA binding interactions in comparison to that of ‘classical’ mono-nuclear Pt(II) drugs. This compound produces long-range covalent inter- and intra-strand DNA platination and is entirely distinct from cisplatin’s short range platination.<sup>38</sup> BBR3464-induced DNA distortions significantly differ from cisplatin-DNA adducts, the latter of which leads to recruitment of recognition repair enzymes and adduct excision. Pre-association of BBR3464 to DNA is mediated by electrostatic interactions transiently engaging with phosphate groups in the minor groove, and is an important mechanistic feature determining the specificity and formation of

covalent long-range crosslinks.<sup>38,39</sup> The complex has demonstrated excellent toxicity within *in-vitro* and *in-vivo* models with a broad spectrum of activity in cancers both sensitive and resistant to cisplatin and those with p53 mutants.<sup>40</sup> This novel activity ensured progression to phase II clinical trials, however, intracellular instability and metabolic byproducts structurally similar to cisplatin halted further advancement.<sup>41</sup>

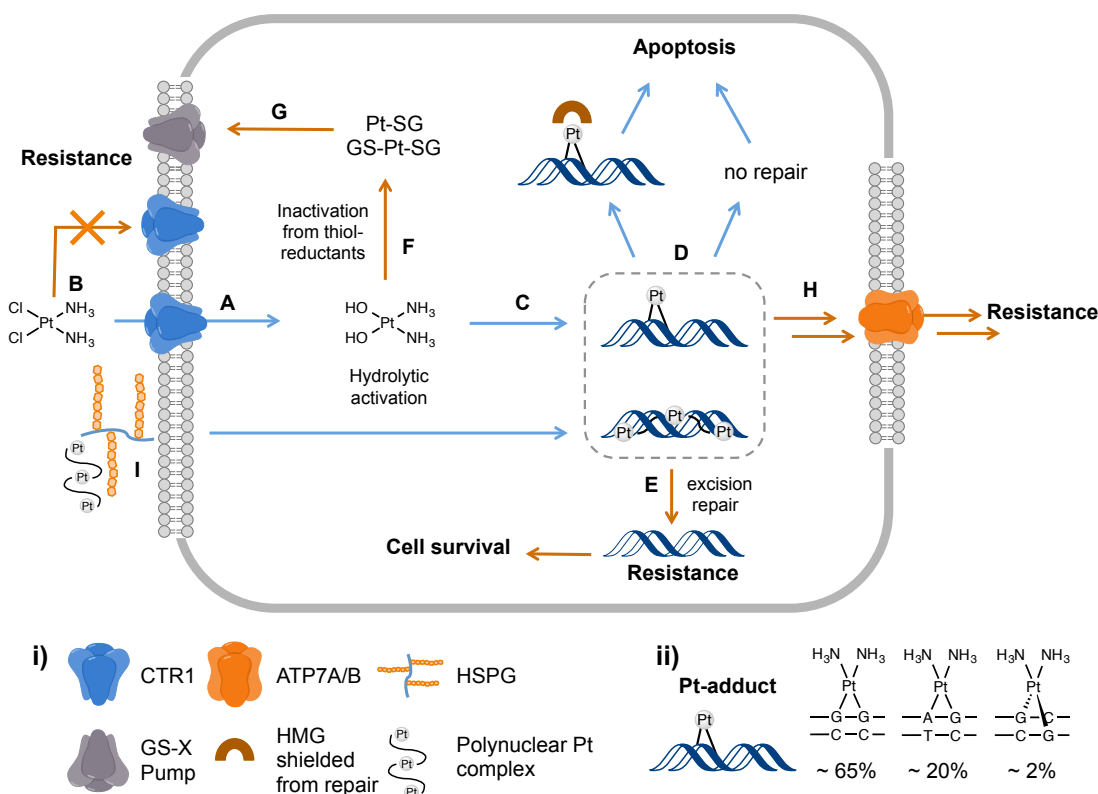


**Figure 1. 3** Pathways of cisplatin cytotoxicity (blue arrows) and resistance (orange arrows). **i)** membrane-bound afflux proteins (copper transport influx pump CTR1, efflux pump ATP7A/B and glutathione adducts afflux pump GS-X) and high mobility group proteins (HMG). **ii)** Pt-adducts in order of occurrence: 1,2-intrastrand G-G (60-65%) and A-G (20%) and 1,3 interstrand G-G (2%). Cisplatin is incorporated into the cell through CTR1 (A). Under-expression of CTR1 results in decreased cellular accumulation of cisplatin (B). Activation through hydrolysis (C), facilitating DNA platination and distortion (D) with no, or little, inhibition of enzymatic repair activity through HMG (D) resulting induced apoptotic cell death. Acquired resistance can occur from enhanced DNA repair mechanisms and Pt adduct excision (E). Other resistance factors such as inactivation through thiol-rich reductants (F), GSH as example) and GS-Pt (and GS-Pt-SG) adduction elimination through GS-X pump (G). Accelerated efflux of cisplatin through overexpression of copper transporters, ATP7A/B (H). Membrane recognition and intracellular accumulation of polynuclear Pt complexes through heparan sulphate proteoglycans (HSPG) (I).

### 1.2.2.2 Non-covalent interactions

#### 1.2.2.2.1 Metallointercalation and metalloinsertion

Intercalation involves insertion of a planar, usually aromatic ligand (or part thereof) between the stacked base pairs of DNA. This interaction was identified and characterised by Lerman in 1961<sup>42</sup> and many organic intercalators have been recognized since.<sup>43,44</sup> Intercalation of metal complexes also has a long history, the first structurally characterized (by X-ray diffraction by fibres) example being the 2-hydroxyethanethiolato(2,2',2''terpyridine)-platinum(II) monocation<sup>45,46</sup> and a number of recent reviews have appeared describing intercalation by complexes of platinum, copper, ruthenium, rhodium<sup>47</sup> and osmium.<sup>3,44,47-50</sup> The essential structural requirement is that the intercalating group must engage in the base stacking interactions, the major factor stabilising the DNA structure. The nature of “ $\pi$ -stacking” is complex and influenced by, for example, electrostatic substituent effects and solvent<sup>51-55</sup> but generally requires both that the ligand is planar and (usually) that it contains a significant delocalized region. It is also necessary that the additional stabilisation on stacking the intercalating ligand outweighs the reorganization energy necessary to permit it. The intercalated groups orient approximately parallel to the plane of the base pairs, and the base pairing is not significantly disturbed. The principal effect on the DNA structure is to extend it by *ca.* 3.6 Å for each intercalated group (3.6 Å being the normal interplanar distance for  $\pi$ -stacking). To permit this, the DNA helix unwinds, reducing the helical twist across the intercalation site. There are also a number of smaller geometric changes<sup>56,57</sup> that together may reduce conformational flexibility in the adjacent portions of the helix, since it is observed that further intercalation does not occur at the neighbouring sites (the “nearest neighbour exclusion principle”).<sup>46,58</sup> Structurally characterized metallointercalators are all bound from the major groove, though there is some NMR evidence for minor groove binding in solution.<sup>59</sup>

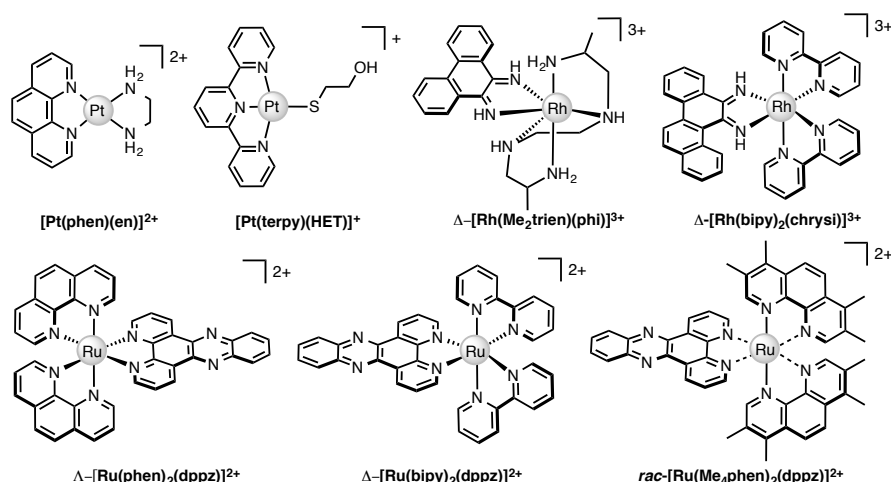


**Figure 1. 4** Molecular structures of platinum(II), Rh(III) and Ru(II) intercalating and insertion complexes.

Since only the planar section of the ligand can intercalate, it needs to be large enough to achieve significant  $\pi$ -overlap, without bringing the remainder of the complex into unfavourable steric or electronic interaction. Ligands such as 1,10-phenanthroline (phen) and terpyridine (terpy) in square planar Pt complexes<sup>3</sup> are able to intercalate effectively but large ligands such as 9,10-phenanthrenequinone diimine (phi) or dipyridophenazine (dppz) are more effective for 6-coordinate complexes.<sup>47</sup> The orientation of the intercalator in the “slot” between two base pairs may be symmetrical, or laterally offset relative to the principal axis of the DNA helix,<sup>60,61</sup> presumably reflecting the best accessible set of stacking and other interactions, hence dependent on the detailed electronic structures of the intercalating ligand and the base pairs lining the intercalation site.<sup>55,62,63</sup> There are ten possible intercalation sites,<sup>46</sup> differing in existing  $\pi$ -interactions between base pairs<sup>51,63</sup> and their affinity for a specific intercalator. For example, in 1979 Lippard and co-workers showed that  $[\text{Pt}(\text{phen})(\text{en})]^{2+}$  and  $[\text{Pt}(\text{terpy})(\text{HET})]^+$  (where HET = 2-hydroxyethanethiolate) exhibit GC selectivity,<sup>64</sup> while  $[\text{Ru}(\text{phen})_2(\text{dppz})]^{2+}$  (**Figure 1.4**) displays preferential intercalation for poly-d(AT) over poly-d(GC).<sup>65</sup> The same complex intercalates symmetrically at the TA/TA step in d(CCGGTACCGG)<sub>2</sub> but not the AT/AT site in d(CCGGATCCGG)<sub>2</sub>.<sup>61</sup> In fact, many metalintercalators bind preferentially to DNA at specific sites, and this function can be amplified by interaction of the ancillary ligands with the DNA duplex. In an early example, the photoactive complex  $\Delta\text{-}\alpha\text{-}[\text{Rh}\{(\text{R,R})\text{-Me}_2\text{trien}\}\text{phi}]^{3+}$  (where Me<sub>2</sub>trien = 2,9-diamino-4,7-diazadecane, **Figure 1.4**) was found to specifically cleave the sequence 5'-TGCA-3'.<sup>66</sup> The structural basis for this specificity was demonstrated in the X-ray structure of the complex bound to 5'-G(5|U)TGCAAC-3' (**Figure 1.5A**) in the major groove specifically at the 5'-TG|CA-3' site (where | indicates phi insertion).<sup>57</sup> The intercalation  $\pi$ -stacking is supported by H-bonds from the amines of the Me<sub>2</sub>trien ancillary ligands to the guanine-O6 acceptors as well as to some ordered water molecules.

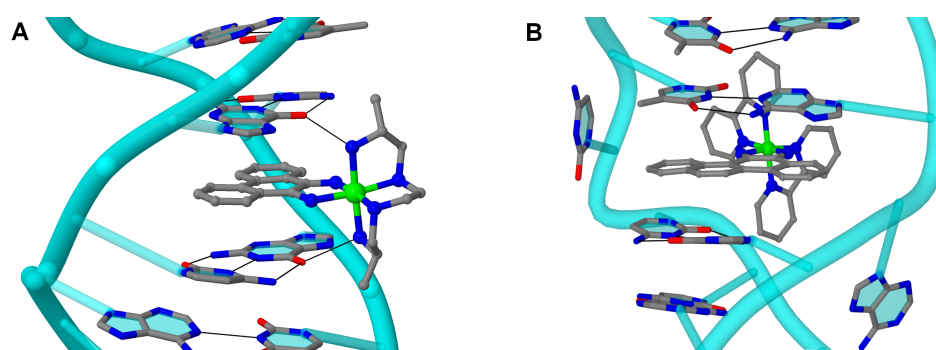


**Figure 1. 5** Intercalation and insertion. **A.**  $\Delta\text{-}\alpha\text{-}[\text{Rh}\{(\text{R,R})\text{-Me}_2\text{trien}\}\text{phi}]^{3+}$  intercalated into 5'-G(5|U)TGCAAC-3' with additional stabilisation by H-bonds from the ancillary ligand (PDB 454d), black lines indicate hydrogen bonds<sup>57</sup> and **B.**  $\Delta\text{-}[\text{Rh}(\text{bpy})_2(\text{chrysi})]^{3+}$  inserted into (5'-CGGAAATTCCTG-3'), displacing a mismatched AC pair (PDB 2O1I).<sup>67</sup>

Metalloinsertion is closely related to intercalation, also involving incorporation of a ligand into the base pair stack. The main difference is that in metalloinsertion one base pair is ejected and replaced by the incoming ligand. This interaction was also predicted by Lerman<sup>1</sup> and first structurally characterised in a metal complex only in 2007 for  $\Delta$ -[Rh(bpy)<sub>2</sub>(chrysi)]<sup>3+</sup> (where chrysi = 5,6-chrysenequinone diimine, **Figure 1.4** and **Figure 1.5B**),<sup>67</sup> extended to a family of chrysi derivatives<sup>68</sup> and more recently for both  $\Delta$ -[Ru(bipy)<sub>2</sub>(dppz)]<sup>2+</sup><sup>69</sup> and  $\Lambda$ -[Ru(phen)<sub>2</sub>(dppz)]<sup>2+</sup> (where bipy = 2,2'-bipyridine, **Figure 1.4**),<sup>61</sup> in all three cases the insertion is at a mis-matched base pair and from the minor groove (in contrast to intercalation). The dppz complexes are capable of both intercalation and insertion and it may be that other known intercalators are also capable of insertion in the presence of base-pair mismatches. Insertion involves less modification to the helical structure of DNA than intercalation. There is no significant extension or change in helicity although the “flipped out” bases are free to interact in other ways with the DNA helix or the inserting complex. The stabilisations due to hydrogen bonding of the displaced base pair and its stacking interactions are both lost and need to be replaced primarily by the new  $\pi$ -stacking interactions (plus any new interactions involving the flipped out base pair). Since base-stacking dominates DNA duplex stability and base pairing contributes relatively little stabilization,<sup>52,63</sup> the loss of the H-bonding component might not be expected to have a high cost. Nonetheless, metalloinsertion is observed to be specific for mismatched base pairs, especially those where resulting base-pairing is poor (CC and CA). For example,  $\Delta$ -[Rh(bipy)<sub>2</sub>(chrysi)]<sup>2+</sup> (**Figure 1.4**) can promote specific cleavage at a single mismatch site in a 2725 base pair linearized plasmid heteroduplex.<sup>70</sup> This specificity is useful in detection of mismatches and potentially diagnostic for cells with impaired mismatch repair (MMR) mechanisms; notably, the series of Rh-chrysi complexes shows selective cytotoxicity for MMR-deficient cancer cells.<sup>68</sup>

As for intercalation, interaction of the ancillary ligands with the DNA can be used to tune the binding properties of the inserting complex. For example, [Ru(bipy)<sub>2</sub>dppz]<sup>2+</sup> binds to DNA *via* both intercalation and insertion at mismatch sites but [Ru(Me<sub>4</sub>phen)<sub>2</sub>(dppz)]<sup>2+</sup> (where Me<sub>4</sub>phen = 3,4,7,8-tetramethyl-1,10-phenanthroline, **Figure 1.4**) is a mismatch-specific metalloinsertor where the methyl groups disfavour intercalation, due to steric interaction with the backbone, and also control the depth of dppz insertion.<sup>71</sup> As might be expected, the metalloinsertion correlates with the stability of the mismatch site, strongest for CC and CA (less stable), less striking for GG AA (more stable).<sup>51</sup> Metallointercalators and metalloinsertors can be combined with groove-binding, sequence-specific components in multifunctional assemblies to extend their recognition and properties. The first structurally characterised example was reported by Nordén in 2001.<sup>72</sup> Much elegant work has been done in this area in recent years but is beyond the scope of the current review.<sup>44,47,48</sup>

#### 1.2.2.2.2 Non-covalent binding by polynuclear platinum complexes (PCCs)

Enhanced DNA binding properties of the polynuclear platinum(II) chemotype led to the subsequent development of analogues with varying linker lengths and replacement of labile chloride groups with ammonia or dangling terminal amines. TriplatinNC, was therefore designed with ‘dangling’ terminal hexanediamine functionality and contains Pt(II) centres linked *via* bridging diam(m)ine groups (**Figure 1.2C**). TriplatinNC forms non-covalent bonds with DNA, without any direct Pt-DNA coordination epitomised in cisplatin-type structures.<sup>39</sup> The architecture of the complex gave rise to a previously undiscovered mode of DNA binding called the ‘phosphate clamp’ that results from the selected affinity of symmetric am(m)ine-to-phosphate ( $\text{N-H}\cdots\text{O=P}$ ) hydrogen bonding through cis-oriented  $\text{NH}_3$  (ammine) and  $-\text{RNH}_2$  (amine) ligands.<sup>39</sup> The discrete mechanism of phosphate clamping gives rise to two binding motifs: phosphate tracking and groove spanning (**Figure 1.6A and B**). Triplatin-DNA coordination leads to a collapse in regular helical structure<sup>73</sup> with subsequent enzymatic inhibition of topoisomerase I and type II restriction endonucleases.<sup>74</sup> Groove spanning is dependent on the local helical topology (localised to the minor groove) and base composition (specifically towards A-T content) and is discrete from that of classical intercalation and minor-groove binding.<sup>75</sup> Despite the highly positive charge of the molecule, cellular uptake is significantly enhanced in comparison to BBR3464.<sup>76</sup> Substitution of chloride ligands in BBR3464 with ammine groups lead to the derivative AH88—otherwise known as TriplatinNC-A—which similarly exhibits this non-covalent phosphate clamping association mode,<sup>77</sup> consequently inducing DNA condensation in the same manner as terminal Pt-dangling amine analogue TriplatinNC.<sup>73</sup> Note that the phosphate clamp formed by the spermine-bridged dinuclear  $[\{\text{Pt}(\text{NH}_3)_3\}_2\text{-}\mu\text{-spermine}]^{6+}$  is effected through a *cis*- $\{\text{Pt}(\text{NH}_3)_2\}$  group, suggesting also a model for initial interaction of cisplatin itself with DNA.<sup>14</sup>

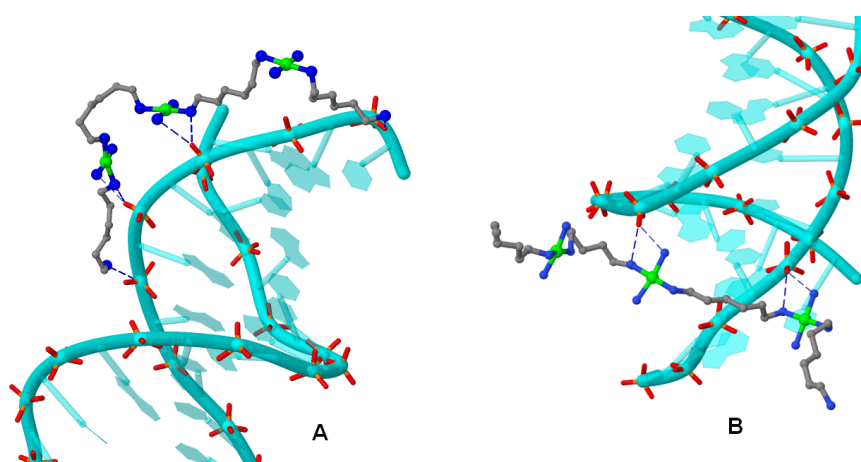


**Figure 1. 6** TriplatinNC bound to Dickerson-Drew dodecamer (B-DNA) through backbone tracking **A.** and groove spanning and, **B.** interactions.<sup>75</sup>  $\text{N-H}\cdots\text{O=P}$  hydrogen bonds shown as dashed blue lines.

Extensive studies of the PPCs class have revealed a novel mechanism of incorporation and accumulation within cancer cells.<sup>78</sup> The polycationic properties of the complexes mimic polyarginine peptide sequences and glycosaminoglycans (GAG) important for protein transduction domains so they can be exploited for tumour selectivity and accumulation. A novel target of PPC is the heparan sulphate proteoglycan, HSPG, (**Figure 1.3I**) verified through cellular uptake of classical platinum complex and polynuclear cationic species in differentially expressed Chinese hamster ovarian (CHO) cells with and without heparan sulphate and chondroitin sulphate deficiencies.<sup>79</sup> PPCs are competitive inhibitors of the polysaccharide degradation enzyme, heparinase, as co-incubation of the complexes with pentasaccharide GAG mimic fondaparinux significantly reduced production of the cleavage products/pattern.<sup>80</sup> Indeed, the metallos shielding effect of PPCs has unveiled a novel area of platinum chemotherapeutic targets and interactions, coined ‘metallo glycomics’.

## **1.3 Electrophoretic-based techniques**

### **1.3.1 DNA damage detection**

DNA damage is known to play a major role in biological processes including ageing, mutagenesis and carcinogenesis as cellular DNA is susceptible to many forms of damage resulting from exposure to endogenous (spontaneous) and exogenous (environmental) sources. Examples of endogenous factors include enzymatic or spontaneous metabolic conversions, while exogenous sources include genotoxic agents such as ionizing radiation, redox metal ion overload, and therapeutic drug exposure. Such mutagens are capable of causing direct or indirect damage to nucleotides resulting in profound biological consequences including replication errors in genetic code and the production of free radical species.<sup>81</sup> Two major types of DNA damage mechanisms exist, hydrolytic and oxidative. Hydrolytic agents result in the cleavage of the phosphate backbone which can be enzymatically repaired by DNA ligases,<sup>82</sup> while oxidative mechanisms involve the production of diffusible free radicals—produced by mitochondria and also through exposure to physical agents such as oxidative nucleases—resulting in DNA cleavage by oxidative attack at a variety of C-H positions of the sugar moiety.<sup>83</sup>

Electrophoretic gel mobility shift assays are a well-established analytical technique used in molecular biology laboratories to analyze, separate and purify DNA samples. It is also a useful technique to probe DNA damage mechanisms. Gel electrophoresis facilitates the movement of DNA molecules based on both their size and conformation, through a solid-phase medium such as agarose or polyacrylamide, under the influence of an electric potential difference. Due to its inherent negative charge, DNA moves in the electric field as an anion, from the cathode to the anode. The rate of DNA migration through the gel is dependent on a number of factors including



the length of the DNA sequence, the conformation of the DNA, whether the DNA is single stranded (ssDNA) or double stranded (dsDNA) and the presence of supercoiling. A number of external parameters can be controlled in order to maximize the resolution of a gel including the voltage applied, the physical length of the gel, running time and nature of stationary phase selected.

Plasmid DNA (FI, SC) is a supercoiled substrate widely used to probe drug-DNA interactions through the medium of agarose gel electrophoresis. ssDNA cleavage induced by a small drug molecules—such as  $[\text{Cu}_2(\mu\text{-terephthalate})(\text{phen})_4]^{2+}$  (Cu-Terph-Phen) (**Figure 1.7**)—results in the formation of nicked open circular DNA (FII, OC),<sup>84</sup> while double stranded cleavage results in the formation of linear (FIII, L). Complete degradation of plasmid DNA, like that induced by copper phenanthrene complexes in the presence of added reductant, can be determined by fragmentation of DNA.<sup>85</sup>

### 1.3.2 Antioxidant traps for oxidative cleavage detection

The cleavage efficiency of  $\text{Cu}^{2+}$  phenanthroline complexes are dependent on the presence of both a reductant (*L*-ascorbic acid) and an oxidant ( $\text{O}_2$  or  $\text{H}_2\text{O}_2$ ) resulting in a cascade of redox reactions initiated by the reduction of  $\text{Cu}^{2+}$  to  $\text{Cu}^+$  species.<sup>86</sup> The ROS species involved in chemical nuclease activity of  $[\text{Cu}(o\text{-phthalate})(1,10\text{-phenanthroline})]$ , Cu-Ph-Phen (**Figure 1.7**) was investigated on superhelical pUC19 DNA in the presence of ROS-specific quenchers and stabilisers; tiron for superoxide ( $\text{O}_2^{\bullet-}$ );<sup>87</sup> DMSO for the hydroxyl radical ( $\text{OH}^\bullet$ );<sup>88</sup>  $\text{NaN}_3$  for singlet oxygen ( $^1\text{O}_2$ );<sup>89</sup> and KI for hydrogen peroxide ( $\text{H}_2\text{O}_2$ )<sup>90</sup> (**Figure 1.8A**). The cleavage efficacy of Cu-Ph-Phen in the presence of scavengers identified the most prelevant species involved in strand scission as  $\text{O}_2^{\bullet-}$ . Co-incubation with 4,5-dihydroxy-1,3-benzenedisulfonic acid (tiron) significantly impeded the cleavage activity of the compound preventing double strand damage. The presence of DMSO diminished activity to a lesser extent while DNA damage was marginally altered by KI and  $\text{NaN}_3$ . Significantly, ovarian adenocarcinoma cancer cells (SKOV3) pretreated with tiron, then subsequently exposed to an  $\text{LD}_{50}$  concentration of Cu-Ph-Phen displayed enhanced survival by ~26%.<sup>91</sup> This method was also employed to probe the redox mechanism of the developmental copper phenazine series,  $[\text{Cu}(\text{DPQ})(\text{phen})]^{2+}$  (Cu-DPQ-Phen),  $[\text{Cu}(\text{DPPZ})(\text{phen})]^{2+}$  (Cu-DPPZ-Phen), and  $[\{\text{Cu}(\text{phen})_2\}_2(\mu\text{-terph})](\text{terph})$  (Cu-Terph-Phen) (where DPQ = dipyridoquinoxaline and terph = terephthalate, **Figure 1.7**) demonstrating the hydroxyl (or metal-hydroxyl) radical as the primary species involved in oxidative DNA degradation.<sup>92</sup>

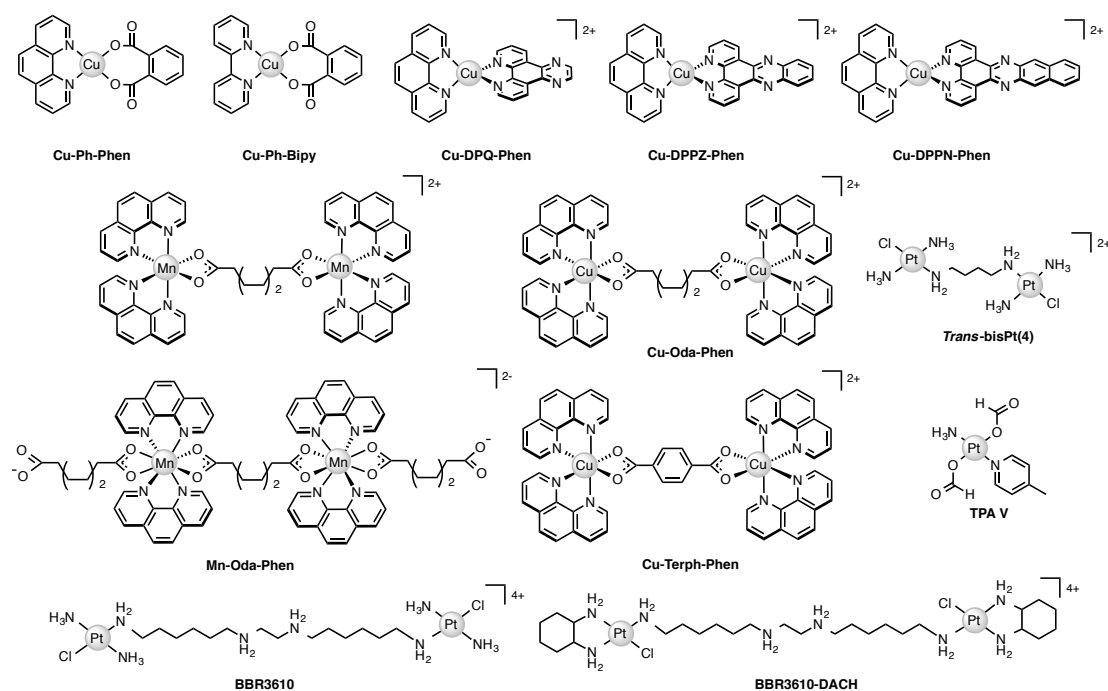


**Figure 1. 7** Molecular structures of selected metal complexes discussed in this review.

### 1.3.3 Intercalation: Topoisomerase I and II inhibition

Topoisomerases (Topo) are a specialised class of nuclear enzymes that catalyse the transient cleavage, passage and resealing of either a single strand (Topo I) or double strand (Topo II) of DNA in order to relax chain intertwinement, release superhelical tension and permit change in topology during replication, transcription, and DNA repair.<sup>93</sup> Topo I mediated relaxation is a robust assay to identify intercalative properties of DNA binding complexes.<sup>94</sup> Metal complexes with intercalating moieties, typically constructed from planar aromatic ligands, unwind and elongate the helical structure inhibiting topoisomerase enzymes from binding to DNA, or alternatively stabilising the enzyme-DNA complex. Topo I isolated from *E. coli* specifically relaxes negatively coiled superhelical plasmid DNA giving a distinct topological pattern of negative, or right handed, topoisomers. In the presence of intercalating agents, plasmid DNA reveals a migratory profile transitioning from this typical topology pattern to fully relaxed DNA or to positively (left-handed) SC plasmid. This is evident for intercalating molecule EtBr (**Figure 1.10A**), which induces helical unwinding by 26°, <sup>95</sup> with positively wound topology of intact scDNA being observed after 0.5  $\mu$ M (**Figure 1.8B**). The treatment of established Topo II poison, doxorubicin (**Figure 1.10A**) renders complete DNA degradation and shearing at higher concentrations (**Figure 1.8C**) likely through ROS generation consequent to redox cycling of quinone moiety.<sup>96,97</sup>

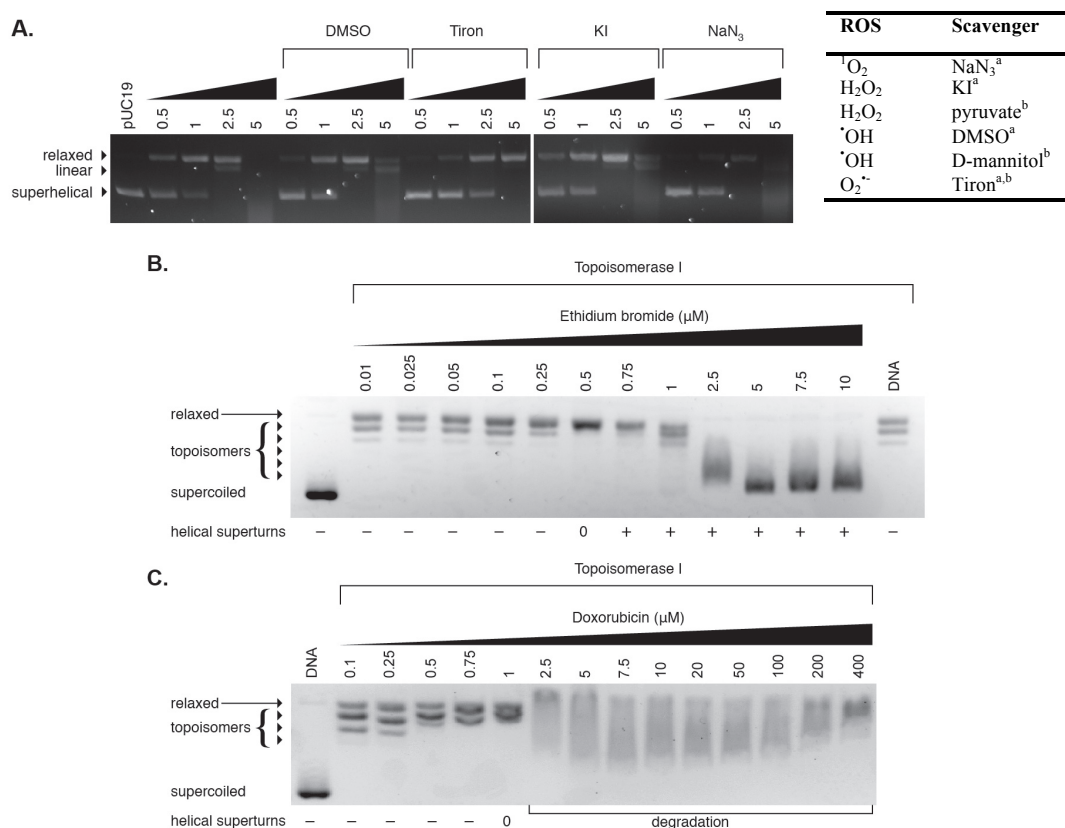


**Figure 1. 8 A.** Cleavage profile of Cu-Ph in the presence of radical-specific antioxidants and trapping agents. Table insert with scavengers<sup>a</sup> utilised in nuclease studies and intracellular antioxidants<sup>b</sup>. Electrophoretic gels of topoisomerase relaxation assay for intercalating agents, **B.** EtBr and **C.** known topoisomerase poison doxorubicin, Doxo (unpublished results).

### 1.3.4 DNA unwinding and bending

Distortion in helical structures and periodicity induced by metal-complexes leads to inhibition of protein-DNA recognition involved in transcriptional and replication processes. With this in mind, conformational modifications such as unwinding and bending can be identified through native gel electrophoresis.<sup>98</sup> Nucleotide monomers, typically 20-24 bp in length, are specifically designed to contain optimal platinum binding sites and a single nucleotide overhang that facilitates polymerization through T4 mediated ligation. The polymerized constructs (100-200 bp in length) result in an overlapping laddering pattern when subjected to gel electrophoresis.<sup>30</sup> Upon platination of oligonucleotides, interplatinum distances are constant in the ligation product due to single orientation with constructive addition of bends facilitated by the non-complementary one nucleotide overhangs. Pt-distances in the plane of helical repeats assemble in the most constructively phased bend yielding the highest degree of anomalous migration.<sup>30,99</sup> Differential gel migration between unmodified and alkylated sequences can therefore be attributed to DNA unwinding where the natural repeat of B-DNA is 10.5 bp. Planar curvature is assessed from relative mobility (K) values, based on the apparent length after electrophoretic migration relative to known

sequence length, with higher values indicating a greater degree of bending. The curvature or retardation maxima gives the precise helical repeat and are obtained through plotting K values versus length of oligonucleotides. The unwinding angle can therefore be calculated on the basis that a helical repeat of 10.5 bp has a periodicity of 360° in B-DNA. The bend angle per helical turn or absolute curvature can be calculated from empirical equations based on sequence length, relative mobility and curvature relative to DNA bending induced by the tracts of A residues.<sup>30,98,100</sup> This procedure has been widely used to determine helical bending and local unwinding angles of site-specific platinated interstrand crosslinks (**Table 1.1**).

**Table 1. 1** Helical unwinding and bending angles for established platinum complexes.

	Interstrand crosslink	Unwinding	Bending
Cisplatin <sup>100</sup>	1,2-GG	79°	45°
Oxaliplatin <sup>101,102</sup>	1,2-GG	96°	55°
<i>Trans</i> -bisPt(4) <sup>† 98</sup>	1,4-GG 5'→5'	9°	10°
BBR3464 <sup>103</sup>	1,4-GG 5'→5'	10°	21°
	1,4-GG 3'→3'	9°	15°

<sup>†</sup> *Trans*-bisPt(4) = [*trans*-{PtCl(NH<sub>3</sub>)<sub>2</sub>}<sub>2</sub>-μ-NH<sub>2</sub>(CH<sub>2</sub>)<sub>4</sub>NH<sub>2</sub>]<sup>2+</sup>

### 1.3.5 Alkylation assays with melphalan

Melphalan is an aromatic nitrogen mustard with high affinity for alkylating the minor groove—inducing A•T→T•A transversions—and when heat-treated with piperidine DNA cleavage at guanine N-7 adducts result (**Figure 1.9A**).<sup>104,105</sup> Since thermolabile sites can be readily visualized by gel electrophoresis, the presence of high affinity minor groove binding agents—such as netropsin and distamycin—can be seen to afford protection to DNA from alkylation.<sup>106</sup> Interestingly, the same protective effect can be seen in the case of PPCs, where melphalan is prevented from accessing A-rich regions, and this protective effect is illustrated in **figure 1.9B**.<sup>107</sup>

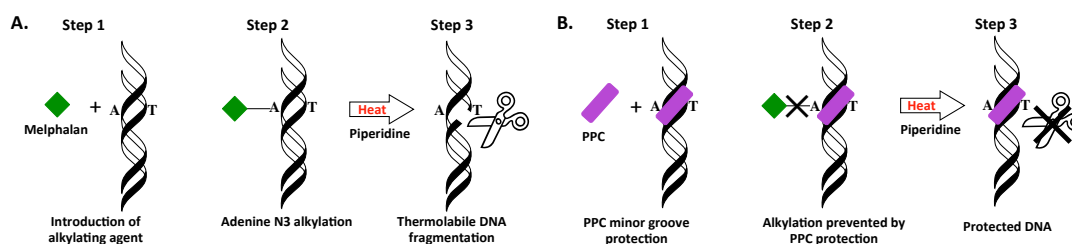


**Figure 1. 9** Minor groove binding competition assay using polynuclear platinum complexes.

### 1.3.6 On-chip microfluidic analysis

Lab on chip technology—such as that commercially available through the Agilent Bioanalyser 2100—has provided a platform to conduct high-throughput gel electrophoretic experiments on a microfluidic chip with up to 12 DNA, RNA or protein samples being analysed and processed sequentially.<sup>108</sup> Data can be processed and generated with output including electrograms, peak

height, peak area and digital electropherograms. Many applications for nucleic acids have been found for this technique including determination of sample size, quality and concentration.<sup>109-111</sup>

Recently, we employed this technique to determine drug-DNA damage and selective binding interactions with double stranded DNA sequences. In the first case, an assay was devised to compare the oxidative degradation profiles of a family of structurally related bis-chelate Cu(II) phenanthroline-phenazine cationic complexes of Cu-DPQ-Phen, Cu-DPPZ-Phen, and Cu-DPPN-Phen (where DPPN = benzo[*i*]dipyridophenazine) on a linearized pUC19 sequence (2686 bp). We employed both peak height and peak area intensity in order to rank the activity of the complex series, revealing Cu-DPQ-Phen (**Figure 1.7**) as the most active complex within the series.<sup>85</sup> In the second case, we employed the Agilent Bioanalyser 2100 to investigate whether cationic Triplatin complexes of varying linker length ( $[\{\text{Pt}(\text{NH}_3)_3\}_2\text{-}\mu\text{-}\{\text{trans-Pt}(\text{NH}_3)_2(\text{NH}_2(\text{CH}_2)_6\text{NH}_2)_2\}]^{6+}$  (AH44, TriplatinNC-A) and  $[\{\text{trans-Pt}(\text{NH}_3)_2(\text{NH}_2(\text{CH}_2)_n\text{NH}_2)\}_2\text{-}\mu\text{-}(\text{trans-Pt}(\text{NH}_3)_2(\text{NH}_2(\text{CH}_2)_n\text{NH}_2)_2)]^{8+}$  cations where *n* = 5 (AH78P), 6 (AH78, TriplatinNC) and 7 (AH78H) (**Figure 1.2C**)) were capable of inhibiting site-selective excision by type II restriction endonucleases. Experiments were setup with pre-incubation of DNA using a variety of PPCs concentrations followed thereafter by exposure to a selection of endonucleases (BamHI, EcoRI, SalI). Concentration dependent endonuclease inhibition was identified in each case, with high intensities of the native pUC19 band visible (in linear form) indicative of protection.<sup>75</sup> Furthermore, a distinct dependency on linker chain length with the pentanediamine complex protecting or inhibiting linearized pUC19 DNA from digestion in the nanomolar range, while a 10-fold concentration increase was required to block restriction activity in the hexane- and heptane- bridged Triplatin cations.

### 1.3.7 Non-covalent recognition elements

Oxidative DNA damage is known to be dependent on a number of factors including and not limited to: DNA plasmid type and conformation, presence/absence of exogenous oxidant and reductant, presence chelating agents and dependence on hydrogen peroxide.<sup>85,112,113</sup> Therefore, it was of interest to further probe the oxidation profiles of the copper(II) phenazine series and determine whether DNA cleavage site specificity could be enhanced or inhibited in the presence of non-covalent recognition elements such as minor groove (netropsin), major groove (methyl green) and electrostatic agents ( $[\text{Co}(\text{NH}_3)_6]\text{Cl}_3$ ) (**Figure 1.10B**). Pre-incubation of DNA with major groove binding agent methyl green resulted in enhanced chemical nuclease activity—most likely by directing drug-DNA interactions towards the minor groove—while the presence of the minor groove binding agent netropsin was found to significantly reduce the oxidative DNA damage profile of the complex series.<sup>92</sup>

## 1.4 Fluorescence and absorbance based techniques

### 1.4.1 Indirect fluorometric assays

Small organic molecules with high specificity and affinity for nucleic acids, becoming optically fluorescent upon binding, are invaluable tools in the molecular biology lab. In particular, when probing DNA binding affinity of metal complexes with low molar extinction coefficients (*e.g.* Cu(II) and Mn(II) metallodrugs), these techniques are valuable given the absence of direct electronic spectroscopic measurements. Examples of such dyes routinely used in fluorescence microscopy and flow cytometry include the blue fluorescent AT specific dye, DAPI (4',6-diamidino-2-phenylindole), commonly used as a nuclear counterstain; intercalating Sybr Green I, used for the detection of double stranded DNA and also as a chromosomal stain, and red fluorescent nuclear and chromosome counterstain, propidium iodide (3,8-diamino-5-[3-(diethylmethylammonio)propyl]-6-phenylphenanthridinium diiodide) (**Figure 1.10A**).<sup>91,114-116</sup> Fluorescent dyes, however, are not just limited to microscope imaging as they have also found use in high-throughput assays designed to indirectly assess the affinity at which a small drug molecule can bind to DNA (including fluorescence resonance energy transfer (FRET) assays extensively reviewed for metallodrug-stabilization and melting curves in G-quadruplex systems<sup>19</sup>). Two such examples are the planar heterocyclic intercalator, ethidium bromide (3,8-diamino-5-ethyl-6-phenylphenanthridinium bromide; EtBr), and the crescent shaped minor groove binding agent, Hoechst 33258. Since these molecules have low fluorescence when free in solution and become highly fluorescent when bound to DNA,<sup>117,118</sup> their photophysical properties can be used to inversely determine the ability of a small molecules to bind DNA through fluorescence depletion.

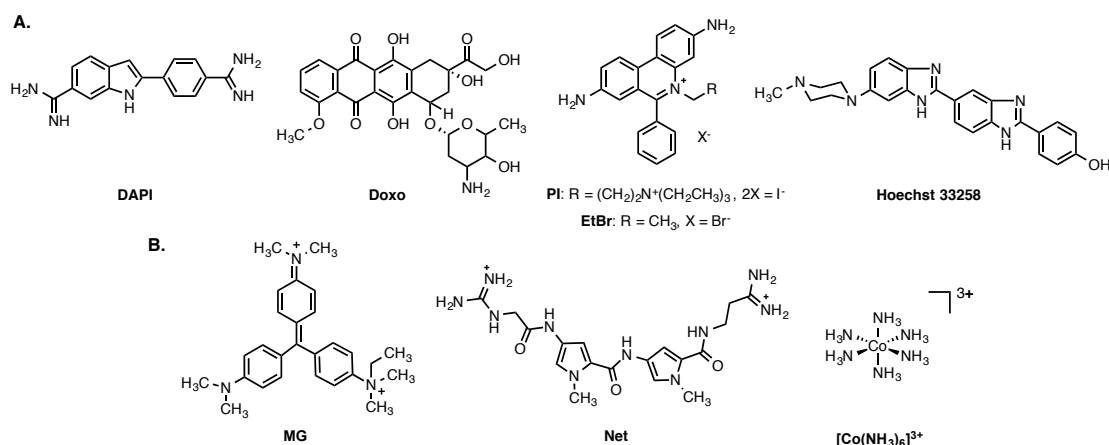


**Figure 1. 10** **A.** Molecules with fluorescent DNA binding properties; DAPI, Doxo (doxorubicin), PI (propidium iodide), EtBr (ethidium bromide) and Hoechst 33258 and **B.** non-covalent DNA recognition elements; MG (methyl green, major groove binder), Net (netropsin, minor groove binder) and cobalt(III) hexammine ([Co(NH<sub>3</sub>)<sub>6</sub>]<sup>3+</sup>, electrostatic agent).

### 1.4.2 Competitive fluorescent displacement

The competitive EtBr displacement assay is an indirect titration technique used to determine the apparent binding constants ( $K_{app}$ ) of non-fluorescent DNA-binding ligands and complexes. This use of EtBr to probe drug-DNA binding constants was originally proposed in 1979 by Morgan *et al.*<sup>119</sup> and conducted in rectangular quartz cuvettes, however in recent years Kellett *et al.* have modified this assay to take advantage of a 96-well fluorescence plate reader to allow for high throughput analysis.<sup>113,120</sup> This procedure involves treating DNA (10  $\mu$ M) with an excess of the intercalating ethidium bromide molecule (12.6  $\mu$ M)—saturating all available binding sites between the DNA base pairs—resulting in strong fluorescence. This quantitative titration method is used to determine the amount of test sample required to induce a 50% decrease in the fluorescence of the EtBr reporter molecule, referred to as the  $C_{50}$  value. Using this high-throughput approach, drug concentrations are measured in triplicate and the apparent binding constants are calculated using  $K_{app} = K_e \times 12.6/C_{50}$  where  $K_e = 8.8 \times 10^6 \text{ M(bp)}^{-1}$ .<sup>75</sup> This reproducible displacement assay can be applied to rank the binding affinity of both individual and families of compounds over a defined concentration range.<sup>75,85</sup>

### 1.4.3 Competitive fluorescence quenching

Fluorescence quenching assays under conditions of excess DNA (*e.g.* 25  $\mu$ M M(Bp)<sup>-1</sup>) treated with limited bound fluorescent EtBr (5  $\mu$ M) allow for complexes to be characterised based on their ability to distinguish between modes of DNA interaction. Not only can fluorescent probe molecules be varied based on mode of interaction (*e.g.* EtBr – intercalator; Hoechst 33258 – minor groove binder) but so too can the %GC content of DNA.<sup>85,113</sup> Quenching ( $Q$ ) values can be determined by the concentration of test sample required to induce 50% quenching of the drug-free control fluorescence giving rise to the identification of potentially new intercalators or groove binders and their sequence dependence.

## 1.5 Absorbance based techniques

### 1.5.1 Overview

UV-visible spectroscopy of nucleic acids is dominated by base absorption since each nucleobase has low symmetry and several heteroatom lone pairs. Transitions for individual bases tend to overlap and produce a single broad strong absorption band for the whole nucleic acid polymer, with an absorbance maximum ( $A_{max}$ ) between 250-280 nm. The maximal absorbance of a nucleic acid ( $\lambda_{max}$ ) is dependent on its composition, AT content vs. GC content (**Figure 1.11A**). Likewise, the molar extinction coefficient ( $\epsilon_{max}$ ) of the nucleic acid is dependent on composition and whether it is single stranded or double stranded (**Figure 1.11B**).<sup>111</sup> A useful resource can be freely accessed

on <http://www.atdbio.com/tools/oligo-calculator>, where the UV and thermodynamic properties of DNA sequences can be calculated.

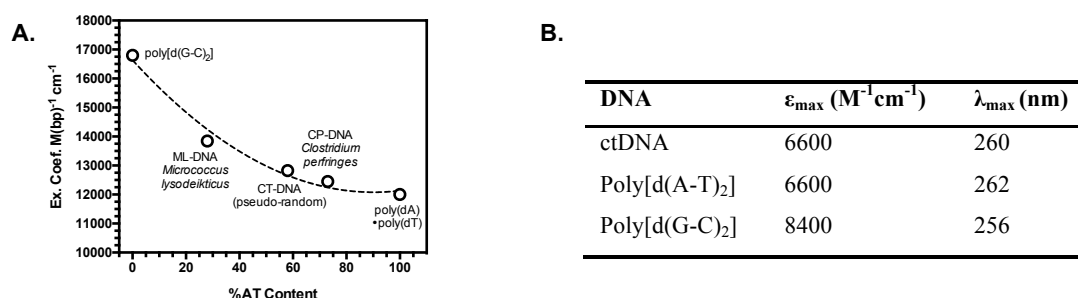


**Figure 1. 11** A. Determination of molar extinction coefficients for double stranded DNA and extinction coefficients and B.  $\lambda_{\max}$  values for synthetic polymers of varying GC content.

### 1.5.2 Thermal melting

Thermal melting ( $T_M$ ) marks the midpoint in the melting process of DNA, when a 50:50 equilibrium exists between helical and single stranded states. Since AT regions contain fewer  $\pi$ - $\pi$  stacking interactions, these hydrogen bonds melt first, promoting the initial unwinding of the DNA helix, followed by the melting of remaining GC rich regions. The thermal melting process is based on the loss of both hydrophobic interactions and  $\pi$ - $\pi$  stacking interactions from nearest neighbor interactions due to the denaturation of the double helix and ultimate loss of secondary structure when bases become unstacked.<sup>121</sup> This process is reversible and full renaturation of duplex DNA can occur approximately 25°C below the denaturation temperature.<sup>122</sup> This is a powerful technique, that relies on the intrinsic extinction coefficients of nucleic acids, to probe the thermodynamic parameters involved in metallodrug-DNA binding interactions.

The differential stability of AT and GC rich regions and splitting of the duplex into single strands, is of paramount importance to many cellular processes such as transcription and recombination and is also critical in the molecular biology lab for techniques such as polymerase chain reaction (PCR). The thermal denaturation of DNA is also strongly influenced by duplex environment including salt and buffered solvent conditions. For example, the higher the salt concentration ( $\leq 1M$ ), the higher the  $T_M$ , as increasing the concentration helps to diffuse the negative charge on the phosphate backbone (electrostatic stabilisation).<sup>123</sup> The relationship between  $T_M$  and ionic strength can be exploited in order to change a  $T_M$  to a more convenient experimental temperature.

The physical property of denaturation can be monitored easily using a UV-vis spectrophotometer by observing the change in absorbance as a function of temperature. The method offers a useful insight into the strength of drug-DNA interactions as the more energy



required to denature the stabilized secondary structure relative to the untreated polynucleotide, the stronger the drug interaction ( $\Delta T_M$ ) and *vice versa*.<sup>85</sup> Structural features of DNA dramatically impact the affinity of a drug molecule toward it. This influence can be clearly seen in **Table 1.2**, as actinomycin D substantially stabilized the thermal denaturation of poly[d(G-C)<sub>2</sub>], while minor groove binding agent netropsin, was seen to have an equal magnitude of stabilisation on the thermal melting profile of poly[d(A-T)<sub>2</sub>]. We have also used this method effectively in order to rank the activity of a triplatin complex series on both calf thymus DNA and alternating copolymers.<sup>75,85</sup>

**Table 1. 2** Influence of standard agents and selected copper phenazine complexes on the thermal melting of synthetic alternating copolymers.<sup>85</sup>

Agent	$\Delta T_M$ (°C)	
	Poly[d(A-T) <sub>2</sub> ]	Poly[d(G-C) <sub>2</sub> ]
Netropsin	12.32 ± 0.79	02.83 ± 0.38
Actinomycin D	-0.32 ± 0.29	12.10 ± 0.95
Cu-DPQ-Phen	0.60 ± 0.18	11.39 ± 1.10
Cu-DPPZ-Phen	0.50 ± 0.10	10.44 ± 1.10

### 1.5.3 Circular dichroism spectroscopy

Circular dichroism spectroscopy probes the absolute configuration and conformation of a system and is dependent on chirality. This UV based method is used extensively for the study of the secondary structure of chiral biomolecules and is particularly useful to determine conformational properties such as the  $\alpha$  and  $\beta$  helix of proteins and the A, B and Z-forms of DNA. In the case of DNA, heterocyclic nitrogenous DNA bases are achiral themselves but when linked to a 5' carbon sugar by a  $\beta$ -glycosidic linkage and placed within the phosphate framework in a stacked helical formation, the molecule as a whole becomes chiral, therefore the electronic transitions of bases are monitored in the UV range of 180-300 nm. DNA structures can be affected by environmental factors in solution—temperature, pH and ionic strength (**Figure 1.12C**)—and also by drug-DNA interactions; inducing significant variations in the resulting spectra.<sup>124</sup>

Many DNA binding agents are achiral and optically inactive, however by observing changes at specific wavelengths in the UV spectrum where DNA typically absorbs (**Figure 1.12B**), it is possible to determine the induced circular dichroism (ICD) of the drug-DNA interaction, through the coupling of electric transition moments of the ligand and the DNA bases.<sup>125</sup> Using this spectroscopic method it is possible to determine a molecules preferred binding mode (minor groove, major groove, intercalation) within the asymmetric DNA environment by observing the induced CD signal relative to untreated DNA at wavelengths of 210, 220, 246 and 268 nm.<sup>126</sup>

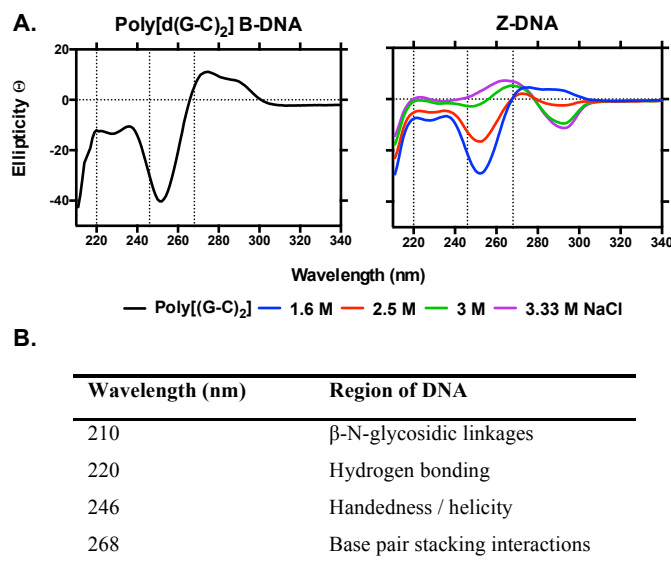


**Figure 1.12** **A.** B  $\rightarrow$  Z NaCl titration of alternating co-polymer poly[d(G-C)<sub>2</sub>] with increasing amounts of salt (unpublished results) and, **B.** and wavelengths of interest for CD DNA studies.

Intercalation typically leads to an increase in the elliptical signal of helicity and base pair stacking interactions of B-DNA, while groove binding agents typically cause an increase in the elliptical signal associated with hydrogen bonding interactions. CD has effectively been used to show a B $\rightarrow$ Z<sup>127</sup> and B $\rightarrow$ A<sup>128</sup> conformational changes when poly(dG-dC)•poly(dG-dC) was treated with both monofunctional and bifunctional platinum complexes.

CD offers many advantages over NMR and X-ray crystallography in the analysis of structural interactions in biological systems as it is an inexpensive technique requiring small amounts of sample, allowing for rapid and highly sensitive analysis of oligonucleotides of both short and long base pair composition offering an alternative absorbance based technique to determine binding mode and affinity of drug-DNA interactions.<sup>129</sup> Linear dichroism—another powerful form of polarized-light spectroscopy complementing CD—has been successfully employed to deduce drug-DNA binding geometries and has been extensively reviewed elsewhere.<sup>130,131</sup>

#### 1.5.4 ELISA detection of 8-oxo-dG lesion formation

8-oxo-2'-deoxyguanosine (8-oxo-dG) is one of the most popular and well-studied biomarkers of oxidative stress since it can be readily detected indirectly in bodily fluids including urine, serum and plasma through the measurement of repaired adducts as the daily flux of repaired adducts should reflect the intracellular rate of oxidative DNA damage.<sup>132</sup> Several chromatography based methods can be employed to assess 8-oxo-dG as a biomarker of oxidative stress including high pressure liquid chromatography with electrochemical detection (HPLC-EC), gas chromatography coupled to mass spectroscopy (GC-MS), and the standard stable isotope dilution liquid

chromatography-MS/MS.<sup>133,134</sup> However, many debates still exist regarding the most suitable method to determine 8-oxo-dG, as nucleotides are prone to oxidation during both sample preparation and analysis. It has been reported in literature that GC-MS estimates of DNA oxidation have been shown to be higher than HPLC-EC estimates by a factor of  $\sim 10$ .<sup>132</sup>

We recently employed a Trevigen high throughput ELISA kit in order to quantify the extent of oxidative lesions induced by the copper phenazine complex series. Detection of oxidative lesions is conducted using a HRP conjugate and TACS Sapphire colorimetric substrate with lesions quantified using a fluorescence plate reader. It was determined that 8-oxo-dG liberation followed the overall trend Cu-DPQ-Phen > Cu-Phen > Cu-DPPZ-Phen (**Figure 1.7**) with higher lesion numbers detected under heavily sheared plasmid conditions where DNA was treated with higher drug concentrations.<sup>92</sup>

## 1.6 Viscosity

Unlike fluorescence and absorbance-based techniques, viscosity does not involve the study of new optical properties arising through metallodrug-nucleic acid binding. Rather, this is a method in which drug-DNA interactions can be studied as a function of the physical hydrodynamic changes induced by the addition of a drug molecule. Experiments are conducted by introducing increasing ratios of drug into a solution containing a fixed concentration of DNA and observing how the velocity of DNA sedimentation influences a change in centipoise (cP). Relative viscosity data can be represented as  $(\eta/\eta_o)$  versus the [compound] / [DNA] ratio  $r$ , where  $\eta$  is the viscosity of complex treated DNA and  $\eta_o$  is the viscosity of untreated DNA.<sup>86</sup> This technique is sensitive to changes in the length of DNA chain and individual modes of binding can be distinguished effectively since covalent and non-covalent binding modes display different hydrodynamic characteristics.

Intercalating molecules induce extension and unwinding of the deoxyribose phosphate backbone due to separation of base pairs in order to accommodate the bound ligand ultimately resulting in the lengthening of the DNA molecule—these hydrodynamic changes can be monitored by viscometry as the length of the molecule is increased in proportion to the amount of drug bound (**Figure 1.13**).<sup>42</sup> Indeed the opposite effect can be noted for non-covalent major and minor groove binding agents since they cause little or no distortion to the phosphate backbone of DNA. In contrast, condensing agents—such as the triplatin series of complexes—are capable of compacting and precipitating sheared DNA, and ultimately decreasing the overall trend of viscosity.<sup>75</sup>

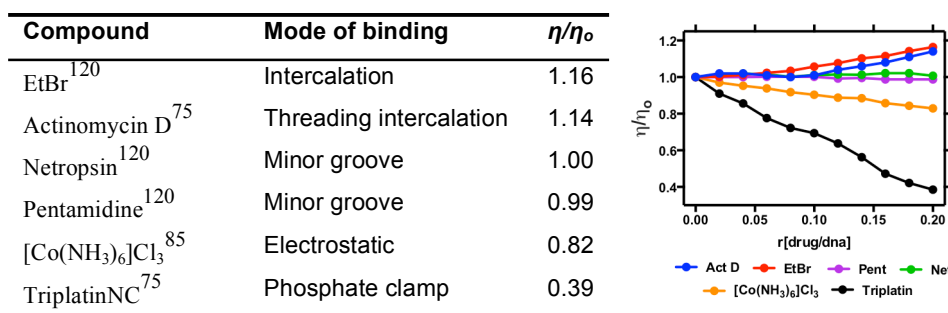


**Figure 1. 13** Relative viscosity values of organic and inorganic compounds bound to duplex stDNA.

## 1.7 Mass Spectrometry

Advances in technologies and ionization techniques now make Electrospray Ionization-Mass Spectrometry (ESI-MS) an indispensable tool for probing drug-nucleic acid interactions with several advantages including the need for only a small sample, speed of use, and ease of analysis.<sup>135,136</sup> Covalent binding with biomolecules in general is easily observed and with appropriate digestion can pinpoint stoichiometry and binding sites of metallodrugs. It is in the study of non-covalent interactions where most interest resides because, if strong enough, the canonical non-covalent binding modes of hydrogen-bonding, electrostatic interactions, and intercalation can be transferred to the gas phase without disruption. Single-stranded, double-stranded and G-quadruplex DNA have all been studied and primary spectra combined with MS-MS techniques can give information on strength and sites of binding.

DNA as a template affects kinetics of substitution reactions occurring within its domain. Mass spectrometric studies using 18-mers showed a kinetic preference for binding of BBR3464 to ssDNA over dsDNA.<sup>137</sup> In this case, electrospray ionization coupled with Fourier transform ion cyclotron resonance mass spectrometry (ESI-FTICR-MS) is sufficiently sensitive to observe the ‘pre-association’ of the covalently binding molecule prior to Pt-DNA bond formation. For single-stranded DNA, the site of binding of the substitution-inert TriplatinNC and AH44 on a 18-mer ssDNA (5'-TCTCCCAGCGTGCGCCAT-3') was ascertained using Tandem MS-MS of the 1:1 adducts (**Figure 1.14**).<sup>40</sup> The binding is sufficiently strong that the fragment ion pattern is distinctly different and upon MS-MS there is no drug-DNA dissociation, only cleavage of the oligonucleotide backbone.

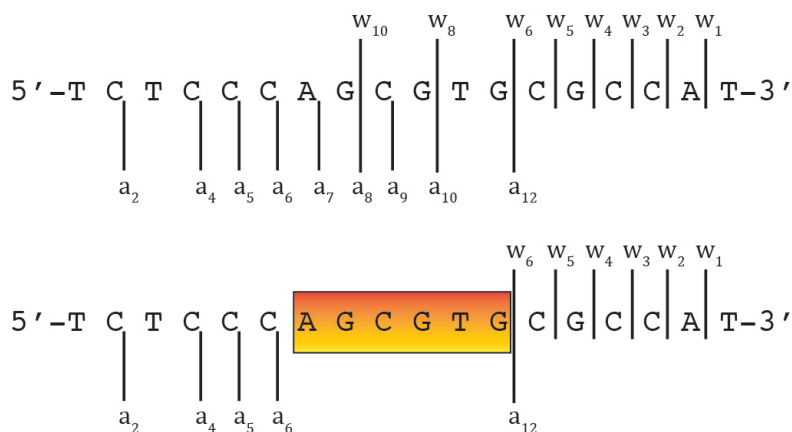


**Figure 1. 14** ESI-MS/MS of free (top) and PPC (either TriplatinNC or AH44) adducted (bottom) 5'-d(TCTCCCAGCGTGCGCCAT) at 100 and 120V of collisional energy, respectively.<sup>40</sup> Fragmentation of the glycosidic bonds is prevalent throughout the free, with the region of enhanced stability in red. The associated fragment ions (w<sub>8</sub><sup>2-</sup>, w<sub>9</sub><sup>2-</sup>, and a<sub>9</sub>-a<sub>12</sub> using standard McLuckey nomenclature<sup>138,139</sup>) are absent in the adduct indicating the area of PPC binding.

Full scan ESI-MS spectra of dsDNA AT duplex {5'-TAGCGCTTTTCCGTA-3'} – {5'-TACGCGAAAAAGCGCTA-3'} complexed with substitution-inert PPCs also confirmed that the non-bonding interaction is strong enough to be transferred from solution to the gas phase.<sup>14</sup> The CID spectra showed duplex unzipping into single strands with again no loss of PPC-DNA binding and duplex stabilization correlates with increasing charge and hydrogen bonding character of the complex. The energy required to separate the PPC-DNA adducts is significantly more than needed for the minor groove binding Hoechst dye. Upon increasing the collisional energy the single-stranded DNA formed dissociates as above.

ESI-MS has also proven useful in probing relative binding affinities of metal complexes to duplex and quadruplex DNA.<sup>140,141</sup> Differences in binding within a series of octahedral metallointercalators based on [Ru(phen)<sub>3</sub>]<sup>2+</sup> and [Ru(phen)<sub>2</sub>(dppz)]<sup>2+</sup> and square-planar analogs such as [Pt(en)(phen)]<sup>2+</sup> demonstrated that the binding affinity in general towards quadruplex DNA is significantly less than that towards dsDNA.<sup>140</sup>

## 1.8 NMR Spectroscopy

NMR spectroscopy, like mass spectrometry, has benefitted significantly from advances in field strength, magnetic shielding and cryogenic probes.<sup>142,143</sup> Spectral analysis of HPLC-purified site-specific oligonucleotide adducts with cisplatin have characterized the major conformational changes upon platination using essentially standard 2D-NMR techniques.<sup>142,143</sup> In the case of BBR3464 and congeners ([{*trans*-PtCl(NH<sub>3</sub>)<sub>2</sub>}<sub>2</sub>μ-H<sub>2</sub>N(CH<sub>2</sub>)<sub>6</sub>NH<sub>2</sub>]<sup>2+</sup> adducted to the self-complementary DNA octamer 5'-d(ATG\*TACAT)<sub>2</sub>-3', the formation of the novel 1,4-interstrand crosslinks was confirmed.<sup>144,145</sup> Strong H8/H1' intraresidue crosspeaks observed for the A1 and A7 resonances are consistent with a *syn*-conformation for these bases as well as the platinated

guanines. The structure suggests unusual cooperative effects unique to this class of anticancer drugs and the lack of severe DNA distortion such as a kink or directed bend may explain the inability of HMG-domain proteins to recognize these lesions, a biological consequence significantly different from that of mononuclear complexes such as cisplatin.<sup>103</sup> A unique feature of long-range {Pt,Pt} interstrand crosslinks is the occurrence of directional isomers—the existence of the unusual 3' → 3' linkage isomer in the sequence was also confirmed by 2D NMR spectroscopy.<sup>146</sup>

The most useful isotopes for NMR studies are  $^1\text{H}$ ,  $^{15}\text{N}$  and  $^{195}\text{Pt}$ . The latter is extremely sensitive to the nature of the ligands attached and can be used for speciation and kinetic studies. The use of  $\{^1\text{H}, ^{15}\text{N}\}$  HMQC/HSQC NMR spectroscopy greatly enhances sensitivity and is especially useful in kinetic studies with biological molecules. The chemical shift and coupling constants (e.g.  $^1J\{^{15}\text{N}-^{195}\text{Pt}\}$ ) are sensitive to the nature of the *trans* ligands, and coupled to the fact that the only protons observed are those bound to the  $^{15}\text{N}$  nucleus makes the technique of great practical use. Pre-association and strong non-covalent binding can be observed as well as kinetics of DNA binding.

Using fully  $^{15}\text{N}$ -labelled TriplatinNC, the presence of the phosphate clamp in solution with the Dickerson-Drew Duplex (DDD) was confirmed by observation of large chemical shift differences of the  $\delta(\text{NH}_3)$  and  $\delta(-\text{NH}_2\text{R})$  in both the  $^1\text{H}$  and  $^{15}\text{N}$  dimensions.<sup>147</sup> The 2D  $\{^1\text{H}, ^{15}\text{N}\}$  HSQC NMR spectrum of  $^{15}\text{N}$ -labelled TriplatinNC shows only two cross-peaks and a weak peak due to dangling amine (**Figure 15**). In the presence of DDD at pH 6, dramatic downfield  $^{15}\text{N}$  shifts of approximately 20 ppm are observed. The coupling constant changes are also consistent with formation of the phosphate clamp.<sup>147</sup>

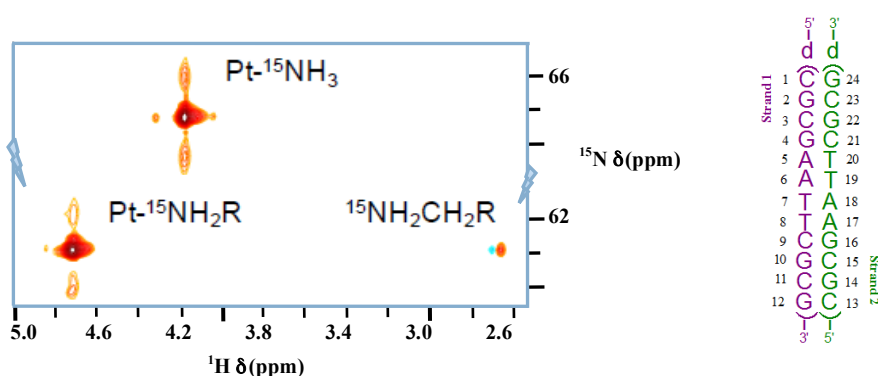


**Figure 1. 15**  $\{^1\text{H}, ^{15}\text{N}\}$  HSQC NMR of TriplatinNC (left) and Dickerson-Drew Duplex (DDD, right). Satellites from  $^1J(^{15}\text{N}-^{195}\text{Pt})$  are clearly visible. Adapted with permission from Qu *et al.*<sup>147</sup>

Pre-association may affect the final conformation of covalently-bound interstrand crosslinks and even the isomer directionality. These features have been studied by 2D  $\{^1\text{H}, ^{15}\text{N}\}$  HSQC NMR.<sup>148</sup> A unique feature of DNA binding modes for PPCs is the kinetic preference for single-strand over dsDNA— as noted by ESI-MS studies. Mass spectrometric studies using 18-mers showed a kinetic preference for binding to ssDNA over dsDNA.<sup>137</sup> For BBR3464 the aquation rate constant is of the same order of magnitude to that of cisplatin, but the chloride anion rate constant is much higher so that the equilibrium favours the dichloro form.<sup>149,150</sup> A 3-fold slowing of the aquation of BBR3464 occurs in the presence of dsDNA but not ssDNA.<sup>151</sup> This feature may account for the kinetic binding preference and may also be relevant in stabilization of G-quartet quadruplex structures using BBR3464.<sup>152</sup> The results emphasize how the alteration of chemical properties of small molecules in the presence of large host interactions is dependent on the conformation and nature of that host and these examples show the utility of NMR techniques in probing these subtle interactions.

## 1.9 *In cellulo* genotoxicity

### 1.9.1 Intracellular ROS damage

The intracellular generation of endogeneous ROS can be monitored *via* the oxidation of the diacetate precursor to the highly fluorogenic 2',7'-dichlorodihydrofluorescein (DCFH).<sup>153</sup> Sequential time-course quantification can reveal time or concentration-dependent liberation of ROS from metal complexes. We have recently reported the  $\text{Mn}^{2+}$  bis-1,10-phenanthroline (phen) di-salt complex, bridged with octanedioate (oda)  $[\text{Mn}_2(\mu\text{-oda})(\text{phen})_4(\text{H}_2\text{O})_2][\text{Mn}_2(\mu\text{-oda})(\text{phen})_4(\text{oda})_2] \cdot 4\text{H}_2\text{O}$  (Mn-Oda-Phen) in conjunction with cationic  $\text{Cu}^{2+}$  analogue,  $[\text{Cu}_2(\mu\text{-oda})(\text{phen})_4]^{2+}$  (Cu-Oda-Phen) (**Figure 1.7**) as potent *in vitro* anticancer agents and ROS induction.<sup>154</sup> Mn-Oda-Phen elicited exceptional levels of endogenous ROS within cancer cells when examined with the intracellular ROS indicator at 15, 30, 60, 120 and 180 min intervals within a concentration range of 250 – 1000 nM with comparable activity at 12.5  $\mu\text{M}$  equivalent to the positive control  $\text{H}_2\text{O}_2$  (500 nM). Substitution of the metal centre notably altered redox properties as the copper analogue did not liberate significant levels when examined at higher concentrations (up to 100  $\mu\text{M}$ ).

### 1.9.2 Intracellular ROS scavengers

Generation of intracellular ROS targets multiple biomolecules such as lipids, proteins and nucleic acids. Sequestering the species through the use of ROS specific antioxidants (similar to those described in section 1.3.2) can elucidate the redox chemistry and generation properties of metal-based anticancer drugs. Radical-selective antioxidants are treated within the cell at concentrations that do not alter cellular viability but are in excessive equivalent to the test complex and as such

those previously mentioned in nuclease gel electrophoresis experiments are not suitable due to innate toxicity of DMSO and KI. The impact of ROS-specific scavengers (D-mannitol for  $\cdot\text{OH}$ ,<sup>155</sup> pyruvate for  $\text{H}_2\text{O}_2$ <sup>156</sup> and tiron for  $\text{O}_2^{\cdot-}$ ,<sup>87</sup>) was examined for Cu-Ph-Phen treated SKOV3 cell survival where co-incubation of antioxidants were found to enhance viability by 12, 16, and 23%, respectively.<sup>91</sup> Results are in excellent agreement with the observed effects on plasmid DNA damage and it is particularly significant that the largest enhancement to viability occurred in the presence of the  $\text{O}_2^{\cdot-}$  scavenger, tiron. Thus we resolved Cu-Ph-Phen exerts cytotoxicity through Haber-Weiss catalytic generation of the superoxide radical accelerating Fenton-like chemistry.

### 1.9.3 Confocal microscopy: detection of DNA fragmentation and condensation

The use of confocal microscopy allows the evaluation of macromolecular structures in fine detail while revealing the intracellular molecular interactions and identification of morphological changes associated with apoptotic cell death. Incorporating DNA specific fluorogenic dyes, such as propidium iodide, Hoechst, acridine orange and DAPI (**Figure 1.10A**), can reveal alterations and distortions in genomic DNA and chromatin structure such as shrinking, condensations, fragmentation and disassembly of the nuclear envelope. This method was used to examine the pharmacological effects of TriplatinNC treated with 20  $\mu\text{M}$  for 24h, stained with DAPI (4',6-diamidino-2-phenylindole), exhibited DNA condensation and compaction in colorectal cancer cell line, HCT116 (**Figure 1.16A**).<sup>157</sup>

### 1.9.4 Immunodetection of double strand breaks (DSBs) with $\gamma\text{H2AX}$

A primary response to dsDNA damage is the site-selective phosphorylation of H2AX, a histone variant that is indiscriminately incorporated into the chromatin structure.<sup>158,159</sup> H2AX differs from other H2A histones through a carboxyl tail containing 139 serine residue that becomes phosphorylated in the presence of dsDNA damage and is denoted  $\gamma\text{H2AX}$ .<sup>160</sup> The accumulation of phosphorylated H2AX creates a signaling beacon and focus for subsequent recruitment of DNA repair mechanisms. A proportional correlation is observed between the extent of DNA damage and formation of  $\gamma\text{H2AX}$  foci thus rendering it as a pertinent method for dsDNA damage detection. Following the advent of phosphorylation, a recognition antibody for  $\gamma\text{H2AX}$  can be utilised to visualise and quantify this process through either fluorogen conjugation to the primary or secondary antibodies. Using  $\gamma\text{H2AX}$ , we have recently reported DNA damage induction by Cu-Ph-Phen and Cu-Ph-Bipy (**Figure 1.7**).<sup>86</sup> In particular, the 1,10-phenanthroline analogue induced a large number of double strand breaks (DSBs) in comparison to the bipyridyl derivative and cisplatin, where DSBs observed in the latter is most likely due to DNA repair mechanisms and excision of platinated adducts (**Figure 1.16B**). Quantification of H2AX was conducted through flow cytometry; by quantifying mean intensity fluorescence (MIF) the trend Cu-Ph-Phen > cisplatin >> Cu-Ph-Bipy was identified and was in agreement with microscopic observations.



### 1.9.5 COMET assay: neutral and alkaline

Single cell gel electrophoresis, otherwise known as the comet assay, is a useful method to evaluate the extent of DNA damage induced by genotoxic chemicals.<sup>161</sup> Various modifications to the COMET assay explores types of strand breaks and alkaline labile sites within the cell.<sup>162</sup> The severity of DNA degradation can be segregated based on the pH of electrophoretic buffer with the use of neutral buffers for DSBs while a more sensitive alkaline method can visualise both ds and ss breaks. Cells embedded onto agarose-coated slides are lysed of membrane and histone structure under high salt and detergent conditions leaving nucleoids of negatively supercoiled DNA. When subjected to electrophoresis, the migration of the DNA is dependent on the integrity and extent of damage. High levels of degradation result in patterns that are comet in shape, where intact DNA is localized to the head, and increasingly damaged DNA results in retarded migration forming the tail shape. Based on the proportion of DNA in the head and tail, scoring a population of COMETs allows statistical comparison between treated and non-treated populations. This method can also be employed to measure the extent of interstrand cross-linking. Irradiation by  $\gamma$ -radiation induced double strand breaks, however in the presence of DNA platinating agents, the reduction in comet tail length are indicative of the extent of interstrand crosslinking.<sup>163</sup> This is observed for the mononuclear trans-platinum carboxylate complex with substituted pyridine (TPA V)<sup>164</sup> and polynuclear complexes BBR3610 and DACH analogue, (**Figure 1.7**), capable of forming long-range inter and intrastrands (**Figure 1.16C**).<sup>163</sup>

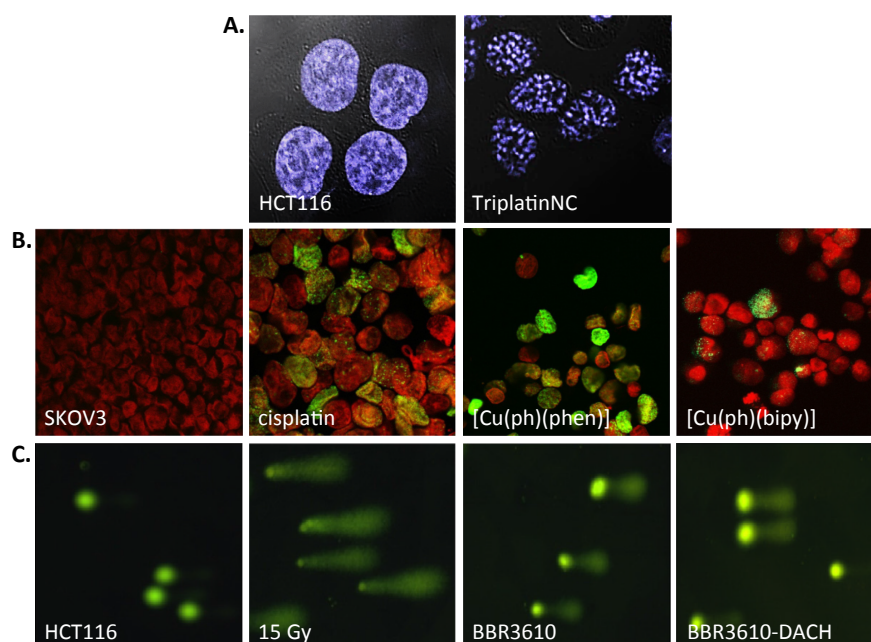


**Figure 1. 16** **A.** Nuclear condensation observed in colorectal cancer cells, HTC116 when treated with TriplatinNC. **B.** Induction of double strand break detected *via*  $\gamma$ H2AX foci (green) and nuclear counterstain (red) in ovarian cancer cells SKOV3. **C.** COMET assay evaluation of BBR3610 and DACH analogue interstrand crosslinks in irradiated HCT116 cells. Images reproduced with permission from original publications.<sup>86,157,160</sup>

## 1.10 Conclusion

DNA is a well-established pharmacological target for metallodrugs and, as such, developmental anticancer complexes continue to be rationally designed for potential clinical use. The elucidation of covalent or non-covalent binding modes, along with helical and groove residency is therefore a crucial area of study in this field. As such, this review has focused on selected molecular and biophysical methods for determining metallodrug-DNA interactions using gel electrophoretic, electronic and fluorescent spectroscopic, immunohistochemical, NMR spectroscopic, and mass spectrometric techniques. Significantly, when combinations of complementary molecular methods are employed, full elucidation of solution binding properties can be defined, which ultimately broaden our understanding of complex-DNA binding. The techniques for covalent binding as demonstrated for the platinum case can, and have been, easily applied to other classes of transition-metal cytotoxics such as those containing Ru(II) or Au(I/III).<sup>165,166</sup> Our recent work on probing the nucleic acid binding mode by ‘phosphate clamping’ Triplatin complexes elegantly reveals how these molecular techniques can function synergistically;<sup>75</sup> using a family of cationic tri-platinum(II) complexes of varying aliphatic linker length [ $\{trans\text{-Pt}(\text{NH}_3)_2(\text{NH}_2(\text{CH}_2)_n\text{NH}_3)\}_2\text{-}\mu\text{-(}trans\text{-Pt}(\text{NH}_3)_2(\text{NH}_2(\text{CH}_2)_n\text{NH}_2)_2\}$ ](NO<sub>3</sub>)<sub>8</sub>, where  $n = 5$  (AH78P), 6 (AH78; TriplatinNC) and 7 (AH78H), high-affinity PPC-DNA interactions were uncovered using ethidium bromide fluorescence quenching, while cooperative fluorescence binding of Hoechst 33258 was observed at the minor groove. Conformational changes on long DNA were then identified using viscosity, electrophoretic, and CD spectroscopic methods where aggregation/condensation of nucleic acids was evidenced in tandem with conversion from B  $\rightarrow$  Z-DNA. 2D-<sup>1</sup>H NMR experiments, in conjunction with several other molecular methods, then indicated two limiting modes of phosphate clamping—backbone tracking (GC dependent) and groove spanning (AT dependent)—could be distinguished and implied DNA condensation was driven, primarily, by minor-groove spanning. Further application of electrophoresis (including ‘on-chip’ microfluidics) showed Triplatin-DNA binding prevented endonuclease activity by type II restriction enzymes. Subsequent work by Farrell and co-workers identified nucleolar condensation in colorectal cancer cells using confocal microscopy<sup>157</sup> with atomic force microscopy (AFM) studies showing this class to condense both tRNA and dsDNA structures.<sup>74</sup> Other examples on the augmentation of molecular methods have been described in this review and, with this in mind, both the overlap and versatility of complementary techniques are further delineated.

## 1.11 References

- (1) Farrell, N. P. (2015) Multi-platinum anti-cancer agents. Substitution-inert compounds for tumor selectivity and new targets. *Chem. Soc. Rev.* 44, 8773–8785.
- (2) Chen, J., and Stubbe, J. (2005) Bleomycins: towards better therapeutics. *Nat. Rev. Cancer* 5, 102–112.
- (3) Johnstone, T. C., Suntharalingam, K., and Lippard, S. J. (2016) The Next Generation of Platinum Drugs: Targeted Pt(II) Agents, Nanoparticle Delivery, and Pt(IV) Prodrugs. *Chem. Rev.* 116, 3436–3486.
- (4) Komor, A. C., and Barton, J. K. (2013) The path for metal complexes to a DNA target. *Chem. Commun.* 49, 3617–3630.
- (5) Watson, J. D., and Crick, F. (1953) Molecular structure of nucleic acids. *Nature* 737–738.
- (6) Rosenberg, B., van Camp, L., and Krigas, T. (1965) Inhibition of Cell Division in *Escherichia coli* by Electrolysis Products from a Platinum Electrode. *Nature* 205, 698–699.
- (7) Chargaff, E. (1971) Preface to a grammar of biology. *Science* 172, 637–642.
- (8) Wing, R., Drew, H., Takano, T., Broka, C., Tanaka, S., Itakura, K., and Dickerson, R. E. (1980) Crystal structure analysis of a complete turn of B-DNA. *Nature* 287, 755–758.
- (9) Drew, H. R., Wing, R. M., Takano, T., Broka, C., Tanaka, S., Itakura, K., and Dickerson, R. E. (1981) Structure of a B-DNA dodecamer: conformation and dynamics. *Proc. Natl. Acad. Sci. U.S.A.* 78, 2179–2183.
- (10) Harteis, S., and Schneider, S. (2014) Making the bend: DNA tertiary structure and protein-DNA interactions. *Int. J. Mol. Sci.* 15, 12335–12363.
- (11) Önfelt, B., Lincoln, P., and Nordén, B. (2001) Enantioselective DNA Threading Dynamics by Phenazine-Linked [Ru(phen)2dppz]2+ Dimers. *J. Am. Chem. Soc.*, 123, 3630–3637.
- (12) Rich, A., and Zhang, S. (2003) Z-DNA: the long road to biological function. *Nat. Rev. Genet.* 4, 566–572.
- (13) Ussery, D. W. (2002) DNA Structure: A-, B- and Z-DNA Helix Families. John Wiley & Sons, Ltd., 0003122
- (14) Komeda, S., Qu, Y., Mangrum, J. B., Hegmans, A., Williams, L. D., and Kelland, L. R. (2016) The phosphate clamp as recognition motif in platinum–DNA interactions. *Inorg. Chim. Acta.* 452, 25–33.
- (15) Georgiades, S. N., Abd Karim, N. H., Suntharalingam, K., and Vilar, R. (2010) Interaction of Metal Complexes with G-Quadruplex DNA. *Angew. Chem. Int. Ed.* 49, 4020–4034.
- (16) Yu, Z., Han, M., and Cowan, J. A. (2015) Toward the Design of a Catalytic Metallo drug: Selective Cleavage of G-Quadruplex Telomeric DNA by an Anticancer Copper–Acridine–ATCUN Complex. *Angew. Chem. Int. Ed.* 54, 1901–1905.
- (17) Phongtongpasuk, S., Paulus, S., Schnabl, J., Sigel, R. K. O., Spingler, B., Hannon, M. J., and Freisinger, E. (2013) Binding of a Designed Anti-Cancer Drug to the Central Cavity of an RNA Three-Way Junction. *Angew. Chem. Int. Ed.* 52, 11513–11516.
- (18) Su, M., Tomás-Gamasa, M., and Carell, T. (2015) DNA based multi-copper ions assembly using combined pyrazole and salen ligandosides. *Chem. Sci.* 6, 632–638.
- (19) Cao, Q., Li, Y., Freisinger, E., Qin, P. Z., Sigel, R. K. O., and Mao, Z.-W. (2016) G-quadruplex DNA targeted metal complexes acting as potential anticancer drugs. *Inorg. Chem. Front.* C6QI00300A.
- (20) Kelland, L. R. (1999) Cisplatin-based Anticancer Agents, in *Uses of Inorganic Chemistry in Medicine*, pp 109–123. Royal Society of Chemistry, Cambridge.
- (21) Wheate, N. J., Walker, S., Craig, G. E., and Oun, R. (2010) The status of platinum anticancer drugs in the clinic and in clinical trials. *Dalton Trans.* 39, 8113–8127.

- (22) Dabrowiak, J. C. (2009) Cisplatin, in *Metals in Medicine*, pp 73–107. John Wiley & Sons, Ltd.
- (23) Miller, S. E., and House, D. A. (1990) The hydrolysis products of cis-dichlorodiammineplatinum(II) 3. Hydrolysis kinetics at physiological pH. *Inorg. Chim. Acta* 173, 53–60.
- (24) Cepeda, V., Fuertes, M. A., Castilla, J., Alonso, C., Quevedo, C., and Pérez, J. M. (2007) Biochemical Mechanisms of Cisplatin Cytotoxicity. *Anti-Cancer Agents Med. Chem.* 7, 3–18.
- (25) Klein, A. V., and Hambley T. (2009) Platinum Drug Distribution in Cancer Cells and Tumors. *Chem. Rev.* 109, 4911–4920.
- (26) Alberto, M. E., Butera, V., and Russo, N. (2011) Which One among the Pt-Containing Anticancer Drugs More Easily Forms Monoadducts with G and A DNA Bases? A Comparative Study among Oxaliplatin, Nedaplatin, and Carboplatin. *Inorg. Chem.* 50, 6965–6971.
- (27) Dabrowiak, J. C. (2009) Cisplatin. *Metals in Medicine*, pp 73–107. John Wiley & Sons, Ltd, Chichester, UK.
- (28) Jones, C. J., and Thornback, J. (2007) Chapter 4. Therapeutic Medicine, in *Medicinal Applications of Coordination Chemistry*, pp 201–323. Royal Society of Chemistry, Cambridge.
- (29) Jamieson, E. R., and Lippard, S. J. (1999) Structure, Recognition, and Processing of Cisplatin-DNA Adducts. *Chem. Rev.* 99, 2467–2498.
- (30) Bellon, S. F., Coleman, J. H., and Lippard, S. J. (1991) DNA unwinding produced by site-specific intrastrand cross-links of the antitumor drug cis-diamminedichloroplatinum(II). *Biochemistry* 30, 8026–8035.
- (31) Chaney, S. G., Campbell, S. L., Temple, B., Bassett, E., Wu, Y., and Faldu, M. (2004) Protein interactions with platinum–DNA adducts: from structure to function. *J. Inorg. Biochem.* 98, 1551–1559.
- (32) Tanida, S., Mizoshita, T., Ozeki, K., Tsukamoto, H., Kamiya, T., Kataoka, H., Sakamuro, D., and Joh, T. (2012) Mechanisms of Cisplatin-Induced Apoptosis and of Cisplatin Sensitivity: Potential of BIN1 to Act as a Potent Predictor of Cisplatin Sensitivity in Gastric Cancer Treatment. *Int. J. Surg. Oncol.* 862879.
- (33) Chvalova, K., Brabec, V., and Kasparkova, J. (2007) Mechanism of the formation of DNA–protein cross-links by antitumor cisplatin. *Nucleic Acids Res.* 35, 1812–1821.
- (34) El-Khateeb, M., Appleton, T. G., Gahan, L. R., Charles, B. G., Berners-Price, S. J., and Bolton, A.-M. (1999) Reactions of cisplatin hydrolytes with methionine, cysteine, and plasma ultrafiltrate studied by a combination of HPLC and NMR techniques. *J. Inorg. Biochem.* 77, 13–21.
- (35) Bose, R. N., and Weaver, E. L. (1997) A long-lived ascorbate radical in the platinum(II) catalysed reductions of platinum(IV) antitumor drugs. *J. Chem. Soc., Dalton Trans.* 1797–1800.
- (36) Kelley, S. L., Basu, A., Teicher, B. A., Hacker, M. P., Hamer, D. H., and Lazo, J. S. (1988) Overexpression of metallothionein confers resistance to anticancer drugs. *Science* 241, 1813–1815.
- (37) Reißner, T., Schneider, S., Schorr, S., and Carell, T. (2010) Crystal structure of a cisplatin-(1,3-GTG) cross-link within DNA polymerase  $\epsilon$ . *Angew. Chem. Int. Ed.* 49, 3077–3080.
- (38) Hegmans, A., Berners-Price, S. J., Davies, M. S., Thomas, D. S., Humphreys, A. S., and Farrell, N. (2004) Long Range 1,4 and 1,6-Interstrand Cross-Links Formed by a Trinuclear Platinum Complex. Minor Groove Preassociation Affects Kinetics and Mechanism of Cross-Link Formation as Well as Adduct Structure. *J. Am. Chem. Soc.* 126, 2166–2180.
- (39) Komeda, S., Moulaei, T., Woods, K. K., Chikuma, M., Kelland, L. R., and Williams, L. D. (2006) A Third Mode of DNA Binding: Phosphate Clamps by a Polynuclear Platinum Complex. *J. Am. Chem. Soc.* 128, 16092–16103.
- (40) Mangrum, J. B., and Kelland, L. R. (2010) Excursions in polynuclear platinum DNA binding. *Chem. Commun.* 46, 6640–6650.

- (41) Jodrell, D. I., Evans, T. R. J., Steward, W., Cameron, D., Prendiville, J., Aschele, C., Noberasco, C., Lind, M., Carmichael, J., Dobbs, N., Camboni, G., Gatti, B., and De Braud, F. (2004) Phase II studies of BBR3464, a novel tri-nuclear platinum complex, in patients with gastric or gastro-oesophageal adenocarcinoma. *Eur. J. Cancer* 40, 1872–1877.
- (42) Lerman, L. S. (1961) Structural considerations in the interaction of DNA and acridines. *J. Mol. Biol.* 3, 18–30.
- (43) Rescifina, A., Zagni, C., Varrica, M. G., Pistrà, V., and Corsaro, A. (2014) Recent advances in small organic molecules as DNA intercalating agents: Synthesis, activity, and modeling. *Eur. J. Med. Chem.* 74, 95–115.
- (44) Liu, H.-K., and Sadler, P. J. (2011) Metal Complexes as DNA Intercalators. *Acc. Chem. Res.* 44, 349–359.
- (45) Jennette, K. W., Lippard, S. J., Vassiliades, G. A., and Bauer, W. R. (1974) Metallointercalation reagents. 2-hydroxyethanethiolato(2,2',2''-terpyridine)-platinum(II) monocation binds strongly to DNA by intercalation. *Proc. Natl. Acad. Sci. U.S.A.* 71, 3839–3843.
- (46) Bond, P. J., Langridge, R., Jennette, K. W., and Lippard, S. J. (1975) X-ray fiber diffraction evidence for neighbor exclusion binding of a platinum metallointercalation reagent to DNA. *Proc. Natl. Acad. Sci. U.S.A.* 72, 4825–4829.
- (47) Zeglis, B. M., Pierre, V. C., and Barton, J. K. (2007) Metallo-intercalators and metallo-insertors. *Chem. Commun.* 4565–4579.
- (48) Pages, B. J., Ang, D. L., Wright, E. P., and Aldrich-Wright, J. R. (2015) Metal complex interactions with DNA. *Dalton Trans.* 44, 3505–3526.
- (49) Galindo-Murillo, R., García-Ramos, J. C., Ruiz-Azuara, L., Cheatham, T. E., and Cortés-Guzmán, F. (2015) Intercalation processes of copper complexes in DNA. *Nucleic Acids Res.* 43, 5364–5376.
- (50) Li, G., Sun, L., Ji, L., and Chao, H. (2016) Ruthenium(II) complexes with dppz: from molecular photoswitch to biological applications. *Dalton Trans.* 45, 13261–13276.
- (51) Zhang, T.-B., Zhang, C.-L., Dong, Z.-L., and Guan, Y.-F. (2015) Determination of Base Binding Strength and Base Stacking Interaction of DNA Duplex Using Atomic Force Microscope. *Sci. Rep.* 5, 9143.
- (52) Matta, C. F., Castillo, N., and Boyd, R. J. (2006) Extended weak bonding interactions in DNA: pi-stacking (base-base), base-backbone, and backbone-backbone interactions. *J. Phys. Chem. B* 110, 563–578.
- (53) Hunter, C. A., and Sanders, J. K. M. (1990) The nature of  $\pi$ - $\pi$  interactions. *J. Am. Chem. Soc.* 112, 5525–5534.
- (54) Wheeler, S. E. (2011) Local Nature of Substituent Effects in Stacking Interactions. *J. Am. Chem. Soc.* 133, 10262–10274.
- (55) Martinez, C. R., and Iverson, B. L. (2012) Rethinking the term “pi-stacking.” *Chem. Sci.* 3, 2191–2201.
- (56) Keck, M. V., and Lippard, S. J. (1992) Unwinding of supercoiled DNA by platinum-ethidium and related complexes. *J. Am. Chem. Soc.* 114, 3386–3390.
- (57) Kielkopf, C. L., Erkkila, K. E., Hudson, B. P., Barton, J. K., and Rees, D. C. (2000) Structure of a photoactive rhodium complex intercalated into DNA. *Nat. Struct. Mol. Biol.* 7, 117–121.
- (58) Rao, S. N., and Kollman, P. A. (1987) Molecular mechanical simulations on double intercalation of 9-amino acridine into d(CGCGCGC) X d(GCGCGCG): analysis of the physical basis for the neighbor-exclusion principle. *Proc. Natl. Acad. Sci. U.S.A.* 84, 5735–5739.
- (59) Collins, J. G., Sleeman, A. D., Aldrich-Wright, J. R., Greguric, I., and Hambley T. (1998) A <sup>1</sup>H NMR Study of the DNA Binding of Ruthenium(II) Polypyridyl Complexes. *Inorg. Chem.* 37, 3133–3141.

- (60) Hall, J. P., Beer, H., Buchner, K., Cardin, D. J., and Cardin, C. J. (2013) Preferred orientation in an angled intercalation site of a chloro-substituted  $\Lambda$ -[Ru(TAP)2(dppz)]<sup>2+</sup> complex bound to d(TCGGCGCCGA)<sub>2</sub>. *Philos. Trans. A Math. Phys. Eng. Sci.* 371, 20120525–20120525.
- (61) Niyazi, H., Hall, J. P., O'Sullivan, K., Winter, G., Sorensen, T., Kelly, J. M., and Cardin, C. J. (2012) Crystal structures of  $\Lambda$ -[Ru(phen)2dppz]<sup>2+</sup> with oligonucleotides containing TA/TA and AT/AT steps show two intercalation modes. *Nature Chem.* 4, 621–628.
- (62) Franco, D., Vargiu, A. V., and Magistrato, A. (2014) Ru[(bpy)2(dppz)]<sup>2+</sup> and Rh[(bpy)2(chrysi)]<sup>3+</sup> Targeting Double Strand DNA: The Shape of the Intercalating Ligand Tunes the Free Energy Landscape of Deintercalation. *Inorg. Chem.* 53, 7999–8008.
- (63) Yakovchuk, P., Protozanova, E., and Frank-Kamenetskii, M. D. (2006) Base-stacking and base-pairing contributions into thermal stability of the DNA double helix. *Nucleic Acids Res.* 34, 564–574.
- (64) Howe-Grant, M., and Lippard, S. J. (1979) Binding of platinum(II) intercalation reagents to deoxyribonucleic acid. Dependence on base-pair composition, nature of the intercalator, and ionic strength. *Biochemistry* 18, 5762–5769.
- (65) R Erik Holmlin, Eric D A Stemp, A., and Barton, J. K. (1998) Ru(phen)2dppz<sup>2+</sup> Luminescence: Dependence on DNA Sequences and Groove-Binding Agents. *Inorg. Chem.* 37, 29–34.
- (66) Krotz, A. H., Hudson, B. P., and Barton, J. K. (1993) Assembly of DNA recognition elements on an octahedral rhodium intercalator: predictive recognition of 5'-TGCA-3' by .DELTA.-[Rh(R,R)-Me2trien]phi<sub>3</sub>. *J. Am. Chem. Soc.* 115, 12577–12578.
- (67) Pierre, V. C., Kaiser, J. T., and Barton, J. K. (2007) Insights into finding a mismatch through the structure of a mispaired DNA bound by a rhodium intercalator. *Proc. Natl. Acad. Sci. U.S.A.* 104, 429–434.
- (68) Komor, A. C., and Barton, J. K. (2014) An Unusual Ligand Coordination Gives Rise to a New Family of Rhodium Metalloinsertors with Improved Selectivity and Potency. *J. Am. Chem. Soc.* 136, 14160–14172.
- (69) Song, H., Kaiser, J. T., and Barton, J. K. (2012) Crystal structure of  $\Lambda$ -[Ru(bpy)2dppz]<sup>2+</sup> bound to mismatched DNA reveals side-by-side metalloinsertion and intercalation. *Nature Chem.* 4, 615–620.
- (70) Jackson, B. A., Alekseyev, V. Y., and Barton, J. K. (1999) A versatile mismatch recognition agent: specific cleavage of a plasmid DNA at a single base mispair. *Biochemistry* 38, 4655–4662.
- (71) Boynton, A. N., Marcélis, L., and Barton, J. K. (2016) [Ru(Me4phen)2dppz]<sup>2+</sup>, a Light Switch for DNA Mismatches. *J. Am. Chem. Soc.* 138, 5020–5023.
- (72) Önfelt, B., Lincoln, P., and Nordén, B. (2001) Enantioselective DNA Threading Dynamics by Phenazine-Linked [Ru(phen) 2dppz] 2+Dimers. *J. Am. Chem. Soc.* 123, 3630–3637.
- (73) Malina, J., Kelland, L. R., and Brabec, V. (2014) DNA Condensing Effects and Sequence Selectivity of DNA Binding of Antitumor Noncovalent Polynuclear Platinum Complexes. *Inorg. Chem.* 53, 1662–1671.
- (74) Malina, J., Kelland, L. R., and Brabec, V. (2014) Substitution-Inert Trinuclear Platinum Complexes Efficiently Condense/Aggregate Nucleic Acids and Inhibit Enzymatic Activity. *Angew. Chem. Int. Ed.* 53, 12812–12816.
- (75) Prisecaru, A., Molphy, Z., Kipping, R. G., Peterson, E. J., Qu, Y., Kellett, A., and Farrell, N. P. (2014) The phosphate clamp: sequence selective nucleic acid binding profiles and conformational induction of endonuclease inhibition by cationic Triplatin complexes. *Nucleic Acids Res.* 42, 13474–13487.

- (76) Harris, A. L., Ryan, J. J., and Farrell, N. (2006) Biological consequences of trinuclear platinum complexes: comparison of  $[[\text{trans-PtCl}(\text{NH}_3)_2]_2\mu\text{-(trans-Pt}(\text{NH}_3)_2(\text{H}_2\text{N}(\text{CH}_2)_6\text{-NH}_2)_2)]^{4+}$  (BBR 3464) with its noncovalent congeners. *Mol. Pharmacol.* 69, 666–672.
- (77) Komeda, S., Moulaei, T., Chikuma, M., Odani, A., Kipping, R., Kelland, L. R., and Williams, L. D. (2011) The phosphate clamp: a small and independent motif for nucleic acid backbone recognition. *Nucleic Acids Res.* 39, 325–336.
- (78) Farrell, N. P. (2015) Multi-platinum anti-cancer agents. Substitution-inert compounds for tumor selectivity and new targets. *Chem. Soc. Rev.* 44, 8773–8785.
- (79) Silva, H., Frézard, F., Peterson, E. J., Kabolizadeh, P., Ryan, J. J., and Kelland, L. R. (2012) Heparan Sulfate Proteoglycan-Mediated Entry Pathway for Charged Tri-Platinum Compounds: Differential Cellular Accumulation Mechanisms for Platinum. *Mol. Pharmaceutics* 9, 1795–1802.
- (80) Mangrum, J. B., Engelmann, B. J., Peterson, E. J., Ryan, J. J., Berners-Price, S. J., and Kelland, L. R. (2014) A new approach to glycan targeting: enzyme inhibition by oligosaccharide metalloshielding. *Chem. Commun.* 50, 4056–4058.
- (81) Helleday, T., Eshtad, S., and Nik-Zainal, S. (2014) Mechanisms underlying mutational signatures in human cancers. *Nat. Rev. Genet.* 15, 585–598.
- (82) Weiss, B., and Richardson, C. C. (1967) Enzymatic breakage and joining of deoxyribonucleic acid, I. Repair of single-strand breaks in DNA by an enzyme system from *Escherichia coli* infected with T4 bacteriophage. *Proc. Natl. Acad. Sci. U.S.A.* 57, 1021–1028.
- (83) Pitié, M., and Pratviel, G. (2010) Activation of DNA Carbon–Hydrogen Bonds by Metal Complexes. *Chem. Rev.* 110, 1018–1059.
- (84) Kellett, A., McCann, M., Howe, O., O'Connor, M., and Devereux, M. (2012) DNA cleavage reactions of the dinuclear chemotherapeutic agent copper(II) bis-1,10-phenanthroline terephthalate. *Int. J. Clin. Pharmacol. Ther.* 50, 79–81.
- (85) Molphy, Z., Prisecaru, A., Slator, C., Barron, N., McCann, M., Colleran, J., Chandran, D., Gathergood, N., and Kellett, A. (2014) Copper phenanthrene oxidative chemical nucleases. *Inorg. Chem.* 53, 5392–5404.
- (86) Kellett, A., Howe, O., O'Connor, M., McCann, M., Creaven, B. S., McClean, S., Foltyn-Arfa Kia, A., Casey, A., and Devereux, M. (2012) Radical-induced DNA damage by cytotoxic square-planar copper(II) complexes incorporating o-phthalate and 1,10-phenanthroline or 2,2'-dipyridyl. *Free Radic. Biol. Med.* 53, 564–576.
- (87) Taiwo, F. A. (2008) Mechanism of tiron as scavenger of superoxide ions and free electrons. *J. Spectrosc.* 22, 491–498.
- (88) Franco, R., Panayiotidis, M. I., and Cidlowski, J. A. (2007) Glutathione Depletion Is Necessary for Apoptosis in Lymphoid Cells Independent of Reactive Oxygen Species Formation. *J. Biol. Chem.* 282, 30452–30465.
- (89) Miyoshi, N., Ueda, M., Fuke, K., Tanimoto, Y., and Itoh, M. (1982) Lifetime of singlet oxygen and quenching by  $\text{NaN}_3$  in mixed solvents. *Z. Naturforsch. B Chem. Sci.* 37, 649–652.
- (90) Dunand, C., Crèvecoeur, M., and Penel, C. (2007) Distribution of superoxide and hydrogen peroxide in *Arabidopsis* root and their influence on root development: possible interaction with peroxidases. *New Phytol.* 174, 332–341.
- (91) Slator, C., Barron, N., Howe, O., and Kellett, A. (2016)  $[\text{Cu}(\text{o-phthalate})(\text{phenanthroline})]$  Exhibits Unique Superoxide-Mediated NCI-60 Chemotherapeutic Action through Genomic DNA Damage and Mitochondrial Dysfunction. *ACS Chem. Biol.* 11, 159–171.
- (92) Molphy, Z., Slator, C., Chatgililoglu, C., and Kellett, A. (2015) DNA oxidation profiles of copper phenanthrene chemical nucleases. *Front. Chem.* 3, 28.
- (93) Wang, J. C. (2002) Cellular roles of dna topoisomerases: a molecular perspective. *Nat. Rev. Mol. Cell Biol.* 3, 430–440.

- (94) Peixoto, P., Bailly, C., and David-Cordonnier, M.-H. (2010) Topoisomerase I-mediated DNA relaxation as a tool to study intercalation of small molecules into supercoiled DNA. *Methods Mol. Biol.* 613, 235–256.
- (95) Wang, J. G. (1974) The degree of unwinding of the DNA helix by ethidium: I. titration of twisted PM2 DNA molecules in alkaline cesium chloride density gradients. *J. Mol. Biol.* 89, 783–801.
- (96) Bachur, N. R., Gordon, S. L., and Gee, M. V. (1977) Anthracycline antibiotic augmentation of microsomal electron transport and free radical formation. *Mol. Pharmacol.* 13, 901–910.
- (97) Gewirtz, D. (1999) A critical evaluation of the mechanisms of action proposed for the antitumor effects of the anthracycline antibiotics adriamycin and daunorubicin. *Biochem. Pharmacol.* 57, 727–741.
- (98) Kasparkova, J., Farrell, N., and Brabec, V. (2000) Sequence specificity, conformation, and recognition by HMG1 protein of major DNA interstrand cross-links of antitumor dinuclear platinum complexes. *J. Biol. Chem.* 275, 15789–15798.
- (99) Rice, J. A., Crothers, D. M., Pinto, A. L., and Lippard, S. J. (1988) The major adduct of the antitumor drug cis-diamminedichloroplatinum(II) with DNA bends the duplex by approximately equal to 40 degrees toward the major groove. *Proc. Natl. Acad. Sci. U.S.A.* 85, 4158–4161.
- (100) Malinge, J.-M., Pérez, C., and Leng, M. (1994) Base sequence-independent distortions induced by interstrand cross-links in cis-diamminedichloroplatinum (II)-modified DNA. *Nucleic Acids Res.* 22, 3834–3839.
- (101) Kasparkova, J., Vojtiskova, M., and Natile, G. (2008) Unique Properties of DNA Interstrand Cross-Links of Antitumor Oxaliplatin and the Effect of Chirality of the Carrier Ligand. *Chem. Eur. J.* 14, 1330–1341.
- (102) Suchánková, T., Kubíček, K., Kasparkova, J., Brabec, V., and Kozelka, J. (2012) Platinum-DNA interstrand crosslinks: molecular determinants of bending and unwinding of the double helix. *J. Inorg. Biochem.* 108, 69–79.
- (103) Kasparkova, J., Zehnulova, J., Farrell, N., and Brabec, V. (2002) DNA interstrand cross-links of the novel antitumor trinuclear platinum complex BBR3464. Conformation, recognition by high mobility group domain proteins, and nucleotide excision repair. *J. Biol. Chem.* 277, 48076–48086.
- (104) Pieper, R. O., and Erickson, L. C. (1990) DNA adenine adducts induced by nitrogen mustards and their role in transcription termination in vitro. *Carcinogenesis* 11, 1739–1746.
- (105) Wang, P., Bauer, G. B., Bennett, R. A. O., and Povirk, L. F. (1991) Thermolabile adenine adducts and A • T base pair substitutions induced by nitrogen mustard analogs in an SV40-based shuttle plasmid. *Biochemistry* 30, 11515–11521.
- (106) Wang, P., Bauer, G. B., Kellogg, G. E., Abraham, D. J., and Povirk, L. F. (1994) Effect of distamycin on chlorambucil-induced mutagenesis in pZ189: evidence of a role for minor groove alkylation at adenine N-3. *Mutagenesis* 9, 133–139.
- (107) Qu, Y., Moniodis, J. J., Harris, A. L., Yang, X., Hegmans, A., Povirk, L. F., Berners-Price, S. J., and Kelland, L. R. (2011) Non-Covalent Polynuclear Platinum Compounds as Polyamine Analogs, in *Polyamine Drug Discovery*, pp 191–204. Royal Society of Chemistry, Cambridge.
- (108) Goidin, D., and Thureau, C. (2002) Lab-on-chip technology. *Spectra Anal.* 31, 32–34.
- (109) Lykidis, D., Van Noorden, S., Armstrong, A., Spencer-Dene, B., Li, J., Zhuang, Z., and Stamp, G. W. H. (2007) Novel zinc-based fixative for high quality DNA, RNA and protein analysis. *Nucleic Acids Res.* 35, e85.
- (110) Brena, R. M., Auer, H., Kornacker, K., Hackanson, B., Raval, A., Byrd, J. C., and Plass, C. (2006) Accurate quantification of DNA methylation using combined bisulfite restriction analysis coupled with the Agilent 2100 Bioanalyzer platform. *Nucleic Acids Res.* 34, e17.



- (111) Brisco, M. J., and Morley, A. A. (2012) Quantification of RNA integrity and its use for measurement of transcript number. *Nucleic Acids Res.* 40, e144.
- (112) Prisecaru, A., Devereux, M., Barron, N., McCann, M., Colleran, J., Casey, A., McKee, V., and Kellett, A. (2012) Potent oxidative DNA cleavage by the di-copper cytotoxin: [Cu<sub>2</sub>(μ-terephthalate)(1,10-phen)<sub>4</sub>]<sub>2</sub>. *Chem. Commun.* 48, 6906–6908.
- (113) (2013) Regulating bioactivity of Cu<sup>2+</sup> bis-1,10-phenanthroline artificial metallonucleases with sterically functionalized pendant carboxylates. *J. Med. Chem.* 56, 8599–8615.
- (114) Tarnowski, B. I., Spinale, F. G., and Nicholson, J. H. (2009) DAPI as a Useful Stain for Nuclear Quantitation. *Biotech. Histochem.* 66, 296–302.
- (115) Trantakis, I. A., Fakis, M., Tragoulias, S. S., Christopoulos, T. K., Persephonis, P., Giannetas, V., and Ioannou, P. (2010) Ultrafast fluorescence dynamics of Sybr Green I/DNA complexes. *Chem. Phys. Lett.* 485, 187–190.
- (116) Krishan, A. (1975) Rapid flow cytofluorometric analysis of mammalian cell cycle by propidium iodide staining. *J. Cell Biol.* 66, 188–193.
- (117) Olmsted, J., and Kearns, D. R. (1977) Mechanism of ethidium bromide fluorescence enhancement on binding to nucleic acids. *Biochemistry* 16, 3647–3654.
- (118) Downs, T. R., and Wilfinger, W. W. (1983) Fluorometric quantification of DNA in cells and tissue. *Anal. Biochem.* 131, 538–547.
- (119) Morgan, A. R., Lee, J. S., Pulleyblank, D. E., Murray, N. L., and Evans, D. H. (1979) Ethidium fluorescence assays. Part 1. Physicochemical studies. *Nucleic Acids Res.* 7, 547–565.
- (120) McCann, M., McGinley, J., Ni, K., O'Connor, M., Kavanagh, K., McKee, V., Colleran, J., Devereux, M., Gathergood, N., Barron, N., Prisecaru, A., and Kellett, A. (2013) A new phenanthroline-oxazine ligand: synthesis, coordination chemistry and atypical DNA binding interaction. *Chem. Commun.* 49, 2341–2343.
- (121) Breslauer, K. J., Frank, R., Blöcker, H., and Marky, L. A. (1986) Predicting DNA duplex stability from the base sequence. *Proc. Natl. Acad. Sci. U.S.A.* 83, 3746–3750.
- (122) Marmur, J., and Doty, P. (1961) Thermal renaturation of deoxyribonucleic acids. *J. Mol. Biol.* 3, 585–594.
- (123) Melchior, W. B., and Hippel, Von, P. H. (1973) Alteration of the relative stability of dA-dT and dG-dC base pairs in DNA. *Proc. Natl. Acad. Sci. U.S.A.* 70, 298–302.
- (124) Bishop, G. R., and Chaires, J. B. (2002) Characterization of DNA Structures by Circular Dichroism, in *Current Protocols in Nucleic Acid Chemistry*, 7.11 pp 1-8. John Wiley & Sons, Inc.
- (125) Garbett, N. C., Ragazzon, P. A., and Chaires, J. B. (2007) Circular dichroism to determine binding mode and affinity of ligand-DNA interactions. *Nat. Protoc.* 2, 3166–3172.
- (126) Chang, Y.-M., Chen, C. K. M., and Hou, M.-H. (2012) Conformational Changes in DNA upon Ligand Binding Monitored by Circular Dichroism. *Int. J. Mol. Sci.* 13, 3394–3413.
- (127) Wu, P. K., Wu, P. K., Qu, Y., Farrell, N., and Van Houten, B. (1994) Chemical reactivity and DNA sequence specificity of formally monofunctional and bifunctional bis(platinum) complexes. *J. Inorg. Biochem.* 54, 207–220.
- (128) McGregor, T. D., Balcarová, Z., Qu, Y., Tran, M.-C., Zaludová, R., Brabec, V., and Farrell, N. (1999) Sequence-dependent conformational changes in DNA induced by polynuclear platinum complexes. *J. Inorg. Biochem.* 77, 43–46.
- (129) Kypr, J., Kejnovská, I., Renčiuk, D., and Vorlíčková, M. (2009) Circular dichroism and conformational polymorphism of DNA. *Nucleic Acids Res.* 37, 1713–1725.
- (130) Nordén, B., and Kurucsev, T. (1994) Analysing DNA complexes by circular and linear dichroism. *J. Mol. Recognit.* 7, 141–156.
- (131) Bailly, C., Hénichart, J. P., Colson, P., and Houssier, C. (1992) Drug—DNA sequence-dependent interactions analysed by electric linear dichroism. *J. Mol. Recognit.* 5, 155–171.

- (132) Beckman, K. B., and Ames, B. N. (1997) Oxidative decay of DNA. *J. Biol. Chem.* 272, 19633–19636.
- (133) Nikitaki, Z., Hellweg, C. E., Georgakilas, A. G., and Ravanat, J.-L. (2015) Stress-induced DNA damage biomarkers: applications and limitations. *Front. Chem.* 3, 1–15.
- (134) Cadet, J., Douki, T., and Ravanat, J.-L. (2010) Oxidatively generated base damage to cellular DNA. *Free Radic. Biol. Med.* 49, 9–21.
- (135) Urathamakul, T., Waller, D. J., Beck, J. L., Aldrich-Wright, J. R., and Ralph, S. F. (2008) Comparison of Mass Spectrometry and Other Techniques for Probing Interactions Between Metal Complexes and DNA. *Inorg. Chem.* 47, 6621–6632.
- (136) Beck, J. L., Colgrave, M. L., Ralph, S. F., and Sheil, M. M. (2001) Electrospray ionization mass spectrometry of oligonucleotide complexes with drugs, metals, and proteins. *Mass Spectrom. Rev.* 20, 61–87.
- (137) Kloster, M. B. G., Hannis, J. C., Muddiman, D. C., and Farrell, N. (1999) Consequences of Nucleic Acid Conformation on the Binding of a Trinuclear Platinum Drug. *Biochemistry* 38, 14731–14737.
- (138) McLuckey, S. A., Van Berker, G. J., and Glish, G. L. (1992) Tandem mass spectrometry of small, multiply charged oligonucleotides. *J. Am. Soc. Mass Spectrom.* 3, 60–70.
- (139) Wu, J., and McLuckey, S. A. Gas-phase fragmentation of oligonucleotide ions. *Inter. J. Mass Spectrom.* 237, 197–241.
- (140) Talib, J., Green, C., Davis, K. J., Urathamakul, T., Beck, J. L., Aldrich-Wright, J. R., and Ralph, S. F. (2008) A comparison of the binding of metal complexes to duplex and quadruplex DNA. *Dalton Trans.* 1018–1026.
- (141) Pierce, S. E., Kiełtyka, R., Sleiman, H. F., and Brodbelt, J. S. (2009) Evaluation of binding selectivities and affinities of platinum-based quadruplex interactive complexes by electrospray ionization mass spectrometry. *Biopolymers* 91, 233–243.
- (142) Berners-Price, S. J., Ronconi, L., and Sadler, P. J. (2006) Insights into the mechanism of action of platinum anticancer drugs from multinuclear NMR spectroscopy. *Prog. Nucl. Magn. Reson. Spectrosc.* 49, 65–98.
- (143) Vinje, J., and Sletten, E. (2007) NMR Spectroscopy of Anticancer Platinum Drugs. *Anti-Cancer Agents Med. Chem.* 7, 35–54.
- (144) Qu, Y., Scarsdale, N. J., Tran, M.-C., and Kelland, L. R. (2003) Cooperative effects in long-range 1,4 DNA-DNA interstrand cross-links formed by polynuclear platinum complexes: an unexpected syn orientation of adenine bases outside the binding sites. *J. Biol. Inorg. Chem.* 8, 19–28.
- (145) Qu, Y., Scarsdale, N. J., Tran, M.-C., and Farrell, N. (2004) Comparison of structural effects in 1,4 DNA–DNA interstrand cross-links formed by dinuclear and trinuclear platinum complexes. *J. Inorg. Biochem.* 98, 1585–1590.
- (146) Qu, Y., Tran, M.-C., and Kelland, L. R. (2009) Structural consequences of a 3' → 3' DNA interstrand cross-link by a trinuclear platinum complex: unique formation of two such cross-links in a 10-mer duplex. *J. Biol. Inorg. Chem.* 14, 969–977.
- (147) Qu, Y., Kipping, R. G., and Farrell, N. P. (2015) Solution studies on DNA interactions of substitution-inert platinum complexes mediated via the phosphate clamp. *Dalton Trans.* 44, 3563–3572.
- (148) Ruhayel, R. A., Moniodis, J. J., Yang, X., Kasparkova, J., Brabec, V., Berners-Price, S. J., and Kelland, L. R. (2009) Factors affecting DNA-DNA interstrand cross-links in the antiparallel 3'-3' sense: a comparison with the 5'-5' directional isomer. *Chem. Eur. J* 15, 9365–9374.
- (149) Davies, M. S., Thomas, D. S., Hegmans, A., Berners-Price, S. J., and Farrell, N. (2002) Kinetic and Equilibria Studies of the Aquation of the Trinuclear Platinum Phase II Anticancer

- Agent [ $\{ \text{trans-PtCl}(\text{NH}_3)_2 \}_2 \{ \mu\text{-trans Pt}(\text{NH}_3)_2(\text{NH}_2(\text{CH}_2)_6\text{NH}_2)_2 \}_4 + (\text{BBR3464})$ ]. *Inorg. Chem.* 41, 1101–1109.
- (150) Hegmans, A., Berners-Price, S. J., Davies, M. S., Thomas, D. S., Humphreys, A. S., and Farrell, N. (2004) Long Range 1,4 and 1,6-Interstrand Cross-Links Formed by a Trinuclear Platinum Complex. Minor Groove Preassociation Affects Kinetics and Mechanism of Cross-Link Formation as Well as Adduct Structure. *J. Am. Chem. Soc.* 126, 2166–2180.
- (151) Davies, M. S., Berners-Price, S. J., Cox, J. W., and Farrell, N. (2003) The nature of the DNA template (single- versus double-stranded) affects the rate of aquation of a dinuclear Pt anticancer drug. *Chem. Commun.* 122–123.
- (152) Ourliac-Garnier, I., Elizondo-Riojas, M.-A., Redon, S., Kelland, L. R., and Bombard, S. (2005) Cross-links of quadruplex structures from human telomeric DNA by dinuclear platinum complexes show the flexibility of both structures. *Biochemistry* 44, 10620–10634.
- (153) Bass, D. A., Parce, J. W., Dechatelet, L. R., Szejda, P., Seeds, M. C., and Thomas, M. (1983) Flow cytometric studies of oxidative product formation by neutrophils: a graded response to membrane stimulation. *J. Immunol* 130, 1910–1917.
- (154) Kellett, A., O'Connor, M., McCann, M., Howe, O., Casey, A., McCarron, P., Kavanagh, K., McNamara, M., Kennedy, S., May, D. D., Skell, P. S., O'Shea, D., and Devereux, M. (2011) Water-soluble bis(1,10-phenanthroline) octanedioate  $\text{Cu}^{2+}$  and  $\text{Mn}^{2+}$  complexes with unprecedented nano and picomolar in vitro cytotoxicity: promising leads for chemotherapeutic drug development. *Med. Chem. Commun.* 2, 579–584.
- (155) Goldstein, S., and Czapski, G. (1984) Mannitol as an OH. scavenger in aqueous solutions and in biological systems. *Int. J. Radiat. Biol.* 46, 725–729.
- (156) Giandomenico, A. R., Cerniglia, G. E., Biaglow, J. E., Stevens, C. W., and Koch, C. J. (1997) The importance of sodium pyruvate in assessing damage produced by hydrogen peroxide. *Free Radic. Biol. Med.* 23, 426–434.
- (157) Peterson, E. J., Menon, V. R., Gatti, L., Kipping, R., Dewasinghe, D., Perego, P., Povirk, L. F., and Kelland, L. R. (2015) Nucleolar Targeting by Platinum: p53-Independent Apoptosis Follows rRNA Inhibition, Cell-Cycle Arrest, and DNA Compaction. *Mol. Pharmaceutics* 12, 287–297.
- (158) Bonner, W. M., Redon, C. E., Dickey, J. S., Nakamura, A. J., Sedelnikova, O. A., Solier, S., and Pommier, Y. (2008)  $\gamma\text{H2AX}$  and cancer. *Nat. Rev. Cancer* 8, 957–967.
- (159) Paull, T. T., Rogakou, E. P., Yamazaki, V., Kirchgessner, C. U., Gellert, M., and Bonner, W. M. (2000) A critical role for histone H2AX in recruitment of repair factors to nuclear foci after DNA damage. *Curr. Biol.* 10, 886–895.
- (160) Rogakou, E. P., Pilch, D. R., Orr, A. H., Ivanova, V. S., and Bonner, W. M. (1998) DNA Double-stranded Breaks Induce Histone H2AX Phosphorylation on Serine 139. *J. Biol. Chem.* 273, 5858–5868.
- (161) Olive, P. L., and Banáth, J. P. (2006) The comet assay: a method to measure DNA damage in individual cells. *Nat. Protoc.* 1, 23–29.
- (162) Collins, A. R., Oscoz, A. A., Brunborg, G., Gaivão, I., Giovannelli, L., Kruszewski, M., Smith, C. C., and Stetina, R. (2008) The comet assay: topical issues. *Mutagenesis* 23, 143–151.
- (163) Menon, V. R., Peterson, E. J., Valerie, K., Kelland, L. R., and Povirk, L. F. (2013) Ligand modulation of a dinuclear platinum compound leads to mechanistic differences in cell cycle progression and arrest. *Biochem. Pharmacol.* 86, 1708–1720.
- (164) Aris, S. M., Gewirtz, D. A., Ryan, J. J., Knott, K. M., and Kelland, L. R. (2007) Promotion of DNA strand breaks, interstrand cross-links and apoptotic cell death in A2780 human ovarian cancer cells by transplatinum planar amine complexes. *Biochem. Pharmacol.* 73, 1749–1757.

- (165) Barry, N. P. E., and Sadler, P. J. (2013) Exploration of the medical periodic table: towards new targets. *Chem. Commun.* 49, 5106–5131.
- (166) Berners-Price, S. J., and Filipovska, A. (2011) Gold compounds as therapeutic agents for human diseases. *Metallomics* 3, 863–873.

## Chapter 2

# DNA Oxidation Profiles of Copper Phenanthrene Chemical Nucleases

---

This work was published in *Frontiers in Chemistry*, 2015, 3, 28.

Zara Molphy, Creina Slator, Chryssostomos Chatgililoglu and Andrew Kellett\*.

Within this work, my colleague, Z. Molphy, and I contributed towards experimental execution and manuscript preparation. I specifically contributed towards the following sections: experimental design and execution of antioxidant experiments and 8-oxodG quantifications. Supporting information associated with this chapter can be found in Appendix A.

## 2.1 Abstract

The deleterious effects of metal-catalyzed reactive oxygen species (ROS) in biological systems can be seen in a wide variety of pathological conditions including cancer, cardiovascular disease, ageing, and neurodegenerative disorder. On the other hand however, targeted ROS production in the vicinity of nucleic acids – as demonstrated by metal-activated bleomycin – has paved the way for ROS-active chemotherapeutic drug development. Herein we report mechanistic investigations into the oxidative nuclease activity and redox properties of copper(II) developmental therapeutics  $[\text{Cu}(\text{DPQ})(\text{phen})]^{2+}$  (Cu-DPQ-Phen),  $[\text{Cu}(\text{DPPZ})(\text{phen})]^{2+}$  (Cu-DPPZ-Phen), and  $[\{\text{Cu}(\text{phen})_2\}_2(\mu\text{-terph})](\text{terph})$  (Cu-Terph), with results being compared directly to Sigman's reagent  $[\text{Cu}(\text{phen})_2]^{2+}$  throughout (phen = 1,10-phenanthroline; DPQ = dipyridoquinoxaline; DPPZ = dipyridophenazine). Oxidative DNA damage was identified at the minor groove through use of surface bound recognition elements of methyl green, netropsin, and  $[\text{Co}(\text{NH}_3)_6]\text{Cl}_3$  that functioned to control complex accessibility at selected regions. ROS-specific scavengers and stabilisers were employed to identify the cleavage process, the results of which infer hydrogen peroxide produced metal-hydroxo or free hydroxyl radicals ( $\cdot\text{OH}$ ) as the predominant species. The extent of DNA damage owing to these radicals was then quantified through 8-oxo-2'-deoxyguanosine (8-oxo-dG) lesion detection under ELISA protocol with the overall trend following Cu-DPQ-Phen > Cu-Terph > Cu-Phen > Cu-DPPZ. Finally, the effects of oxidative damage on DNA replication processes were investigated using the polymerase chain reaction (PCR) where amplification of 120 base pair DNA sequences of varying base content were inhibited – particularly along A-T rich chains – through oxidative damage of the template strands.

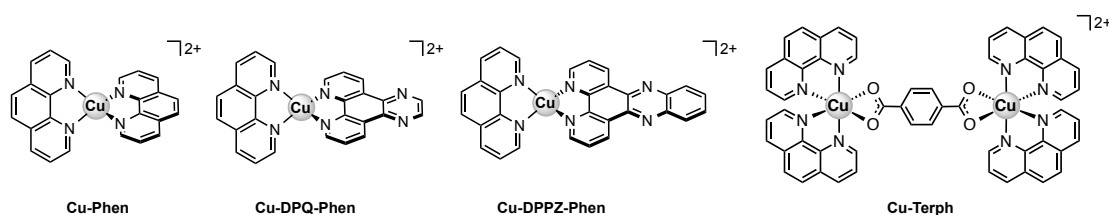
## 2.2 Introduction

Oxygen radical generation is an inevitable consequence of aerobic existence and has been implicated in a wide variety of pathological conditions including cancer, cardiovascular disease, ageing, and neurodegenerative disease (Cooke & Evans, 2007). Reactive oxygen species (ROS) are created in a variety of endogenous chemical and biological processes in the human body – predominantly through oxygen metabolism. The sequential reduction of molecular oxygen can generate reactive intermediates such as superoxide ( $O_2^{\bullet-}$ ) and hydrogen peroxide ( $H_2O_2$ ) that initiate a cascade of redox reactions toward the production of hydroxyl radicals ( $\bullet OH$ ) and related metal-oxo species (Kellett et al., 2012). Molecular targets of ROS include proteins, lipids, and nucleic acids – the deleterious effects of which include base and deoxyribose modifications that ultimately precipitate single or double strand breaks. To counteract this, the majority of cells possess defence mechanisms such as base excision repair (BER) – *e.g.* 8-oxoguanine glycosylase (OGG1) (Xu et al., 2014) – and nucleotide excision repair (NER) pathways that prevents genome instability to ultimately limit cytotoxicity, the accumulation of deleterious mutations, and maintain genome integrity. Two major  $\bullet OH$  induced DNA lesions are 8-oxoguanine (8-oxo-dG), a mutagenic lesion which induces  $G \rightarrow T$  transversions widely seen in mutated oncogenes and tumour suppressor genes, and the poorly mutagenic thymine glycol (Basu, Loechler, Leadon, & Essigmann, 1989; Chatgililoglu & O'Neill, 2001). Recent evidence suggests  $\bullet OH$  attacks occur primarily at base moieties and account for the majority of total hydrogen atom abstraction on DNA alone (Chatgililoglu, Ferreri, & Terzidis, 2011). Thus, 8-oxo-dG has been subjected to intensive investigation due to its prominence as a biomarker within ROS-mediated disease pathology, and its ease of detection in bodily fluids and tissue samples has allowed a variety of detection methods to accurately assess 8-oxo-dG lesions including high-pressure liquid chromatography (HPLC), gas chromatography (GC), mass spectrometry (MS), and the enzyme linked immunosorbent assay (ELISA).

In addition to the induction of endogenous DNA damage, exogenous sources including UV light, ionizing radiation, environmental agents, pharmaceuticals, and industrial chemicals can also initiate ROS production (Klaunig, Kamendulis, & Hocevar, 2010). Indeed the clinical antineoplastic agent bleomycin (BLM) is a redox active agent capable of DNA oxidative cleavage in the presence of Fe(II) (and Cu(I)), molecular oxygen, and endogenous one electron reductants (Burger, 1998; Stubbe and Kozarich, 1987; Chen et al., 2008). Bleomycin can abstract hydrogen atoms from deoxyribose in the DNA backbone, specifically from C4' position (Breen and Murphy, 1995). The active form of Fe(II)-BLM is a ternary, high-valence Fe(III)- $O^{\bullet}$  species (Rodriguez and Hecht, 1982; Gajewski et al., 1991; Pratviel and Bernadou, 1989) that undergoes an electron reduction by endogenous reductants (*e.g.* *L*-ascorbate) or by another molecule of Fe(II)-BLM (Burger et al., 1981; Natrajan et al., 1990). Fe(II)-BLM can form 8-oxo-dG and other base

propenals, however these are known to occur in small amounts; the formation of such DNA degradation products results from  $\cdot\text{OH}$  oxidative damage – a side product only of the ferryl-oxo species – that does not functionally contribute to biological systems or participate in the nuclease activity of activated Fe(II)-BLM (Rodriguez and Hecht, 1982).

Our group have recently investigated a range of  $[\text{Cu}(\text{phen})_2]^{2+}$  (Cu-Phen) (Phen = 1,10-phenanthroline) type systems as potential lead compounds for therapeutic and biochemical application (Kellett et al., 2011; Prisecaru et al., 2012; 2013; Molphy et al., 2014).  $[\text{Cu}(\text{phen})_2]^{2+}$ , originally reported by Sigman *et al.* (Sigman, Graham, Aurora, & Stern, 1979), is believed to cleave DNA through a variety of copper bound oxidants including  $\text{Cu}^{3+}\text{-OH}$  and  $\text{Cu}^+\text{-OOH}$  with the possibility of free  $\cdot\text{OH}$  playing a role in the overall process (Johnson & Nazhat, 1987; Marshall, Graham, Reich, & Sigman, 1981). Recent work on the development of bis-chelate  $\text{Cu}^{2+}$  phenanthroline-phenazine cationic complexes of  $[\text{Cu}(\text{DPQ})(\text{phen})]^{2+}$  (Cu-DPQ-Phen) and  $[\text{Cu}(\text{DPPZ})(\text{phen})]^{2+}$  (Cu-DPPZ-Phen) (DPQ = dipyridoquinoxaline; DPPZ = dipyridophenazine) have demonstrated how extension of the ligated phenazine ligand influences DNA recognition and oxidative degradation (Molphy et al., 2014). Indeed, when designer phenazine ligands (DPQ and DPPZ) are incorporated into the ‘copper bis-phen’ chemical nuclease model, these agents display enhanced DNA recognition and intercalation among the highest reported on ctDNA (Table 1,  $K_{\text{app}} \approx 3 \times 10^7 \text{ M}(\text{bp})^{-1}$ ). Since nuclearity is also established as an important factor in oxidative DNA cleavage (van der Steen et al., 2010; Li et al., 2005), we also reported the dinuclear complex,  $[\{\text{Cu}(\text{phen})_2\}_2(\mu\text{-terph})](\text{terph})$  (Cu-Terph) (terph = terephthalate), which is capable of inducing oxidative DNA strand breaks in the absence of exogenous reductant (Kellett et al., 2011). Cu-Terph has promising *in vitro* cytotoxicity toward human derived breast, prostate, colon, ovarian, and lung human cancer cell lines, with comparable activity to mitoxantrone – a clinical anthracene topoisomerase II inhibitor (Kellett et al., 2011; Prisecaru et al., 2012).



**Scheme 2. 1** Molecule structures of the copper(II) complex cations examined in this study.



**Table 2. 1** Summary of DNA binding properties of tested complexes toward calf thymus DNA (ctDNA) along with synthetic nucleic acid polymers poly[d(A-T)<sub>2</sub>] and poly[d(G-C)<sub>2</sub>].

Compound	C <sub>50</sub> <sup>a</sup>	K <sub>app</sub> M(bp) <sup>-1 b</sup>	Q (μM) poly[d(A-T) <sub>2</sub> ] <sup>c</sup>	Q (μM) poly[d(G-C) <sub>2</sub> ] <sup>c</sup>	ΔT <sub>M</sub> (°C) poly[d(A-T) <sub>2</sub> ] <sup>d</sup>	ΔT <sub>M</sub> (°C) poly[d(G-C) <sub>2</sub> ] <sup>d</sup>
<b>Cu-Phen</b>	179.21	0.67 × 10 <sup>6</sup>	13.34	7.96	-0.02 ± 0.29	06.64 ± 1.58
<b>Cu-DPQ-Phen</b>	3.93	30.45 × 10 <sup>6</sup>	8.34	3.97	0.60 ± 0.18	11.39 ± 1.10
<b>Cu-DPPZ-Phen</b>	4.63	25.85 × 10 <sup>6</sup>	11.60	10.12	0.50 ± 0.10	10.44 ± 1.10
<b>Cu-Terph</b>	39.36	0.30 × 10 <sup>6</sup>	8.6	10.3	NT	NT

<sup>a</sup> C<sub>50</sub> = concentration required to reduce 50% fluorescence of saturated bound ethidium bromide (12.6 μM) on ctDNA (10 μM).

<sup>b</sup> K<sub>app</sub> = K<sub>e</sub> × 12.6/C<sub>50</sub> where K<sub>e</sub> = 9.5 × 10<sup>6</sup> M(bp)<sup>-1</sup> (apparent binding constant on ctDNA).

<sup>c</sup> Fluorescence Quenching (Q) of limited bound Ethidium Bromide (5 μM) bound poly[d(A-T)<sub>2</sub>] and poly[d(G-C)<sub>2</sub>] by Cu<sup>2+</sup> complexes.

<sup>d</sup> ΔT<sub>M</sub> = difference in thermal melting (T<sub>M</sub>) of drug-treated nucleotide at r = 0.1 compared with drug-untreated nucleotide.

NT = not tested.

In this contribution we identify, using head-to-head analysis, the comparative oxidative DNA cleavage properties of DNA binding Cu<sup>2+</sup> complexes Cu-Phen, Cu-DPQ-Phen, Cu-DPPZ-Phen, and Cu-Terph (**Scheme 2.1**) through a variety of biophysical and molecular biological methods. Additionally, we report these agents inhibit DNA polymerase activity—particularly at A-T rich sites—through oxidative degradation of template strands. To that end, we report *i.*) oxidative DNA profiles in the presence of DNA recognition agents of netropsin, methyl green, and [Co(NH<sub>3</sub>)<sub>6</sub>]Cl<sub>3</sub>, *ii.*) DNA cleavage profiles in the presence of radical trapping and stabilising co-factors, *iii.*) quantitation of 8-oxo-dG lesions arising from complex treated superhelical plasmid DNA, and *iv.*) DNA polymerase inhibition on DNA templates of differential A-T content. The DNA binding profiles for this series have previous been reported and are summarised in Table 1 (McCann et al., 2013; Molphy et al., 2014; Kellett et al., 2011; Prisecaru et al., 2013); simple phenanthroline containing complexes (Cu-Phen and Cu-Terph) have moderate binding constants toward ctDNA while phenazine compounds (Cu-DPQ-Phen and Cu-DPPZ-Phen) can be considered as high-affinity dsDNA intercalators. Further, ethidium bromide fluorescence quenching on alternating duplex polymers—poly[d(A-T)<sub>2</sub>] and poly[d(G-C)<sub>2</sub>]<sup>2</sup>—has shown complexes bind at both minor and major grooves. It has not been established, as yet, if chemical nuclease activity occurs preferentially at either or both recognition sites.

## 2.3 Materials and Methods

### 2.3.1 Preparation of the complexes

Chemicals were purchased from Sigma-Aldrich Ireland and used without further purification. DPQ and DPPZ ligands were initially generated through the Schiff base condensation reactions of 1,10-phenanthroline-5,6-dione with ethylenediamine and *o*-phenylenediamine respectively. The bis-phenanthroline complex [Cu(phen)<sub>2</sub>](NO<sub>3</sub>)<sub>2</sub> (Cu-Phen) was prepared by refluxing 1,10-phenanthroline with copper(II) nitrate in a 2:1 molar ratio in aqueous-ethanol (Prisecaru et al., 2013). The phenazine complexes [Cu(DPQ)(Phen)](NO<sub>3</sub>)<sub>2</sub> (Cu-DPQ-Phen) and [Cu(DPPZ)(Phen)](NO<sub>3</sub>)<sub>2</sub> (Cu-DPPZ-Phen) were prepared by treating the mono-phenanthroline complex [Cu(Phen)](NO<sub>3</sub>)<sub>2</sub> with 1 molar equivalent of the corresponding phenazine ligand in

ethanol (Molphy et al., 2014). The  $[\text{Cu}_2(\mu\text{-terephthalate})(1,10\text{-phen})_4]^{2+}$  was prepared by ethanolic reflux of copper(II) terephthalate hydrate and 1,10-phenanthroline in a 1:2 ratio according to the reported method (Kellett et al., 2011).

### 2.3.2 DNA cleavage studies

#### 2.3.2.1 DNA cleavage in the presence of added reductant

The ability of the complexes to oxidatively damage DNA in the presence of added reductant was determined using a method previously published by this laboratory with minor changes (Molphy et al., 2014). Reactions were carried out according to the following general procedure: in a total volume of 20  $\mu\text{L}$  using 80 mM HEPES buffer (pH 7.2) with 25 mM NaCl, 1 mM Na-L-ascorbate, 400 ng superhelical pUC19 (NEB, N3041) and varying concentrations of test complex (250 nM, 500 nM, 1  $\mu\text{M}$  and 2.5  $\mu\text{M}$ ). Complexes were initially prepared in DMF and further diluted in HEPES buffer (Fisher). Samples were incubated at 37  $^\circ\text{C}$  for 30 minutes. Reactions were quenched by adding 6 $\times$  loading buffer (Fermentas) containing 10 mM Tris-HCl, 0.03 % bromophenol blue, 0.03 % xylene cyanole FF, 60 % glycerol, 60 mM EDTA and samples were loaded onto an agarose gel (1.2 %) containing 8  $\mu\text{L}$  EtBr. Electrophoresis was completed at 70 V for 2 hours in 1 $\times$  TAE buffer.

#### 2.3.2.2 DNA cleavage in the presence of non-covalently bound recognition elements

This protocol was adapted from a previously reported procedure (Tabassum *et al.*, 2012). Briefly, 400 ng pUC19 was incubated with 25 mM NaCl, 1 mM Na-L-ascorbate, and 8, or 16  $\mu\text{M}$  of either methyl green, netropsin or hexamine cobalt(III) chloride in 80 mM HEPES buffer (pH 7.2) for 45 minutes at 37  $^\circ\text{C}$ . Sample tubes were then vortexed and varying concentrations of test complex were added (250 nM, 500 nM, 1  $\mu\text{M}$  and 2.5  $\mu\text{M}$ ). The reaction mixture was further incubated at 37  $^\circ\text{C}$  for 30 minutes. The reaction was then quenched with 6 $\times$  loading buffer and subjected to gel electrophoresis (prepared and stained as previously described).

#### 2.3.2.3 DNA oxidation with ROS scavengers and stabilisers

The presence of ROS specific scavengers was used to determine the effect on the DNA cleavage abilities of each copper complex. The procedure was adapted to the previously reported method (Zhou et al., 2014). Briefly, to a final volume of 20  $\mu\text{L}$ , 80 mM HEPES (pH = 7.2), 25 mM NaCl, 1 mM Na-L-ascorbate, and 400 ng of pUC19 DNA were treated with drug concentrations of 250 nM, 500 nM, 1  $\mu\text{M}$  and 2.5  $\mu\text{M}$  in the presence ROS scavengers / stabilisers; KI (10 mM),  $\text{NaN}_3$  (10 mM), DMSO (10 %), and  $\text{D}_2\text{O}$  (77 %). Reactions were incubated for 30 min at 37  $^\circ\text{C}$ , quenched with DNA loading dye and loaded onto 1.2 % agarose gel and run under conditions previously described.

### 2.3.3 HT quantitation of 8-oxo-dG

Quantitation of 8-oxo-dG lesions present in 3000 ng pUC19 plasmid DNA pre-incubated with test complexes (10 and 20  $\mu$ M) at 37 °C for 30 minutes was achieved utilising a high throughput 8-oxo-dG ELISA kit (Trevigen) and performed as per manufacturers guidelines. Samples of damaged DNA were examined in triplicate using a 96 well plate, pre-coated with 8-oxo-dG along with varying concentrations of a standard 8-oxo-dG (200, 100, 50, 25, 12.5, 6.25 and 3.13 nM). An 8-oxo-dG monoclonal antibody, which competitively binds to 8-oxo-dG immobilized to each well, was added to the plate with excess antibody being washed with PBST (1 $\times$  PBS, 0.1% Tween 20). The concentration of 8-oxo-dG was determined based on antibody retention in each well using goat anti-mouse IgG-HRP conjugated antibody and colorimetric detection substrate TACS-Sapphire. Product formation was inversely proportional to 8-oxo-dG present in the DNA sample. Samples were determined using a Bio-Tek synergy HT multimode microplate reader at 450 nm and quantitation of 8-oxo-dG was extrapolated from the standard curve.

### 2.3.4 PCR inhibition studies

This protocol was adapted from a previously reported procedure (Sanchez-Cano et al., 2010). 400 ng pUC19 DNA was initially exposed to each test complex in the presence and absence of 1 mM added reductant at 37 °C for 30 minutes (**Figure S-2** and **S-3**). 20 ng of damaged DNA template was removed and PCR reactions (35 cycles) were carried out with each varying G-C content primer set (**Figure S-4**) at optimum annealing temperatures and analysed using gel electrophoresis. This investigation was replicated in the absence of added reductant (**Figure S-5**) and also at lower drug loading (250 nM, 500 nM, 1  $\mu$ M and 2.5  $\mu$ M) with 1 mM reductant (**Figure S-6**).

## 2.4 Results and Discussion

### 2.4.1 DNA cleavage in the presence of non-covalently bound recognition elements

We have previously shown that DNA oxidative cleavage by copper complexes is dependent on a range of factors including (but not limited to): plasmid DNA conformation and type, presence of competing metal chelating agents (*e.g.* EDTA), reaction / exposure time, and presence / concentration of exogenous reductant or oxidant. In the current work we examine chemical nuclease activity of supercoiled pUC19 plasmid DNA in the presence of 1 mM reductant (Na-L-ascorbate) using agarose gel electrophoresis. In order to ensure the copper(I) active species (*i.e.* the nuclease) was fully generated, each complex was initially reduced with 1 mM of added reductant prior to pUC19 titration. Relaxation of supercoiled (SC, FI) pUC19 DNA into open circular (OC, FII) and linear (LC, FIHI) conformations was employed to qualitatively measure the cleavage efficiency of complexes over a concentration range of 250 nM, 500 nM, 1.0  $\mu$ M and 2.5  $\mu$ M for 30 minutes at 37 °C (**Figure 2.1 A-D**, lanes 1-4). Complexes show concentration-dependent relaxation

of FI (superhelical) to FII (open circular / nicked), while FIII (linear conformation) is evident at 2.5  $\mu$ M Cu-DPQ-Phen exposure and with 500 nM of the dinuclear agent Cu-Terph. Complete digestion of SC DNA occurs only with the maximum tested concentration (2.5  $\mu$ M) of Cu-Terph. The overall trend in chemical nuclease activity is Cu-Terph > Cu-DPQ-Phen > Cu-Phen > Cu-DPPZ-Phen. The activity profiles observed here are in good agreement with those previously reported by this group; Cu-Terph has previously displayed nicking at 1.0  $\mu$ M on the plasmid pBR322 with complete digestion occurring thereafter (Prisecaru et al., 2012). We also established that both 2.5 and 5.0  $\mu$ M of Cu-Phen induced nicking (OC) on both pBR322 (McCann et al., 2013; Prisecaru et al., 2012) with activity being impeded in the presence of EDTA (Prisecaru et al., 2013). The nuclease activity of both Cu-DPQ-Phen and Cu-DPPZ-Phen has been identified previously (Molphy et al., 2014), however, direct analysis with the current conditions cannot be made.

In an attempt to determine DNA cleavage site specificity, minor groove (netropsin, Net) and major groove (methyl green, MG) binders, along a surface electrostatic binding and condensing agent ( $[\text{Co}(\text{NH}_3)_6]\text{Cl}_3$ , Co(III)) were pre-incubated with pUC19 DNA prior to the addition of test complex (**Figure 2.1 A-D**, lanes 5-16). In all cases, presence of the major groove binder MG enhanced chemical nuclease activity with greater nicking (OC) and linearisation (LC) frequency compared with control experiments. Conversely, the minor groove binder Net impedes chemical nuclease activity as pUC19 is clearly protected from both OC and LC damage across all experiments. The cationic surface binding agent  $[\text{Co}(\text{NH}_3)_6]^{3+}$  had no major impact on the chemical nuclease activity of Cu-Phen and Cu-DPPZ-Phen but did reduce nicking by Cu-DPQ-Phen at 1  $\mu$ M and was also effective in protecting pUC19 damage by Cu-Terph. Taken together, evidence here points toward the minor groove as the major site of DNA oxidation by this complex series; MG bound pUC19 primes the minor groove for chemical nuclease activity while titrated Net clearly diminishes this damage. Indeed this observation of minor groove targeting is consistent with previous analysis on the rapid cleavage of poly(dA-dT) by 2:1 phenanthroline- $\text{Cu}^+$  mixtures (Sigman et al., 1979).

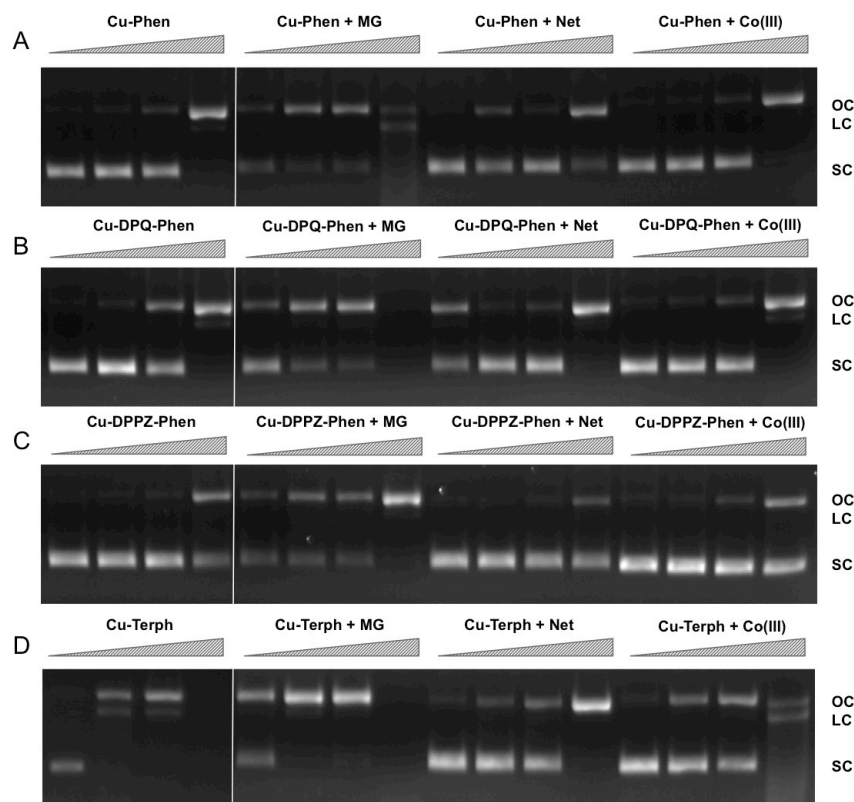


**Figure 2.** 1 Lane 1-4 (A-D) DNA cleavage reactions with 250 nM, 500 nM, 1.0  $\mu$ M and 2.5  $\mu$ M test complex (A: Cu-Phen, B: Cu-DPQ-Phen, C: Cu-DPPZ-Phen and D: Cu-Terph), 400 ng superhelical pUC19 and 1 mM added Na-L-ascorbate incubated at 37 °C for 30 minutes. Lanes 5-16 (A-D) DNA cleavage reactions in the presence of recognition elements, methyl green (MG), netropsin (Net) and [Co(NH<sub>3</sub>)<sub>6</sub>]Cl<sub>3</sub> (Co(III)), where 400 ng pUC19 was initially pre-treated with 8  $\mu$ M of respective non-covalent binding control at 37 °C for 45 minutes and then with 250 nM, 500 nM, 1  $\mu$ M and 2.5  $\mu$ M test complex in the presence of 1 mM added Na-L-ascorbate at 37 °C for 30 minutes.

#### 2.4.2 DNA oxidation with ROS scavengers and stabilisers.

In order to examine ROS species involved in DNA oxidation, activity was investigated in the presence of radical-specific scavengers and stabilisers (Table 2) with results shown in Figure 2.2. Before complex analysis, scavengers were confirmed to have no impact on pUC19 conformation (data not shown). Control experiments are in excellent agreement with those observed in Figure 2.1 (lanes 1-4), however, a fraction of superhelical (FI) pUC19 was found to remain upon 2.5  $\mu$ M exposure of Cu-Phen. Results here suggest that  $\cdot$ OH is the most prevalent radical species involved in strand scission as the presence of DMSO considerably impedes cleavage activity of all complexes. It is noteworthy DMSO had a major impact on cleavage activity of Cu-Terph as only the maximum tested concentrations (1.0 and 2.5  $\mu$ M) contained nicked cleavage products. The presence of the H<sub>2</sub>O<sub>2</sub> scavenger, KI, was also found to inhibit chemical nuclease activity of tested complexes—again most notably within Cu-Terph reactions—and this observation is consistent with previous trapping studies conducted on these model systems (Johnson & Nazhat, 1987; Prisecaru et al., 2013). It is interesting to note the catalase enzyme is a more effective scavenger of

H<sub>2</sub>O<sub>2</sub> compared with KI as previous work revealed complete inhibition of DNA oxidation by Cu-Phen, Cu-DPQ-Phen, and Cu-DPPZ-Phen complexes (Molphy et al., 2014).

The role of <sup>1</sup>O<sub>2</sub> was next examined utilising the NaN<sub>3</sub> scavenger (Franco et al., 2007) and D<sub>2</sub>O as a <sup>1</sup>O<sub>2</sub> stabiliser (Merkel et al., 1972; Xia et al., 2006). Nuclease activity by Cu-Phen, Cu-DPQ-Phen, and Cu-DPPZ-Phen complexes was only marginally inhibited by NaN<sub>3</sub> while no change in activity (relative to control) was observed in D<sub>2</sub>O thus suggesting a limited role in DNA oxidation by <sup>1</sup>O<sub>2</sub>. NaN<sub>3</sub> did, however, impede activity by Cu-Terph but the role of <sup>1</sup>O<sub>2</sub> in the scission process could not be verified as D<sub>2</sub>O was also found to remove activity.

**Table 2. 2** Scavengers and stabilisers utilised within this study.

Scavenger <sup>a</sup> / Stabiliser <sup>b</sup>	ROS	References
NaN <sub>3</sub> <sup>a</sup>	<sup>1</sup> O <sub>2</sub>	(Franco et al., 2007)
KI <sup>a</sup>	H <sub>2</sub> O <sub>2</sub>	(Dunand et al., 2007; Steffens et al., 2012)
DMSO <sup>a</sup>	<sup>•</sup> OH	(Franco et al., 2007; Mazzer et al., 2007)
D <sub>2</sub> O <sup>b</sup>	<sup>1</sup> O <sub>2</sub>	(Merkel et al., 1972; Xia et al., 2006)

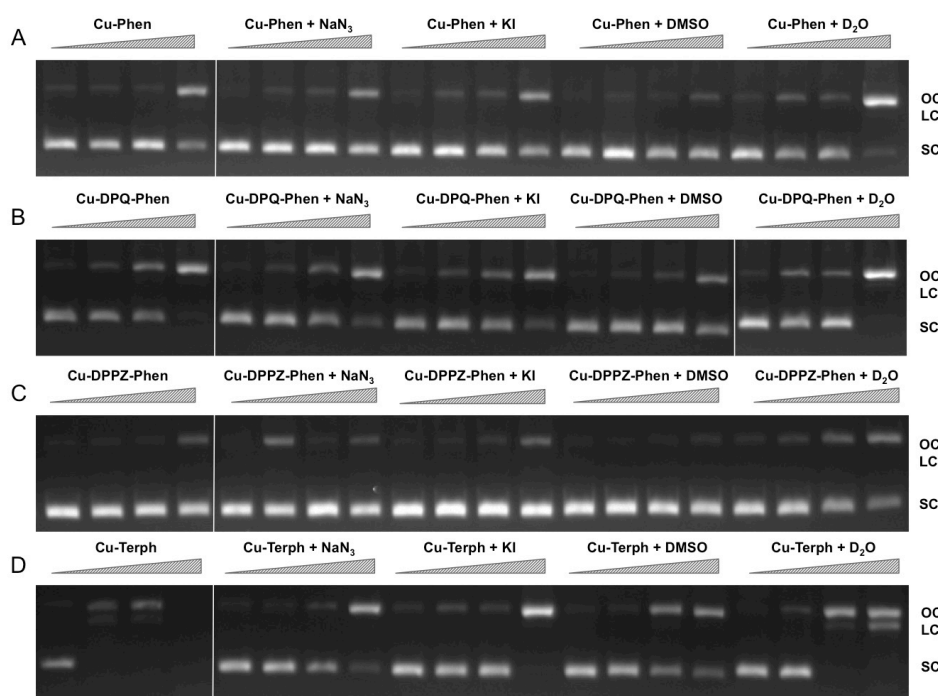


**Figure 2. 2** DNA cleavage reactions in the presence of ROS scavengers. 400 ng of SC pUC19 was incubated for for 30 min at 37 °C with 250 nM, 500 nM, 1 μM and 2.5 μM of test complex (A: Cu-Phen, B: Cu-DPQ-Phen, C: Cu-DPPZ-Phen and D: Cu-Terph) in the presence of 1 mM added Na-L-ascorbate for 30 minutes. Lanes 1-4 metal complex only, lanes 5-8: complex + 10 mM NaN<sub>3</sub>, lanes 9-12: complex + 10 mM KI, lanes 13-16: complex + 10% DMSO, and lanes 17-20: complex + 77% D<sub>2</sub>O.

### 2.4.3 Quantitation of 8-oxo-dG

To examine if the oxidative DNA lesion, 8-oxo-dG, is formed during complex reactions with DNA, an HT 8-oxo-dG ELISA kit was employed for immunological detection and quantification. The complex series was investigated at 10 and 20  $\mu\text{M}$  with 3000 ng of SC pUC19, with 8-oxo-dG being quantified in both nM and ng/mL (**Figure 2.3**). Nuclease activity was firstly confirmed at 10  $\mu\text{M}$  and 20  $\mu\text{M}$  (**Figure S-2.1**). Low numbers of lesions were detected in the untreated control ( $3.92 \pm 0.79$  nM) and the exposure of pUC19 to each of the complexes at 10  $\mu\text{M}$  resulted in detectable increases in 8-oxo-dG (between 35.24 – 5.05 nM) with the trend following Cu-Terph > Cu-DPPZ-Phen > Cu-DPQ-Phen > Cu-Phen. Upon 20  $\mu\text{M}$  complex exposure significant levels of 8-oxo-dG (between 129.22 – 17.77 nM) were produced with the trend changing toward Cu-DPQ-Phen > Cu-Terph > Cu-Phen > Cu-DPPZ-Phen. Given the  $\cdot\text{OH}$  radical is fundamental in the production of 8-oxo-dG, results here demonstrate DNA oxidation by copper phenanthrene complexes, particularly under extensive shearing conditions (**Figure S-2.1**), drive formation of 8-oxo-dG lesions.

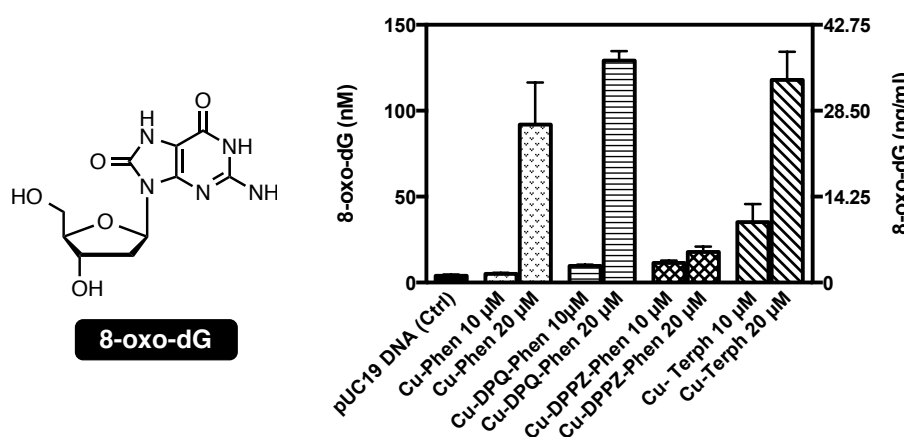


**Figure 2. 3** Structure and quantification of 8-oxo-dG. Graph represents level of generated 8-oxo-dG as nM (left axis) and ng/mL (right axis). 3000 ng of SC pUC19 with 10 and 20  $\mu\text{M}$  of test complexes Cu-Phen, Cu-DPQ-Phen, Cu-DPPZ-Phen and Cu-Terph with 1 mM Na-L-ascorbate were incubated at 37  $^{\circ}\text{C}$  for 30 minutes and followed by ELISA protocol.

### 2.4.4 PCR inhibition studies

Our next aim was to investigate how oxidative lesions – induced through complex exposure – can ultimately impact on *in vitro* DNA processing by the polymerase chain reaction (PCR) (**Figure 2.4**). During the normal PCR process, a DNA template is initially denatured through heating to more than 90  $^{\circ}\text{C}$  to separate double stranded DNA into constituent single strands. The second step involves lowering the temperature (40 – 60  $^{\circ}\text{C}$ ) to allow specifically designed forward and reverse primers to anneal at targeted regions (for selective amplification) through complementary base pairing. At this point the temperature is increased again to allow Taq polymerase to attach at each priming site and extend to synthesise a new DNA strand. This thermal cycling process allows for a

chain reaction to occur in which the selected DNA template is exponentially amplified creating millions of copies of the targeted sequence (**Figure 2.4A**). In our study 400 ng of pUC19 plasmid DNA was initially exposed to increasing concentrations (2.5, 5, 10, 20, 30, 40 and 50  $\mu\text{M}$ ) of test complexes in the absence and presence of exogenous reductant at 37 °C for 30 minutes and used as a substrate for the PCR reaction along with specific primer sets to generate three 120 bp sequences of varying G·C content (35%, 50% and 63%). PCR inhibition (up to 50  $\mu\text{M}$ ) was not achieved by any tested agent (**Figure S-2.2**) in the absence of added reductant indicating physical blocking of the PCR process (**Figure 2.4B**) does not occur. With added reductant, however, the pattern emerges as described in **Figure 4C**. In the high A·T amplification set (35% G·C), PCR was inhibited by 5.0  $\mu\text{M}$  of the mono-nuclear complexes (Cu-Phen, Cu-DPQ-Phen and Cu-DPPZ-Phen). In the case of the di-nuclear agent (Cu-Terph), complete inhibition of template amplification was observed at all exposure levels (**Figure 2.5A**). Within the 50% and 63% G·C templates (Figure 2.5 B and C respectively), the PCR reaction was impeded at 5.0  $\mu\text{M}$  for both Cu-DPQ-Phen and Cu-Terph complexes whereas template DNA, oxidatively damaged by 5.0  $\mu\text{M}$  of Cu-Phen and Cu-DPPZ-Phen, was still suitable for amplifying 120 base pair DNA sequences.

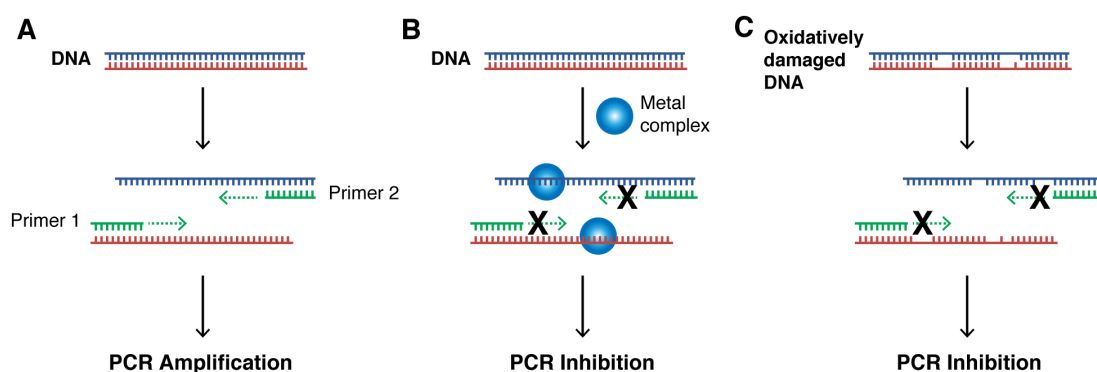


**Figure 2. 4** Illustration of steps involved in a successful PCR reaction (denaturation, primer annealing, primer extension and template amplification), B. the impact of a bound metal complex as physical block of the primer extension step, C. inhibition of DNA amplification in the PCR cycle through the oxidative damage of template strand.



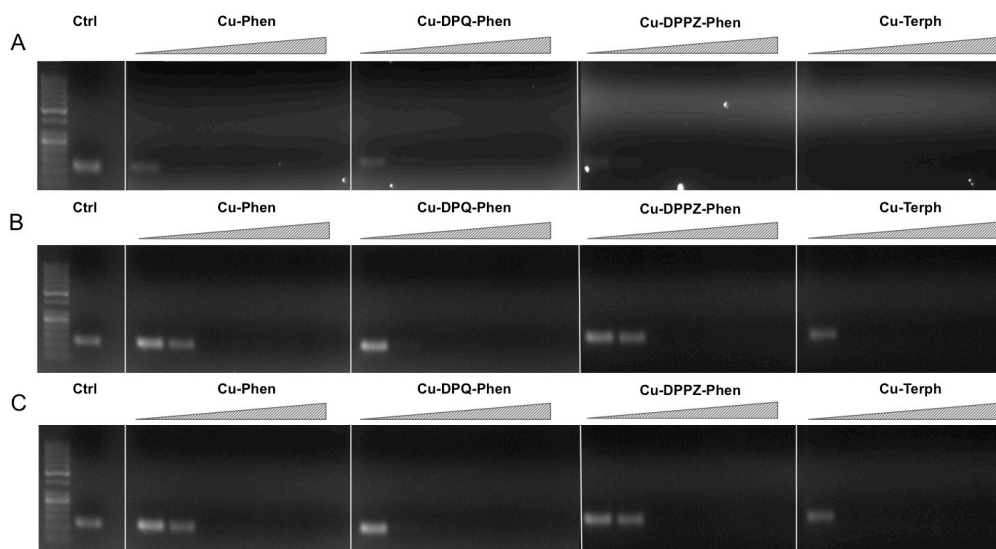


**Figure 2.** 5 400 ng pUC19 DNA was initially exposed to 2.5, 5, 10, 20, 30, 40 and 50  $\mu$ M of each test complex in the presence of 1 mM added reductant at 37  $^{\circ}$ C for 30 minutes. 20 ng of damaged DNA template was removed and PCR reaction was carried out with each varying GC content primer set at optimum annealing temperatures and analysed using gel electrophoresis. Fig. A Lane 1: 35% GC control, lane 2-8 35% GC + Cu-Phen, lane 9-15 35% GC + Cu-DPQ-Phen and lane 15-21: 35% GC + Cu-Terph. Fig. B 50% GC and Fig. C 63% GC respectively. All sequences generated were 120 base pairs.

## 2.5 Conclusions

Mechanistic investigations into oxidative cleavage properties of the copper(II) complex series  $[\text{Cu}(\text{phen})_2]^{2+}$  (Cu-Phen)  $[\text{Cu}(\text{DPQ})(\text{phen})]^{2+}$  (Cu-DPQ-Phen),  $[\text{Cu}(\text{DPPZ})(\text{phen})]^{2+}$  (Cu-DPPZ-Phen), and  $[\{\text{Cu}(\text{phen})_2\}_2(\mu\text{-terph})](\text{terph})$  (Cu-Terph) reveal chemical nuclease activity occurs primarily at the minor groove; titration of the major groove binder, methyl green, enhances DNA degradation – most likely by directing (priming) complex-DNA interactions to the minor groove – while the presence of the minor groove binder, netropsin, was found to significantly reduce oxidative damage on pUC19. It is also interesting to note that no correlation exists between chemical nuclease activity (**Figure 2.1**) and apparent DNA binding constant (**Table 2.1**). Instead, nuclearity has a more dramatic effect as evidenced by Cu-Terph mediated DNA damage. ROS-specific scavengers employed to identify the cleavage mechanism revealed metal-hydroxo or free hydroxyl radicals ( $\cdot\text{OH}$ ), and not  $^1\text{O}_2$ , as the predominant species generated; DMSO was found to limit DNA oxidation – most likely through the trapping of hydroxyl radicals ( $(\text{CH}_3)_2\text{SO} + \cdot\text{OH} \rightarrow \text{CH}_3\text{SO}_2\text{H} + \cdot\text{CH}_3$ ) (Burkitt and Mason, 1991) – with sodium azide ( $\text{NaN}_3$ ) having negligible influence on all complexes except Cu-Terph. It is also likely that hydrogen peroxide ( $\text{H}_2\text{O}_2$ ) is the key intermediary in  $\cdot\text{OH}$  production as the peroxide scavenger KI (Dunand et al., 2007; Steffens et al., 2012) was refractory to oxidative damage by tested agents. The generation of hydroxyl-based radicals was corroborated through identification of 8-oxo-2'-deoxyguanosine (8-oxo-dG) DNA lesions quantified under an ELISA protocol. 8-oxo-dG liberation followed the overall trend Cu-DPQ-Phen > Cu-Terph > Cu-Phen > Cu-DPPZ with higher lesion numbers detected under heavily

sheared (damaged) plasmid conditions. Finally, oxidative damage by the complex series was found to inhibit the DNA replication process; polymerase chain reaction (PCR) reactions were impeded – particularly along A-T rich chains – through oxidative damage of template strands with the dinuclear Cu-Terph, and mono-nuclear Cu-DPQ-Phen, being particularly potent oxidants to this process.

## 2.6 Supporting Material

Supplementary data associated with this chapter can be found in Appendix A.

## 2.7 References

- Basu, A. K., Loechler, E. L., Leadon, S. A., and Essigmann, J. M. (1989). Genetic effects of thymine glycol: Site-specific mutagenesis and molecular modeling studies. *Proc. Natl. Acad. Sci. United States* 86, 7677–7681.
- Breen, A. P., and Murphy, J. A. (1995). Reactions of oxyl radicals with DNA. *Free Radic. Biol. and Med.* 18, 1033–1077. doi:10.1016/0891-5849(94)00209-3.
- Burger, R. M. (1998). Cleavage of nucleic acids by Bleomycin. *Chem. Rev.* 98, 1153–1169. doi:10.1021/cr960438a.
- Burger, R. M., Peisach, J., and Horwitz, S. B. (1981). Activated bleomycin. A transient complex of drug, iron, and oxygen that degrades DNA. *J. Biol. Chem.* 256, 11636–11644.
- Burkitt, M. J., and Mason, R. P. (1991). Direct evidence for in vivo hydroxyl-radical generation in experimental iron overload: an ESR spin-trapping investigation. *Proc. Natl. Acad. Sci. U. S. A.* 88, 8440–8444. doi:10.1073/pnas.88.19.8440.
- Chatgililoglu, C., Ferreri, C., and Terzidis, M. A. (2011). Purine 5',8-cyclonucleoside lesions: chemistry and biology. *Chem. Soc. Rev.* 40, 1368–82. doi:10.1039/c0cs00061b.
- Chatgililoglu, C., and O'Neill, P. (2001). Free radicals associated with DNA damage. *Exp. Gerontol.* 36, 1459–71. doi:10.1016/S0531-5565(01)00132-2.
- Chen, J., Ghorai, M. K., Kenney, G., and Stubbe, J. (2008). Mechanistic studies on bleomycin-mediated DNA damage: multiple binding modes can result in double-stranded DNA cleavage. *Nucleic Acids Res.* 36, 3781–3790. doi:10.1093/nar/gkn302.
- Cooke, M. S., and Evans, M. D. (2007). 8-Oxo-deoxyguanosine: Reduce, reuse, recycle? *Proc. Natl. Acad. Sci. United States* 104, 13535–13536. doi:10.1073/pnas.0706878104.
- Douki, T., Martini, R., Ravanat, J. L., Turesky, R. J., and Cadet, J. (1997). Measurement of 2,6-diamino-4-hydroxy-5-formamidopyrimidine and 8-oxo-7,8-dihydroguanine in isolated DNA exposed to gamma radiation in aqueous solution. *Carcinogenesis* 18, 2385–2391. doi:10.1093/carcin/18.12.2385
- Dunand, C., Crèvecoeur, M., and Penel, C. (2007). Distribution of superoxide and hydrogen peroxide in Arabidopsis root and their influence on root development: possible interaction with peroxidases. *New Phytol.* 174, 332–341. doi:10.1111/j.1469-8137.2007.01995.x.
- Franco, R., Panayiotidis, M. I., and Cidlowski, J. A. (2007). Glutathione depletion Is necessary for apoptosis in lymphoid cells independent of reactive oxygen species formation. *J. Biol. Chem.* 282, 30452–30465. doi:10.1074/jbc.M703091200.
- Gajewski, E., Aruoma, O. I., Dizdaroglu, M., and Halliwell, B. (1991). Bleomycin-dependent damage to the bases in DNA is a minor side reaction. *Biochemistry* 30, 2444–2448. doi:10.1021/bi00223a021.

- Johnson, G. R. A., and Nazhat, N. B. (1987). Kinetics and Mechanism of the Reaction of the Bis(1,10-phenanthroline)copper(I) Ion with Hydrogen Peroxide in Aqueous Solution. *J. Am. Chem. Soc.* 109, 1990–1994. doi:10.1021/ja00241a015.
- Kellett, A., Howe, O., O'Connor, M., McCann, M., Creaven, B. S., McClean, S., Foltyn-Arfa Kia, A., Casey, A., and Devereux, M. (2012). Radical-induced DNA damage by cytotoxic square-planar copper(II) complexes incorporating o-phthalate and 1,10-phenanthroline or 2,2'-dipyridyl. *Free Radic. Biol. Med.* 53, 564–76. doi:10.1016/j.freeradbiomed.2012.05.034.
- Kpricf P., Rosair, G., McKee, V., Creaven, B., Walsh, M., McClean, S., et al. (2011). Bis-phenanthroline copper(II) phthalate complexes are potent in vitro antitumour agents with “self-activating” metallo-nuclease and DNA binding properties. *Dalton Trans.* 40, 1024–7. doi:10.1039/c0dt01607a.
- Klaunig, J. E., Kamendulis, L. M., and Hocevar, B. a (2010). Oxidative stress and oxidative damage in carcinogenesis. *Toxicol. Pathol.* 38, 96–109. doi:10.1177/0192623309356453.
- Li, L., Karlin, K. D., and Rokita, S. E. (2005). Changing selectivity of DNA oxidation from deoxyribose to guanine by ligand design and a new binuclear copper complex. *J. Am. Chem. Soc.* 127, 520–521. doi:10.1021/ja044209e.
- Marshall, L. E., Graham, D. R., Reich, K. A., and Sigman, D. S. (1981). Cleavage of Deoxyribonucleic Acid by the 1,10-Phenanthroline-Cuprous Complex. Hydrogen Peroxide Requirement and Primary and Secondary Structure Specificity. *Biochemistry* 20, 244–250. doi:10.1021/bi00505a003.
- Mazzer, P. A., Maurmann, L., and Bose, R. N. (2007). Mechanisms of DNA damage and insight into mutations by chromium(VI) in the presence of glutathione. *J. Inorg. Biochem.* 101, 44–55. doi:10.1016/j.jinorgbio.2006.08.008.
- McCann, M., McGinley, J., Ni, K., O'Connor, M., Kavanagh, K., McKee, V., Colleran, J., Devereux, M., Gathergood, N., Barron, N., et al. (2013). A new phenanthroline-oxazine ligand: synthesis, coordination chemistry and atypical DNA binding interaction. *Chem. Comm.* 49, 2341–2343. doi:10.1039/c3cc38710k.
- Merkel, P. B., Nilsson, R., and Kearns, D. R. (1972). Deuterium effects on singlet oxygen lifetimes in solutions. New test of singlet oxygen reactions. *J. Am. Chem. Soc.* 94, 1030–1031. doi:10.1021/ja00758a072.
- Molphy, Z., Prisecaru, A., Slator, C., Barron, N., McCann, M., Colleran, J., Chandran, D., Gathergood, N., and Kellett, A. (2014). Copper phenanthrene oxidative chemical nucleases. *Inorg. Chem.* 53, 5392–5404. doi:10.1021/ic500914j.
- Natrajan, A., Hecht, S. M., and Van der Marel, G. A. (1990). A study of oxygen-versus hydrogen peroxide-supported activation of iron. cntdot. bleomycin. *J. Am. Chem. Soc.* 112, 3997–4002. doi:10.1021/ja00166a042.
- Pflaum, M., Will, O., and Epe, B. (1997). Determination of steady-state levels of oxidative DNA base modifications in mammalian cells by means of repair endonucleases. *Carcinogenesis* 18, 2225–2231.
- Pouget, J. P., Douki, T., Richard, M. J., and Cadet, J. (2000). DNA Damage Induced in Cells by  $\gamma$  and UVA Radiation As Measured by HPLC/GC-MS and HPLC-EC and Comet Assay. *Chem. Res. Toxicol.* 13, 541–549. doi:10.1021/tx000020e.
- Pratviel, G., and Bernadou, J. (1989). Evidence for high-valent iron-oxo species active in the DNA breaks mediated by iron-bleomycin. *Biochem. Pharmacol.* 38, 133–140. doi: 10.1093/carcin/18.12.2385
- Prisecaru, A., Devereux, M., Barron, N., McCann, M., Colleran, J., Casey, A., McKee, V., and Kellett, A. (2012). Potent oxidative DNA cleavage by the di-copper cytotoxin:  $[\text{Cu}_2(\mu\text{-terephthalate})(1,10\text{-phen})_4]^{2+}$ . *Chem. Commun.* 48, 6906–6908. doi:10.1039/c2cc31023f.

Prisecaru, A., McKee, V., Howe, O., Rochford, G., Mccann, M., Colleran, J., Pour, M., Barron, N., Gathergood, N., and Kellett, A. (2013). Regulating Bioactivity of Cu<sup>2+</sup> Bis-1,10-phenanthroline Artificial Metallonucleases with Sterically Functionalized Pendant Carboxylates. *J. Med. Chem.* 56, 8599–8615. doi:10.1021/jm401465m.

Rodriguez, L. O., and Hecht, S. M. (1982). Iron(II)-bleomycin. Biochemical and spectral properties in the presence of radical scavengers. *Biochem. Biophys. Res. Commun.* 164, 1470–1476. doi:10.1016/0006-291X(82)91416-4

Sanchez-Cano, C., Huxley, M., Ducani, C., Hamad, A. E., Browning, M. J., Navarro-Ranninger, C., Quiroga, A. G., Rodger, A., and Hannon, M. J. (2010). Conjugation of testosterone modifies the interaction of mono-functional cationic platinum(II) complexes with DNA, causing significant alterations to the DNA helix. *Dalton Trans.* 39, 11365–74. doi:10.1039/c0dt00839g.

Sigman, D. S., Graham, D. R., Aurora, V. D., and Stern, A. M. (1979). Oxygen-dependent cleavage of DNA by the 1,10-phenanthroline cuprous complex. Inhibition of Escherichia coli DNA polymerase I. *J. Biol. Chem.* 254, 12269–12272.

Steffens, B., Kovalev, A., Gorb, S. N., and Sauter, M. (2012). Emerging Roots Alter Epidermal Cell Fate through Mechanical and Reactive Oxygen Species Signaling. *The Plant Cell* 24, 3296–3306. doi:10.1105/tpc.112.101790.

Stubbe, J. A., and Kozarich, J. W. (1987). Mechanisms of bleomycin-induced DNA degradation. *Chem. Rev.* 87, 1107–1136. doi:10.1021/cr00081a011.

Tyrrell, R. M., and Keyse, S. M. (1990). New trends in photobiology. The interactions of UVA radiation with cultured cells. *J. Photochem. Photobiol., B* 4, 349–361. doi:10.1016/1011-1344(90)85014-N

Tabassum, S., Al-Asbahy, W. M., Afzal, M., Arjmand, F., and Bagchi, V. (2012). Molecular drug design, synthesis and structure elucidation of a new specific target peptide based metallo drug for cancer chemotherapy as topoisomerase I inhibitor. *Dalton Trans.* 41, 4955–64. doi:10.1039/c2dt12044e.

van der Steen, S., de Hoog, P., van der Schilden, K., Gamez, P., Pitié, M., Kiss, R., and Reedijk, J. (2010). Novel heteronuclear ruthenium–copper coordination compounds as efficient DNA-cleaving agents. *Chem. Commun.* 46, 3568. doi:10.1039/c000077a.

Xia, Q., Chou, M. W., Yin, J. J., Howard, P. C., Yu, H., and Fu, P. P. (2006). Photoirradiation of representative polycyclic aromatic hydrocarbons and twelve isomeric methylbenz[α]anthracene with UVA light: formation of lipid peroxidation. *Toxicol. Ind. Health* 22, 147–156. doi:10.1191/0748233706th259oa.

Xu, M., Lai, Y., Jiang, Z., Terzidis, M. A., Masi, A., Chatgililoglu, C., and Liu, Y. (2014). A 5', 8-cyclo-2'-deoxypurine lesion induces trinucleotide repeat deletion via a unique lesion bypass by DNA polymerase β. *Nucleic Acids Res.* 42, 13749–63. doi:10.1093/nar/gku1239.

Zhou, W., Wang, X., Hu, M., Zhu, C., and Guo, Z. (2014). A mitochondrion-targeting copper complex exhibits potent cytotoxicity against cisplatin-resistant tumor cells through multiple mechanisms of action. *Chem. Sci.* 5, 2761–2770. doi:10.1039/c4sc00384e.

# **Chapter 3**

## **[Cu(*o*-phthalate)(phenanthroline)] Exhibits Unique Superoxide-Mediated NCI-60 Chemotherapeutic Action through Genomic DNA Damage and Mitochondrial Dysfunction**

---

Published in *ACS Chemical Biology*, 2016, 11 (1), 159–171

Creina Slator, Niall Barron, Orla Howe and Andrew Kellett\*.

Within this chapter, I was the primary contributor to all aspects of experiential design, execution, analysis and manuscript preparation. A significant proportion of my PhD research was dedicated towards this body of work. Supporting information associated with this chapter can be found in Appendix B.

### 3.1 Abstract

The *in cellulo* catalytic production of reactive oxygen species (ROS) by copper(II) and iron(II) complexes is now recognized as a major mechanistic model in the design of effective cytotoxins of human cancer. The developmental complex, [Cu(*o*-phthalate)(1,10-phenanthroline)] (**Cu-Ph**), was recently reported as an intracellular ROS-active cytotoxic agent that induces double strand breaks (DSBs) in the genome of human cancer cells. In this work we report the broad-spectrum action of **Cu-Ph** within the National Cancer Institute's (NCI) Developmental Therapeutics Program (DTP), 60 human cancer cell line screen. The activity profile is compared to established clinical agents—via the COMPARE algorithm—and reveals a novel mode of action to existing metal-based therapeutics. In this study we identify the mechanistic activity of **Cu-Ph** through a series of molecular biological studies that are compared directly to the clinical DNA intercalator and topoisomerase II poison, doxorubicin. The presence of ROS-specific scavengers were employed for *in vitro* and intracellular evaluation of prevailing radical species responsible for DNA oxidation with superoxide identified as playing a critical role in this mechanism. The ROS targeting properties of **Cu-Ph** on mitochondrial membrane potential were investigated, which showed that it had comparable activity to the uncoupling ionophore, carbonyl cyanide *m*-chlorophenyl hydrazine (CCCP). The induction, and origins, of apoptotic activation are probed through detection of Annexin V, activation of initiator (8,9) and executioner caspases (3/7), and are structurally visualized using confocal microscopy. Results here confirm a unique radical-induced mechanistic profile with intracellular hallmarks of both damage to genomic DNA and mitochondria.

### 3.2 Introduction

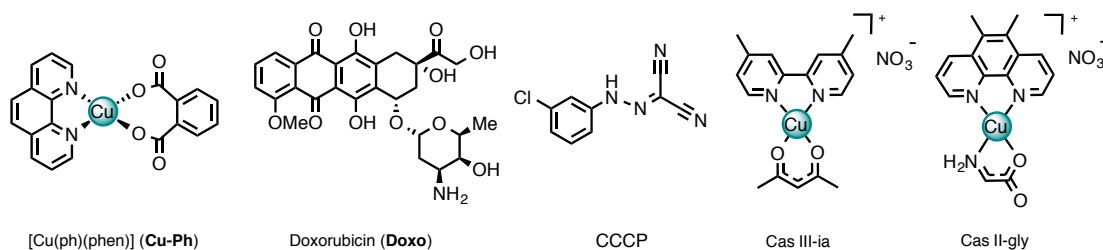
The advancement of metal complex mediated chemotherapeutic design has been spurred largely due to the success of the corner-stone anticancer agent, cisplatin.<sup>1</sup> Due to resistance and toxicity issues, however, the discovery of alternative metallodrug therapies with differential mechanisms of action are now required.<sup>2</sup> As such, copper complexes are now being considered due to attractive features such as: coordination range, biologically accessible redox states, and inherent cationic charged complex properties.<sup>3</sup> Copper is a fundamental component of many biologically important metalloproteins, and while it also plays a crucial role in neoplastic diseases<sup>4</sup>—particularly for invasion and angiogenesis<sup>3,5</sup> during development of tumor growth and metastasis—the incorporation of copper ions into small molecules has demonstrated considerable therapeutic potential.<sup>6</sup> More specifically, the utility of copper-based anticancer agents can be exploited as potential tumour-specific targets; copper levels are intrinsically amplified in a range of cancers such as breast, cervix, liver, lung, Hodgkin's lymphoma, leukaemia, gastrointestinal tract cancer and brain tumours,<sup>7,8</sup> where ordinarily, levels are tightly regulated in cells and organs.<sup>4,9,10</sup> The innovation of copper complexes as anticancer agents has gained rapid growth over the last number of years, the most notable advances of which have been extensively reviewed by Santini *et al.*<sup>11</sup> Encouragingly, two copper(II) complexes of the Casiopeínas class that feature *N'N'*, *O'O'*, or *N'N'*, *N'O'*, chelated symmetry (Scheme 1) have recently entered phase I clinical trials.<sup>12</sup> This group has previously reported on the cytotoxic properties of copper phenanthrene-based agents with oxidative chemical nuclease activity. We have identified ROS formation, such as superoxide ( $O_2^{\bullet-}$ ), hydrogen peroxide ( $H_2O_2$ ), hydroxyl radical ( $\bullet OH$ ), and metal-oxo species as critical components to their oxidative DNA damaging profile.<sup>13-17</sup> The mononuclear copper(II) complex [Cu(*o*-phthalate)(1,10-phenanthroline)] (**Cu-Ph**, Scheme 1) is a candidate antitumoral agent that features bis-chelate—dicarboxylate and *N,N'*-intercalative—square planar coordination scaffold.<sup>17</sup> Encouraging *in vitro* cytotoxicity against breast (MCF-7), colon (HT29), lung (A549), and ovarian (SKOV3) human epithelial cancer cells have revealed both an alternative kinetic and mechanistic profile compared with cisplatin. The agent bears greater potency than its attenuated 2,2'-dipyridyl analogue, particularly within intrinsically cisplatin resistant ovarian (SKOV3) cells, where intracellular reactive oxygen species (ROS) in conjunction with genomic double strand breaks (DSBs) have previously been established using 2',7'-dichlorodihydrofluorescein, and immunodetection of  $\gamma H2AX$  foci.<sup>17</sup>

In this contribution we describe the cytotoxic activity profile of **Cu-Ph** within the National Cancer Institute's Developmental Therapeutics Program (DTP) 60 human cancer cell panel and identify the mechanistic profile, via the COMPARE algorithm, in comparison to an established base of clinical anticancer drugs.<sup>23</sup> We have selected ovarian cancer cell line, SKOV3, for further in-depth mechanistic analyses owing to a typical observed  $LC_{50}$  response (5.2  $\mu M$ ) by **Cu-Ph** that

was common among solid epithelial cancer cells examined, and also due to its innate resistance to cisplatin. The cell line was originally derived from an adenocarcinoma tumor patient that previously underwent non-platinum based therapies.<sup>24</sup> The cell line is classified as serous subtype of ovarian cancer, accounting for 90% of ovarian cancers.<sup>25,26</sup> A partial role in intrinsic resistance of cisplatin to SKOV3 is the cellular accumulation of the drug. A 4.3 fold increase is required in order to inhibit cell growth compared with cisplatin-sensitive cells,<sup>27</sup> where the cell line can also develop acquired resistance to paclitaxel.<sup>28,29</sup> This, along with associated cross-resistance of platinum compounds, eliminates primary chemotherapeutics options, such as lone or combination regimens of carboplatin and paclitaxel for the treatment of recurrent or metastatic ovarian cancers. Furthermore, as SKOV3 is p53 null,<sup>30,31</sup> the loss of p53 function is accountable for decreased sensitivity to a number of DNA-alkylating therapeutics.<sup>32</sup> SKOV3 is also shown to be estrogen receptor (ER) positive,<sup>33</sup> however they are nonresponsive to estradiol induced growth and antiestrogens such as tamoxifen.<sup>34,35</sup>

An extensive range of molecular methods—flow cytometry, confocal microscopy, and fluorescence spectroscopy—have been applied to delineate *in cellulo* cytotoxic action of the complex. In particular, the identification of apoptosis,<sup>36,37</sup> and activation of intrinsic initiator and executioner caspases (9 and 3/7) along with extrinsic caspase 8 activation and subsequent activation of caspase 3/7,<sup>38-40</sup> uncoupling of mitochondrial membrane potential (MMP),<sup>41,42</sup> and ROS-specific scavengers have all been studied in order to identify a broad spectrum molecular targeting expected by the liberation of toxic ROS and/or the generation of reactive metal-oxo species. In this work we have compared the cytotoxic action of **Cu-Ph** with those of the mitochondrial transmembrane poison, carbonyl cyanide *m*-chlorophenyl hydrazone (**CCCP**),<sup>43,44</sup> and the DNA intercalating topoisomerase (II $\alpha$ ) poison, doxorubicin (**Doxo**, **Scheme 3.1**).<sup>45</sup> Indeed **Doxo** was selected, not alone for its topoisomerase inhibition, but due to a myriad of additional nucleic acid targeting and DNA damage effects including DNA alkylation,<sup>46</sup> formation of cross-links, strand separation,<sup>47</sup> unwinding,<sup>48</sup> intercalation,<sup>49,50</sup> as well as ROS formation,<sup>51-53</sup> which all precipitate the inhibition of DNA replication processes<sup>47</sup> and free radical induced lipid peroxidation.<sup>54</sup> Doxorubicin and various analogues from the anthracyclines are also used in combination or lone chemotherapies for a range of cancers, including ovarian.<sup>55</sup> Although this class of compound is one of the most successful anticancer agents, associated toxicity to healthy cells has been shown to limit its use as chemotherapeutic treatment.<sup>55,56</sup>





**Scheme 3. 2** Molecular structures of the Cu(II) complex [Cu(ph)(phen)] (**Cu-Ph**) and clinical antitumor agent doxorubicin (**Doxo**), carbonyl cyanide m-chlorophenyl hydrazine (CCCP), casiopeínas [Cu(4,4'-dimethyl-2,2'-bipyridine)(acetylacetonate)(H<sub>2</sub>O)](NO<sub>3</sub>) (Cas III-ia) and [Cu(4,7-dimethyl-1,10-phenanthroline)(glycine)(H<sub>2</sub>O)](NO<sub>3</sub>) (Cas II-gly).

### 3.3 Materials and Methods

#### 3.3.1 Materials and reagents

The following assay were purchased from Merck Millipore and relevant protocols were followed as per product reagent: Guava Nexin® Reagent (4500-0450), Guava EasyCyte™ MitoPotential Kit (4500-0250), Guava Caspase 8 FAM and Caspase 9 SR (4500-0640) and Guava Caspase 3/7. All other chemicals and reagents were purchased from Sigma Aldrich.

#### 3.3.2 Preparation of Cu-Ph

[Cu(ph)(1,10-phen)]·2H<sub>2</sub>O (**Cu-Ph**) was prepared according to the method reported by Kellett *et al.*<sup>17</sup>

#### 3.3.3 NCI-60 analysis

The tested sample, **Cu-Ph**, was submitted to National Cancer Institute's (NCI) Developmental Therapeutics Program (DTP) where the cytotoxicity profile was investigated across their 60 human cancer cell line panel according to protocol available on <http://dtp.nci.nih.gov/branches/btb/ivclsp.html>. The COMPARE algorithm, <http://dtp.nci.nih.gov/compare/>, was utilized to evaluate the activity profile of **Cu-Ph** in comparison to those of known cytotoxins established in marketed drugs, mechanistic and standard agent datasets in order to correlate plausible modes of action.

#### 3.3.4 DNA interaction studies

##### 3.3.4.1 DNA binding analysis

Binding affinity to Calf Thymus (Invitrogen 15633-019), *Micrococcus Lysodeikicus* (Sigma Aldrich D8259) and artificial double stranded alternating copolymers; poly[d(G-C)<sub>2</sub>] (Sigma Aldrich P9389) and poly[d(A-T)<sub>2</sub>] (Sigma Aldrich P0883) were used to investigate DNA binding properties of **Cu-Ph** on DNA sequences containing varying AT content. Experiments were

conducted in an identical manner to those recently reported by Prisecaru *et al.*<sup>117</sup> Briefly, assay conditions were prepared in 96 plates with complex concentrations between 1-150  $\mu$ M, 12.6  $\mu$ M EtBr, 20 mM NaCl and 10  $\mu$ M of dsDNA sequences in a final volume of 100  $\mu$ L and analyzed with Bio-Tek, Synergy HT fluorescent microplate reader with data collecting using Gen5 software. A  $C_{50}$  value—the concentration required to reduce bound ethidium bromide fluorescence by 50%—was used to calculate the apparent DNA binding constant ( $K_{app}$ ) of **Cu-Ph** to each sequence;  $K_{app} = K_e \times 12.6/C_{50}$  where  $K_e = 9.5 \times 10^6 \text{ M (bp)}^{-1}$ .

#### 3.3.4.2 Nuclease activity in the presence of ROS scavengers

The presence of ROS specific scavengers was used to determine the effect on the DNA cleavage abilities of each copper complex. The procedure was adapted to the previously reported method<sup>15</sup>. Briefly, to a final volume of 20  $\mu$ L, 80 mM HEPES (pH = 7.2), 25 mM NaCl, 1 mM Na-L-ascorbate, and 400 ng of pUC19 DNA were treated with drug concentrations of 500 nM, 1  $\mu$ M and 2.5 and 5  $\mu$ M in the presence ROS scavengers / stabilizers; KI (10 mM),  $\text{NaN}_3$  (10 mM), DMSO (10 %), and Tiron (10mM). Reactions were incubated for 1 h at 37 °C, and quenched with 6 $\times$  loading buffer (Fermentas) containing 10 mM Tris-HCl, 0.03 % bromophenol blue, 0.03 % xylene cyanole FF, 60 % glycerol, 60 mM EDTA and loaded onto an agarose gel (1.2 %) containing 8  $\mu$ L EtBr. Electrophoresis was completed at 70 V for 2 hours in 1 $\times$  TAE buffer.

### 3.3.5 *Ex cellulo* investigations

#### 3.3.5.1 Cell culture

SKOV3 cells were cultured in RPMI 1640 media (Sigma) supplemented with 10% FCS (PAA gold) and were incubated at 37°C in a humidified atmosphere with 5%  $\text{CO}_2$ . Cells were passaged twice a week with 1X PBS wash and detached with trypsin:EDTA (0.25%:0.02% in PBS). In all cytometric experiments (Annexin V, caspases and mitochondrial depolarization), SKOV3 cells were seeded at densities of  $4 \times 10^4$  cells/mL in 24-well tissue culture plates 18-20 h before drug incubation. Viability experiments were seeding in 96-well plates at  $2.5 \times 10^4$  cell/mL and samples for confocal imaging were seeded at  $4 \times 10^4$  cell  $\text{mL}^{-1}$  in 35 mm glass bottom petri dishes. Adherent cells were then incubated with drug-containing RPMI with 10% FCS at various concentrations corresponding to approximate  $\text{LC}_{25}$ ,  $\text{LC}_{50}$  and  $\text{LC}_{75}$  concentrations over 24 h (**Cu-Ph** at 1, 3 and 5  $\mu$ M— $\text{LC}_{75}$ ,  $\text{LC}_{50}$ ,  $\text{LC}_{25}$  respectively- **Doxo** at 1  $\mu$ M - $\text{LC}_{50}$ - and **CCCP** at 75  $\mu$ M- $\text{LC}_{50}$ ). After treatment, spent media was removed and cells were washed with 1x Phosphate Buffered Saline (PBS) prior to being detached with trypsin and re-suspended in equal volume of fresh media. Detached cells and washings were pooled and centrifuged at 1300 rpm for 5 min before aspirating supernatant and subsequently resuspended in an appropriate volume of fresh RPMI, 10% FCS media to give sufficient cell densities per respective assay protocol. Cell densities

were determined by staining with Guava Viacount reagent (Millipore) and counted on Guava EasyCyte flow cytometer.

### **3.3.5.2 Viability profile in the presence of ROS Antioxidants**

Initial stocks of D-mannitol (Sigma-M9546) and tiron (Sigma-89460) were dissolved in water and subsequent dilutions in PBS and final working stocks in 10 % FBS supplemented RPMI 1640. Sodium pyruvate (Sigma-S8636) was available as a 100 mM aqueous solution and working stock dilutions were prepared in 10 % FBS supplemented RPMI 1640. Cells were incubated with 1 mM of scavengers for 1 h prior to addition of Cu-Ph with final concentration of 3  $\mu$ M. Cells were incubated under normal culture conditions for 24 h. After drug treatment, media was removed and cells were washed with PBS. The cells were then detached with 50  $\mu$ L trypsin and equal volume of complete media was added. Cells were resuspended and total sample (100  $\mu$ L) was added to 100  $\mu$ L of Guava Viacount Reagent in 96-well round bottom plate and acquired on Guava EasyCyte HT flow cytometer.

### **3.3.5.3 Nexin® assay**

Cell densities were adjusted to range between  $2 \times 10^5 - 1 \times 10^6$  cell  $\text{mL}^{-1}$ . 100  $\mu$ L of cultured cells were then transferred to 96 well round bottom plates before adding 100  $\mu$ L of Guava Nexin® Reagent. This mixture was then incubated for 20 min, at room temperature in darkness. Prepared samples were analyzed using the Guava EasyCyte HT flow cytometer with data being captured using Nexin® software. Compensation to correct fluorescent overlap between filters was conducted pre-acquisition and innate doxorubicin fluorescence in filter 583/26 nm was accounted for and subtracted within the relevant quadrants.

### **Mitochondrial membrane potential**

Cells were resuspended in 600  $\mu$ L of fresh supplemented media to give a cell concentration density between  $2 \times 10^4$  to  $5 \times 10^5$  cell  $\text{mL}^{-1}$  from which 200  $\mu$ L per sample was taken and transferred to 96-well round bottom plates. The required amount of 50x cell staining solution was prepared from 100x JC-1 and MitoPotential 7-AAD components in the kits provided. 4  $\mu$ L of 50x staining solution was added to each well and thoroughly mixed through gentle pipetting. Samples were subsequently incubated at 37 °C in darkness for 30 min and analyzed using the Guava EasyCyte HT flow cytometer using MitoPotential software. Compensation to correct fluorescent overlap between filters was conducted pre-acquisition.

### **3.3.5.4 Caspase 8 FAM and 9 SR, Caspase 3/7 FAM**

The following fluorescent labelled inhibitor of Caspase (FLICA) were used to ascertain the activation of Caspase 3/7, 8 and 9 respectively; FAM-DEVD-FMK, FAM-LETD-FMK and SR-

LEHD-FMK. After 24 h of incubation, cells were detached with trypsin and concentrated in 1.5ml microtubes by centrifugation at 1300 rpm for 5 min. Cells were resuspended in 100  $\mu$ L of media. 10  $\mu$ L of a 10x Caspase 9 SR working solution and/or 10  $\mu$ L of Caspase 8 FAM or Caspase 3/7 working solution was added to each tube before being thoroughly mixed and incubated for 1 h at 37 °C in darkness. The tubes were then centrifuged, as above, with the supernatant being removed and cells resuspended in 1x Apoptosis Wash Buffer. Centrifugation and Apoptosis Buffer washes were repeated twice. 200  $\mu$ L of Caspase 7-AAD working solution was thoroughly mixed and transferred to 96-well round bottom plates and incubated for 10 min at room temperature in darkness. Samples were measured on Guava EasyCyte HT flow cytometer as previously indicated. Compensation to correct fluorescent overlap between filters was conducted pre-acquisition and innate doxorubicin fluorescence in filter 583/26 nm was accounted for and subtracted within the relevant quadrants.

### 3.3.5.5 Confocal analysis

Cells were seeded at  $4 \times 10^4$  cell  $\text{mL}^{-1}$  in 35 mm glass bottom petri dishes and allowed to attach overnight. Samples were incubated with complex containing media at their  $\text{IC}_{50}$  concentrations for 24 h (**Cu-Ph** 3  $\mu$ M, **Doxo** 1  $\mu$ M and **CCCP** 75  $\mu$ M). The media was then removed and cells were washed with 1x PBS. Cells were then incubated at 37°C for 30 min in darkness with media containing MitoTracker Deep Red to give a final concentration of 150 nM in 400  $\mu$ L supplemented media. Samples were then washed 3 times with 1x PBS (3 min) and fixed with a 4 % paraformaldehyde (PFA) solution for 30 min at room temperature. The PFA solution was removed and cells washed repeatedly with PBS (3 x 3 min) and permeabilized with 0.2 % Triton X-100 for 5 min. Cells were subsequently stained at room temperature in darkness with PBS solutions of Alexa Fluor-488 phalloidin (10U/100  $\mu$ L, 30 min) and followed by DAPI (1:10,000, 10 min). Images were obtained using laser scanning Leica DMIRE2 confocal microscope with oil immersion x40 lens. DAPI was excited at 405 nm by diode laser and emission captured at 470 nm with +/- 30 nm bandwidth. Alexa Fluor 488-phalloidin was excited at 488 nm by Ar laser and emission wavelength was captured at 520 with a bandwidth +/- 25 nm. Mitotracker Deep Red was excited at 633 nm by HeNe laser and emission was captured at 668 +/- 20 nm. Experiments were performed where by combinations of excitation wavelengths and emission filters for specific dyes are applied sequentially.

### 3.3.6 Statistical analysis

All ex vivo data is presented as mean  $\pm$  standard deviation and statistical analysis was performed in GraphPad Prism version 6. Student's t-test were applied to evaluate the significances of difference between samples, and considered to be significant if  $p \leq 0.05$ .

## 3.4 Results and Discussion

### 3.4.1 NCI-60 analysis

**Cu-Ph** was submitted to the National Cancer Institute's (NCI) Developmental Therapeutics Program (DTP), NCI-60 human cell line screen where both one (10  $\mu$ M) and five dose (0.01 – 100  $\mu$ M) cytotoxicity analysis were completed. The panel consists of 60 human cancer cell lines from a variety of cancers including breast, colon, central nervous system, leukemia, non-small cell lung, melanoma, ovarian, prostate, and renal cancers. Five-dose NCI 60 analysis was used to calculate 50% growth inhibition of tested cells ( $GI_{50}$ ), total growth inhibition (TGI), and lethal dose concentration inducing 50% cell death ( $LC_{50}$ ) (raw values are available in **Table S-3.1**).<sup>57</sup> A heat map was developed to visualize the **Cu-Ph**  $LC_{50}$  concentrations (**Figure 3.1**). While leukemic cell lines proved to be least sensitive, the complex exhibited consistent low micromolar activity against the majority of solid tumor cell lines within the panel. A variety of activity was observed within non-small cell lung cancer (NSCLC), melanoma and renal cell lineages with  $LC_{50}$  concentrations ranging between 1 to 100  $\mu$ M. Overall, **Cu-Ph** exhibits highest potency within NCI-H522 (NSCLC), SK-MEL-2 (melanoma), UACC-257 (melanoma), and A489 (renal) cells.

Activity profiles from  $GI_{50}$  and  $LC_{50}$  analysis for **Cu-Ph** (NSC 767443) were analyzed within the COMPARE algorithm (<http://dtp.nci.nih.gov/compare/>). This algorithm provides an automated and quantitative comparison of newly designed cytotoxins that associates the pattern of NCI-60 activity to standard clinical agent in order to delineate mechanisms of action within the NCI database.<sup>23</sup> The comparison results are represented as Pearson's correlation coefficients ( $r$ ) ranging from -1 to +1. Values closer to +1 indicate a high degree of homology (in terms of cytotoxic profile) with the known chemotherapeutic drug. In our COMPARE analysis we examined both the mechanistic and market drugs data sets using both  $GI_{50}$  and  $LC_{50}$  data with the highest ranked matches shown in Table 1. Mitotane (Lysodren) exhibited the topmost coefficient (0.895) and is employed against adrenocortical carcinoma through the inhibition of hormone production localized to adrenal cortex cells where induction of apoptosis has been identified.<sup>58,59</sup> Although there is little chemical or biological data available for the second leading drug generated from the COMPARE algorithm, antineoplastic S353527, the tin(IV) complex possess a notable comparison ranking of 0.875 with **Cu-Ph**. Another comparison noted is that of the prodrug Tamoxifen—which hydrolyses to 4-hydroxy tamoxifen (**Figure 3.2**)—a competitive antagonist of the estrogen receptor in hormone dependent breast cancer.<sup>60</sup> The final two compounds within the top five COMPARE matches are the topoisomerase 1 inhibitor, 7-*o*-methyl nogalarol, and cantharidin, an inhibitor of protein phosphatase 2A (PP2A),<sup>61</sup> which is an important regulatory protease involved in cell cycle and apoptosis. Indeed cantharidin has previously exhibited antitumor activity towards a variety of cancers such as breast, colorectal, bladder, leukaemia and hepatoma.<sup>62-66</sup> Although the Pearson's

coefficients of these cytotoxins positively correlate with **Cu-Ph**, it is worth mentioning the complex does not show activity profiles similar to bleomycin, cisplatin (0.287) or any related platinum therapeutics, indicating a potentially unique metallodrug activity profile and mechanism.

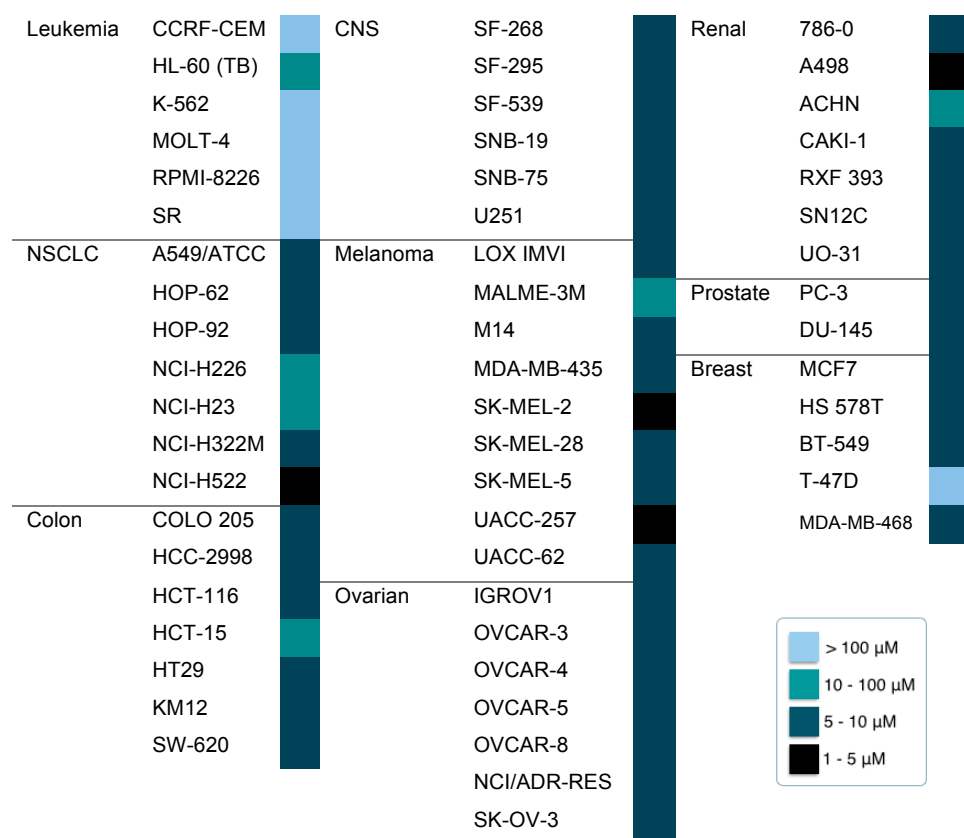


**Figure 3. 1** Heat map data representing LC<sub>50</sub> concentrations of **Cu-Ph** across the NCI 60 human cancer cell line panel. Concentration ranges from most cytotoxic (1 – 5 μM shown in black) to least cytotoxic (>100 μM shown in light blue).

**Table 3. 1** Pearson's correlation coefficients (*r*) generated from the NCI DTP COMPARE algorithm.

Drug	NSC No.	Cu-Ph ( <i>r</i> )
Mitotane	S38721	0.895
Antineoplastic-353527	S353527	0.875
Tamoxifen	S180973	0.774
7-O-methylnogalarol	S102815	0.766
Cantharidin	S61805	0.759
Doxorubicin	S123127	0.418
Cisplatin	S119875	0.287

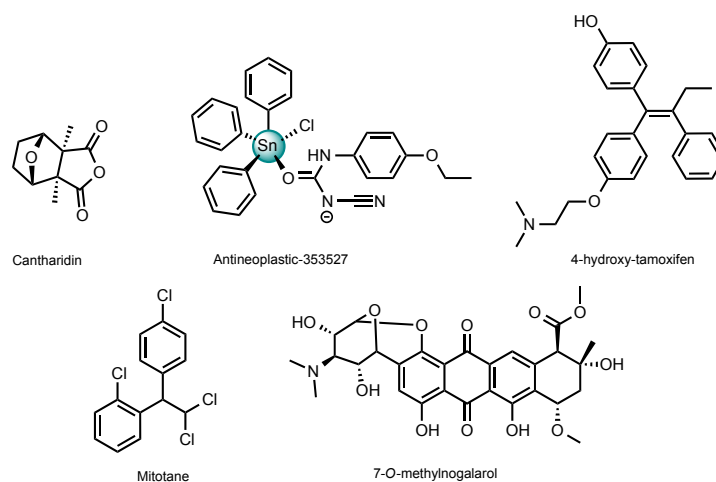


**Figure 3. 2** Molecular structure of Cantharidin (NSC S61805), antineoplastic-353527 (NSC S353527), the active form of prodrug tamoxifen, 4-hydroxy-tamoxifen (NSC S180973), Mitotane (NSC S38721), and 7-*O*-methylnogalarol (NSC S102815).

### 3.3.2 Base specific DNA binding interactions

Previous DNA binding interactions by **Cu-Ph** on calf thymus fibers (ctDNA) reveal the complex potentially intercalates from the minor groove with an apparent binding constant ( $K_{app}$ ) of  $\sim 10^5$  M(bp)<sup>-1</sup>.<sup>17</sup> These studies, however, were conducted within an EDTA-buffered media thus creating a metal chelating environment that could potentially obstruct **Cu-Ph** DNA binding affinity through competitive sequestering of Cu<sup>2+</sup> ions. In order to re-evaluate  $K_{app}$  values under noncompeting conditions, a selection of DNA sequences containing varying A·T content were investigated (**Figure 3.3** and **Table 3.2**). ML-DNA (*Micrococcus luteus*) and ctDNA (calf thymus) are canonical DNA sequences, while poly[d(A·T)<sub>2</sub>] and poly[d(G·C)<sub>2</sub>] are synthetic double stranded alternating co-polymers. Classical DNA binding drugs actinomycin D and netropsin are reported in parallel. Actinomycin D is widely known as a classical intercalator that retains a preference for G·C rich copolymers,<sup>67</sup> which are known to form left-handed Z-DNA. As displayed in **figure 3.3**, actinomycin D is a high affinity target for the G·C copolymer with the gradual decrease of G·C content proportionally conveying disfavored conditions for classical intercalation. Netropsin, a minor groove binder, forms preferable interactions with a compressed minor groove in T-tracts of A·T rich DNA and this observation is evident from its binding constant to nucleic acid sequences of increasing A·T content.<sup>68</sup> **Cu-Ph** displayed greater affinity toward G·C rich nucleotides of poly[d(G·C)<sub>2</sub>] and ML-DNA and evidence here confirms the intercalative nature of the complex as suggested in previous work.<sup>17</sup>

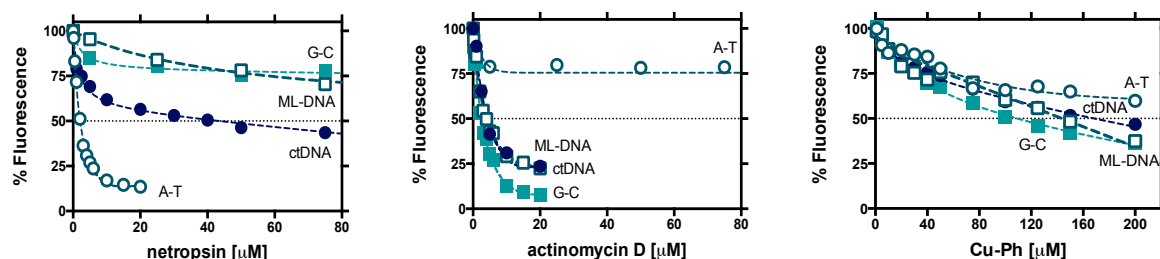


**Figure 3. 3** Competitive fluorescence binding of netropsin, actinomycin D, and **Cu-Ph** to ethidium bromide (12.6  $\mu\text{M}$ ) saturated solutions of calf thymus DNA, *Micrococcus lysodeikticus* DNA (ML-DNA), poly[d(A-T)<sub>2</sub>], and poly[d(G-C)<sub>2</sub>] polynucleotides (10  $\mu\text{M}$ ).

**Table 3. 2** Apparent binding constants ( $K_{\text{app}}$ ) of Cu-Ph, actinomycin D and netropsin.  $K_{\text{app}} = K_e \times (12.6 / C_{50})$  where  $K_e = 9.5 \times 10^6 \text{ M/bp}$  and  $C_{50}$  = concentration that causes 50% reduction in EtBr fluorescence, where  $n=3$ .

	$K_{\text{app}} \text{ M(bp)}^{-1}$			
	poly[d(A·T) <sub>2</sub> ] (100% AT)	ctDNA (58% AT)	ML-DNA (28% AT)	poly[d(G·C) <sub>2</sub> ] (0% AT)
Actinomycin D	N/A	$2.92 \times 10^7$	$3.03 \times 10^7$	$5.25 \times 10^7$
Netropsin	$5.75 \times 10^7$	$2.50 \times 10^6$	N/A	N/A
<b>Cu-Ph</b>	$4.06 \times 10^5 \pm 6.05 \times 10^4$	$7.17 \times 10^5 \pm 1.78 \times 10^5$	$8.30 \times 10^5 \pm 3.10 \times 10^4$	$1.14 \times 10^6 \pm 7.32 \times 10^4$

### 3.4.3 In Vitro and Intracellular DNA Oxidation with ROS Scavengers

In order to identify the predominant ROS species involved in chemical nuclease activity, we investigated the activity profile of **Cu-Ph** in the presence of ROS-specific scavengers (**Figure 3.5B**) with results shown in **Figure 3.4**. Treatment of superhelical (SC) pUC19 (FI) with **Cu-Ph** only (lanes 2-5) results in single strand damage (relaxation) to open circular DNA (OC, FII) at 0.5 and 1  $\mu\text{M}$ , double strand damage (linear) (LC, FIII) at 2.5  $\mu\text{M}$  exposure, and complete DNA degradation at 5  $\mu\text{M}$ . Before complex analysis, scavengers were confirmed to have no impact on pUC19 conformation (results not shown). The cleavage efficacy of **Cu-Ph** in the presence of ROS-specific scavengers identified the most prevalent species involved in strand scission as superoxide ( $\text{O}_2^{\cdot -}$ ) as the presence tiron<sup>69,70</sup> (4,5-dihydroxy-1,3-benzenedisulfonic acid disodium salt or TH<sub>2</sub>, Figure 5C) (lanes 10-13) significantly impedes the cleavage activity of the compound and prevents double strand damage. The presence of the hydroxyl radical ( $\cdot\text{OH}$ ) scavenger, DMSO,<sup>71,72</sup> also inhibited cleavage activity (lane 6-9) however to a lesser extent than tiron as FIII was still present upon 2.5 and 5  $\mu\text{M}$  drug treatment. The chemical nuclease activity of the complex was only marginally altered by KI, a  $\text{H}_2\text{O}_2$  scavenger,<sup>73,74</sup> while  $\text{NaN}_3$ —specific quencher of singlet oxygen<sup>75</sup>—had negligible effects also.



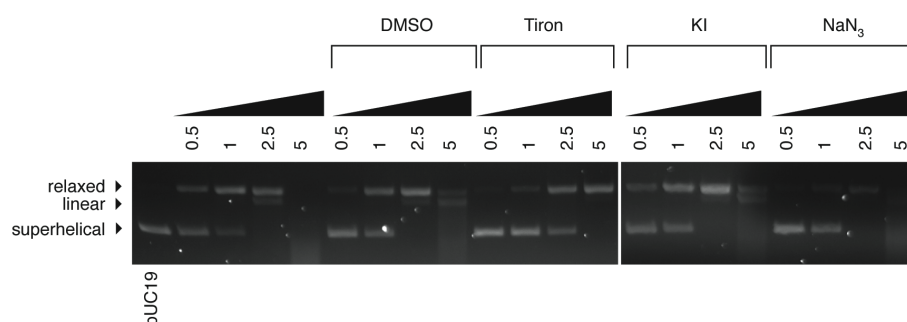


**Figure 3. 4** DNA cleavage reactions in the presences of ROS-specific scavengers. 400 ng of SC pUC19 was incubated for 1 h at 37°C with complex concentrations of 0.5, 1, 2.5 and 5  $\mu$ M in the presence of 25 mM NaCl, 0.5 mM L-Asc in 80 mM HEPES. Lane 1: DNA only, Lanes 2-5: 0.5, 1, 2.5, 5  $\mu$ M Cu-Ph, Lanes 6-9: + 10 % DMSO, Lanes 10-13: + 10 mM tiron, Lane 14-17: + 10 mM KI, Lanes 18-21: + 10mM NaN<sub>3</sub>.

Next, we identified the impact of ROS-specific scavengers (D-mannitol,<sup>76</sup> tiron,<sup>70,77</sup> and pyruvate<sup>78</sup>) on SKOV3 cell survival post exposure to a toxic dose of **Cu-Ph** (**Figure 3.5**). In these experiments cells were pre-treated for 1 h with 1 mM of each antioxidant scavenger prior to the addition of 3  $\mu$ M **Cu-Ph** with cells then being incubated for a further 24 h (**Figure 3.5A**). The pre-treatment of mannitol, pyruvate, and tiron were found to enhance cell survival by 12, 16, and 23 %, respectively. These results are in excellent agreement with the observed effects on plasmid DNA damage and it is particularly significant that the largest enhancement to viability occurred in the presence of the O<sub>2</sub><sup>•-</sup> scavenger, tiron. Results here support Fenton-mediated cytotoxicity with the superoxide anion radical most likely accelerating this process catalytically through the Haber-Weiss reaction.<sup>16,79</sup>

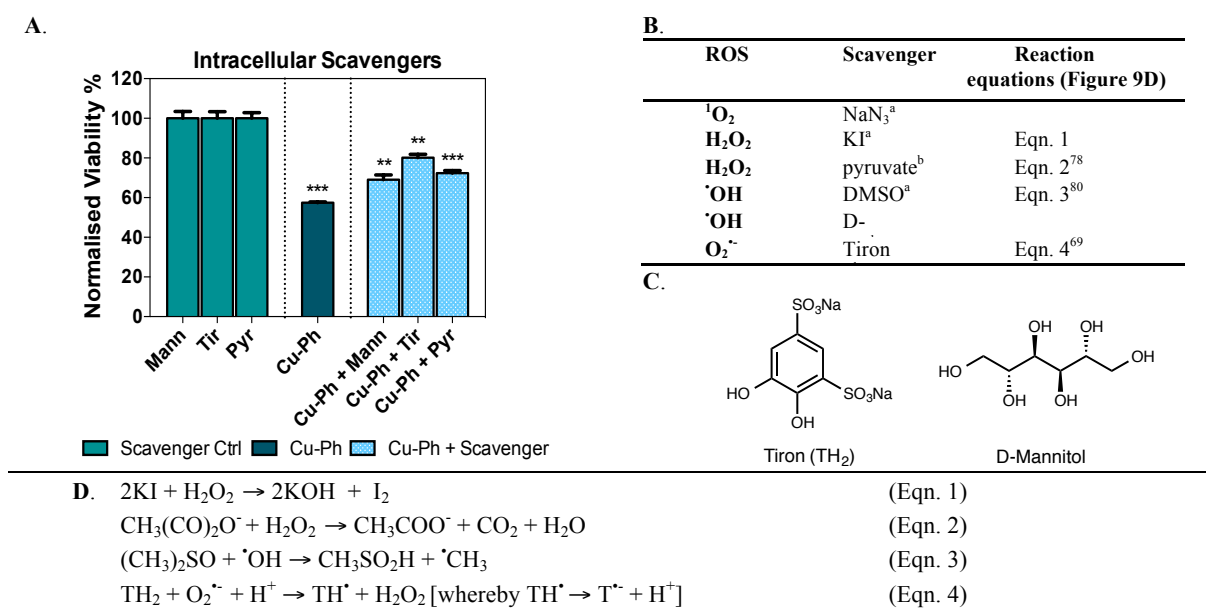


**Figure 3. 5 A.** Viability profile of Cu-Ph in SKOV3 cells in the presence of intracellular scavengers. Cells were treated with 1 mM of tiron (Tir), D-mannitol (Mann) and pyruvate (Pyr) for 1 h prior to Cu-Ph addition (3  $\mu\text{M}$ ) and incubated for 24 h. **B.** Scavengers utilized within this study where <sup>a</sup> ROS scavengers present in *in vitro* DNA oxidation experiment and <sup>b</sup> scavengers used in intracellular work. **C.** Molecular structure of tiron (TH<sub>2</sub>) and D-mannitol. **D.** Reaction equations of radical species and their respective scavengers. Not significant (ns)  $p > 0.05$ ,  $**P \leq 0.01$ ,  $***P \leq 0.0001$ .

### 3.4.4 Apoptotic detection through Annexin V and Caspases

Identification of endogenous activation triggers of apoptosis within SKOV3 cells were evaluated by detection of Annexin V and activation of caspase 3, 7, 8, and 9. A common indicator of apoptosis can be monitored through the lipid-membrane translocation of phosphatidyl serine (PS), a component normally restricted to the inner surface of the membrane in non-apoptotic cells.<sup>36,81</sup> The externalization of PS is one of the early events in apoptosis where it is accessible to the high affinity membrane-impermeable recombinant protein, Annexin V.<sup>36,37,81-84</sup> Here, Annexin V was conjugated to a fluorophore moiety, phycoerythrin (PE), which fluoresces upon PS binding (emission 578 nm). A second membrane impermeable stain, 7-amino-actinomycin D (7-AAD), was used to determine late stage apoptosis; 7-AAD is a DNA intercalator gaining access to the nucleus only upon decomposition of cell membrane integrity.<sup>85</sup> The scatter plots shown in **Figure 3.6** present a population migration from viable quadrants (lower left) to early and late apoptosis (lower and upper right) in complex treated cells across the cytotoxic concentration gradient (1.0 – 5.0  $\mu\text{M}$ ). Samples treated with increasing concentrations of **Cu-Ph** clearly demonstrate an exodus from a viable population to early (16 %), and then late apoptotic stages (22 %). These results contrast markedly with **Doxo**, which showed the highest population of induced of cell death with 46 % of cells undergoing late-stage apoptosis.

Next, we probed the origins of apoptotic initiation more extensively through the activation of initiator and executioner caspases. Apoptosis can be induced through triggering stimuli in two principal routes; an intrinsic pathway which is stimulated by most cytotoxic agents including radiation and toxins which then activate the mitochondria within the cell through pro-apoptotic Bcl-2 proteins such as Bax and Bid.<sup>86-88</sup> Apoptosis can also be triggered by specific transmembrane death receptors, which bind to specific ligands and signal the extrinsic pathway. Both pathways activate cysteine-aspartic proteases, called caspases, from their monomeric pro-caspase counterparts and thus activate molecular machinery to execute the process of apoptosis.<sup>38,89</sup> The intrinsic pathway develops from mitochondrial stress, and compromises mitochondrial outer transmembrane potential, resulting in cytochrome *c* release that aids in the activation of initiator caspase 9 for the formation of the apoptosome. The apoptosome lead to the activation of executioner caspases 3 and 7, which marks the beginning of the executioner pathway, resulting in degradation of the nucleus and cytoskeletal framework due to the prior release of endonucleases and proteases.<sup>90</sup> The extrinsic pathway—also known as the death receptor pathway—is initiated through Fas/Apop-1 or tumor necrosis factor (TNF) binding to form membrane bound signaling complexes, or death inducing signaling complexes (DISCs),<sup>40,91-93</sup> resulting in the activation of caspase 8 that in turn cleaves and activates executioner caspases 3, 7 and 4.

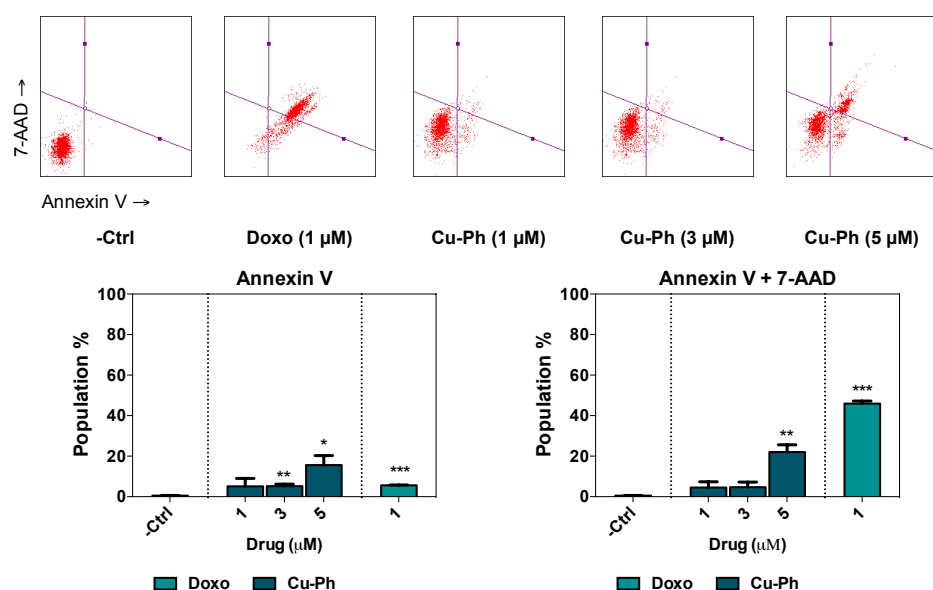


**Figure 3.6** Nexin Assay scatter plots; population represented in quadrants for viable cells (lower left), mid (lower right) and late stages of apoptosis (upper right). Graph depicting mid-apoptosis show positive for annexin V only, population for late apoptosis are positive for annexin V and 7-AAD. Not significant (ns)  $p > 0.05$ , \* $p \leq 0.05$ , \*\* $p \leq 0.01$ , \*\*\* $p \leq 0.001$ .

The quantitative detection of caspase 3/7, 8, and 9 were analyzed through sulforhodamine (SR) or carboxyfluorescein (FAM) conjugates of amino acid functionalized caspase-specific inhibitors DEVD, LETD, and LEHD sequences. SKOV3 cells were treated with **Cu-Ph** and **Doxo** as

previously described and results are represented in **Figure 3.7**. **Doxo** was found to primarily trigger the intrinsic pathway with 29 % of the cellular population being caspase 9 positive. In comparison, 27 % of cells were caspase 9 positive at the highest tested concentration (5  $\mu$ M) of **Cu-Ph**. Elevated levels of executioner caspases 3 and 7 were also detected upon treatment of **Cu-Ph**. In mid-apoptotic stages, the fluorogen inhibitor of 3/7 is detectable, whereas in late stage apoptosis, the membrane impermeable DNA intercalator (7-AAD) is also discernible as a result of cellular membrane degradation. The detection of caspase 3/7, alone, was evident in just 10 % of the population treated with **Cu-Ph** (5  $\mu$ M) while **Doxo** (1  $\mu$ M) induced ~ 80 %. The presence of both caspase inhibitor and DNA fluorescent biomarkers, indicative of late stage apoptosis, were observed in 30 % of SKOV3 cells treated with **Cu-Ph** (5  $\mu$ M) while the DNA intercalator **Doxo** induced <10 %.

Although caspase 8 is activated by **Cu-Ph** cytotoxicity, it is possible for this process to occur independently of the death receptor / extrinsic pathway. Firstly, since **Cu-Ph** enhances ROS production within SKOV3 a multitude of biomolecules including phospholipids of membranes may be affected. For example, superoxide-mediated damage to the carbonyl function groups at the ester bond in lipid membranes have been well characterized and are implicated in lipid peroxidation.<sup>94</sup> Thus, ROS generation could lead to oxidative cell membrane damage that, in turn, activates caspase 8 in an analogous way to ROS mediated cell death.<sup>95</sup> Significantly, bleomycin is known to induce apoptosis through the activation of caspase 8 from oxidative damage.<sup>96</sup>

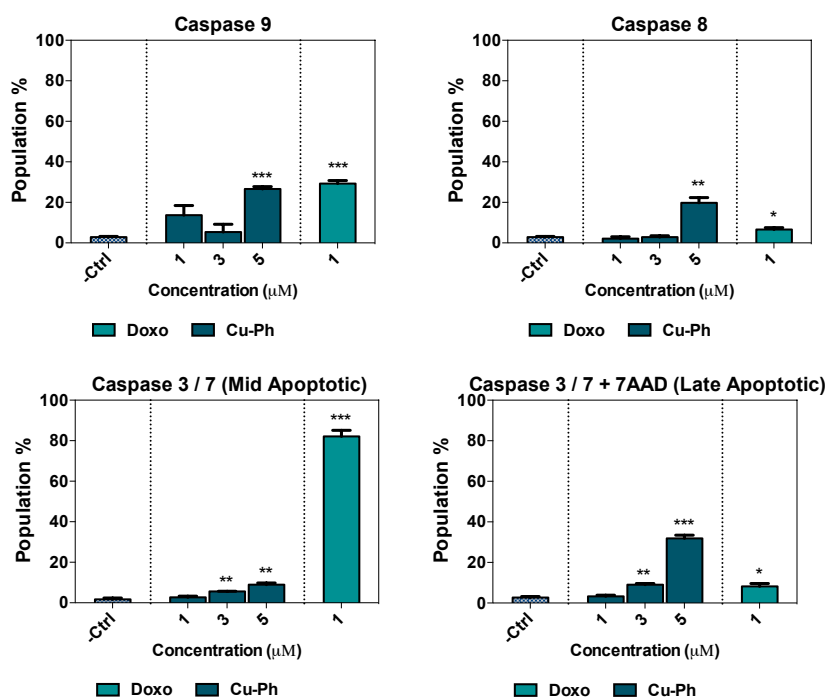


**Figure 3. 7** Caspase 3/7, 8 and 9 activation after 24 h incubation with drug. Not significant (ns)  $p > 0.05$ , \* $p \leq 0.05$ , \*\* $p \leq 0.01$ , \*\*\* $p \leq 0.001$ .

### 3.4.5 Mitochondrial depolarization

The evidence of **Cu-Ph**-mediated superoxide cytotoxicity and DNA degradation prompted us to widen our analysis to include mitochondrial damage.<sup>17</sup> Mitochondrial depolarization correlates to transmembrane permeability, which when compromised releases pro-apoptotic factors into the cytosol.<sup>41,42</sup> In order to identify dose-dependent damage response of SKOV3 mitochondria, cells were incubated with **Cu-Ph** across their approximate LC<sub>25</sub>, LC<sub>50</sub>, and LC<sub>75</sub> doses. Carbonyl cyanide *m*-chlorophenyl hydrazone (**CCCP**, **Scheme 3.1**) served as a positive control for mitochondrial depolarization as it known to reduce mitochondrial transmembrane potential ( $\Delta\Psi_m$ ), due to its spectral proton ionophore properties,<sup>97</sup> and thus rendering the membrane permeable. **CCCP** is a lipid-soluble, amphipathic molecule where the anionic form combines with an aqueous proton and then utilizes pH diffusion to translocate across the lipid membrane where the proton readily dissociates.<sup>44,98,99</sup> Electrostatic interactions promptly efflux the anionic **CCCP** to the opposing side of the lipid-bilayer. Continuous, and rapid repetition of this process swiftly destroys the proton gradient and  $\Delta\Psi_m$ . Both positive controls **CCCP** and **Doxo** were incubated above their LC<sub>50</sub> doses under identical conditions. An indicative dye JC-1 (5,5',6,6'-tetrachloro-1,1',3,3'-tetraethylbenzimidazolocarbocyanine iodide) (**Figure 3.8**) was used to determine  $\Delta\Psi_m$  for all tested compounds. In viable cells, cationic JC-1 localizes within the mitochondria forming j-aggregates due to the net negative charge over 140 mV,<sup>100</sup> resulting in orange emitting aggregates.<sup>101,102</sup> As mitochondria function is disrupted, JC-1 localization and aggregation is prevented through the dissipation of membrane potential, and thus resides in a monomeric state in the cytosol. JC-1 monomers emit green fluorescence at 530 nm that undergo a bathochromic shift to 595 nm through the formation of orange emissive j-aggregates.

Scatter plots are shown in **Figure 3.8** representing samples treated with **Cu-Ph**, **Doxo** and **CCCP**. Cells incubated with **CCCP** show over 40 % reduction in  $\Delta\Psi_m$  whereas doxorubicin exhibits minimal disruption in comparison to drug free cells. The presence of **Cu-Ph** induces mitochondrial potential collapse in a concentration-dependent manner and is particularly evident through excessive monomer detection at 5.0  $\mu$ M. At this highest exposed complex concentration, 83 % of mitochondrial population is depolarized as opposed to 54 % upon **CCCP** treatment (75  $\mu$ M). The degradation of the mitochondrial proton gradients and dissipation of transmembrane potential is known to have a direct influence in cellular toxicity; increasing mitochondrial porosity permits translocation of cytochrome *c* into the cytosol, and in turn initiates the intrinsic apoptotic pathway.<sup>103</sup> Since we have previously identified **Cu-Ph** generates  $O_2^{\cdot-}$ ,  $\cdot OH$  and  $H_2O_2$  as potent mediators of cytotoxicity, it is highly plausible that free radical damage to the mitochondria is responsible for depolarization of the membrane potential. Indeed, the mitochondria is particularly susceptible to oxidative damage due to radical generation, in particular *via*  $O_2^{\cdot-}$ , during metabolic processes such as oxidative phosphorylation during ATP generation in the electron transport

chain.<sup>94,104</sup> Roughly 1-3% of molecular oxygen consumed during ATP synthesis results in the formation of  $O_2^{\cdot-}$  from escaping electrons reacting with molecular oxygen.<sup>104</sup> The formation of this radical is the preeminent precursor in the production of alternative, destructive ROS through a series of free radical cascade reactions that are likely catalyzed by **Cu-Ph**.<sup>94,104</sup>

Induced depolarization, to this extent, has clearly identified the mitochondria as a potential target for this class of compound. Site-selective targeting of the mitochondria has recently been identified in the treatment of the aggressive cancers resistant to previously administered chemotherapeutic treatment, in particular platinum-based therapies and multidrug resistance. Marrache *et al.* have synthesized a platinum prodrug-nano particle delivery system where the Platin-M, a Pt(IV) analogue of cisplatin with mitochondrial targeting triphenylphosphonium (TPP) administered in formulation with poly(lactic-co—glycolic acid) (PLGA), polyethyleneglycol (PEG) tethered to a terminal TPP, strategically designed to overcome nuclear excision repair (NER) mechanism associated with cisplatin resistant cancers.<sup>105</sup> The biodistribution of this dual-targeting formulation, improved drug circulation and delivery across the blood brain barrier have highlighted the novel prodrug-delivery combination as a therapeutic strategy for the treatment of platinum drug-resistant cancers and those of the central nervous system. Another approach to overcome the susceptibility to multi-drug resistance has been assessed with doxorubicin linked to mitochondrial penetrating peptide. Engineering the clinical standard with a mitochondrial targeting moiety induced selective damage of mtDNA over genomic DNA, while still retaining topoisomerase II stabilization properties, while overcoming multi-drug resistance mediated by the over-expression of the antiapoptotic factor, P-glycol-protein (Pgp) efflux pumps in doxorubicin sensitive and resistant strains for ovarian cancer cell line, A2780.<sup>106</sup>

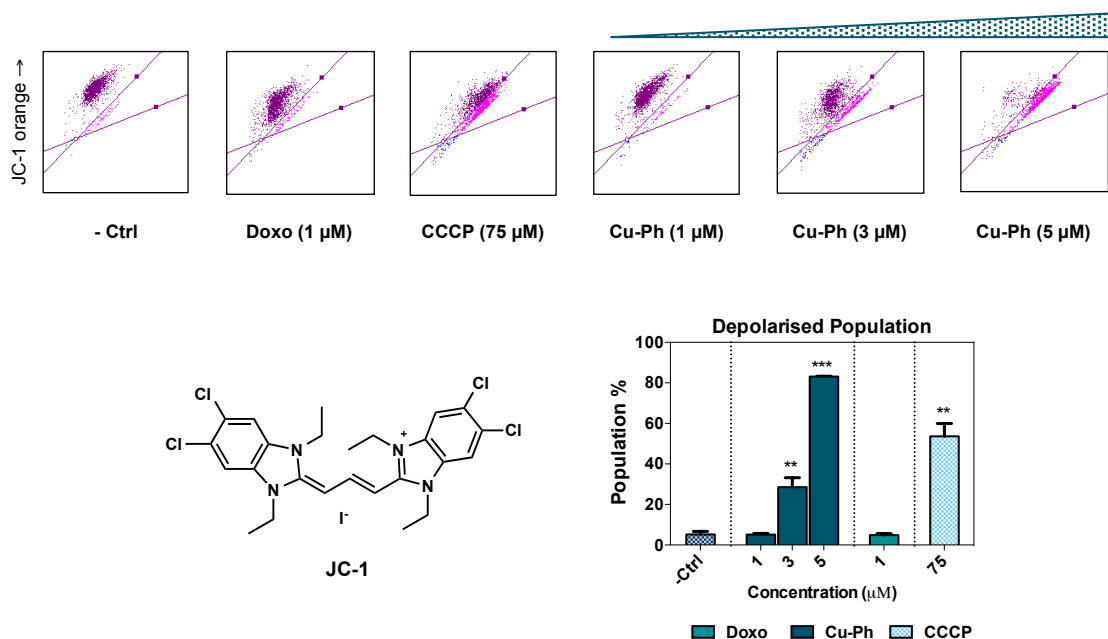


**Figure 3. 8** Mitochondrial depolarization scatter plots for Doxo, CCCP and Cu-Ph where polarized mitochondria are shown in purple, to depolarized mitochondria in pink and blue (Y axis = JC-1 orange, X axis = JC-1 green) The molecular structure of indicative mitochondrial dye JC-1 (5,5',6,6'-tetrachloro-1,1',3,3'-tetraethylbenzimidazolocarbo-cyanine iodide) also shown. Graph represents population percentages of depolarized mitochondria for Doxo, CCCP and Cu-Ph. Not significant (ns)  $p > 0.05$ ,  $*p \leq 0.05$ ,  $**P \leq 0.01$ ,  $***P \leq 0.001$ .

### 3.4.6 Confocal microscopy

In order to investigate morphological modification within drug treated SKOV3 cellular structure, confocal microscopy experiments were specifically designed with an extensive range of selective cellular dyes (**Figure 3.9**). Cancer cells were stained with DAPI (4',6-diamidino-2-phenylindole), a nuclear stain which fluoresces strongly upon binding to A·T rich DNA tracts along the minor groove,<sup>107</sup> while F-actin in the cytoskeleton was selectively labeled with an Alexa Fluor conjugate of phalloidin.<sup>108,109</sup> MitoTracker Deep Red, a cationic carbocyanine,<sup>110</sup> was also utilized as it resides within the mitochondria prior to cell fixation due to the highly efficient cationic accumulation across the negative potential of the hydrophobic, inner mitochondrial membrane,<sup>100,111</sup> and is sensitive to MMP.<sup>112,113</sup> The induction of apoptosis can be elucidated through microscopic detection of apoptotic morphological changes in the cell.<sup>90</sup> During execution of late stage apoptosis the formation of granular mass appear within the nucleus, with the subsequent condensation of chromatin,<sup>114,115</sup> and DNA fragmentation.<sup>115,116</sup> The cytoplasmic structure is also condensed with compaction of organelles.<sup>90</sup> In the later stages of apoptosis membrane blebbing occurs where the cell segregates into fragments with intact cellular membranes and cytoplasm ultimately forming apoptotic bodies,<sup>90,114,115</sup>

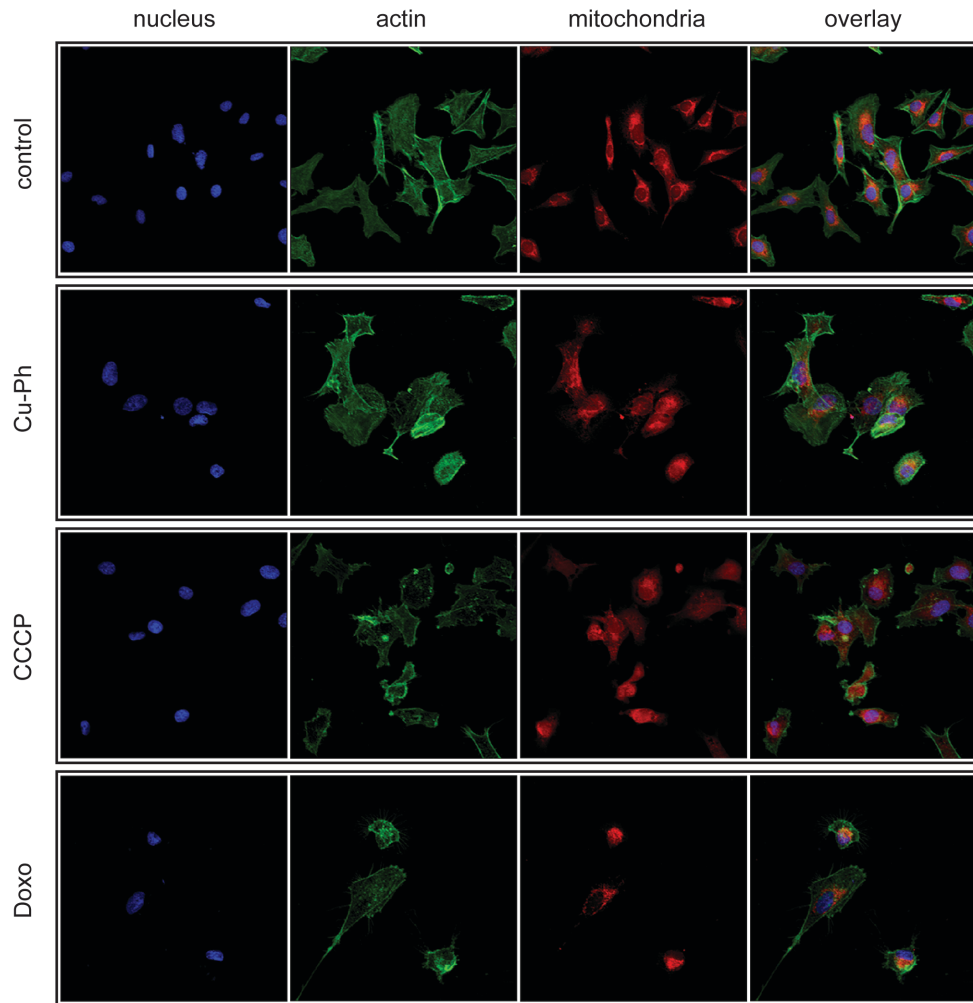
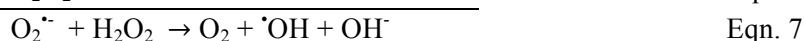


**Figure 3. 9** 40X confocal images of SKOV3 cells treated with Cu-Ph (3  $\mu$ M), CCCP (75  $\mu$ M) and Doxo (1  $\mu$ M). The nucleus is stained with DAPI (blue), cytoskeleton with Alexa Fluor 488-Phalloidin and mitochondria with MitoTracker Deep Red.



## 2.5 Conclusion

**Cu-Ph** was originally reported along with a bipyridyl analogue by Kellett *et al.*,<sup>17</sup> where the complex exhibited a broad spectrum of activity against breast (MCF-7), colon (HT29), prostate (DU145), and ovarian (SKOV3) cancer cell lines. DNA binding studies revealed intercalation, while intracellular ROS generation properties were in line with control H<sub>2</sub>O<sub>2</sub> exposure and demonstrated the induction of genomic double strand breaks (DSBs) by **Cu-Ph** through detection of  $\gamma$ H2AX foci within the previous body of work.<sup>17</sup> In the present study an array of mechanistic toxicity experiments were designed in order to investigate the mode of action induced by **Cu-Ph** within SKOV3 human cancer cells. NCI60 results demonstrate **Cu-Ph** is a low micromolar cytotoxin of solid epithelial cells, particularly within melanoma and renal sensitive cell lines. **Cu-Ph** exhibits broad-spectrum activity across numerous cancer types with the exception of leukemic cancers (LC<sub>50</sub> > 100  $\mu$ M). The COMPARE activity patterns for **Cu-Ph** revealed no overlap was observed with existing metallodrugs (*r* values < 0.5). The spectrum of results did, however, match effective organic chemotherapeutic agents such as tamoxifen and mitotane. Following these promising results, drug tolerance and toxicity will need to be assessed within *in vivo* models and primary non-cancerous human cells in order to examine preferential activity towards rapidly proliferating tumor cells. In this study fluorescent DNA binding studies were evaluated using DNA sequences of differential A-T content and *K*<sub>app</sub> values demonstrate **Cu-Ph** preferentially binding toward G-C rich nucleotides. Together with previous analysis, evidence here supports intercalation at the minor groove as the principal DNA binding motif.<sup>17</sup>



The use of ROS-specific scavengers enhanced cell survival and, in particular, identified the generation of superoxide as the predominant species that mediates the copper-catalyzed Haber Weiss reaction (eqn. 5-7) *via* Fenton-type chemistry (eqn. 6) in the generation of the overtly toxic  $\cdot\text{OH}$  in the net reaction (eqn. 7).<sup>79</sup> Apoptotic induction was assessed, and confirmed, by Annexin V and cleaved caspases 3 and 7. The origins of apoptotic initiation were also examined through detection of caspase 9 (intrinsic pathway) and caspase 8 (extrinsic) where levels of induction were lower than that of **Doxo**; **Cu-Ph** predominately activated caspase 9, however, noteworthy levels of caspase 8 were also detected. Confocal microscopy analysis supports multimodal targeting properties by **Cu-Ph** within SKOV3 as reduced mitochondrial fluorescence due to loss of membrane potential and evidence of morphological changes characteristic of apoptosis and the remnants of apoptotic bodies are evident.

### 3.6 Supporting Material

Supplementary data associated with this chapter can be found in Appendix B.

### 3.7 References

- (1) Jung, Y., and Lippard, S. J. (2007) Direct cellular responses to platinum-induced DNA damage. *Chem. Rev.* *107*, 1387–1407.
- (2) Kelland, L. (2007) The resurgence of platinum-based cancer chemotherapy. *Nature Reviews Cancer* *7*, 573–584.
- (3) Santini, C., Pellei, M., Gandin, V., Porchia, M., Tisato, F., and Marzano, C. (2014) Advances in Copper Complexes as Anticancer Agents. *Chem. Rev.* *114*, 815–862.
- (4) Turski, M. L., and Thiele, D. J. (2009) New roles for copper metabolism in cell proliferation, signaling, and disease. *J. Biol. Chem.* *284*, 717–721.
- (5) Tardito, S., Bassanetti, I., Bignardi, C., Elviri, L., Tegoni, M., Mucchino, C., Bussolati, O., Franchi-Gazzola, R., and Marchiò, L. (2011) Copper binding agents acting as copper ionophores lead to caspase inhibition and paraptotic cell death in human cancer cells. *J. Am. Chem. Soc.* *133*, 6235–6242.
- (6) Finney, L., Vogt, S., Fukai, T., and Glesne, D. (2009) COPPER AND ANGIOGENESIS: UNRAVELLING A RELATIONSHIP KEY TO CANCER PROGRESSION. *Clinical and Experimental Pharmacology and Physiology* *36*, 88–94.
- (7) Gupte, A., and Mumper, R. J. (2009) Elevated copper and oxidative stress in cancer cells as a target for cancer treatment. *Cancer Treat. Rev.* *35*, 32–46.
- (8) Loganathan, R., Ramakrishnan, S., Suresh, E., Riyasdeen, A., Akbarsha, M. A., and Palaniandavar, M. (2012) Mixed Ligand Copper(II) Complexes of N, N-Bis(benzimidazol-2-ylmethyl)amine (BBA) with Diimine Co-Ligands: Efficient Chemical Nuclease and Protease Activities and Cytotoxicity. *Inorg. Chem.* *51*, 5512–5532.
- (9) Banci, L., Bertini, I., Ciofi-Baffoni, S., Kozyreva, T., Zovo, K., and Palumaa, P. (2010) Affinity gradients drive copper to cellular destinations. *Nature* *465*, 645–648.
- (10) Labbé, S., and Thiele, D. J. (1999) Pipes and wiring: the regulation of copper uptake and distribution in yeast. *Trends Microbiol.* *7*, 500–505.
- (11) Santini, C., Pellei, M., Gandin, V., Porchia, M., Tisato, F., and Marzano, C. (2014) Advances in Copper Complexes as Anticancer Agents. *Chem. Rev.* *114*, 815–862.
- (12) Galindo-Murillo, R., García-Ramos, J. C., Ruiz-Azuara, L., Cheatham, T. E., III, and Cortés-Guzmán, F. (2015) Intercalation processes of copper complexes in DNA. *Nucleic Acids Res.* gkv467.
- (13) Prisecaru, A., Devereux, M., Barron, N., McCann, M., Collieran, J., Casey, A., McKee, V., and Kellett, A. (2012) Potent oxidative DNA cleavage by the di-copper cytotoxin:  $[\text{Cu}_2(\mu\text{-terephthalate})(1,10\text{-phen})_4]^{2+}$ . *Chem. Commun.* *48*, 6906–6908.
- (14) Prisecaru, A., McKee, V., Howe, O., Rochford, G., McCann, M., Collieran, J., Pour, M., Barron, N., Gathergood, N., and Kellett, A. (2013) Regulating Bioactivity of  $\text{Cu}^{2+}$ /Bis-1,10-phenanthroline Artificial Metallonucleases with Sterically Functionalized Pendant Carboxylates *J. Med. Chem.* *56*, 8599–8615.
- (15) Molphy, Z., Prisecaru, A., Slator, C., Barron, N., McCann, M., Collieran, J., Chandran, D., Gathergood, N., and Kellett, A. (2014) Copper Phenanthrene Oxidative Chemical Nucleases. *Inorg. Chem.* *53*, 5392–5404.
- (16) Molphy, Z., Slator, C., Chatgililoglu, C., and Kellett, A. (2015) DNA oxidation profiles of copper phenanthrene chemical nucleases. *Front. Chem.* *3*.
- (17) Kellett, A., Howe, O., O'Connor, M., McCann, M., Creaven, B. S., McClean, S., Foltyn-Arfa

- Kia, A., Casey, A., and Devereux, M. (2012) Radical-induced DNA damage by cytotoxic square-planar copper(II) complexes incorporating o-phthalate and 1,10-phenanthroline or 2,2'-bipyridyl. *Free Radical Biology and Medicine* 53, 564–576.
- (18) Halliwell, B., and Whiteman, M. (2004) Measuring reactive species and oxidative damage in vivo and in cell culture: how should you do it and what do the results mean? *British Journal of Pharmacology* 142, 231–255.
- (19) Bonner, W. M., Redon, C. E., Dickey, J. S., Nakamura, A. J., Sedelnikova, O. A., Solier, S., and Pommier, Y. (2008) GammaH2AX and cancer. *Nature Reviews Cancer* 8, 957–967.
- (20) Rogakou, E. P., Pilch, D. R., Orr, A. H., Ivanova, V. S., and Bonner, W. M. (1998) DNA Double-stranded Breaks Induce Histone H2AX Phosphorylation on Serine 139. *J. Biol. Chem.* 273, 5858–5868.
- (21) Paull, T. T., Rogakou, E. P., Yamazaki, V., Kirchgessner, C. U., Gellert, M., and Bonner, W. M. (2000) A critical role for histone H2AX in recruitment of repair factors to nuclear foci after DNA damage. *Curr. Biol.* 10, 886–895.
- (22) Jackson, S. P. (2002) Sensing and repairing DNA double-strand breaks. *Carcinogenesis* 23, 687–696.
- (23) Shoemaker, R. H. (2006) The NCI60 human tumour cell line anticancer drug screen. *Nature Reviews Cancer* 6, 813–823.
- (24) Hills, C. A., Kelland, L., Abel, G., Siracky, J., Wilson, A. P., and Harrap, K. R. (1989) Biological properties of ten human ovarian carcinoma cell lines: calibration *in vitro* against four platinum complexes. *British Journal of Cancer* 527–534.
- (25) Beaufort, C. M., Helmijr, J. C. A., Piskorz, A. M., Hoogstraat, M., Ruigrok-Ritstier, K., Besselink, N., Murtaza, M., van IJcken, W. F. J., Heine, A. A. J., Smid, M., Koudijs, M. J., Brenton, J. D., Berns, E. M. J. J., and Helleman, J. (2014) Ovarian cancer cell line panel (OCCP): clinical importance of *in vitro* morphological subtypes. *PLoS ONE* 9, e103988.
- (26) Sieh, W., Köbel, M., Longacre, T. A., and Bowtell, D. D. (2013) Hormone-receptor expression and ovarian cancer survival: an Ovarian Tumor Tissue Analysis consortium study. *The lancet oncology*.
- (27) Mistry, P., Kelland, L., and Swee, Y. L. (1992) Comparison of Cellular Accumulation and Cytotoxicity of Cisplatin with That of Tetraplatin and Amminedibutyratodichloro(cyclohexylamine)platinum(IV) (JM221) in Human Ovarian Carcinoma Cell Lines. *Cancer Research* 6188–6193.
- (28) Yan, X.-D., Li, M., Yuan, Y., Mao, N., and Pan, L.-Y. (2007) Biological comparison of ovarian cancer resistant cell lines to cisplatin and Taxol by two different administrations. *Oncol. Rep.* 17, 1163–1169.
- (29) Jinawath, N., Vasoontara, C., Yap, K.-L., Thiaville, M. M., Nakayama, K., Wang, T.-L., and Shih, I.-M. (2009) NAC-1, a potential stem cell pluripotency factor, contributes to paclitaxel resistance in ovarian cancer through inactivating Gadd45 pathway. *Oncogene* 28, 1941–1948.
- (30) Anglesio, M. S., Wiegand, K. C., Melnyk, N., Chow, C., Salamanca, C., Prentice, L. M., Senz, J., Yang, W., Spillman, M. A., Cochrane, D. R., Shumansky, K., Shah, S. P., Kalloger, S. E., and Huntsman, D. G. (2013) Type-specific cell line models for type-specific ovarian cancer research. *PLoS ONE* 8, e72162.
- (31) Yaginuma, Y., and Westphal, H. (1992) Abnormal structure and expression of the p53 gene in human ovarian carcinoma cell lines. *Cancer Research* 52, 4196–4199.
- (32) Hagopian, G. S., Mills, G. B., Khokhar, A. R., Bast, R. C., and Siddik, Z. H. (1999) Expression of p53 in cisplatin-resistant ovarian cancer cell lines: modulation with the novel platinum analogue (1R, 2R-diaminocyclohexane)(trans-diacetato)(dichloro)-platinum(IV). *Clinical*

*Cancer Research* 5, 655–663.

- (33) Lau, K. M., Mok, S. C., and Ho, S. M. (1999) Expression of human estrogen receptor- $\alpha$  and - $\beta$ , progesterone receptor, and androgen receptor mRNA in normal and malignant ovarian epithelial cells. *Proc. Natl. Acad. Sci. U.S.A.* 96, 5722–5727.
- (34) Hua, W., Christianson, T., Rougeot, C., Rochefort, H., and Clinton, G. M. (1995) SKOV3 ovarian carcinoma cells have functional estrogen receptor but are growth-resistant to estrogen and antiestrogens. *J. Steroid Biochem. Mol. Biol.* 55, 279–289.
- (35) O'Donnell, A. J. M., Macleod, K. G., Burns, D. J., Smyth, J. F., and Langdon, S. P. (2005) Estrogen receptor- $\alpha$  mediates gene expression changes and growth response in ovarian cancer cells exposed to estrogen. *Endocrine Related Cancer* 12, 851–866.
- (36) Verhoven, B., Schlegel, R. A., and Williamson, P. (1995) Mechanisms of phosphatidylserine exposure, a phagocyte recognition signal, on apoptotic T lymphocytes. *J Exp Med* 182, 1597–1601.
- (37) Koopman, G., Reutelingsperger, C. P., Kuijten, G. A., Keehnen, R. M., Pals, S. T., and van Oers, M. H. (1994) Annexin V for flow cytometric detection of phosphatidylserine expression on B cells undergoing apoptosis. *Blood* 84, 1415–1420.
- (38) Boatright, K. M., and Salvesen, G. S. (2003) Mechanisms of caspase activation. *Current Opinion in Cell Biology* 15, 725–731.
- (39) Degterev, A., Boyd, M., and Yuan, J. (2003) A decade of caspases. *Oncogene* 22, 8543–8567.
- (40) Hengartner, M. O. (2000) The biochemistry of apoptosis. *Nature* 407, 770–776.
- (41) Ly, J. D., Grubb, D. R., and Lawen, A. (2003) The mitochondrial membrane potential ( $\Delta\psi(m)$ ) in apoptosis; an update. *Apoptosis* 8, 115–128.
- (42) Gottlieb, E., Armour, S. M., Harris, M. H., and Thompson, C. B. (2003) Mitochondrial membrane potential regulates matrix configuration and cytochrome c release during apoptosis. *Cell Death Differ* 10, 709–717.
- (43) Burkhardt, J. K., and Argon, Y. (1989) Intracellular transport of the glycoprotein of VSV is inhibited by CCCP at a late stage of post-translational processing. *J. Cell. Sci.* 92 (Pt 4), 633–642.
- (44) Benz, R., and McLaughlin, S. (1983) The molecular mechanism of action of the proton ionophore FCCP (carbonylcyanide p-trifluoromethoxyphenylhydrazone). *Biophysical Journal* 41, 381–398.
- (45) Burden, D. A., and Osheroff, N. (1998) Mechanism of action of eukaryotic topoisomerase II and drugs targeted to the enzyme. *Biochim. Biophys. Acta* 1400, 139–154.
- (46) Sinha, B. K., Trush, M. A., Kennedy, K. A., and Mimnaugh, E. G. (1984) Enzymatic activation and binding of adriamycin to nuclear DNA. *Cancer Research* 44, 2892–2896.
- (47) Gewirtz, D. (1999) A critical evaluation of the mechanisms of action proposed for the antitumor effects of the anthracycline antibiotics adriamycin and daunorubicin. *Biochem. Pharmacol.* 57, 727–741.
- (48) Fornari, F. A., Randolph, J. K., Yalowich, J. C., Ritke, M. K., and Gewirtz, D. A. (1994) Interference by doxorubicin with DNA unwinding in MCF-7 breast tumor cells. *Mol. Pharmacol.* 45, 649–656.
- (49) Meriwether, W. D., and Bachur, N. R. (1972) Inhibition of DNA and RNA metabolism by daunorubicin and adriamycin in L1210 mouse leukemia. *Cancer Research* 32, 1137–1142.
- (50) Goodman, M. F., Bessman, M. J., and Bachur, N. R. (1974) Adriamycin and daunorubicin inhibition of mutant T4 DNA polymerases. *Proc. Natl. Acad. Sci. U.S.A.* 71, 1193–1196.
- (51) Bachur, N. R., Gordon, S. L., and Gee, M. V. (1978) A general mechanism for microsomal activation of quinone anticancer agents to free radicals. *Cancer Research* 38, 1745–1750.
- (52) Bates, D. A., and Winterbourn, C. C. (1982) Deoxyribose breakdown by the adriamycin semiquinone and H<sub>2</sub>O<sub>2</sub>: evidence for hydroxyl radical participation. *FEBS Letters* 145, 137–142.
- (53) Muindi, J. R., Sinha, B. K., Gianni, L., and Myers, C. E. (1984) Hydroxyl radical production

- and DNA damage induced by anthracycline-iron complex. *FEBS Letters* 172, 226–230.
- (54) Hrelia, S., Fiorentini, D., Maraldi, T., Angeloni, C., Bordoni, A., Biagi, P. L., and Hakim, G. (2002) Doxorubicin induces early lipid peroxidation associated with changes in glucose transport in cultured cardiomyocytes. *Biochim. Biophys. Acta* 1567, 150–156.
- (55) Holmgren, G., Synnergren, J., Bogestål, Y., Améen, C., Åkesson, K., Holmgren, S., Lindahl, A., and Sartipy, P. (2015) Identification of novel biomarkers for doxorubicin-induced toxicity in human cardiomyocytes derived from pluripotent stem cells. *Toxicology* 328, 102–111.
- (56) Minotti, G., Cairo, G., and Monti, E. (1999) Role of iron in anthracycline cardiotoxicity: new tunes for an old song? *FASEB J.* 13, 199–212.
- (57) Boyd, M., and Paull, K. (1995) Some Practical Considerations and Applications of the National Cancer Institute In Vitro Anticancer Drug Discovery Screen. *Drug Development Research* 91–109.
- (58) Poli, G., Guasti, D., Rapizzi, E., Fucci, R., Canu, L., Bandini, A., Cini, N., Bani, D., Mannelli, M., and Luconi, M. (2013) Morphofunctional effects of mitotane on mitochondria in human adrenocortical cancer cells. *Endocrine Related Cancer* 20, 537–550.
- (59) Lehmann, T. P., Wrzesiński, T., and Jagodziński, P. P. (2013) The effect of mitotane on viability, steroidogenesis and gene expression in NCI-H295R adrenocortical cells. *Mol Med Report* 7, 893–900.
- (60) Wood, A. J. J., and Osborne, C. K. (1998) Tamoxifen in the Treatment of Breast Cancer. *N Engl J Med* 339, 1609–1618.
- (61) Dorn, D. C., Kou, C. A., Png, K. J., and Moore, M. A. S. (2009) The effect of cantharidins on leukemic stem cells. *Int. J. Cancer* 124, 2186–2199.
- (62) LA, W., W, M., E, M., W, K., and H, R. (2003) In vitro anti-proliferation/cytotoxic activity of cantharidin (Spanish Fly) and related derivatives. *West Indian Med J* 52, 10–13.
- (63) Peng, F., Wei, Y. Q., Tian, L., Yang, L., Zhao, X., Lu, Y., Mao, Y. Q., Kan, B., Lei, S., Wang, G. S., Jiang, Y., Wang, Q. R., Luo, F., Zou, L. Q., and Liu, J. Y. (2002) Induction of apoptosis by norcantharidin in human colorectal carcinoma cell lines: involvement of the CD95 receptor/ligand. *J Cancer Res Clin Oncol* 128, 223–230.
- (64) Huan, S. K.-H., Lee, H.-H., Liu, D.-Z., Wu, C.-C., and Wang, C.-C. (2006) Cantharidin-induced cytotoxicity and cyclooxygenase 2 expression in human bladder carcinoma cell line. *Toxicology* 223, 136–143.
- (65) Huh, J.-E., Kang, K.-S., Chae, C., Kim, H.-M., Ahn, K.-S., and Kim, S.-H. (2004) Roles of p38 and JNK mitogen-activated protein kinase pathways during cantharidin-induced apoptosis in U937 cells. *Biochem. Pharmacol.* 67, 1811–1818.
- (66) Chen, Y. N., Chen, J. C., Yin, S. C., Wang, G. S., Tsauer, W., Hsu, S. F., and Hsu, S. L. (2002) Effector mechanisms of norcantharidin - induced mitotic arrest and apoptosis in human hepatoma cells. *Int. J. Cancer* 100, 158–165.
- (67) Goodisman, J., Reh fuss, R., Ward, B., and Dabrowiak, J. C. (1992) Site-specific binding constants for actinomycin D on DNA determined from footprinting studies. *Biochemistry* 31, 1046–1058.
- (68) Zimmer, C., Marck, C., Schneider, C., and Guschlbauer, W. (1979) Influence of nucleotide sequence on dA.dT-specific binding of Netropsin to double stranded DNA. *Nucleic Acids Res.* 6, 2831–2837.
- (69) Taiwo, F. A. (2008) Mechanism of tiron as scavenger of superoxide ions and free electrons. *Journal of Spectroscopy* 22, 491–498.
- (70) Kiss, T., Sovago, I., and Martin, R. B. (1989) Complexes of 3, 4-dihydroxyphenyl derivatives. 9. Aluminum (3+) binding to catecholamines and tiron. *Journal of the American Chemical ...* 111,

3611–3614.

- (71) Franco, R., Panayiotidis, M. I., and Cidlowski, J. A. (2007) Glutathione Depletion Is Necessary for Apoptosis in Lymphoid Cells Independent of Reactive Oxygen Species Formation. *J. Biol. Chem.* 282, 30452–30465.
- (72) Mazzer, P. A., Maurmann, L., and Bose, R. N. (2007) Mechanisms of DNA damage and insight into mutations by chromium(VI) in the presence of glutathione ☆. *J. Inorg. Biochem.* 101, 44–55.
- (73) Dunand, C., Crèvecoeur, M., and Penel, C. (2007) Distribution of superoxide and hydrogen peroxide in Arabidopsis root and their influence on root development: possible interaction with peroxidases. *New Phytol* 174, 332–341.
- (74) Steffens, B., Kovalev, A., Gorb, S. N., and Sauter, M. (2012) Emerging Roots Alter Epidermal Cell Fate through Mechanical and Reactive Oxygen Species Signaling. *The Plant Cell* 24, 3296–3306.
- (75) Miyoshi, N., Ueda, M., Fuke, K., Tanimoto, Y., and Itoh, M. (1982) Lifetime of singlet oxygen and quenching by NaN 3 in mixed solvents. *Zeitschrift fur Naturforschung B* 37, 649–652.
- (76) Gutteridge, J. M., Maitt, L., and Poyer, L. (1990) Superoxide dismutase and Fenton chemistry. Reaction of ferric-EDTA complex and ferric-bipyridyl complex with hydrogen peroxide without the apparent formation of .... *Biochem. J.*
- (77) Taiwo, F. A. (2008) Mechanism of tiron as scavenger of superoxide ions and free electrons. *Journal of Spectroscopy* 22, 491–498.
- (78) Lee, Y., Zacharias, N. M., Piwnica-Worms, D., and Bhattacharya, P. K. (2014) Chemical reaction-induced multi-molecular polarization (CRIMP). *Chem. Commun.* 50, 13030–13033.
- (79) Kehrer, J. P. (2000) The Haber–Weiss reaction and mechanisms of toxicity. *Toxicology* 43–50.
- (80) Burkitt, M. J., and Mason, R. P. (1991) Direct evidence for in vivo hydroxyl-radical generation in experimental iron overload: an ESR spin-trapping investigation. *Proc. Natl. Acad. Sci. U.S.A.* 88, 8440–8444.
- (81) Fadok, V. A., Savill, J. S., Haslett, C., Bratton, D. L., Doherty, D. E., Campbell, P. A., and Henson, P. M. (1992) Different populations of macrophages use either the vitronectin receptor or the phosphatidylserine receptor to recognize and remove apoptotic cells. *J. Immunol.* 149, 4029–4035.
- (82) Andree, H. A., Reutelingsperger, C. P., Hauptmann, R., Hemker, H. C., Hermens, W. T., and Willems, G. M. (1990) Binding of vascular anticoagulant alpha (VAC alpha) to planar phospholipid bilayers. *J. Biol. Chem.* 265, 4923–4928.
- (83) Wood, B. L., Gibson, D. F., and Tait, J. F. (1996) Increased erythrocyte phosphatidylserine exposure in sickle cell disease: flow-cytometric measurement and clinical associations. *Blood* 88, 1873–1880.
- (84) Tait, J. F., Gibson, D., and Fujikawa, K. (1989) Phospholipid binding properties of human placental anticoagulant protein-I, a member of the lipocortin family. *J. Biol. Chem.* 264, 7944–7949.
- (85) Schmid, I., Krall, W. J., Uittenbogaart, C. H., Braun, J., and Giorgi, J. V. (1992) Dead cell discrimination with 7-amino-actinomycin D in combination with dual color immunofluorescence in single laser flow cytometry. *Cytometry* 13, 204–208.
- (86) Tait, S. W. G., and Green, D. R. (2010) Mitochondria and cell death: outer membrane permeabilization and beyond. *Nat. Rev. Mol Cell Biol.* 11, 621–632.
- (87) Riedl, S. J., and Shi, Y. (2004) Molecular mechanisms of caspase regulation during apoptosis. *Nat. Rev. Mol. Cell Biol.* 5, 897–907.

- (88) Ouyang, L., Shi, Z., Zhao, S., Wang, F. T., Zhou, T. T., Liu, B., and Bao, J. K. (2012) Programmed cell death pathways in cancer: a review of apoptosis, autophagy and programmed necrosis. *Cell Prolif.* 45, 487–498.
- (89) Degterev, A., Boyd, M., and Yuan, J. (2003) A decade of caspases. *Oncogene* 22, 8543–8567.
- (90) Elmore, S. (2007) Apoptosis: A Review of Programmed Cell Death. *Toxicol Pathol* 35, 495–516.
- (91) Nagata, S., and Golstein, P. (1995) The Fas death factor. *Science* 267, 1449–1456.
- (92) Muzio, M. (1996) FLICE, A Novel FADD-Homologous ICE/CED-3-like Protease, Is Recruited to the CD95 (Fas/APO-1) Death-Inducing Signaling Complex. *Cell* 85, 817–827.
- (93) Boldin, M. P., Goncharov, T. M., Goltsev, Y. V., and Wallach, D. (1996) Involvement of MACH, a novel MORT1/FADD-interacting protease, in Fas/APO-1- and TNF receptor-induced cell death. *Cell* 85, 803–815.
- (94) Hileman, E. A., Achanta, G., and Huang, P. (2001) Superoxide dismutase: an emerging target for cancer therapeutics. *Expert Opin. Ther. Targets* 5, 697–710.
- (95) Kang, K. S., Wang, P., Yamabe, N., Fukui, M., Jay, T., and Zhu, B. T. (2010) Docosahexaenoic Acid Induces Apoptosis in MCF-7 Cells In Vitro and In Vivo via Reactive Oxygen Species Formation and Caspase 8 Activation. *PLoS ONE* 5, e10296.
- (96) Wallach-Dayana, S. B., Izbicki, G., Cohen, P. Y., Gerstl-Golan, R., Fine, A., and Breuer, R. (2006) Bleomycin initiates apoptosis of lung epithelial cells by ROS but not by Fas/FasL pathway. *AJP: Lung Cellular and Molecular Physiology* 290, L790–L796.
- (97) Perry, S., Norman, J., Barbieri, J., Brown, E., and Gelbard, H. (2011) Mitochondrial membrane potential probes and the proton gradient: a practical usage guide. *Biotech.* 50, 98–115.
- (98) Ozaki, S., Kano, K., and Shirai, O. (2008) Electrochemical elucidation on the mechanism of uncoupling caused by hydrophobic weak acids. *Phys. Chem. Chem. Phys.* 10, 4449–4455.
- (99) Park, J.-W., Lee, S.-Y., Yang, J.-Y., Rho, H.-W., Park, B.-H., Lim, S.-N., Kim, J.-S., and Kim, H.-R. (1997) Effect of carbonyl cyanide m-chlorophenylhydrazone (CCCP) on the dimerization of lipoprotein lipase. *Biochimica et Biophysica Acta (BBA) - Lipids and Lipid Metabolism* 1344, 132–138.
- (100) Cottet-Rousselle, C., Ronot, X., Leverve, X., and Mayol, J.-F. (2011) Cytometric assessment of mitochondria using fluorescent probes. *Cytometry* 79A, 405–425.
- (101) Reers, M., Smith, T. W., and Chen, L. B. (1991) J-Aggregate formation of a carbocyanine as a quantitative fluorescent indicator of membrane potential 4480–4486.
- (102) Würthner, F., Kaiser, T. E., and Saha-Möller, C. R. (2011) J-Aggregates: From Serendipitous Discovery to Supramolecular Engineering of Functional Dye Materials. *Angew. Chem. Int. Ed.* 50, 3376–3410.
- (103) Kroemer, G., Galluzzi, L., and Brenner, C. (2007) Mitochondrial Membrane Permeabilization in Cell Death. *Physiological Reviews* 87, 99–163.
- (104) Halliwell, B., and Gutteridge, J. M. C. (1999) Free Radicals in Biology and Medicine 3rd ed. Oxford University Press, Inc., New York.
- (105) Marrache, S., Pathak, R. K., and Dhar, S. (2014) Detouring of cisplatin to access mitochondrial genome for overcoming resistance. *Proc. Natl. Acad. Sci. U.S.A.* 111, 10444–10449.
- (106) Chamberlain, G. R., Tulumello, D. V., and Kelley, S. O. (2013) Targeted delivery of doxorubicin to mitochondria. *ACS Chem. Biol.* 8, 1389–1395.
- (107) Wilson, W. D., Tanious, F. A., Barton, H. J., Jones, R. L., Fox, K., Wydra, R. L., and Strekowski, L. (1990) DNA sequence dependent binding modes of 4',6-diamidino-2-phenylindole (DAPI). *Biochemistry* 29, 8452–8461.
- (108) Estes, J. E., Selden, L. A., and Gershman, L. C. (1981) Mechanism of action of phalloidin on the polymerization of muscle actin. *Biochemistry* 20, 708–712.

- (109) Cooper, J. A. (1987) Effects of cytochalasin and phalloidin on actin. *J. Cell Biol.* 105, 1473–1478.
- (110) Shim, S. H., Xia, C., Zhong, G., Babcock, H. P., Vaughan, J. C., Huang, B., Wang, X., Xu, C., Bi, G. Q., and Zhuang, X. (2012) Super-resolution fluorescence imaging of organelles in live cells with photoswitchable membrane probes. *Proc. Natl. Acad. Sci. U.S.A.* 109, 13978–13983.
- (111) Yousif, L. F., Stewart, K. M., and Kelley, S. O. (2009) Targeting mitochondria with organelle-specific compounds: strategies and applications. *ChemBioChem* 10, 1939–1950.
- (112) Cassina, P., Cassina, A., Pehar, M., Castellanos, R., Gandelman, M., de León, A., Robinson, K. M., Mason, R. P., Beckman, J. S., Barbeito, L., and Radi, R. (2008) Mitochondrial dysfunction in SOD1G93A-bearing astrocytes promotes motor neuron degeneration: prevention by mitochondrial-targeted antioxidants. *J. Neurosci.* 28, 4115–4122.
- (113) Zhang, Z., Xu, X., Ma, J., Wu, J., Wang, Y., Zhou, R., and Han, J. (2013) Gene deletion of Gabarap enhances Nlrp3 inflammasome-dependent inflammatory responses. *J. Immunol.* 190, 3517–3524.
- (114) Kerr, J. F., Wyllie, A. H., and Currie, A. R. (1972) Apoptosis: a basic biological phenomenon with wide-ranging implications in tissue kinetics. *British Journal of Cancer* 26, 239–257.
- (115) Kerr, J. F. R., Winterford, C. M., and Harmon, B. V. (1994) Apoptosis. Its significance in cancer and cancer Therapy. *Cancer* 73, 2013–2026.
- (116) Hockenbery, D. (1995) Defining apoptosis. *The American Journal of Pathology* 146, 16.
- (117) Prisecaru, A., Molphy, Z., Kipping, R. G., Peterson, E. J., Qu, Y., Kellett, A., and Farrell, N. P. (2014) The phosphate clamp: sequence selective nucleic acid binding profiles and conformational induction of endonuclease inhibition by cationic Triplatin complexes. *Nucleic Acids Res.* gku1157.
- (118) Zhou, W., Wang, X., Hu, M., Zhu, C., and Guo, Z. (2014) A mitochondrion-targeting copper complex exhibits potent cytotoxicity against cisplatin-resistant tumor cells through multiple mechanisms of action. *Chem. Sci.* 5, 2761–2770.



## **Chapter 4**

### **Dual Targeting Di-Copper Complexes Promote NCI-60 Chemotherapy by Intracellular Superoxide and Singlet Oxygen Production**

---

Manuscript in preparation

Creina Slator, Zara Molphy, Andrew Kellett\*

Within this chapter, I was the primary contributor to all aspects of experiential design, execution, analysis and manuscript preparation. A significant proportion of my PhD research was dedicated

towards this body of work. Z. Molphy conducted circular dichroism studies. Supporting information associated with this chapter can be found in Appendix C.

## 4.1 Abstract

The therapeutic application of established cytostatic anticancer metallodrugs is limited by drug resistance issues and auxiliary undesired toxic effects. Therefore, the development of pre-clinical agents with new mechanisms of action is fundamental to meet the global demand for more advanced and sophisticated chemotherapeutics. Herein, we present a cationic *di*-copper<sup>2+</sup> complex class incorporating intercalating 1,10-phenanthroline (phen) ligands as high potency chemotherapeutic leads capable of disrupting mitochondrial function and genomic DNA integrity. The activity profile of two agents of this series, [ $\{\text{Cu}(\text{phen})_2\}_2(\mu\text{-oda})\]^{2+} (**Cu-Oda**, where oda = octanedioate) and [ $\{\text{Cu}(\text{phen})_2\}_2(\mu\text{-terph})\]^{2+} (**Cu-Terph**, where terph = terephthalate), was assessed within the National Cancer Institute's 60 human cancer cell line screen (NCI-60) where, in addition to selective toxicity toward solid epithelial cancers, a unique pattern of activity—fundamentally different from established clinical metallodrugs—was identified by the COMPARE algorithm. Both *di*-Cu<sup>2+</sup> complexes intercalate duplex DNA from the minor groove along AT rich tracts and oxidatively mediate both single and double strand breaks that were identified by immunohistochemical detection of  $\gamma\text{H2AX}$  and the alkaline comet assay. Mitochondrion function is also severely impeded resulting from free radical production of superoxide within this organelle with consequential loss of mitochondrial membrane potential ( $\Delta\Psi_m$ ) that precipitates caspase release and the formation of apoptotic bodies. The role of superoxide in the cytotoxic mechanism is strongly supported by cell survival analysis using the antioxidant trapping agent tiron, and in this study a second free radical species—singlet oxygen—was also implicated in the mechanism of toxic action. This dual pro-oxidant activity manifests radical uncoupling of mitochondrion function and genomic DNA sequence integrity and may now expedite the clinical development of a new class of antineoplastic metallodrug.$$

## 4.2 Introduction

Homeostasis of reactive oxygen species (ROS) produced from metabolic processes is essential for cell survival due to its integral role in signaling pathways.<sup>1</sup> However, elevated ROS levels have destructive effects consequent of environmental or exogenous toxic stimuli and so a critical equilibrium is maintained in biological systems through endogenous antioxidants. While the most stable form of oxygen is the inert ground-state *di*-radical ( $^3\text{O}_2$  or more commonly denoted  $\text{O}_2$ ), energy input can promote excitation to singlet oxygen ( $^1\text{O}_2$ ) that readily oxidises C-C bonds and specifically reacts at cysteine, histidine, methionine and tryptophan residues.<sup>2</sup> Intracellular production of singlet oxygen can occur from lipid peroxidation, oxidation of phenolic groups, alkoxyl radical dismutation<sup>3</sup> and cysteine oxidation via Russell-type mechanism.<sup>4</sup> Furthermore, one-electron reduction of oxygen within the electron transport chain yields superoxide ( $\text{O}_2^{\bullet-}$ )—a gateway radical that is detoxified by the superoxide dismutase (SOD)<sup>5</sup> enzyme class to hydrogen peroxide ( $\text{H}_2\text{O}_2$ ) that is, in-turn, acted upon by the enzyme catalase (CAT).<sup>2</sup> First row transition elements including copper and iron are known to decouple ROS homeostasis by redox chemistry to invoke alternative free radical reactions such as the production of the hydroxyl radical ( $\text{OH}^\bullet$ ) by Fenton chemistry or *via* superoxide-promoted hydroxyl formation by the Haber-Weiss process (Figure 1).<sup>6</sup> Given their neutrality and small molecular footprint,  $\text{OH}^\bullet$  radicals can freely diffuse biological membranes and non-discriminately oxidise lipids, proteins and nucleic acids at near diffusion-limited rates.<sup>7</sup> Accordingly, the incorporation of catalytic first-row transition metals into small molecules is now an important avenue for ROS-active drug discovery<sup>8</sup> alongside the development of more established organic free radical pro-oxidants.<sup>9</sup>

Since ROS generation occurs from a variety of pro-oxidant exogenous stimuli including chemotherapeutic drug treatment, researchers have studied the underlying mechanistic aspects of free radical production in biological environments, especially within human cancers. As such, therapeutic anthracyclines such as doxorubicin (Figure 1) and daunorubicin that, along with intercalating DNA from the major groove and poisoning topoisomerase (II), undergo redox-cycling of the quinone moiety with  $\text{O}_2$  resulting in  $\text{O}_2^{\bullet-}$  production.<sup>10</sup> Another family of antitumoral antibiotics are the enediyenes that possess an unusual bicyclic structure; these agents, in the presence of a thiol group, are converted into *di*-radical species that attack deoxyribose units of DNA and mediate strand scission.<sup>11</sup> Indeed, one of the best studied chemotherapeutics of this class is neocarzinostatin, which forms oxidative DNA lesions through hydrogen atom (H)-abstraction at accessible C5' sites by *di*-radical species orientated within the minor groove, leading directly to single strand breaks (SSBs) at thymine (T) residues.<sup>12</sup> To a lesser extent, neocarzinostatin can promote the more difficult to repair double strand breaks (DSBs) by damaging C4' thymine residues at GT and AGT steps, and also at C1' cytosine bases in AGC sequences.<sup>12</sup> Another established clinical agent to intercalate DNA through the minor groove is the naturally occurring

glycopeptide bleomycin. It is widely regarded that bleomycin exerts biologically activity upon chelation of first row transition elements (including copper and iron)<sup>13</sup> and subsequently oxidises DNA through metallo-hydroperoxo (*e.g.* bleomycin-Fe<sup>3+</sup>-OOH) causing C4' H-abstraction that precipitate SSB and DSBs.<sup>14</sup>

Given the established base of minor groove intercalating drugs to mediate DNA damage *via* redox chemistry, the current study seeks to identify the broad therapeutic potential of a *di*-copper<sup>2+</sup> complex class incorporating intercalating 1,10-phenanthroline (phen) ligands. In the 30 years since the discovery of this first chemical nuclease,<sup>15</sup> [Cu(phen)<sub>2</sub>]<sup>+</sup> has endured as an important template for the construction of small-molecule DNA damaging reagents that are widely applied as high-fidelity DNA footprinting agents and,<sup>16,17</sup> more recently, as tools in protein engineering for the generation of recombinant mutagenesis libraries.<sup>18</sup> The predominant feature of [Cu(phen)<sub>2</sub>]<sup>+</sup> and numerous analogues is their ability to mediate SSBs along AT tracts in the minor groove through oxidative C-H bond activation at accessible C1' deoxyribose positions (Figure 1).<sup>9</sup> Furthermore, previous work by our group has shown while the [Cu(phen)<sub>2</sub>] chemotype is a promising template for the construction of small molecule cytotoxins,<sup>19-22</sup> it is in itself a promiscuous agent with low therapeutic index.<sup>22</sup> Thus, while mononuclear copper phenanthroline complexes may have promising clinical properties in their own right,<sup>23</sup> polynuclear copper<sup>2+</sup> oxidative nucleases have shown an alternative profile with potent *in vitro* 'self-activated' oxidative DNA damage and nano-molar anticancer properties against selected solid epithelial human cancer cells.<sup>20,24,25</sup> In this work, we have identified two *di*-Cu<sup>2+</sup> complexes from this class, [{Cu(phen)<sub>2</sub>}<sub>2</sub>(*u*-oda)]<sup>2+</sup> (**Cu-Oda**) and [{Cu(phen)<sub>2</sub>}<sub>2</sub>(*u*-terph)]<sup>2+</sup> (**Cu-Terph**) (Figure 2A and B), as high potential therapeutic leads for the treatment of solid human cancers and uncovered their capacity to invoke a unique—and therapeutically distinct—pro-oxidant profile that uncouples mitochondrial function and mediates double strand breaks (DSBs) within genomic DNA. While both **Cu-Oda** and **Cu-Terph** complexes have shown potent *in vitro* DNA damaging profiles compared with mono-Cu<sup>+</sup> analogues, a large question remains unanswered regarding their clinical potential and cellular mode of action in the context of redox chemical biology. On this basis, we have collaborated with the National Cancer Institute through their 60 human cancer cell line screen (NCI-60) and accessed the COMPARE algorithm in the Developmental Therapeutic Program (DTP) to identify the utility of these complexes in comparison to clinically applied agents. Additionally, this contribution further explores the cytotoxic mechanism underpinning the *di*-Cu<sup>2+</sup> agents by examining their nucleic acid targeting properties, modulation of intracellular free radical content, probing mitochondrial function along with nuclear DNA integrity, and classifying cellular death mechanisms in comparison to established DNA damaging drug controls.

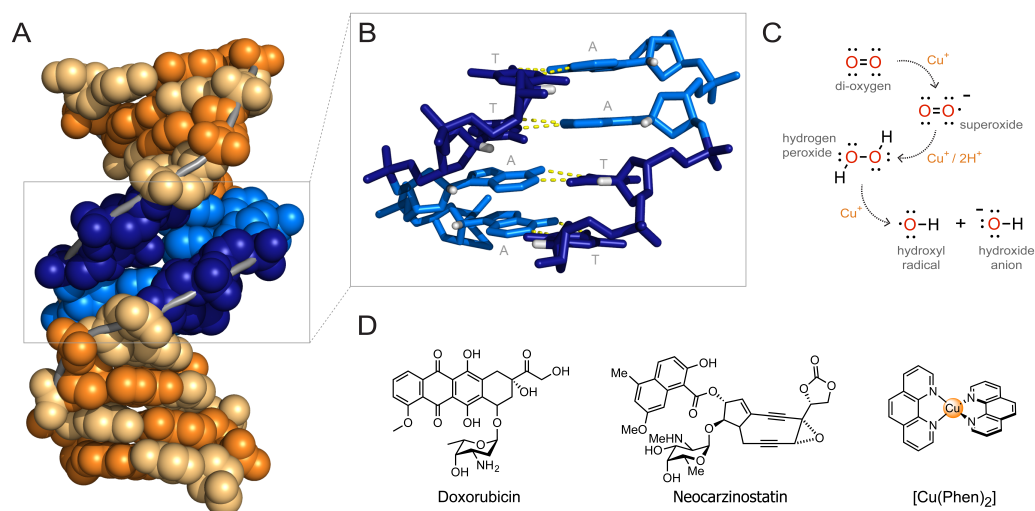


**Figure 4. 1** **A.** Structure of the B-DNA Dickerson-Drew dodecamer (DDD)  $d[\text{CGCGAATTCGCG}]_2$  positioned from the minor groove (PDB entry 1BNA). DNA backbone (connecting P positions), gray60; colour code for DNA bases: guanine, orange; cytosine, light orange; adenine, slate; thymine, density (cartoon mode, bases shown as spheres). **B.** Inset structure of the AATT minor groove tract with accessible C1' deoxyribose hydrogens shown (H, white) along with Watson-Crick H-bonding pairs (yellow dashes). Colour code for DNA bases: adenine, slate; thymine, density (shown as sticks). Figure A and B generated by PyMOL Molecular Graphics System, Version 1.5.0.4 Schrödinger, LLC. **C.**  $\text{Cu}^+$  mediated electron transfer reactions: a cascade of reactive oxygen species (ROS) proceeds from molecular oxygen undergoing 1-electron reduction to superoxide, followed then by dismutation to hydrogen peroxide (and oxygen - not shown), and finally Fenton-like reduction to the hydroxyl radical. **D.** Structures of the major groove binder doxorubicin, and minor groove targeting compounds neocarzinostatin and  $[\text{Cu}(1,10\text{-phenanthroline})_2]^+$ .

## 4.3 Methods

### 4.3.1 Materials and Reagents

All chemicals used for complex synthesis were purchased from Sigma Aldrich without further purification. The following assays were purchased from Merck Millipore and procedures were followed as per manufacturer protocol: Guava Nexin® Reagent (4500-0450), Guava EasyCyte™ MitoPotential Kit (4500-0250), Guava Caspase 8 FAM and Caspase 9 SR (4500-0640) and Guava Caspase 3/7 (4500-0540). Propidium iodide (BTIU40017) was purchased from VWR. Carbonyl cyanide *m*-chlorophenylhydrazone (10175140), calf thymus DNA (15633-019), RNase A (12091-021), Alexa Flour 488 goat anti-mouse IgG F(ab)<sub>2</sub> fragment (A11020), Alexa flour 488-phalloidin (A12379), DAPI (D1306) and Mitotracker Deep Red (M22426) were purchased from ThermoFisher Scientific. Anti-phospho-histone H2AX (05-636) was purchased from Merck Millipore. Doxorubicin hydrochloride (D2975000), salmon testes DNA (D1626), synthetic double stranded alternating co-polymers, poly[d(G · C)<sub>2</sub>] (P9389) and poly[d(A · T)<sub>2</sub>] (P0883) and *Micrococcus Lysodeikticus* (D8259) were purchased from Sigma Aldrich. pUC19 plasmid DNA (N3041), CutSmart® buffer (B7204), 100X BSA (B9000) and topoisomerase I (E. coli) (M0301) were all purchased from New England Biolabs.

### 4.3.2 Preparation of complexes

[{Cu(phen)<sub>2</sub>}<sub>2</sub>(μ-octanedioate)](ClO<sub>4</sub>)<sub>2</sub> was prepared according to procedures reported by Devereux *et al.*<sup>26</sup> Mononuclear [Cu(μ-octanedioate)(phen)<sub>2</sub>]<sup>27</sup> was dissolved in an ethanolic solution of sodium perchlorate and refluxed under very mild conditions to form a light blue precipitate that was recrystallised in ethanol:water (1:1) to yield dark blue crystals.<sup>26</sup> [{Cu(phen)<sub>2</sub>}<sub>2</sub>(μ-terephthalate)](terephthalate) was prepared by ethanolic reflux of copper(II) terephthalate hydrate and phen in a 1:2 ratio according to reported methods by Kellett *et al.*<sup>20</sup>

### 4.3.3 NCI-60 analysis

The *di*-copper agents, **Cu-Oda** and **Cu-Terph** were submitted to the National Cancer Institute (NCI) Developmental Therapeutics Program (DTP) where their cytotoxicity profile was investigated across the 60 human cancer cell line panel according to Sulforhodamine B protocol (also available at [https://dtp.cancer.gov/discovery\\_development/nci-60/default.htm](https://dtp.cancer.gov/discovery_development/nci-60/default.htm)).<sup>28,29</sup> The COMPARE algorithm ([https://dtp.cancer.gov/databases\\_tools/compare.htm](https://dtp.cancer.gov/databases_tools/compare.htm)) was utilised to evaluate the activity profile of **Cu-Oda** and **Cu-Terph** in comparison to known cytotoxins established in marketed drugs, mechanistic and standard agent datasets in order to correlate plausible modes of action. Criteria were set so that Pearson correlation coefficients (*r*) were >0.2 in a minimum of 40 common cell lines with standard deviation of 0.05.

#### 4.3.4 Topoisomerase Inhibition

The topoisomerase I relaxation assay was carried out using a modified method to previously reported protocols.<sup>30</sup> 400 ng of pUC19 plasmid DNA was exposed to varying concentrations of drug (0.1 - 400  $\mu$ M) for 30 min at room temperature in a final volume of 20  $\mu$ l containing 80 mM HEPES buffer (pH 7.2), CutSmart® buffer and 100X BSA. Topoisomerase I (1 unit) was added to the mixture and incubated for 15 min at 37 °C to ensure relaxation of plasmid DNA. The enzymatic reaction was quenched with SDS (0.25%), protein kinase (250  $\mu$ g/ml) and 30 min incubation at 50 °C. Samples were loaded onto 1.2% agarose gel with 6X loading buffer. Topoisomers of DNA were separated by electrophoresis in 1X TBE buffer at room temperature 40 V (3 h) followed by 50 V (2.5 h). The agarose gel was post-stained using an ethidium bromide bath (25  $\mu$ M) for 20 min at room temperature. Finally, the gel was soaked in deionised water for 24 h and imaged using a UV transilluminator.

#### 4.3.5 DNA binding

Calf thymus DNA, artificial double stranded (ds) alternating copolymers poly[d(G·C)<sub>2</sub>] and poly[d(A·T)<sub>2</sub>] and DNA extracted from *Micrococcus Lysodeikticus* were used to investigate DNA binding properties of **Cu-Oda** and **Cu-Terph** on sequences containing varying AT content. Experiments were conducted in an identical manner to those recently reported by Kellett *et al.*<sup>31</sup> Briefly, samples were prepared in 96 plates format with complex concentrations between 1.0 - 150  $\mu$ M, 12.6  $\mu$ M EtBr, 20 mM NaCl and 10  $\mu$ M of dsDNA sequences to a final volume of 100  $\mu$ l and analysed using a Bio-Tek, Synergy HT fluorescent microplate reader with data collection using Gen5 software. A  $C_{50}$  value—the concentration required to reduce ethidium bromide fluorescence by 50%—was used to calculate apparent DNA binding constants ( $K_{app}$ );  $K_{app} = K_e \times 12.6/C_{50}$  where  $K_e = 9.5 \times 10^6$  M (bp)<sup>-1</sup>.

#### 4.3.6 Circular dichroism spectrometry

Complex-DNA interactions were analysed within Starna quartz cuvettes in 10 mM PBS solution (pH 7.0) in the presence of 25 mM NaCl. Solutions of salmon testes DNA (stDNA,  $\epsilon_{260} = 12824$  M(bp)<sup>-1</sup> cm<sup>-1</sup>), poly[(d(A·T)<sub>2</sub>] ( $\epsilon_{260} = 13100$  M(bp)<sup>-1</sup> cm<sup>-1</sup>) and poly[(d(G·C)<sub>2</sub>] ( $\epsilon_{260} = 16800$  M(bp)<sup>-1</sup> cm<sup>-1</sup>) were initially denatured by heat treatment and then allowed to slowly renature prior to quantification using an Agilent Cary 100 dual beam spectrophotometer equipped with a 6 × 6 Peltier multicell system with temperature controller, to give working solutions with a final DNA concentration of ~100  $\mu$ M. Spectra were captured in the range of 200-400 nm and measurements were recorded at a rate of 1 nm per second. DNA solutions were incubated for 30 min periods at 37 °C with **Cu-Oda** at varying  $r$  loading values ( $r = [\text{drug}]/[\text{DNA}]$   $\mu$ M) of 0.010, 0.025, 0.050 and

0.075. **Cu-Terph** DNA interactions were not investigated within this study due to solubility issues in CD assessable solvents.

#### 4.3.7 Cell Culture

SKOV3 cells were cultured in RPMI-1640 media, supplemented with 10% FBS and incubated at 37 °C in 5% CO<sub>2</sub> and routinely tested for mycoplasma. Cells were seeded and left to adhere and enter cell cycle (> 12 h) prior to complex exposure. **Cu-Oda**, **Cu-Terph** and carbonyl cyanide *m*-chlorophenyl hydrazone (CCCP) stock solutions were prepared in DMSO with Doxorubicin (Dox) in 50:50 DMSO:H<sub>2</sub>O and further dilutions prepared in culture media daily. Stocks containing DMSO were prepared in the mM range to ensure final incubation concentrations did not exceed 0.1% v/v.

#### 4.3.8 Cellular Viability

SKOV3 cells were seeded at  $5 \times 10^3$  cells in a 96-well plate and exposed to drug treatment for 24 h with dinuclear complexes (0.5, 1.0, and 2.0  $\mu$ M), Dox (1.0  $\mu$ M) or CCCP (75  $\mu$ M). For co-treatment experiments, antioxidants Tiron (4,5-Dihydroxy-1,3-benzenedisulfonic acid disodium salt), D-mannitol (Man), L-histidine (His), ( $\pm$ )- $\alpha$ -lipoic acid (Lip), taurine (2-aminoethanesulfonic acid, Taur), L-methionine (Met) and sodium pyruvate (Py) were treated at 1 mM for 2 h prior to drug exposure to facilitate intracellular accumulation. Spent media was removed, cells were detached with trypsin:EDTA (0.25%:0.02% in PBS) and whole samples (100  $\mu$ l) were added to 100  $\mu$ l Guava Viacount reagent and incubated for 10 min at room temperature. Viability samples were acquired on Guava EasyCyte HT with Viacount software.

#### 4.3.9 Cell Cycle analysis

Cellular DNA content was examined in a similar manner to previously reported methods.<sup>32</sup> SKOV3 cells ( $3 \times 10^4$  cell/well) were seeded in 24-well culture plates, drug treated and collected in 1.5 ml microtubes. Cells were fixed in 70% ice-cold EtOH and stored at -20°C (>12 h). Samples were then stained with 200  $\mu$ l of a propidium iodide (PI) staining solution (50  $\mu$ g/ml PI, 100  $\mu$ g/ml DNase-free RNase A, 0.1% triton X-100 in 1X PBS) for 30 min at room temperature. Samples were acquired on Guava EasyCyte HT flow cytometer and normalised to the sum events in G<sub>0</sub>/G<sub>1</sub>, S and G<sub>2</sub>/M phases.

#### 4.3.10 Immunodection of DSBs

Samples were prepared similarly to previously reported methods.<sup>33</sup>  $6 \times 10^4$  cells were seeded in 12-well plates and treated with complexes and Dox for 24 h. Transferred samples in 1.5 ml microtubes were fixed with 1.5% formaldehyde (15 min, room temperature) followed by ice-cold 70% ethanol and stored at -20 °C. Samples were resuspended in permeabilisation buffer (0.25% Triton X-100 in



PBS) for 30 min on ice and blocked with 2% BSA (30 min, room temperature). The primary antibody (1:500) was incubated for 2 h at room temperature followed by secondary antibody (1:1000) for 1 h at room temperature and co-stained for 10 min with 5 µg/ml of propidium iodide. Samples were acquired using ExpressPro software on the Guava EasyCyte instrument.

#### **4.3.11 DNA degradation with comet assay**

Cells were seeded overnight at  $1.5 \times 10^5$  cells/well in 6-well plates prior to drug addition. After 24 h of drug incubation, cells were harvested and 50 µl was resuspended in 500 µl low melting point agarose to give a final density of  $1.5 \times 10^5$  cell/ml. 50 µl of this was spread onto Trevigen Comet slides and allowed to solidify for 1 h at 4 °C. Samples were lysed in a coplin jar (2.5 M NaCl, 100 mM EDTA, 10 mM Tris·HCl, pH 10) overnight at 4 °C.<sup>34</sup> Slides were allowed to equilibrate in cold electrophoresis buffer (300 mM NaOH, 1.0 mM EDTA, pH 13) for 30 mins at 4°C prior to electrophoresis run at 300 mA for 30 min with buffer levels adjusted to give a consistent voltage of 25 V. Slides were then washed with water, neutralised in buffer (400 mM Tris.HCl, pH 7.5), fixed with 70% ethanol (30 min) and dried for desiccated storage. Prior to scoring, slides were rehydrated for 15 min before staining with a PI solution (10 µg/ml, 10 min) and imaged through a 10× lens and Leica DFC 500 epi-fluorescent microscope. Images were then analysed with Open Comet plugin on Image J.

#### **4.3.12 Nexin® Assay**

SKOV3 cells were seeded at  $3 \times 10^4$  cells in 24-well plates and incubated with drug containing media. After the exposure period, spent media was removed, cells were washed with PBS and washings were kept in 1.5 ml microtubes. Cells were detached with trypsin, neutralised with fresh media, transferred to microtubes with PBS and centrifuged at 1300 rpm for 5 min. A sufficient volume of media was added to cell pellet for densities ranging from  $2 \times 10^5$  to  $1 \times 10^6$  cell/ml. 100 µl of sample was transferred to 96-well round bottom plate, containing 100 µl of Guava Nexin® Reagent and incubated for 20 min at room temperature. Samples were acquired on the Guava EasyCyte HT flow cytometer using Nexin software. Inherent doxorubicin fluorescence in filter 583/26 nm was accounted for and subtracted within the relevant quadrants.

#### **4.3.13 Caspase 8 FAM and 9 SR, Caspase 3/7 FAM**

The following fluorescent labelled inhibitors of caspase (FLICA) were used to ascertain the activation of caspase 3/7, 8 and 9 respectively; FAM-DEVD-FMK, FAM-LETD-FMK and SR-LEHD-FMK. Samples were prepared prior to staining in a similar manner as that described in the Nexin Assay. Cells were transferred to 1.5 ml microtubes and resuspended in 100 µl media. 10 µl of 10X caspase 9 SR working solution and 10 µl of caspase 8 FAM were added and incubated for 1 h at 37 °C. Cells were resuspended in 200 µl of caspase 7-aminoactinomycin D (7-AAD) working

solution and transferred to 96-well round bottom plate, which was left to incubate for 10 min at room temperature. Samples were acquired on the Guava EasyCyte HT flow cytometer using Guava Caspase software. Compensation to correct fluorescent overlap between filters was conducted pre-acquisition and innate doxorubicin fluorescence in filter 583/26 nm was accounted for within the relevant quadrants.

#### **4.3.14 Confocal Microscopy**

Cells ( $1.4 \times 10^5$ ) were seeded in 35 mm glass bottom petri dishes and exposed to drug for 24 h. Cells were incubated with media containing MitoTracker Deep Red (150 mM, 30 min, 37°C) and fixed with 4% paraformaldehyde (30 min, room temperature). Samples were permeabilised with 0.25% Triton X-100 (15 min). To avoid non-specific staining, cells were blocked with 1% BSA in PBS (30 min, 37 °C) and subsequently stained with Alexa Flour 488-phalloidin (10U/100ul, 30 min), followed by DAPI (4:10,000, 10 min) and mounted in ProLong Gold. Images were acquired on a STED-Leica DMI8 super resolution confocal microscope equipped with CCD camera and 100× oil-immersion objective. DAPI was excited with a 405 nm picoquant laser unit and emission captured between 387 - 474 nm. Alexa Fluor 488 was excited at 499 nm with emission captured between 490 - 566 nm, and MitoTracker Deep Red was excited at 653 nm where emission was captured at 658 - 779 nm. Images were acquired whereby combinations of excitation wavelengths and emission filters for specific dyes are applied sequentially.

#### **4.3.15 Mitochondrial Membrane Potential**

Cells were treated as previously described in the Nexin V assay. Samples were resuspended in 600 µl of fresh media to give cell concentration  $2 \times 10^4$  to  $5 \times 10^5$  cells/ml from which 200 µl was transferred to a 96-well round bottom plate. 50X staining solution (4 µl) containing JC-1 and 7-AAD was added to each sample, subsequently incubated at 37 °C in darkness (30 min) and acquired on Guava EasyCyte HT using MitoPotential software. Compensation to correct fluorescent overlap between filters was conducted pre-acquisition.

#### **4.3.16 Mitochondrial Superoxide (MitoSOX) Detection**

SKOV3 cells ( $6 \times 10^4$ ) were seeded in 12-well plates. After drug treatment, samples were harvested, washed with PBS, resuspended in 200 µl of 5.0 µM MitoSOX Red in PBS and left to incubate for 15 min at 37 °C. Samples were then resuspended in PBS and transferred to 96-well round bottom plates, and acquired on Guava EasyCyte flow cytometer using ExpressPro software.

#### **4.3.17 Statistical Analysis**

Data collected from intracellular and DNA binding experiments are presented as mean  $\pm$  S.D. ( $n = 3$ ) and plotted in GraphPad Prism V6.0. Comparisons between the data were analysed with two-

way ANOVAs in GraphPad Prism V6.0. Differences between means were analysed post-hoc with Dunnett's test at 95% confidence level. Differences between the groups were considered to be statistically significant if  $p \leq 0.05$ .

## 4.4 Results and Discussion

### 4.4.1 NCI-60 analysis

The *di*-copper complexes investigated within this study were submitted to the National Cancer Institute (NCI) Developmental Therapeutics Program (DTP) for cell line screening based upon previously identified anticancer potential within a small cancer panel.<sup>20,24</sup> The NCI screen consists of 60 human cancer cell lines from a variety of cancer origins including breast, colon, central nervous system (CNS), leukaemia, non-small cell lung (NSCL), melanoma, ovarian, prostate and renal.<sup>28,35</sup> Following one-dose cytotoxicity analysis, both complexes were eligible to proceed to five-dose analysis assessing 50% growth inhibition (GI<sub>50</sub>), cytotoxic or lethal effect (50% lethal dose, LC<sub>50</sub>) and cytostatic effect (total growth inhibition, TGI)<sup>28</sup> (Table S1). Visual representations of GI<sub>50</sub> concentrations are displayed in the form of a heat map in Figure S2, with an extensive range of growth inhibitory effects visible from 5 µM to less than 100 nM. Cancer lines from all lineages displayed significant sensitivity to **Cu-Terph**, as the entire panel exhibited growth inhibitions less than 500 nM. Exceptional activity was noted within the melanoma cell line, SK-MEL-5, with a GI<sub>50</sub> value of 49 nM. **Cu-Oda**, however, displayed higher GI<sub>50</sub> result of less than 5 µM with a 10-fold universal decrease in activity compared to **Cu-Terph**, with particular sensitivity noted in melanoma and renal cancers. LC<sub>50</sub> concentrations, indicating the extent of complex lethality, were also identified and are shown in heat map form in Figure 2C. In agreement with the growth inhibition results, **Cu-Terph** displayed enhanced cytotoxic effects across the majority of cell lines within the panel (< 1 µM) with increasing toxic towards CNS, colon and ovarian cancer types and hypersensitivity in SK-MEL-5. **Cu-Oda** had varying activities in colon carcinoma and ovarian adenocarcinomas and was most effective in melanoma, renal and prostate cancers with all LC<sub>50</sub> concentrations being less than 10 µM. Interestingly, leukemic cell lines were particularly resistant to both *di*-Cu<sup>2+</sup> complexes, where lethal concentrations are in excess of 100 µM, with the exception of CCRF-CEM (50 µM) for **Cu-Oda**. Results here suggest both compounds have high potential utility and selectivity for solid neoplasias but limited toxicity towards leukaemia, lymphoma, myeloma or bone sarcomas.

Five-dose activity profiles for both compounds were entered into the COMPARE algorithm supplied by the NCI.<sup>36</sup> This algorithm is an automated comparison programme that associates the pattern of activity of all or selected cancer cell lines within the panel to standards and mechanistic agents, or marketed drugs, many of which have known mechanisms of cytotoxicity. The comparative results are represented as Pearson correlation coefficients (PPC), or *r* values, ranging from -1 to +1, where a seed (**Cu-Oda** or **Cu-Terph**) threshold of >0.20 was considered for comparative analysis to compounds of known activity (*i.e.* clinical standards) for potential mechanism of action. Limited comparisons of growth inhibition profiles (GI<sub>50</sub>) were observed in

the COMPARE algorithm for both tested agents (Table S2). Studies utilising the this algorithm for mode of action comparatives generally consider  $GI_{50}$   $r$  values of  $>0.50$  as a significant correlation,<sup>37-39</sup> thus demonstrating a highly unique profile for both  $di-Cu^{2+}$  complexes where  $r$  values were unanimously  $<0.5$ . As such, we used  $LC_{50}$  values for comparative analysis categorised between signalling, antimetabolites, DNA damaging, hormonal and tubulin targeting agents, and topoisomerase poisons, along with a selection of miscellaneous or undefined therapeutics. From a total of  $\sim 175$  standard agents analysed through COMPARE, the highest  $r$  values common for both compounds ranged between 0.84 - 0.20 (Figure 2D). Uppermost values found were hormonal agents, however, the greatest number of correlations appeared for DNA damaging agents. Furthermore, both copper complexes had a very low activity profile in comparison with cisplatin, where  $r$  values of 0.26 and 0.33 for **Cu-Oda** and **Cu-Terph** were respectively found. Finally, metallodrugs such as bleomycin and alternative platinum agents (carboplatin, oxaliplatin) did not show comparative analysis within the criterion threshold, demonstrating the novelty of this  $di-Cu^{2+}$  class.

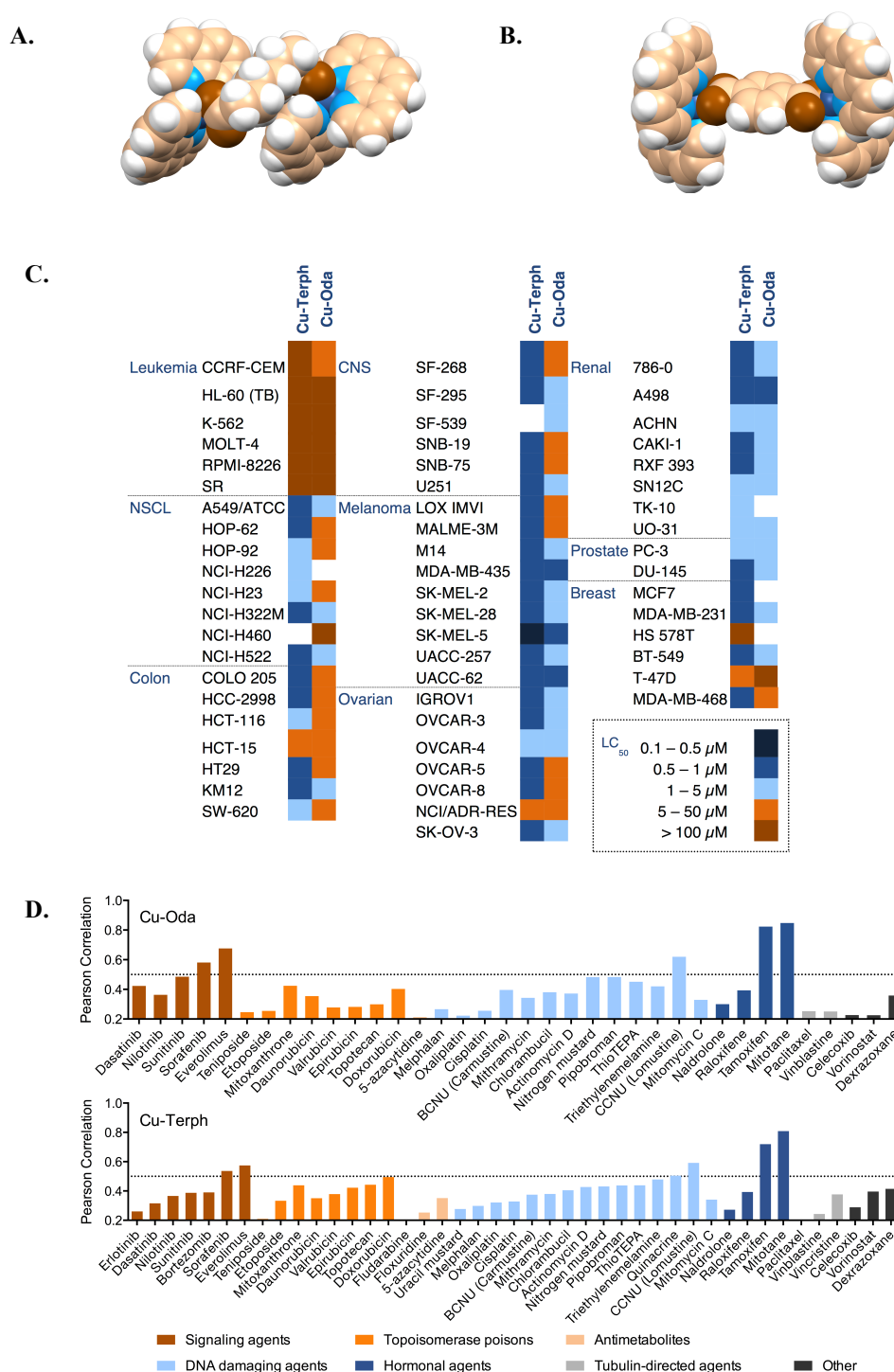


**Figure 4.** **2A.** Molecular structure of *di*-nuclear copper complexes  $[\{\text{Cu}(\text{phen})_2\}_2(\mu\text{-oda})]^{2+}$  (**Cu-Oda**) and **B.**  $[\{\text{Cu}(\text{phen})_2\}_2(\mu\text{-terph})]^{2+}$  (**Cu-Terph**). Molecular structures found in Figure S1. **C.** Heat map representation of  $\text{LC}_{50}$  concentrations calculated from 5-dose cytotoxicity screen across the NCI-60 human cancer cell line panel. Concentration ranges from most cytotoxic ( $0.1 - 0.5 \mu\text{M}$  shown in navy) through to least cytotoxic ( $>100 \mu\text{M}$  shown in brown). **D.** Pearson correlation coefficients of  $\text{LC}_{50}$  profiles generated from the NCI DTP COMPARE algorithm, where standard agents and market drugs are grouped according to their mode of cytotoxic action.

## 4.4.2 Mechanistic binding and DNA interactions

### 4.4.2.1 DNA binding affinities

A high-throughput ethidium bromide displacement assay was employed to probe the DNA binding affinities and base specificity of both *di*-nuclear complexes on sequences of varying AT content in comparison to the minor groove binder netropsin, and classical intercalator Actinomycin D (Table S3 and Figure S3). This indirect method revealed similar binding affinities for **Cu-Oda** ( $3.79 - 5.77 \times 10^6$ ) and **Cu-Terph** ( $1.84 - 3.65 \times 10^6$ ) with a slight preference towards calf thymus DNA for both species.

### 4.4.2.2 Topoisomerase I (Top I) mediated relaxation

Given the number of topoisomerase poisons and DNA damaging agents present in our COMPARE analysis (albeit many with low PCCs), coupled with our previous DNA damaging experimental results,<sup>20,24,40</sup> nucleic acid unwinding experiments with topoisomerase I and negatively supercoiled pUC19 DNA were undertaken. Topoisomerases are a specialised class of nuclear enzymes that regulate transient cleavage, passage and resealing of DNA through either single strand (Topo I), or double strand (Topo II) scission in order to remodel DNA or release superhelical tension from under (–) or over winding (+).<sup>41</sup> **Cu-Oda** and **Cu-Terph** were found to induce concentration-dependent release of plasmid supercoils with complete relaxation at 10.0  $\mu$ M (Figure 3A). Beyond this exposure level, a fraction of positive supercoiled pUC19 becomes visible, indicating that an intercalative saturation point was reached. A portion of plasmid DNA, however, remained in a relaxed state (highlighted in Figure 3A), indicative of site-specific oxidative strand cutting of pUC19 that transformed the plasmid to a permanent open circular conformation. Thus, the absence of total conversion of pUC19 into a right-handed topoisomeric (+) form, commonly observed for classical DNA intercalators such as ethidium bromide (Figure S4), implicates both intercalative unwinding and complex-mediated oxidative degradation by the *di*-Cu<sup>2+</sup> complexes. Under identical conditions, the Topo II poison doxorubicin (Dox) was identified to stabilise DNA-Topo I enzyme complex at 1.0  $\mu$ M with no distinct topoisomers observed at concentrations exposed thereafter (Figure S4).

### 4.4.2.3 Circular dichroism (CD) analysis

In order to validate the intercalative binding mode of *di*-Cu<sup>2+</sup> agents indicated by topoisomerase relaxation, complex-DNA interactions were investigated through CD spectroscopy. While **Cu-Terph** was precluded from this study (due to a lack of solubility in CD assessable solvents),<sup>42</sup> the mode of **Cu-Oda** binding was examined using three B-form DNA sequences. B-form duplex DNA exhibits negative elliptical signals at 210 and 246 nm arising from  $\beta$ -N-glycosidic linkages and helicity respectively, and positive bands at 220 nm and 268 nm due to H-bonding and base-pair

stacking interactions, though variation in these regions can arise from sequence diversity and AT content.<sup>43</sup> Upon increasing **Cu-Oda** drug load, an intercalative profile was observed in salmon testes DNA (stDNA) and alternating copolymer poly[d(G·C)<sub>2</sub>] characterised by pronounced elliptical shifts at 275 nm for nitrogenous-base stacking interactions (Figure 3B). The ellipticity of this signal was dramatically pronounced in poly[d(A·T)<sub>2</sub>], indicating preferential intercalation along AT rich tracts that are found within the narrow minor groove of this duplex. Structural distortions in the form of DNA unwinding are also identified from helicity and right-handedness signals (246 nm) in poly[d(A·T)<sub>2</sub>], most likely as a result of the complex being selectively incorporated into the minor groove. Cu-Oda intercalation at AT rich tracts fall within the expected behaviour of [Cu(phen)<sub>2</sub>]<sup>+</sup>,<sup>44</sup> where preferential DNA interactions are known to be sequence-specific at the central A residue in TAT triplet steps.<sup>45</sup>

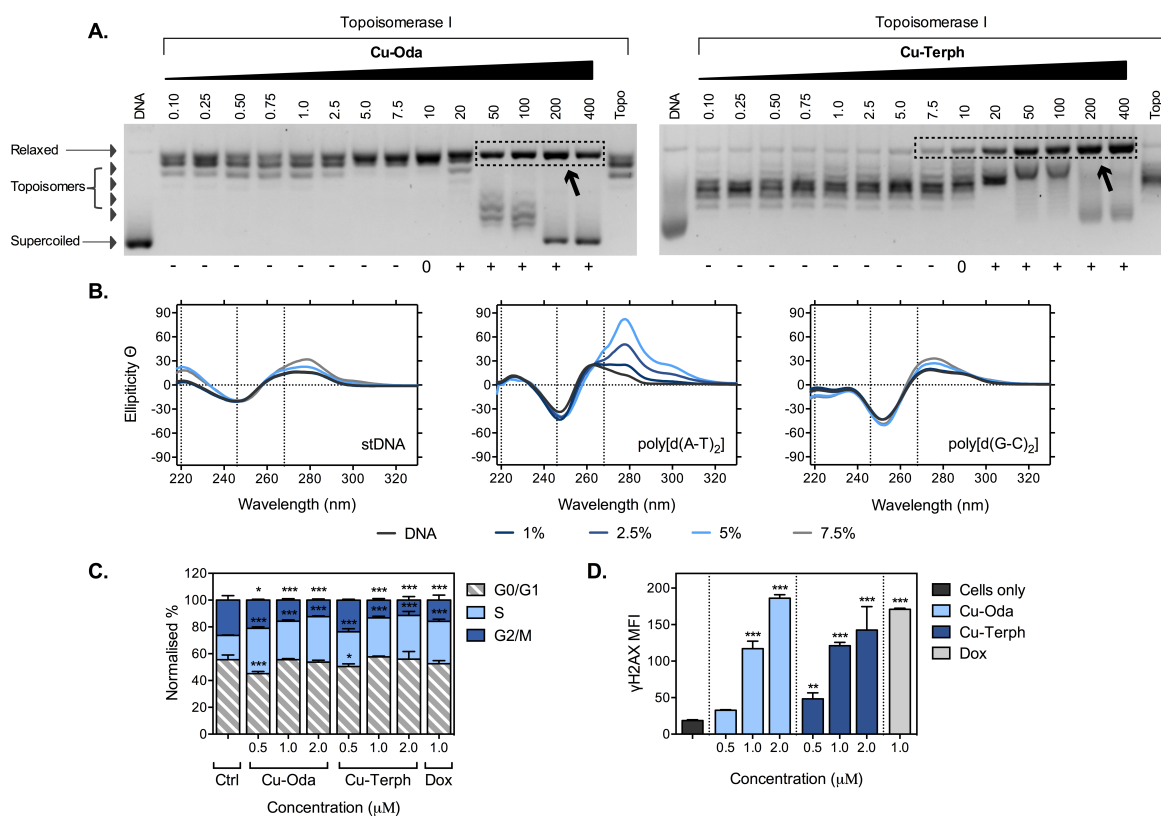


**Figure 4.3** **A.** Topoisomerase I unwinding across concentration range 0.10 - 400 μM for **Cu-Oda** and **Cu-Terph**. **B.** CD spectra of **Cu-Oda** with stDNA and alternating co-polymers poly[d(A·T)<sub>2</sub>] and poly[d(G·C)<sub>2</sub>] at 1 - 7.5% loading ratios. **C.** Cell cycle phase fractionations for **Cu-Oda** and **Cu-Terph** incubated for 24 h at 0.5, 1.0 and 2.0 μM. **D.** Double strand breaks (DSBs) induced by **Cu-Oda** and **Cu-Terph**, detected by immunostaining of γH2AX with median intensity fluorescence (MFI) presented for di-Cu<sup>2+</sup> complexes and Dox. Nonsignificant (ns)  $p > 0.05$ ; \*  $p \leq 0.05$ ; \*\*  $p \leq 0.01$ ; \*\*\*  $p \leq 0.001$ .

#### 4.4.2.4 Cell cycle analysis

The ovarian adenocarcinoma cell line SKOV3 was selected to probe intracellular genotoxic properties of **Cu-Oda** and **Cu-Terph** as this cancer form has the leading rate of gynaecological



cancer mortality and poor prognosis, and is further characterised by chemoresistance and recurrence.<sup>46</sup> SKOV3 elicited sensitivity to both **Cu-Terph** and **Cu-Oda** treatment within the NCI-60 panel, yet distinctive GI<sub>50</sub> activities (160 nM and 1  $\mu$ M, respectively) were encountered making this cell line an important choice to probe for differences between both agents. SKOV3 is also innately resistant to cisplatin<sup>47</sup> with malfunctioning p53,<sup>48</sup> the occurrence of which is rampant amongst many neoplasias.<sup>49</sup> Mutants of this tumour suppressive gene are known to significantly reduce cancer vulnerability to chemotherapeutic and radiation treatment and wild-type primary specimen transformation to mutant variants is commonly observed in cases of relapse.<sup>50</sup> SKOV3 also lacks functional DNA mismatch repair protein MLH1, where deficiencies in this pathway are frequently resistant to alkylating therapeutic agents.<sup>51</sup> To probe the intracellular impact of **Cu-Oda** and **Cu-Terph** on nuclear DNA and cell cycle progression, phase distributions were examined *via* flow-cytometric quantification of DNA content. All cells have an innate cell cycle, revolution of which consists of distinct phases culminating in the growth (G<sub>0</sub>/G<sub>1</sub>), duplication of chromosome (S) and production of daughter cells (G<sub>2</sub>/M), with various checkpoints to monitor DNA damage or incomplete replication.<sup>52</sup> Increased rates of cancer cell proliferation stems from aberrant regulation of the cycle,<sup>53</sup> however, this can also be exploited as dysfunctional checkpoint controls render the cell increasingly susceptible to genetic or microtubular toxicity.<sup>54</sup> The effects of the *di*-nuclear Cu<sup>2+</sup> complexes on cell cycle-phase distributions in SKOV3 cells were examined with treatment of **Cu-Oda** and **Cu-Terph** (0.5 – 2.0  $\mu$ M) and Dox (1.0  $\mu$ M). Both complexes show concentration-dependent phase accumulation in S and progressive reduction in G<sub>2</sub>/M (Figure 3C). Dox was selected for comparative mechanistic investigation due to its multimodal cytotoxic properties—such as ROS generation<sup>55</sup> and Topo II-DNA complex stabilisation through intercalative binding<sup>56</sup>—common features of *di*-Cu<sup>2+</sup> agents, where phase transverse from G<sub>2</sub>/M to S is also evident.

#### 4.4.2.5 Immunodetection of $\gamma$ H2AX

The formation of DSBs was next explored through immunodetection of  $\gamma$ H2AX. Histones are indiscriminately incorporated into the nucleosome for higher order chromatin formation. The H2AX histone variant differs from others through a carboxyl tail containing a serine residue that becomes phosphorylated ( $\gamma$ H2AX) in response to localised DSBs,<sup>57</sup> and thus act as signalling foci for the recruitment of DNA repair factors.<sup>58</sup> In this study, DNA damage was recorded as the median intensity fluorescence (MFI) of  $\gamma$ H2AX in the cell population (Figure 3D). Both complexes displayed concentration-dependent DSB formation, the highest order of formation comparable to toxic dose of Dox (1.0  $\mu$ M). Significantly, increased nuclearity within these complexes considerably alters the capacity to form DSBs as mononuclear analogues developed within the group exhibited one-order of magnitude lower MFI.<sup>21</sup>

#### 4.4.2.6 Comet Assay

Ensuing SSBs, DSBs and alkali liable sites arising from genomic DNA damage mediated by *di*-Cu<sup>2+</sup> agents were explored *via* the electrophoretic alkaline comet assay.<sup>59</sup> The lysis of cell membranes, nuclear bound proteins and histones allows DNA to migrate under electrophoresis, based on nucleic acid integrity.<sup>60</sup> **Cu-Oda** and **Cu-Terph** were found to fragment DNA with corresponding tail moments of 69.6 and 52.8 a.u. (Figure 4) with **Cu-Terph** exhibiting a broader distribution of residual DNA damage. This further corroborates the site-selective cleavage observed in topoisomerase relaxation assays, particularly for **Cu-Oda**. Dox produced the highest extent of DNA damage with mean tail moments of 76.3 a.u. with frequency distributions indicative of non-discriminate oxidative cleavage. This is in agreement with studies conducted by Manjanatha *et al.*, whose work further probed direct and in-direct ROS induced DNA damage by employing DNA repair endonucleases Fpg (oxidised pyrimidines), hOOG1 (oxidised purines) and Endo III (oxidised pyrimidines).<sup>61</sup>

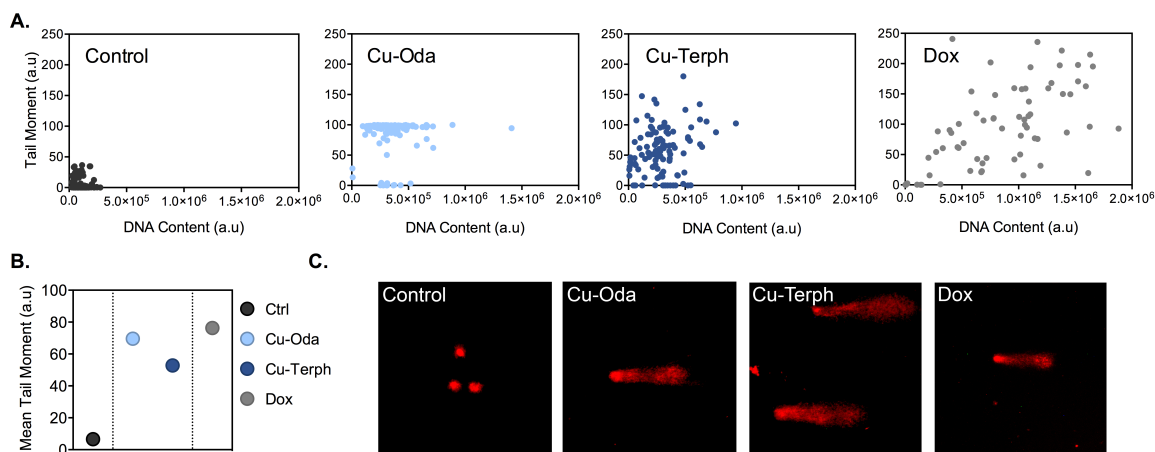


**Figure 4.4.** DNA damage detected through the alkaline comet assay, **A.** Tail moments and DNA content of control and 1.0  $\mu$ M **Cu-Oda**, **Cu-Terph** and **Dox**, **B.** Mean tail moment of >80 comets analysed, **C.** Typical comet images acquired for SKOV3 non-treated cells, and those treated with **Cu-Oda**, **Cu-Terph** and **Dox**.

#### 4.4.3 Detection of Apoptosis

##### 4.4.3.1 Apoptotic induction

Given the severe genotoxic influence witnessed by both dinuclear complexes, apoptotic induction was investigated through the detection of Annexin V. Membrane-impermeable and fluorogen-tagged, Annexin V selectively binds to substrate phosphatidylserine upon translocation from the inner to outer surface of the cellular membrane during apoptosis.<sup>62,63</sup> Samples were incubated with various concentrations of complex and controls, and counterstained with the DNA intercalator, 7-aminoactinomycin D (7-AAD), which only gains access to the nucleus when the cellular membrane integrity is compromised during the latter stages of apoptosis. The activation of early-stage apoptosis was apparent at a maximal exposed concentration of 2.0  $\mu$ M (Figure 5A) for both

complexes, whereas late stage apoptosis (defined by the positive staining of both dyes) was particularly evident for **Cu-Terph** where 34.2% of the population is represented in this period (Figure 5B). The same concentration of **Cu-Oda**, however, was found to induce 10.8%, is significantly different when compared to the clinical agent Dox (45.9%).

#### 4.4.3.2 Caspase 3/7, 8 and 9 activation

In order to identify the underpinning mechanism of apoptotic activation, exclusive endoproteases associated with this pathway in the form of caspases were examined. As key regulators of apoptosis, caspases are present in their cellular pro-enzymatic form, where they become activated through dimerization or proteolytic cleavage based on their sequential role in the apoptotic pathway.<sup>64,65</sup> Initiator caspases identify the origin of apoptotic induction as intrinsic (BH-3 only proteins translocation to the mitochondria, and release apoptogenic factors, thus activating of caspase 9)<sup>66</sup> or extrinsic (extracellular stress signals ligate to membrane-bound TNF $\alpha$  or death receptors and activate caspase 8).<sup>67</sup> The predominant mode of *di*-Cu<sup>2+</sup> apoptotic induction is *via* the intrinsic pathway, depicted through detection of caspase 9 in 22.2 and 30.7% of cellular populations when exposed to 2.0  $\mu$ M of **Cu-Oda** and **Cu-Terph** (Figure 5F). Caspase 8 was also detected in lower ratios (Figure 5E) and can be attributed to intercellular dialogue from preceding apoptotic cells or potentially consequent of intracellular ROS generation,<sup>24,40</sup> known to transmit caspase 8.<sup>68,69</sup> The positive control Dox indicates clear activation through the intrinsic pathway with 29.6% in the caspase 9 in comparison to 6.6% for caspase 8. Executioner caspases 3/7 initiate an irreversible cascade of global proteolytic and endonucleic degradation,<sup>64</sup> the detection of which was segregated into the early and later stages of apoptosis upon cellular co-staining with 7-ADD (Figure 5C and 5D accordingly). In the early stages of apoptosis the activation of caspase 3 and 7 is significantly greater for **Dox** (82.1%) in comparison to the attenuated 10.0 - 11.8% found by **Cu-Oda** and **Cu-Terph** exposure. In the latter stages, however, the complexes surpass Dox activation (8.2%) of with executioner caspase, with 39.7 and 36.1% detection at 2.0  $\mu$ M of metallodrug exposure, indicating a kinetically higher rate toxic action.

#### 4.4.3.3 Confocal Imaging

Mammalian cellular structures can undergo morphologic changes characteristic of the apoptotic cell death mechanism. By employing organelle specific dyes—to monitor the structure and integrity of mitochondria, cytoskeleton and nucleus—visualised through confocal microscopy, can identify distinctive hallmarks such as cytosolic and organelle contractions, condensation and increased chromatin granularity, membrane blebbing and the formation of apoptotic bodies (apobodies).<sup>70</sup> These characteristics are particularly evident upon CCCP and Dox exposure, where nuclear fragmentation is clearly visible, in comparison to non-treated SKOV3 cells that are typically elongated, polygonal and dome-like in morphology (Figure 5G). Cells treated with **Cu-**

**Oda** and **Cu-Terph** showed organelle condensation, fragmentation of nuclear content, remnants of apobodies, and reduction in Mitotracker Deep Red fluorescence. Given that this dye is sensitive to mitochondrial membrane potential,<sup>71,72</sup> **Cu-Oda** and **Cu-Terph** may induce mitochondrial dysfunction, independent of apoptosis.

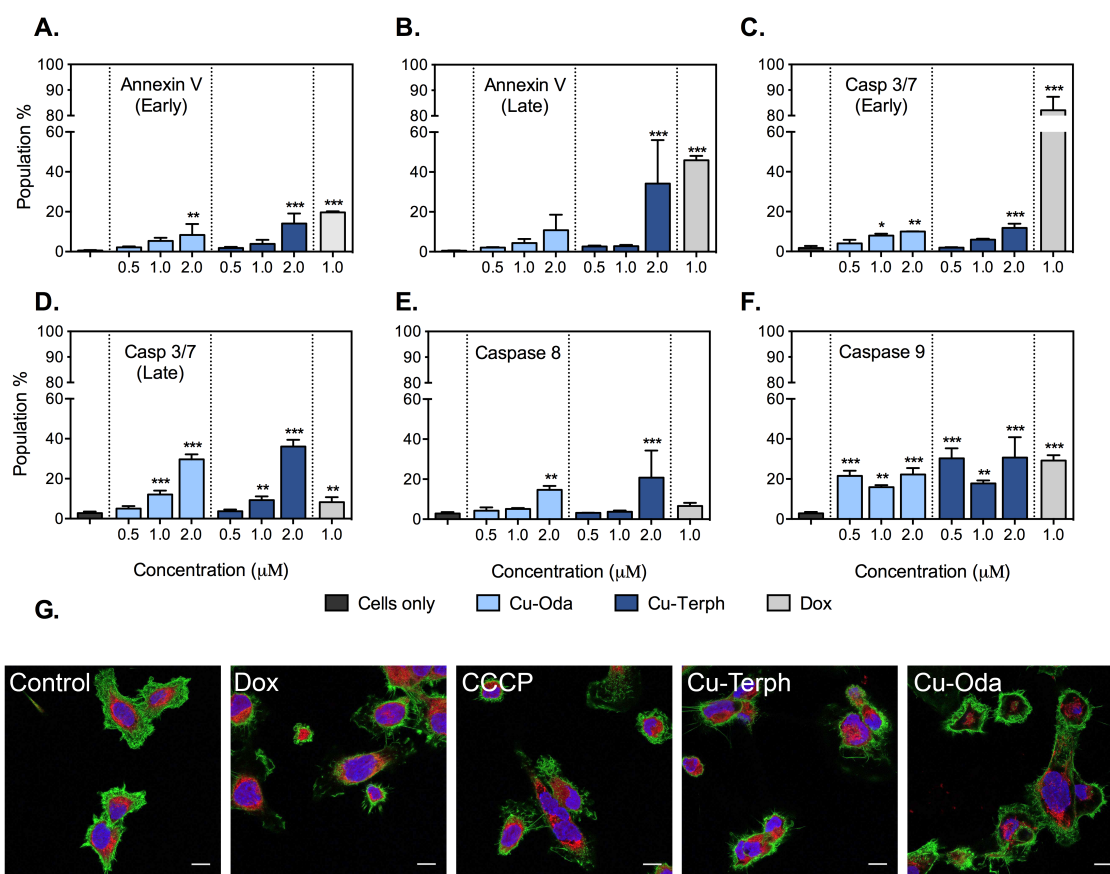


**Figure 4.5** A. SKOV3 cells are treated over 24 h with varying concentration of **Cu-Oda** and **Cu-Terph** (0.5 - 2.0 μM) and control agent Dox (1.0 μM). **A.** Populations of early apoptotic cells exhibiting positive staining for Annexin V only. **B.** Late apoptotic population detected through positive staining for Annexin V and 7-AAD. **C.** Detection of caspase 3/7 in the absences of 7-AAD positive staining indicative of mid-apoptotic activation. **D.** Detection of late apoptotic release of caspase 3/7 through the detection of 7-AAD positive cells. **E.** Population of caspase 8 (extrinsic pathway) **F.** Activation of caspase 9 (intrinsic pathway). **G.** 100× magnification of SKOV3 cells treated with Dox (1.0 μM), CCCP (75 μM) and dinuclear copper complexes, **Cu-Oda** and **Cu-Terph** (1.0 μM). The nucleus is stained with DAPI, F-actin with Alexa Fluor 488-Phalloidin and mitochondria with MitoTracker Deep Red. Scale bar indicates 10 μm. Individual channels are shown in Figure S5. Nonsignificant (ns)  $p > 0.05$ ; \*  $p \leq 0.05$ ; \*\*  $p \leq 0.01$ ; \*\*\*  $p \leq 0.001$ .

#### 4.4.4 Investigations of mitochondrial dysfunction

##### 4.4.4.1 Mitochondrial Membrane Potential ( $\Delta\Psi_m$ )

Further experiments into mitochondrial dysfunction were conducted by examining the hypsochromic shift in fluorescent emission of potential-sensitive JC-1 (5,5',6,6'-tetrachloro-1,1',3,3'-tetraethylbenzimidazolocarbo-cyanine iodide). The cationic JC-1 dye accumulates within

polarised mitochondria (high  $\Delta\Psi_m$ ), forming orange fluorescent j-aggregates, while green emitting monomers reside within the cytosol upon depolarisation.<sup>73,74</sup> Mitochondrial depolarisation correlates to transmembrane permeability, and when compromised releases pro-apoptotic factors, such as cytochrome *c*, into the cytosol.<sup>75,76</sup> Cu-Oda and Cu-Terph stimulated depolarised mitochondria in a concentration-dependent manner where >84.8% of cellular populations displayed a loss in membrane potential at 2.0  $\mu$ M (Figure 6A). The positive control CCCP (carbonyl cyanide *m*-chlorophenyl hydrazone) was selected due to its proton ionophore properties, transporting protons across the mitochondrial transmembrane and thus readily dissipating mitochondrial transmembrane potential.<sup>77</sup> Higher concentrations of CCCP (75  $\mu$ M) are required to induce a decreased proportion of membrane depolarization. The transient mitochondrial permeability of this magnitude does not directly correlate to the modest detection of intrinsic apoptotic biomarkers (annexin V and caspases). In this case, the extent of depolarization results from selective localisation and ROS generation of the copper complexes, thus instigating the apoptotic process. Mitochondrial accumulation is most likely due to the delocalised cationic charge and lipophilicity of 1,10-phenanthroline ligands, common features of dyes and targeting vehicles that selectively assemble within this organelle.<sup>78</sup>

#### 4.4.4.2 Mitochondrial superoxide production

The predominant source of intracellular  $O_2^{\cdot-}$  generation is the mitochondrial power house, primarily from site-specific electron release within the respiratory chain such as complex I and III,<sup>90</sup> quinone electron shuttle Coenzymes Q10 and enzymatic processes such as NADPH oxidases.<sup>91</sup> In order to investigate the source of transmembrane potential degeneracy and ROS production properties of **Cu-Oda** and **Cu-Terph**, we selectively probed the liberation of superoxide within the mitochondrial matrix through the use of MitoSOX Red. With its fluorogenic dihydroethidium (HE) core, this dye is readily internalised within the cell,<sup>92</sup> and further mitochondrial-specific localisation is refined by a triphenylphosphine conjugate.<sup>93</sup> HE undergoes discreet two-electron oxidation by  $O_2^{\cdot-}$ , and the reduced cationic derivative ethidium intercalates mitochondrial DNA through the minor groove.<sup>93</sup> Results shown in Figure 6B, revealed extensive and selective  $O_2^{\cdot-}$  generation by **Cu-Oda** and **Cu-Terph**, with 52.6% and 76.1% of the cellular populations showing positive MitoSOX Red fluorescence at the highest drug exposure (2.0  $\mu$ M).

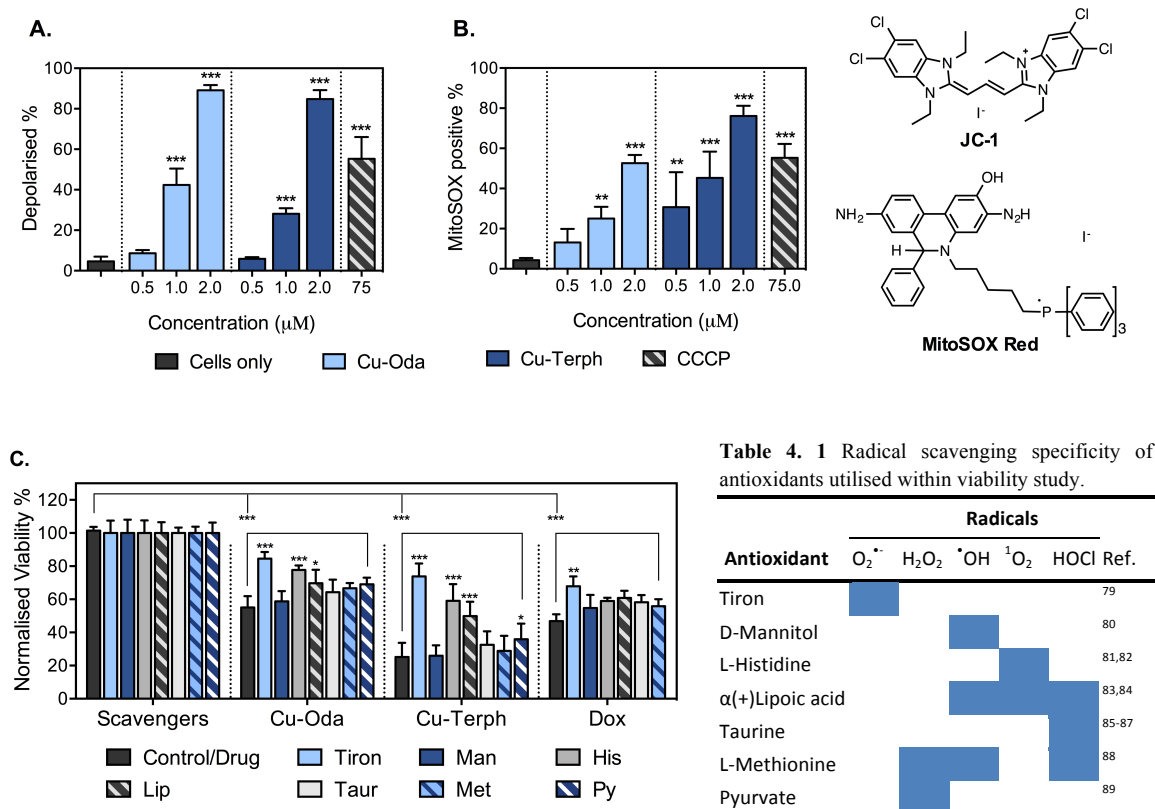


**Figure 4.6** SKOV3 cells were treated with **Cu-Oda**, **Cu-Terph** and positive controls Dox and CCCP at indicated concentrations for 24 h. **A.** Population of depolarised mitochondria through the detection of potential-sensitive shift in JC-1 emission. Hypsochromic shifts, evident in scatter plot, demonstrates drug-induced depolarisation (Figure S6). **B.** Detection of MitoSOX red population indicative of superoxide-selective fluorescence activation. The molecular structures of dyes employed are given (top right). **C.** Viability results of **Cu-Oda**, **Cu-Terph** and Dox at 1.0 μM in the absence and presence of 1 mM ROS specific scavengers (Table 4.1 insert). Nonsignificant (ns)  $p > 0.05$ ; \*  $p \leq 0.05$ ; \*\*  $p \leq 0.01$ ; \*\*\*  $p \leq 0.001$ .

#### 4.4.4.3 Intracellular radical production

Since increased levels of MitoSOX red fluorescence demonstrated the intense O<sub>2</sub><sup>•-</sup> generation, we were prompted to conduct a detailed examination of intracellular ROS species promoted by toxic insults of both *di*-Cu<sup>2+</sup> agents. This was achieved through monitoring cell viability upon co-treatment of radical specific scavengers and trapping agents tiron, mannitol, histidine, lipoic acid, taurine, methionine and sodium pyruvate (Figure 6C and Table 1). It is remarkable to note the extent to which the cytotoxic effect is averted through the use of ROS-selective antioxidants, with viability profiles of **Cu-Terph** and **Cu-Oda** fluctuating from 25.2 - 73.8% and 55.1 - 84.6%, respectively. The most potent scavenging agent was the electron trap tiron—sequestering the production of O<sub>2</sub><sup>•-</sup> through direct-oxidation and formation of semiquinone radicals<sup>79</sup>—which increased cellular viability by 29.5% for **Cu-Oda** and 48.6% for **Cu-Terph**. The second most abundant toxic species liberated was singlet oxygen (<sup>1</sup>O<sub>2</sub>), which readily oxidises the imidazole ring within histidine and in doing so, selectively traps the radical.<sup>94</sup> Overall, elevated cellular viability due to inhibition of ROS production follows tiron >> histidine > lipoic acid > pyruvate >

taurine > methionine > mannitol with the more structurally rigid complex **Cu-Terph** showing the greater potential of the two toward catalytic pro-oxidant  $\text{O}_2^{\bullet -}$  and  $^1\text{O}_2$  production.

## 4.5 Conclusion

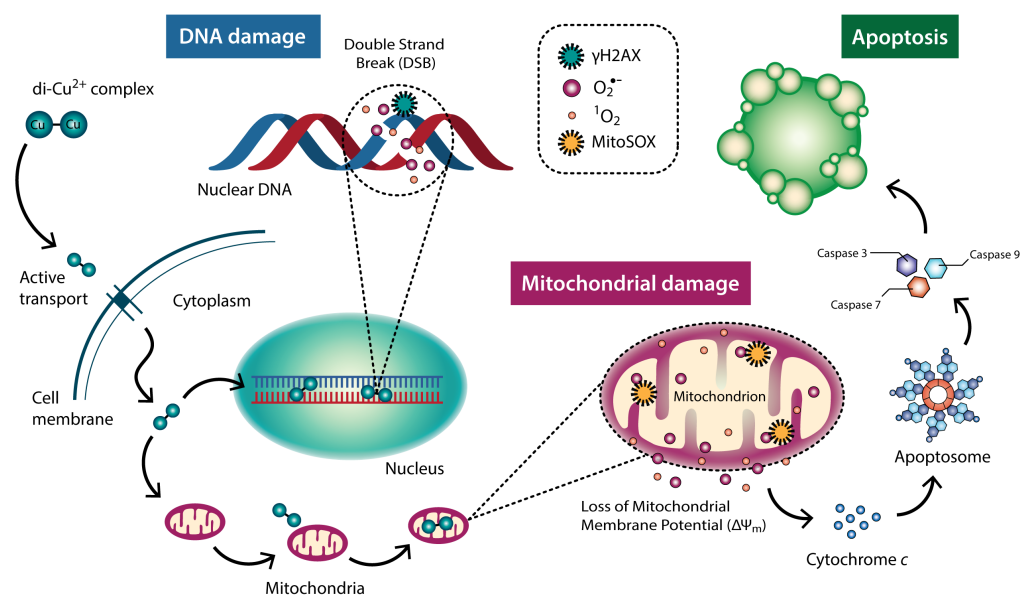


**Figure 4. 7** Proposed mechanism of action for *di*-copper(II) agents **Cu-Oda** and **Cu-Terph**. Complexes are incorporated into the cell through copper transport protein (Ctr1). *Di*-Cu<sup>2+</sup> complexes take one of two pathways i.) nuclear localisation and intercalative binding at the minor groove of duplex DNA (anionic); ii.) mitochondrial accumulation due to MMP ( $\Delta\Psi_m$ ), facilitated by the cationic complex charge and lipophilicity of phenanthroline groups. Intracellular generation of superoxide ( $O_2^{\bullet-}$ ) and singlet oxygen ( $^1O_2$ ), detected through radical specific antioxidants, induce significant DNA degradation through the formation of double strand breaks (DSBs) when quantified by  $\gamma$ H2AX and comet. Enhanced levels of superoxide within the mitochondria (MitoSOX) causes collapse transmembrane potential measured through the extent of mitochondrial depolarisation (JC-1). This results in the release of cytochrome *c* and activation of the intrinsic pathway through apoptosome formation and activation of initiator caspase 9 and executioner caspase 3 or 7. Apoptosis was quantitatively measured through Annexin V and visualised by confocal microscopy.

The use of metal-based chemotherapeutics that exploit innate cellular delivery—and incorporation mechanisms—to facilitate toxic dose accumulation and biomolecular target accessibility forms the basis of strategic anticancer drug design. The current class of *di*-Cu<sup>2+</sup> agents with 1,10-phenanthroline chelating ligands, **Cu-Oda** and **Cu-Terph**, display broad spectrum activity elucidated from NCI-60 cell line analysis that revealed a unique, yet multi-modal, mechanism of cytotoxic action according to the COMPARE algorithm. Intracellular accumulation by **Cu-Oda** and **Cu-Terph** is most likely facilitated through active transport by copper influx protein Ctr1 (Figure 7), a high-affinity transporter and ion channel for the delivery of cupric nutrients and which, in turn, are hijacked by platinum-based agents to facilitate cellular localisation.<sup>95</sup> Upon treatment, cisplatin can rapidly degrade the functional capability of Ctr1 proteins at elevated rates to copper insult, thus preventing its own uptake.<sup>96</sup> Overexpression of this agents is a common feature in some forms transformed cells, particularly colon carcinomas,<sup>97</sup> which were found to be particularly sensitive to *di*-Cu<sup>2+</sup> complex insult within the NCI-60 panel. As well as displaying no correlation to the cytotoxic profiles of clinically established platinum agents by COMPARE



analysis, *di*-nuclear **Cu-Oda** and **Cu-Terph** complexes also possess an alternative kinetic profile to cisplatin by exerting toxic effects within a shorter time frame of 24 h.

We have shown unambiguously, through topoisomerase unwinding and circular dichroism experiments, that both *di*-Cu<sup>2+</sup> complexes selectively bind to DNA using an intercalative mode in AT rich tracts. An interesting structural feature of these agents is the increased number of coordinated polyaromatic and heterocyclic phenanthroline ligands they contain—this ligand geometry clearly facilitates high-affinity DNA binding through selective intercalation while also directing genomic DNA double-strand scission (Figure 7, nuclear pathway) as seen in the detection of  $\gamma$ H2AX, cell cycle phase distributions and comet formation. The incorporation of phenanthrene-type ligands is of current interest to overcome the limitation of established chemotherapeutics; ligation of such ligands into the cisplatin framework, in the form of the phenanthriplatin series, enhances intracellular accumulation with decreased detoxification through thiol containing reducing agents commonly associated with platinum resistance.<sup>98</sup> Additionally, Au(III)-phen was recently shown to exert its cytotoxic action through poly(ADP-ribose) polymerase (PARP) inhibition as a competitive binder within the zinc-finger motif.<sup>99</sup>

The use of radical-specific scavenging and trapping agents in this study revealed the remarkable ROS-selective generation properties of **Cu-Oda** and **Cu-Terph**, where catalytic formation of oxidants superoxide (O<sub>2</sub><sup>•-</sup>) and singlet oxygen (<sup>1</sup>O<sub>2</sub>) were identified. The ROS-regulatory function of these destructive species causes irreparable oxidative damage within nuclear DNA in the form of DSBs, thus inducing apoptotic cell death. Since increased nuclearity is the one the defining features of cytotoxic action within this *di*-Cu<sup>2+</sup> class, it is significant to note the incorporation of multiple copper centres into molecular scaffolds has previously been shown to significantly enhance the redox potential of pro-oxidising agents.<sup>100,101</sup> When compared their mono-nuclear analogue with *O,O'* (*o*-phthalate) ligand, the *di*-Cu<sup>2+</sup> agents displayed a 10 - 100 fold increase in toxic effect within the NCI-60 panel.<sup>102</sup> Furthermore, the proximity of the metal centres can constitute and potentiate synergistic redox recycling, facilitating the formation of catalytic intermediates required for deleterious radical generation.<sup>100</sup> In the case of our *di*-Cu<sup>2+</sup> agents, alteration of the *di*-carboxylate bridging ligand has significant effects in terms of their toxic activity. The more active complex, **Cu-Terph**, contains a rigid terephthalate linker and has a fixed intermetal Cu-Cu distance of 11.014 Å thus fixing the relative orientation of the phenanthroline ligands. The more malleable **Cu-Oda**, with a Cu-Cu distance of 9.741 Å in its crystallised form, has free rotation around the octanedioate and flexible orientation of intercalating moieties. Indeed, it was previously shown that ligating rigidity within pyridylalkylamine multinuclear copper<sup>2+</sup> systems can alter complex oxidising efficiency and specificity towards nucleobase or deoxyribose attack involved in single or double strand scission.<sup>101</sup>

The extent of selective intramatrix production of  $O_2^{\bullet-}$  and dissipation of mitochondrial transmembrane potential (as seen through the use of indicative dyes, MitoSOX Red and JC-1) results in the intrinsic release of pro-apoptotic transmission signals in the form of cytochrome *c* (Figure 7, mitochondrial pathway). This, in turn, activates the formation of apoptosomes and facilitates the initiation and execution of caspase 9, 3 and 7, rendering a proteolytic cascade of global cellular degradation and therefore apoptotic cell death—revealed by flow-cytometric detection of respective biomarkers and morphological analysis. Unambiguous targeting of the mitochondria has generated increased attention in the development of novel chemotherapeutic agents as well as the progressing of ROS-modulating agents into clinical trials.<sup>8,103</sup> Multiple facets of transformed cancer cells exude differential bioenergetic, biosynthetic and redox requirements in order to support rapid cell proliferation, regulatory checkpoint evasion,<sup>104,105</sup> malfunction of mitochondrial respiratory chain,<sup>106</sup> along with other stressful metabolic conditions associated with tumorigenesis. In order to facilitate these metabolic shifts,<sup>107</sup> many cancer cells display an increased rate of aerobic glycolysis, a phenomenon known as the Warburg effect.<sup>108</sup> Mitochondrial delivery of anticancer agents utilises a variety of localisation mechanisms such as penetrating peptide sequences, liposomes, nanocarriers, lipophilic cations including triphenylphosphonium (TPP) or small molecules that traverse pH gradients.<sup>109-111</sup> These delivery mechanisms have been exploited to re-evaluate established clinical agents such as doxorubicin<sup>112</sup> and cisplatin,<sup>113</sup> as well as novel therapeutics with discreet ROS generation properties in the form of copper-based agents<sup>114</sup> and fluorogenic dyes.<sup>115,116</sup> The pro-oxidant properties of this *di*-Cu<sup>2+</sup> series, **Cu-Oda** and **Cu-Terph**, reveal selective catalytic production of  $^1O_2$  and  $O_2^{\bullet-}$  resulting in dual genomic DNA strand integrity and bioenergetic redundancy of the mitochondria. These agents therefore contain intrinsic small-molecule targeting properties that are not based on conventional delivery scaffolds and, this effect, coupled with dual-action ROS production constitutes the activation of a unique mode of action triggered by intrinsic apoptotic cell death.

## 4.6 Supporting Information

Supplementary information associated with this chapter can be found in Appendix C

## 4.7 References

- (1) D'Autréaux, B., and Toledano, M. B. (2007) ROS as signalling molecules: mechanisms that generate specificity in ROS homeostasis. *Nat. Rev. Mol. Cell Biol.* 8, 813–824.
- (2) Halliwell, B., and Gutteridge, J. M. C. (2007) Free Radicals in Biology and Medicine, in *Redox Chemistry: The Essentials* 4 ed., pp 30–74. Oxford University Press, Inc.
- (3) Onyango, A. N. (2016) Endogenous Generation of Singlet Oxygen and Ozone in Human and Animal Tissues: Mechanisms, Biological Significance, and Influence of Dietary Components. *Oxid. Med. Cell Longev* 2016, 2398573.
- (4) Wefers, H., and Sies, H. (1983) Oxidation of glutathione by the superoxide radical to the disulfide and the sulfonate yielding singlet oxygen. *Eur. J Biochem.* 137, 29–36.
- (5) Fridovich, I. (1995) Superoxide radical and superoxide dismutases. *Annu. Rev. Biochem.* 64, 97–112.
- (6) Halliwell, B., and Gutteridge, J. M. (1984) Oxygen toxicity, oxygen radicals, transition metals and disease. *Biochem. J.* 219, 1–14.
- (7) Nimse, S. B., and Pal, D. (2015) Free radicals, natural antioxidants, and their reaction mechanisms. *RSC Adv.* 5, 27986–28006.
- (8) Trachootham, D., Alexandre, J., and Huang, P. (2009) Targeting cancer cells by ROS-mediated mechanisms: a radical therapeutic approach? *Nat. Rev. Mol. Cell Biol.* 8, 579–591.
- (9) Pitié, M., and Pratviel, G. (2010) Activation of DNA Carbon–Hydrogen Bonds by Metal Complexes. *Chem. Rev.* 110, 1018–1059.
- (10) Gewirtz, D. (1999) A critical evaluation of the mechanisms of action proposed for the antitumor effects of the anthracycline antibiotics adriamycin and daunorubicin. *Biochem. Pharmacol.* 57, 727–741.
- (11) Goldberg, I. H., Kappen, L. S., Xu, Y. J., Zeng, X., Xi, Z., and Yang, C. F. (1996) Eneidyne as Probes of Nucleic Acid Structure, in *DNA and RNA Cleavers and Chemotherapy of Cancer and Viral Diseases* (Meunier, B., Meunier, Eds.) 1st ed., pp 1–21.
- (12) Goldberg, I. H. (1991) Mechanism of neocarzinostatin action: role of DNA microstructure in determination of chemistry of bistranded oxidative damage. *Acc. Chem. Res.* 24, 191–198.
- (13) Chen, J., and Stubbe, J. (2005) Bleomycins: towards better therapeutics. *Nat. Rev. Cancer* 5, 102–112.
- (14) Chen, J., Ghorai, M. K., Kenney, G., and Stubbe, J. (2008) Mechanistic studies on bleomycin-mediated DNA damage: multiple binding modes can result in double-stranded DNA cleavage. *Nucleic Acids Res.* 36, 3781–3790.
- (15) Sigman, D. S., Graham, D. R., D'Aurora, V., and Stern, A. M. (1979) Oxygen-dependent cleavage of DNA by the 1,10-phenanthroline. cuprous complex. Inhibition of Escherichia coli DNA polymerase I. *J. Biol. Chem.* 254, 12269–12272.
- (16) Spassky, A., and Sigman, D. S. (1985) Nuclease activity of 1, 10-phenanthroline-copper ion. Conformational analysis and footprinting of the lac operon. *Biochemistry* 24, 8050–8056.
- (17) Bales, B. C., Pitié, M., Meunier, B., and Greenberg, M. M. (2002) A Minor Groove Binding Copper-Phenanthroline Conjugate Produces Direct Strand Breaks via  $\beta$ -Elimination of 2-Deoxyribonolactone. *J. Am. Chem. Soc.* 124, 9062–9063.
- (18) Larragy, R., Fitzgerald, J., Prisecaru, A., McKee, V., Leonard, P., and Kellett, A. (2015) Protein engineering with artificial chemical nucleases. *Chem. Commun.* 51, 12908–12911.
- (19) Molphy, Z., Prisecaru, A., Slator, C., Barron, N., McCann, M., Colleran, J., Chandran, D.,

- Gathergood, N., and Kellett, A. (2014) Copper Phenanthrene Oxidative Chemical Nucleases. *Inorg. Chem.* **53**, 5392–5404.
- (20) Kellett, A., O'Connor, M., McCann, M., McNamara, M., Lynch, P., Rosair, G., McKee, V., Creaven, B., Walsh, M., McClean, S., Foltyn, A., O'Shea, D., Howe, O., and Devereux, M. (2011) Bis-phenanthroline copper(II) phthalate complexes are potent *in vitro* antitumour agents with “self-activating” metallo-nuclease and DNA binding properties. *Dalton Trans.* **40**, 1024–1027.
- (21) Kellett, A., Howe, O., O'Connor, M., McCann, M., Creaven, B. S., McClean, S., Foltyn-Arfa Kia, A., Casey, A., and Devereux, M. (2012) Radical-induced DNA damage by cytotoxic square-planar copper(II) complexes incorporating *o*-phthalate and 1,10-phenanthroline or 2,2'-dipyridyl. *Free Radic. Biol. Med.* **53**, 564–576.
- (22) Prisecaru, A., McKee, V., Howe, O., Rochford, G., McCann, M., Colleran, J., Pour, M., Barron, N., Gathergood, N., and Kellett, A. (2013) Regulating bioactivity of Cu<sup>2+</sup> bis-1,10-phenanthroline artificial metallonucleases with sterically functionalized pendant carboxylates. *J. Med. Chem.* **56**, 8599–8615.
- (23) Galindo-Murillo, R., García-Ramos, J. C., Ruiz-Azuara, L., Cheatham, T. E., III, and Cortés-Guzmán, F. (2015) Intercalation processes of copper complexes in DNA. *Nucleic Acids Res.* gkv467.
- (24) Kellett, A., O'Connor, M., McCann, M., Howe, O., Casey, A., McCarron, P., Kavanagh, K., McNamara, M., Kennedy, S., May, D. D., Skell, P. S., O'Shea, D., and Devereux, M. (2011) Water-soluble bis(1,10-phenanthroline) octanedioate Cu<sup>2+</sup> and Mn<sup>2+</sup> complexes with unprecedented nano and picomolar *in vitro* cytotoxicity: promising leads for chemotherapeutic drug development. *Med. Chem. Commun.* **2**, 579–584.
- (25) Suntharalingam, K., Hunt, D. J., Duarte, A. A., White, A. J. P., Mann, D. J., and Vilar, R. (2012) A Tri-copper(II) Complex Displaying DNA-Cleaving Properties and Antiproliferative Activity against Cancer Cells. *Chem. Eur. J.* **18**, 15133–15141.
- (26) Devereux, M., McCann, M., Cronin, J. F., and Ferguson, G. (1999) Binuclear and polymeric copper(II) dicarboxylate complexes: syntheses and crystal structures of [Cu<sub>2</sub>(pda)(Phen)<sub>4</sub>](ClO<sub>4</sub>)<sub>2</sub> · 5H<sub>2</sub>O · C<sub>2</sub>H<sub>5</sub>OH, [Cu<sub>2</sub>(oda)(Phen)<sub>4</sub>](ClO<sub>4</sub>)<sub>2</sub> · 2.67H<sub>2</sub>O · C<sub>2</sub>H<sub>5</sub>OH and {[Cu<sub>2</sub>(pda)<sub>2</sub>(NH<sub>3</sub>)<sub>4</sub>(H<sub>2</sub>O)<sub>2</sub>] · 4H<sub>2</sub>O}<sub>n</sub>. *Polyhedron* **18**, 2141–2148.
- (27) McCann, M., Cronin, J. F., Devereux, M., and Ferguson, G. (1995) Copper(II) complexes of heptanedioic acid (hdaH<sub>2</sub>) and octanedioic acid (odaH<sub>2</sub>): X-ray crystal structures of [Cu(η<sup>2</sup>hda)(phen)<sub>2</sub>] · 11.73H<sub>2</sub>O and [Cu(η<sup>2</sup>-oda)(phen)<sub>2</sub>] · 12H<sub>2</sub>O (phen=1,0-phenanthroline). *Polyhedron* **14**, 2379–2387.
- (28) Holbeck, S. L., Collins, J. M., and Doroshow, J. H. (2010) Analysis of Food and Drug Administration-approved anticancer agents in the NCI60 panel of human tumor cell lines. *Mol Cancer Ther.* **9**, 1451–1460.
- (29) Monks, A., Scudiero, D., Skehan, P., Shoemaker, R., Paull, K., Vistica, D., Hose, C., Langley, J., Cronise, P., and Vaigro-Wolff, A. (1991) Feasibility of a high-flux anticancer drug screen using a diverse panel of cultured human tumor cell lines. *J. Natl. Cancer Inst.* **83**, 757–766.
- (30) Peixoto, P., Bailly, C., and David-Cordonnier, M.-H. (2010) Topoisomerase I-mediated DNA relaxation as a tool to study intercalation of small molecules into supercoiled DNA. *Methods Mol. Biol.* **613**, 235–256.
- (31) McCann, M., McGinley, J., Ni, K., O'Connor, M., Kavanagh, K., McKee, V., Colleran, J., Devereux, M., Gathergood, N., Barron, N., Prisecaru, A., and Kellett, A. (2013) A new phenanthroline-oxazine ligand: synthesis, coordination chemistry and atypical DNA binding interaction. *Chem. Commun.* **49**, 2341–2343.
- (32) Pozarowski, P., and Darzynkiewicz, Z. (2004) Analysis of Cell Cycle by Flow Cytometry, in

*Methods in Molecular Biology*, pp 301–311.

- (33) Brzozowska, K., Pinkawa, M., Eble, M. J., Müller, W.-U., Wojcik, A., Kriehuber, R., and Schmitz, S. (2012) In vivo versus in vitro individual radiosensitivity analysed in healthy donors and in prostate cancer patients with and without severe side effects after radiotherapy. *Int. J. Radiat. Biol.* 88, 405–413.
- (34) Speit, G., and Rothfuss, A. (2012) The comet assay: a sensitive genotoxicity test for the detection of DNA damage and repair. *Methods Mol. Biol.* 920, 79–90.
- (35) Shoemaker, R. H. (2006) The NCI60 human tumour cell line anticancer drug screen. *Nat. Rev. Cancer* 6, 813–823.
- (36) Paull, K. D., Shoemaker, R. H., Hodes, L., Monks, A., Scudiero, D. A., Rubinstein, L., Plowman, J., and Boyd, M. R. (1989) Display and analysis of patterns of differential activity of drugs against human tumor cell lines: development of mean graph and COMPARE algorithm. *J. Natl. Cancer Inst.* 81, 1088–1092.
- (37) Hearn, J. M., Romero-Canelón, I., Qamar, B., Liu, Z., Hands-Portman, I., and Sadler, P. J. (2013) Organometallic Iridium(III) Anticancer Complexes with New Mechanisms of Action: NCI-60 Screening, Mitochondrial Targeting, and Apoptosis. *ACS Chem. Biol.* 8, 1335–1343.
- (38) Gills, J. J., Holbeck, S., Hollingshead, M., Hewitt, S. M., Kozikowski, A. P., and Dennis, P. A. (2006) Spectrum of activity and molecular correlates of response to phosphatidylinositol ether lipid analogues, novel lipid-based inhibitors of Akt. *Mol Cancer Ther.* 5, 713–722.
- (39) Ng, C. H., Kong, S. M., Tiong, Y. L., Maah, M. J., Sukram, N., Ahmad, M., and Khoo, A. S. B. (2014) Selective anticancer copper(ii)-mixed ligand complexes: targeting of ROS and proteasomes. *Metallomics* 6, 892–15.
- (40) Prisecaru, A., Devereux, M., Barron, N., McCann, M., Colleran, J., Casey, A., McKee, V., and Kellett, A. (2012) Potent oxidative DNA cleavage by the di-copper cytotoxin:  $[\text{Cu}_2(\mu\text{-terephthalate})(1,10\text{-phen})_4]^{2+}$ . *Chem. Commun.* 48, 6906–6908.
- (41) Khadka, D. B., and Cho, W.-J. (2013) Topoisomerase inhibitors as anticancer agents: a patent update. *Expert Opin. Ther. Pat.* 23, 1033–1056.
- (42) Kelly, S. M., Jess, T. J., and Price, N. C. (2005) How to study proteins by circular dichroism. *Biochim. Biophys. Acta* 1751, 119–139.
- (43) Chang, Y.-M., Chen, C. K. M., and Hou, M.-H. (2012) Conformational Changes in DNA upon Ligand Binding Monitored by Circular Dichroism. *Int. J. Mol. Sci.* 13, 3394–3413.
- (44) Sigman, D. S., Mazumder, A., and Perrin, D. M. (1993) Chemical nucleases. *Chem. Rev.* 93, 2295–2316.
- (45) Veal, J. M., and Rill, R. L. (1989) Sequence Specificity of Dna Cleavage by Bis (1, 10)-Phenanthroline Copper (I): Effects of Single Base Pair Transitions on the Cleavage of Preferred Pyrimidine-Purine-Pyrimidine Triplets. *Biochemistry* 28, 3243–3250.
- (46) Shaw, T. J., Senterman, M. K., Dawson, K., Crane, C. A., and Vanderhyden, B. C. (2004) Characterization of intraperitoneal, orthotopic, and metastatic xenograft models of human ovarian cancer. *Mol. Ther.* 10, 1032–1042.
- (47) Hills, C. A., Kelland, L., Abel, G., Siracky, J., Wilson, A. P., and Harrap, K. R. (1989) Biological properties of ten human ovarian carcinoma cell lines: calibration *in vitro* against four platinum complexes. *Br. J. Cancer* 527–534.
- (48) Yaginuma, Y., and Westphal, H. (1992) Abnormal structure and expression of the p53 gene in human ovarian carcinoma cell lines. *Cancer Res.* 52, 4196–4199.
- (49) Muller, P. A. J., and Vousden, K. H. (2014) Mutant p53 in cancer: new functions and therapeutic opportunities. *Cancer Cell* 25, 304–317.
- (50) Lowe, S. W., Ruley, H. E., Jacks, T., and Housman, D. E. (1993) p53-dependent apoptosis

- modulates the cytotoxicity of anticancer agents. *Cell* 74, 957–967.
- (51) Taverna, P., Liu, L., Hanson, A. J., Monks, A., and Gerson, S. L. (2000) Characterization of MLH1 and MSH2 DNA mismatch repair proteins in cell lines of the NCI anticancer drug screen. *Cancer Chemother. Pharmacol.* 46, 507–516.
- (52) Bertoli, C., Skotheim, J. M., and de Bruin, R. A. M. (2013) Control of cell cycle transcription during G1 and S phases. *Nat. Rev. Mol. Cell Biol.* 14, 518–528.
- (53) Malumbres, M., and Barbacid, M. (2009) Cell cycle, CDKs and cancer: a changing paradigm. *Nat. Rev. Cancer* 9, 153–166.
- (54) Shapiro, G. I., and Harper, J. W. (1999) Anticancer drug targets: cell cycle and checkpoint control. *J. Clin. Invest.* 104, 1645–1653.
- (55) Gutteridge, J. M., and Quinlan, G. J. (1985) Free radical damage to deoxyribose by anthracycline, aureolic acid and aminoquinone antitumour antibiotics. *Biochem. Pharmacol.* 34, 4099–4103.
- (56) Beretta, G. L., and Zunino, F. (2008) Molecular mechanisms of anthracycline activity. *Top. Curr. Chem.* 283, 1–19.
- (57) Rogakou, E. P., Pilch, D. R., Orr, A. H., Ivanova, V. S., and Bonner, W. M. (1998) DNA Double-stranded Breaks Induce Histone H2AX Phosphorylation on Serine 139. *J. Biol. Chem.* 273, 5858–5868.
- (58) Paull, T. T., Rogakou, E. P., Yamazaki, V., Kirchgessner, C. U., Gellert, M., and Bonner, W. M. (2000) A critical role for histone H2AX in recruitment of repair factors to nuclear foci after DNA damage. *Curr. Biol.* 10, 886–895.
- (59) Azqueta, A., Slysokova, J., Langie, S. A. S., O'Neill Gaivão, I., and Collins, A. (2014) Comet assay to measure DNA repair: approach and applications. *Front Genet* 5, 288.
- (60) Azqueta, A., and Collins, A. R. (2013) The essential comet assay: a comprehensive guide to measuring DNA damage and repair. *Arch. Toxicol.* 87, 949–968.
- (61) Manjanatha, M. G., Bishop, M. E., and Pearce, M. G. (2014) Genotoxicity of Doxorubicin in F344 Rats by Combining the Comet Assay, Flow-Cytometric Peripheral Blood Micronucleus Test, and Pathway-Focused Gene Expression Profiling. *Environ. Mol. Mutagen.* 55, 24–34.
- (62) Verhoven, B., Schlegel, R. A., and Williamson, P. (1995) Mechanisms of phosphatidylserine exposure, a phagocyte recognition signal, on apoptotic T lymphocytes. *J. Exp. Med.* 182, 1597–1601.
- (63) Koopman, G., Reutelingsperger, C. P., Kuijten, G. A., Keehnen, R. M., Pals, S. T., and van Oers, M. H. (1994) Annexin V for flow cytometric detection of phosphatidylserine expression on B cells undergoing apoptosis. *Blood* 84, 1415–1420.
- (64) Hengartner, M. O. (2000) The biochemistry of apoptosis. *Nature* 407, 770–776.
- (65) Degterev, A., Boyd, M., and Yuan, J. (2003) A decade of caspases. *Oncogene* 22, 8543–8567.
- (66) Fulda, S., and Debatin, K.-M. (2006) Extrinsic versus intrinsic apoptosis pathways in anticancer chemotherapy. *Oncogene* 25, 4798–4811.
- (67) Kruidering, M., and Evan, G. I. (2000) Caspase-8 in apoptosis: the beginning of "the end"? *IUBMB Life* 50, 85–90.
- (68) Kang, K. S., Wang, P., Yamabe, N., Fukui, M., Jay, T., and Zhu, B. T. (2010) Docosahexaenoic Acid Induces Apoptosis in MCF-7 Cells In Vitro and In Vivo via Reactive Oxygen Species Formation and Caspase 8 Activation. *PLoS ONE* 5, e10296.
- (69) Inoue, A., Muranaka, S., Fujita, H., Kanno, T., Tamai, H., and Utsumi, K. (2004) Molecular mechanism of diclofenac-induced apoptosis of promyelocytic leukemia: dependency on reactive oxygen species, Akt, Bid, cytochrome and caspase pathway. *Free Radic. Biol. Med.* 37, 1290–1299.

- (70) Kerr, J. F., Wyllie, A. H., and Currie, A. R. (1972) Apoptosis: a basic biological phenomenon with wide-ranging implications in tissue kinetics. *Br. J. Cancer* 26, 239–257.
- (71) Mot, A. I., Liddell, J. R., White, A. R., and Crouch, P. J. (2016) Circumventing the Crabtree Effect: A method to induce lactate consumption and increase oxidative phosphorylation in cell culture. *Int. J. Biochem. Cell Biol* 79, 128–138.
- (72) Nakahira, K., Haspel, J. A., Rathinam, V. A. K., Lee, S.-J., Dolinay, T., Lam, H. C., Englert, J. A., Rabinovitch, M., Cernadas, M., Kim, H. P., Fitzgerald, K. A., Ryter, S. W., and Choi, A. M. K. (2011) Autophagy proteins regulate innate immune responses by inhibiting the release of mitochondrial DNA mediated by the NALP3 inflammasome. *Nat. Rev. Mol. Cell Biol.* 12, 222–230.
- (73) Reers, M., Smith, T. W., and Chen, L. B. (1991) J-Aggregate formation of a carbocyanine as a quantitative fluorescent indicator of membrane potential. *Biochemistry* 30, 4480–4486.
- (74) Würthner, F., Kaiser, T. E., and Saha-Möller, C. R. (2011) J-Aggregates: From Serendipitous Discovery to Supramolecular Engineering of Functional Dye Materials. *Angew. Chem. Int. Ed.* 50, 3376–3410.
- (75) Ly, J. D., Grubb, D. R., and Lawen, A. (2003) The mitochondrial membrane potential ( $\Delta\psi_m$ ) in apoptosis; an update. *Apoptosis* 8, 115–128.
- (76) Gottlieb, E., Armour, S. M., Harris, M. H., and Thompson, C. B. (2003) Mitochondrial membrane potential regulates matrix configuration and cytochrome c release during apoptosis. *Cell Death Differ.* 10, 709–717.
- (77) Benz, R., and McLaughlin, S. (1983) The molecular mechanism of action of the proton ionophore FCCP (carbonylcyanide p-trifluoromethoxyphenylhydrazone). *Biophysical Journal* 41, 381–398.
- (78) Horobin, R. W., Trapp, S., and Weissig, V. (2007) Mitochondriotropics: A review of their mode of action, and their applications for drug and DNA delivery to mammalian mitochondria. *J. Control. Release* 121, 125–136.
- (79) Taiwo, F. A. (2008) Mechanism of tiron as scavenger of superoxide ions and free electrons. *J. Spectrosc.* 22, 491–498.
- (80) Goldstein, S., and Czapski, G. (1984) Mannitol as an OH. scavenger in aqueous solutions and in biological systems. *Int. J. Radiat. Biol.* 46, 725–729.
- (81) Matheson, I. B. C., and Lee, J. (1979) Chemical Reaction Rates of Amino Acids with Singlet Oxygen. *Photochem. Photobiol.* 29, 879–881.
- (82) Foote, C. S., and Clennan, E. L. (1995) Properties and Reactions of Singlet Dioxygen, in *Active Oxygen in Chemistry* (Foote, C. S., Valentine, J. S., Greenberg, A., and Liebman, J. F., Eds.), pp 105–140.
- (83) Scott, B. C., Aruoma, O. I., Evans, P. J., O'Neill, C., Van der Vliet, A., Cross, C. E., Tritschler, H., and Halliwell, B. (1994) Lipoic and dihydrolipoic acids as antioxidants. A critical evaluation. *Free Radic. Res.* 20, 119–133.
- (84) Packer, L., Witt, E. H., and Tritschler, H. J. (1995) alpha-Lipoic acid as a biological antioxidant. *Free Radic. Biol. Med.* 19, 227–250.
- (85) Huxtable, R. J. (1992) Physiological actions of taurine. *Physiol. Rev* 72, 101–163.
- (86) Cunningham, C., Tipton, K. F., and Dixon, H. B. (1998) Conversion of taurine into N-chlorotaurine (taurine chloramine) and sulphaacetaldehyde in response to oxidative stress. *Biochem. J.* 330, 939–945.
- (87) Weiss, S. J., Klein, R., Slivka, A., and Wei, M. (1982) Chlorination of Taurine by Human Neutrophils. *J. Clin. Invest.* 70, 598–607.
- (88) Vogt, W. (1995) Oxidation of methionyl residues in proteins: tools, targets, and reversal. *Free Radic. Biol. Med.* 18, 93–105.

- (89) Giandomenico, A. R., Cerniglia, G. E., Biaglow, J. E., Stevens, C. W., and Koch, C. J. (1997) The importance of sodium pyruvate in assessing damage produced by hydrogen peroxide. *Free Radic. Biol. Med.* 23, 426–434.
- (90) Brand, M. D. (2010) The sites and topology of mitochondrial superoxide production. *Exp. Gerontol* 45, 466–472.
- (91) Holmström, K. M., and Finkel, T. (2014) Cellular mechanisms and physiological consequences of redox-dependent signalling. *Nat. Rev. Mol. Cell Biol.* 15, 411–421.
- (92) Bucana, C., Saiki, I., and Nayar, R. (1986) Uptake and accumulation of the vital dye hydroethidine in neoplastic cells. *J. Histochem. Cytochem.* 34, 1109–1115.
- (93) Robinson, K. M., Janes, M. S., Pehar, M., Monette, J. S., Ross, M. F., Hagen, T. M., Murphy, M. P., and Beckman, J. S. (2006) Selective fluorescent imaging of superoxide in vivo using ethidium-based probes. *Proc. Natl. Acad. Sci. U.S.A.* 103, 15038–15043.
- (94) Méndez-Hurtado, J., López, R., Suárez, D., and Menéndez, M. I. (2012) Theoretical Study of the Oxidation of Histidine by Singlet Oxygen. *Chem. Eur. J.* 18, 8437–8447.
- (95) Howell, S. B., Safaei, R., Larson, C. A., and Sailor, M. J. (2010) Copper transporters and the cellular pharmacology of the platinum-containing cancer drugs. *Mol. Pharmacol.* 77, 887–894.
- (96) Holzer, A. K., Manorek, G. H., and Howell, S. B. (2006) Contribution of the major copper influx transporter CTR1 to the cellular accumulation of cisplatin, carboplatin, and oxaliplatin. *Mol. Pharmacol.* 70, 1390–1394.
- (97) Holzer, A. K., Varki, N. M., Le, Q. T., Gibson, M. A., Naredi, P., and Howell, S. B. (2006) Expression of the human copper influx transporter 1 in normal and malignant human tissues. *J. Histochem. Cytochem.* 54, 1041–1049.
- (98) Park, G. Y., Wilson, J. J., and Song, Y. (2012) Phenanthriplatin, a monofunctional DNA-binding platinum anticancer drug candidate with unusual potency and cellular activity profile, in, pp 11987–11992.
- (99) Mendes, F., Groessl, M., Nazarov, A. A., Tsybin, Y. O., Sava, G., Santos, I., Dyson, P. J., and Casini, A. (2011) Metal-Based Inhibition of Poly(ADP-ribose) Polymerase – The Guardian Angel of DNA. *J. Med. Chem.* 54, 2196–2206.
- (100) Humphreys, K. J., Karlin, K. D., and Rokita, S. E. (2002) Targeted Strand Scission of DNA Substrates by a Tricopper(II) Coordination Complex. *J. Am. Chem. Soc.* 124, 8055–8066.
- (101) Li, L., Karlin, K. D., and Rokita, S. E. (2005) Changing Selectivity of DNA Oxidation from Deoxyribose to Guanine by Ligand Design and a New Binuclear Copper Complex. *J. Am. Chem. Soc.* 127, 520–521.
- (102) Slator, C., Barron, N., Howe, O., and Kellett, A. (2016) [Cu(*o*-phthalate)(phenanthroline)] Exhibits Unique Superoxide-Mediated NCI-60 Chemotherapeutic Action through Genomic DNA Damage and Mitochondrial Dysfunction. *ACS Chem. Biol.* 11, 159–171.
- (103) Fulda, S., Galluzzi, L., and Kroemer, G. (2010) Targeting mitochondria for cancer therapy. *Nat. Rev. Drug. Discov.* 9, 447–464.
- (104) Holmström, K. M., and Finkel, T. (2014) Cellular mechanisms and physiological consequences of redox-dependent signalling. *Nat. Rev. Mol. Cell Biol.* 15, 411–421.
- (105) Cairns, R. A., Harris, I. S., and Mak, T. W. (2011) Regulation of cancer cell metabolism. *Nat. Rev. Mol. Cell Biol.* 11, 85–95.
- (106) Pelicano, H., Carney, D., and Huang, P. (2004) ROS stress in cancer cells and therapeutic implications. *Drug Resist. Updates* 7, 97–110.
- (107) Liou, G.-Y., and Storz, P. (2010) Reactive oxygen species in cancer. *Free Radic. Res.* 44, 479–496.
- (108) Warburg, O. (1956) On the origin of cancer cells. *Science* 123, 309–314.
- (109) Biasutto, L., Dong, L.-F., Zoratti, M., and Neuzil, J. (2010) Mitochondrially targeted anti-



cancer agents. *Mitochondrion* 10, 670–681.

(110) Rin Jean, S., Tulumello, D. V., Wisnovsky, S. P., Lei, E. K., Pereira, M. P., and Kelley, S. O. (2014) Molecular Vehicles for Mitochondrial Chemical Biology and Drug Delivery. *ACS Chem. Biol.* 9, 323–333.

(111) Wisnovsky, S., Lei, E. K., Jean, S. R., and Kelley, S. O. (2016) Mitochondrial Chemical Biology: New Probes Elucidate the Secrets of the Powerhouse of the Cell. *Cell Chem. Biol* 23, 917–927.

(112) Chamberlain, G. R., Tulumello, D. V., and Kelley, S. O. (2013) Targeted delivery of doxorubicin to mitochondria. *ACS Chem. Biol.* 8, 1389–1395.

(113) Marrache, S., Pathak, R. K., and Dhar, S. (2014) Detouring of cisplatin to access mitochondrial genome for overcoming resistance. *Proc. Natl. Acad. Sci. U.S.A.* 111, 10444–10449.

(114) Zhou, W., Wang, X., Hu, M., Zhu, C., and Guo, Z. (2014) A mitochondrion-targeting copper complex exhibits potent cytotoxicity against cisplatin-resistant tumor cells through multiple mechanisms of action. *Chem. Sci.* 5, 2761–2770.

(115) Mahon, K. P., Potocky, T. B., Blair, D., Roy, M. D., Stewart, K. M., Chiles, T. C., and Kelley, S. O. (2007) Deconvolution of the Cellular Oxidative Stress Response with Organelle-Specific Peptide Conjugates. *Chem. Biol.* 14, 923–930.

(116) Wisnovsky, S., Jean, S. R., and Kelley, S. O. (2016) Mitochondrial DNA repair and replication proteins revealed by targeted chemical probes. *Nat. Chem. Biol.* 12, 567–573.



## Chapter 5

### **Bis-Mn<sup>2+</sup> bis-1,10-phenanthroline octanedioate induces autophagic cell death *via* ROS-mediated DNA damage**

---

Submitted to *Redox Biology*, accepted.

Creina Slator, Zara Molphy, Vickie McKee and Andrew Kellett\*.

Within this chapter, I was the primary contributor to all aspects of experimental design, execution, analysis and manuscript preparation. A significant proportion of my PhD research was dedicated towards this body of work. Z. Molphy conducted circular dichroism and viscosity studies. Supporting information associated with this chapter can be found in Appendix D.

## 5.1 Abstract

There is an unmet need for novel metal-based chemotherapeutics with alternative modes of action compared to clinical agents such as cisplatin and metallo-bleomycin. Recent attention in this field has focused on designing intracellular ROS-mediators as powerful cytotoxins of human cancers and identifying potentially unique toxic mechanisms underpinning their utility. Herein we report the developmental *di*-Mn<sup>2+</sup> therapeutic [Mn<sub>2</sub>(μ-oda)(phen)<sub>4</sub>(H<sub>2</sub>O)<sub>2</sub>][Mn<sub>2</sub>(μ-oda)(phen)<sub>4</sub>(oda)<sub>2</sub>]·4H<sub>2</sub>O (**Mn-Oda**) induces autophagy-promoted apoptosis in human ovarian cancer cells (SKOV3). The complex was initially identified to intercalate DNA by topoisomerase I unwinding and circular dichroism spectroscopy. Intracellular DNA damage, detected by γH2AX and the COMET assay, however, is not linked to direct **Mn-Oda** free radical generation, but is instead mediated through the promotion of intracellular reactive oxygen species (ROS) leading to autophagic vacuole formation and downstream nuclear degradation. To elucidate the cytotoxic profile of **Mn-Oda**, a wide range of biomarkers specific to apoptosis and autophagy including caspase release, mitochondrial membrane integrity, fluorogenic probe localisation, and cell cycle analysis were employed. Through these techniques, the activity of **Mn-Oda** was compared directly to *i.*) the pro-apoptotic clinical anticancer drug doxorubicin, *ii.*) the multimodal histone deacetylase inhibitor suberoyanilide hydroxamic acid, and *iii.*) the autophagy inducer rapamycin. In conjunction with ROS-specific trapping agents and established inhibitors of autophagy, we have identified autophagy-induction linked to superoxide production, with confocal image analysis of SKOV3 cells further supporting autophagosome formation.

## 5.2 Introduction

Metals ions including  $\text{Mn}^{2+}$ ,  $\text{Mg}^{2+}$ ,  $\text{Cu}^{2+}$  and  $\text{Zn}^{2+}$  are essential in the biochemistry and physiology of living organisms as they are required cofactors for ubiquitous enzymes, transcription factors, transmembrane transporters, growth factors and receptors.<sup>1</sup> Deficiencies in these metal ions result in the onset of neurodegenerative diseases including Alzheimer's, Parkinson's and Menkes syndrome, while  $\text{Cu}^{2+}$  overload is associated with Wilson's disease.<sup>2</sup> The incorporation of metal ions into complex scaffolds containing targeting ligands, however, has resulted in the development of anti-tumoural drug candidates<sup>3-5</sup> capable of mediating apoptotic cell death through a combination of intrinsic and extrinsic pathways.<sup>6</sup> Numerous examples of metal complexes inducing cancer cytotoxicity through apoptosis have been reported in the literature;<sup>7</sup> this fatal mechanism relies on a class of cysteine-dependent aspartate-specific proteases (caspases) that activate and execute the apoptotic process leading to characteristic morphological changes and ultimately cell death.

While the majority of cytotoxic metallodrugs act through the induction of apoptosis, the alternative pathway of autophagy has recently emerged as an attractive process to effect cytotoxicity.<sup>8</sup> The phenomenon of autophagy was mechanistically unknown prior to the 1990's until seminal work by Ohsumi revealed the systematic activation and identification of genes essential in the overall process.<sup>9-12</sup> Autophagy is considered as an evolutionary-conserved self-digestion, and quality control mechanism where cell survival and degradation processes compete in order to sustain homeostasis and regulate the longevity of proteins, nucleic acids, whole organelles and pathogenic agents.<sup>13</sup> Under the constraints of increased and/or external stress factors, however, elevated accumulation of autophagic vacuoles and organelle elimination renders the cell incapable of normal function and thus results in cell death.<sup>14</sup> Furthermore, autophagy can be induced and up-regulated in response to intracellular reactive oxygen species (ROS),<sup>15,16</sup> and acts as a protective antioxidant pathway for oxidative stress associated with neurodegenerative diseases.<sup>17</sup> The hormone therapy agent tamoxifen induces elevated levels of intracellular ROS resulting in positive feedback of  $\text{Zn}^{2+}$  accumulation, mediating the initiation of autophagy in breast cancer cell line, MCF-7.<sup>18</sup> Metal complexes of Ru(II), Pt(II), Mn(II) and Cu(II) are also known to activate the autophagic pathway,<sup>8</sup> however, with the exception of selected Pt(II)-based complexes, the co-activation of apoptosis and autophagy occurs for almost all other metal compounds and is known to be ROS dependent. The current paradigm of autophagy research (in respect to human cancer) is considered to be multifold and somewhat contradictory: *i.*) it acts as a suppressor toward tumorigenesis;<sup>19</sup> *ii.*) it is known to promote tumour survival under starvation or hypoxic conditions of low blood supply and other stress factors attributed to tumour stroma,<sup>20,21</sup> and *iii.*) the efficient induction of autophagy can be exploited as a pro-death mechanism, particularly in apoptotic defective cancer cells.<sup>22</sup>

This group has recently reported the title compound—Mn<sup>2+</sup> *bis*-1,10-phenanthroline (phen) *di*-salt complex, bridged with octanedioate (oda) ([Mn<sub>2</sub>(μ-oda)(phen)<sub>4</sub>(H<sub>2</sub>O)<sub>2</sub>][Mn<sub>2</sub>(μ-oda)(phen)<sub>4</sub>(oda)<sub>2</sub>]·4H<sub>2</sub>O (**Mn-Oda**))—in conjunction with a cationic Cu<sup>2+</sup> analogue, [Cu<sub>2</sub>(μ-oda)(phen)<sub>4</sub>]<sup>2+</sup> (**Cu-Oda**) as potent *in vitro* anticancer agents with toxicity toward a panel of colorectal cancers (HT29, SW480 and SW620) linked to DNA binding and ROS induction.<sup>4</sup> Comparison of the two agents revealed distinctive modes of action as both complexes were found to bind DNA ( $K_{\text{app}} \sim 10^5 \text{ M}(\text{bp}^{-1})$ ) with fluorescent quenching indicating possible intercalation. However, the **Mn-Oda** complex was shown to powerfully act as both a superoxide dismutase (SOD) and catalase (CAT) mimetic and elicited exceptional levels of endogenous ROS within cancer cells when examined using the intracellular indicator 2',7'-dichlorofluorescein diacetate. Given the promising results observed for **Mn-Oda**, coupled with recent interest in the discovery of new autophagic-activating therapeutic leads, this contribution describes the sequential cytotoxic mechanism of this compound leading to autophagy and intrinsic apoptosis, initiated by superoxide (O<sub>2</sub><sup>•-</sup>) production. To unravel these properties, an extensive range of biophysical, molecular biological, and microscopy experiments were undertaken using a variety of dsDNA polymers along with the ovarian solid epithelial cancer cell line SKOV3. Our motivation for using SKOV3 stems from its intrinsic resistance to cisplatin and our experience in using this cell line to identify the mechanistic profile of the pro-apoptotic anticancer lead [Cu(*o*-phthalate)(phen)].<sup>6</sup> Thus, in this work we delineate the cytotoxic properties of **Mn-Oda** with the Cu<sup>2+</sup>-phen chemotype and reveal the complex as an inducer of autophagic cell death *via* ROS-mediated DNA damage. Further, while the complex was identified as an efficient intercalator of dsDNA, we propose intracellular DNA damage is not induced directly by the **Mn-Oda** complex, but rather by cytoplasmic exogenous stress factors that contribute toward ROS production—notably autophagosome formation, prior to apoptotic activation.

## 5.3 Materials and Methods

### 5.3.1 Materials and reagents.

All chemicals used for complex synthesis were purchased from Sigma Aldrich without further purification. The following assays were purchased from Merck Millipore and procedures were followed as per manufacturers protocols: Guava Nexin® Reagent (4500-0450), Guava EasyCyte™ MitoPotential Kit (4500-0250), Guava Caspase 8 FAM and Caspase 9 SR (4500-0640) and Guava Caspase 3/7. Propidium iodide (BTIU40017) was purchased from VWR. RNase A (12091-021), Alexa Flour 488 goat anti-mouse IgG F(ab)<sub>2</sub> fragment (A-11020), Alexa flour 488-phalloidin (A12379), DAPI (D1306) and Mitotracker Deep Red (M22426) were purchased from Biosciences Ireland. Anti-phospho-histone H2AX (05-636) was purchased from Merck Millipore. Salmon testes DNA (D1626) and synthetic double stranded alternating co-polymers, Poly[d(G-C)<sub>2</sub>] (P9389) and Poly[d(A-T)<sub>2</sub>] (P0883) used in CD studies were purchased from Sigma Aldrich. pUC19 plasmid DNA (N3041), CutSmart® buffer (B7204), 100x BSA (B9000) and topoisomerase I (E. coli) (M0301) were all purchased from New England Biolabs. LC3 isoform LC3A rabbit monoclonal antibody (Cell Signalling) was kindly donated by Dr. Joanne Keenan while goat anti-rabbit conjugated Alex Fluor-647 (ThermoFisher) was donated by Dr. Clair Gallagher.

### 5.3.2 Drug-DNA binding interactions.

#### 5.3.2.1 Circular dichroism spectrometry.

Complex-DNA interactions were analysed using Starna quartz cuvettes in 10 mM PBS solution (pH 7.0) in the presence of 25 mM NaCl. Solutions of salmon testes DNA (stDNA,  $\epsilon_{260} = 12824 \text{ M(bp)}^{-1} \text{ cm}^{-1}$ ), Poly[(d(A-T)<sub>2</sub>] ( $\epsilon_{260} = 13100 \text{ M(bp)}^{-1} \text{ cm}^{-1}$ ) and Poly[(d(G-C)<sub>2</sub>] ( $\epsilon_{260} = 16800 \text{ M(bp)}^{-1} \text{ cm}^{-1}$ ) were initially heat treated to denature and then allowed to slowly renature prior to quantification using an Agilent Cary 100 dual beam spectrophotometer equipped with a 6 × 6 Peltier multicell system with temperature controller, to give working solutions with a final DNA concentration of ~100 µM. Spectra were captured in the range of 200-400 nm and measurements were recorded at a rate of 1 nm per second. DNA solutions were incubated for 30 minute periods at 37 °C with **Mn-Oda** at varying concentration loadings of 1.0, 1.5, 2.0 and 2.5%.

#### 5.3.2.2 Viscosity.

Experiments were conducted using DV-II-Programmable Digital Viscometer equipped with Enhanced Brookfield UL Adapter.<sup>23</sup> Briefly, a concentrated solution of salmon testes dsDNA was prepared by dissolving the fibres in 80 mM of HEPES buffer (pH = 7.2). In order to shear dsDNA, a 15 ml solution was passed rapidly through a 19- gauge needle 15 times before being sonicated for 90 min. A 15 ml stDNA solution was then prepared at ~1.0 mM in 80 mM HEPES buffer and the complex was added in ratios from 0.10-0.20 (where  $r = [\text{compound/DNA}]$ ) and viscosity was

recorded as previously reported.<sup>23</sup> Viscosity values,  $\eta$ , (unit: cP) were presented as  $\eta / \eta_0$  versus [compound]/[DNA] ratio, in which  $\eta_0$  refers to the viscosity of DNA alone and  $\eta$  refers to that of the DNA-complex solution.

#### **5.3.2.2 Topoisomerase I mediated relaxation.**

Topoisomerase I relaxation was carried out using a modified method to previously reported protocols.<sup>24</sup> 400 ng of pUC19 plasmid DNA was exposed to varying concentrations of drug (0.1 - 400  $\mu$ M) for 30 min at room temperature in a final volume of 20  $\mu$ L containing 80 mM HEPES buffer (pH 7.2), CutSmart® buffer and 100x BSA. Topoisomerase I (1 unit) was added to the mixture and incubated for 15 min at 37 °C to ensure relaxation of plasmid DNA. The enzymatic reaction was quenched with SDS (0.25%), protein kinase (250  $\mu$ g/ml) and incubated for 30 minutes at 50 °C. Samples were loaded onto 1.2% agarose gel with 6x loading buffer. Topoisomers of DNA were separated by electrophoresis in 1x TBE buffer at room temperature for 3 h min at 40 V followed by 2.5 h at 50 V. The agarose gel was post-stained using an ethidium bromide bath (25  $\mu$ M) for 20 min at room temperature. Finally, the gel was soaked in deionized water for 24 h and imaged using a UV transilluminator.

### **5.3.3 *In cellulo* studies.**

#### **5.3.3.1 Cell culture.**

SKOV3 cells were cultured in RPMI-1640 media, supplemented with 10% FBS and incubated at 37 °C in 5% CO<sub>2</sub> and routinely tested for mycoplasma. Cells were seeded and left to adhere and enter cell cycle overnight. **Mn-Oda** stock solutions were prepared in PBS, CCCP, Rapa and SAHA solutions in DMSO and Dox in 50:50 DMSO:H<sub>2</sub>O and further diluted in culture media. Stocks containing DMSO were prepared in the mM range to ensure final incubation concentrations contained < 0.1% v/v.

#### **5.3.3.2 Viability.**

Cells were seeded at 5 x 10<sup>3</sup> cells/well in a 96-well plate overnight and subsequently exposed to drug treatment for 24 h (1  $\mu$ M Mn-Oda, 1  $\mu$ M Dox, 75  $\mu$ M CCCP, 50  $\mu$ M Rapa and 100  $\mu$ M SAHA, Figure S3). For co-treatment experiments, antioxidants and autophagy inhibitors tiron, D-mannitol (Man), histidine (His), sodium pyruvate (Py), 3-methyladenine (3-MA) and NH<sub>4</sub>Cl, chloroquine (CQ) were treated at 1mM (with exception of CQ at 10  $\mu$ M) 2 h prior to drug exposure to facilitate intracellular accumulation. Spent media was removed, cells were detached with trypsin:EDTA (0.25%:0.02% in PBS) and whole samples (100  $\mu$ L) were added to 100  $\mu$ L Guava Viacount reagent and incubated for 10 min at room temperature. Viability was acquired on Guava EasyCyte HT with Viacount software.



#### **5.3.3.3 Nexin® assay.**

SKOV3 cells were seeded at  $3 \times 10^4$  cells/well in 24-well plates overnight and incubated with drug containing media. After the exposure period, spent media was removed, cells were washed with PBS and washings were kept in 1.5 ml microtubes. Subsequently, cells were detached with trypsin and neutralized with fresh media. PBS washings were transferred back into microtubes containing detached cells and centrifuged at 1300 rpm for 5 min and culture media was aspirated. A sufficient volume of media was added to give a concentration range of  $2 \times 10^5$  to  $1 \times 10^6$  cell/ml. 100  $\mu$ l of sample was transferred to 96-well round bottom plate and 100  $\mu$ L of Guava Nexin® Reagent was added and incubated for 20 min at room temperature. Samples were acquired on Guava EasyCyte HT using Nexin software. Innate doxorubicin fluorescence in filter 583/26 nm was accounted for and subtracted within the relevant quadrants.

#### **5.3.3.4 Mitochondrial membrane potential.**

Cells were treated as previously described. Cells were resuspended in 600  $\mu$ l of fresh media to give cell concentration  $2 \times 10^4$  to  $5 \times 10^5$  cells/ml from which 200  $\mu$ l was transferred to a 96-well round bottom plate. 50X staining solution (4  $\mu$ l) containing JC-1 and 7-aminoactinomycin D (7-AAD) was added to each sample, subsequently incubated at 37 °C in darkness (30 min) and acquired on Guava EasyCyte HT using MitoPotential software. Compensation to correct fluorescent overlap between filters was conducted pre-acquisition.

#### **5.3.3.5 Caspase 8 FAM and 9 SR, Caspase 3/7 FAM.**

The following fluorescent labelled inhibitors of caspase (FLICA) were used to ascertain the activation of Caspase 3/7, 8 and 9 respectively; FAM-DEVD-FMK, FAM-LETD-FMK and SR-LEHD-FMK. Samples were prepared prior to staining in a similar manner as that described in the Nexin Assay. Cells were transferred to 1.5 ml microtubes and resuspended in 100  $\mu$ l media. 10  $\mu$ l of 10X caspase 9 SR working solution and 10  $\mu$ l of caspase 8 FAM were added and incubated for 1 h at 37 °C in the dark. Cells were resuspended in 200  $\mu$ l of caspase 7-AAD working solution and transferred to 96-well round bottom plate, which was left to incubate for 10 min at room temperature. Samples were acquired on Guava EasyCyte HT flow cytometer using Guava Caspase software. Compensation to correct fluorescent overlap between filters was conducted pre-acquisition and innate doxorubicin fluorescence in filter 583/26 nm was accounted for and subtracted within the relevant quadrants.

#### **5.3.3.6 Cell cycle analysis.**

Cellular DNA content was conducted in a similar manner to previously reported methods.<sup>25</sup>  $3 \times 10^4$  cell/well were seeded in 24-well culture plates, drug treated and collected as previously stated. After detachment, cells were fixed in 70% ice-cold EtOH and stored at -20°C (>12 h). Samples

were stained with 200  $\mu$ L PI staining solution (containing 50  $\mu$ g/ml propidium iodide, 100  $\mu$ g/ml DNase-free RNase A, 0.1% triton X-100 in 1X PBS) (30 min, room temperature). Samples were acquired on Guava EasyCyte HT flow cytometer and normalized to the sum of events in G<sub>0</sub>/G<sub>1</sub>, S and G<sub>2</sub>/M phases.

#### **5.3.3.7 Immunodection of $\gamma$ H2AX.**

Samples were prepared similarly to previously reported methods.<sup>26</sup>  $6 \times 10^4$  cells/well were seeded in 12-well plates and treated for 24 h with compounds and fixed with 1.5% formaldehyde (15 min, room temperature) followed by ice-cold 70% ethanol and stored at -20 °C. Samples were resuspended in permeabilisation buffer (0.25% Triton X-100 in PBS) for 30 min on ice and blocked with 2% BSA (30 min, room temperature). Primary antibody (1:500) was incubated for 2 h at room temperature followed by secondary antibody (1:1000) for 1h at room temperature and co-stained for 10 min with 5  $\mu$ g/ml propidium iodide. Samples were acquired using ExpressPro software on Guava EasyCyte.

#### **5.3.3.8 DNA degradation with COMET assay.**

Cells were seeded at  $1.5 \times 10^5$  cells/well in 6-well plates the evening prior to drug addition. After 24 h drug incubation, cells were harvested and 50  $\mu$ L was resuspended in 500  $\mu$ L low melting point agarose to give a final density of  $1.5 \times 10^5$  cell/ml. 50  $\mu$ L was spread onto Trevigen COMET slides and allowed to solidify (1 h, 4 °C). Samples were lysed (2.5 M NaCl, 100 mM EDTA, 10 mM Tris.HCl, pH 10) overnight at 4 °C. Slides were allowed to equilibrate in cold electrophoresis buffer (300 mM NaOH, 1.0 mM EDTA, pH 13) for 30 mins at 4°C. Electrophoresis was run at 300 mA for 30 min with buffer levels adjusted to give a consistent voltage of 25 V. Slides were then washed with water, neutralised in buffer (400 mM Tris.HCl, pH 7.5) (3 x 5 min), fixed with 70% ethanol (30 min) and dried for desiccated storage (15 min at 37 °C). Prior to scoring, slides were rehydrated for 15 min before staining with propidium iodide solution (10  $\mu$ g/ml, 10 min room temperature) and imaged through a 10X lens on a Leica DFC 500 epi-fluorescent microscope. Images were then analysed using Open COMET plugin in Image J (80 comets for Dox and >100 comets for control and Mn-Oda) and plotted using GraphPad Prism software.

### **5.3.4 Acquisition of confocal images.**

#### **5.3.4.1 Cell morphology.**

Cells ( $1.4 \times 10^5$ ) were seeded in 35 mm glass bottom petri dishes and allowed to attach overnight. Samples were then exposed to drugs for 24 h (1  $\mu$ M Mn-Oda, Rapa 50  $\mu$ M and SAHA 100  $\mu$ M). Cells were incubated with media containing MitoTracker Deep Red (150 mM, 30 min, 37°C) and fixed with 4% paraformaldehyde (PFA) (30 min, room temperature). Samples were permeabilised

with 0.25% Triton X-100 (15 min). To avoid non-specific staining, cells were blocked with 1% BSA in PBS solution (30 min, 37 °C) and subsequently stained with Alexa Fluor 488-phalloidin (10U/100ul, 30 min), followed by DAPI (4:10,000, 10 min) and mounted in ProLong Gold. Images were acquired on STED-Leica DMI8 confocal microscope equipped with CCD camera and 100X oil-immersion objective. DAPI was excited with 405 nm picoquant laser unit and emission captured between 387 - 474 nm. Alexa Fluor 488 was excited at 499 nm with emission captured between 490 - 566 nm, and MitoTracker Deep Red was excited at 653 nm where emission was captured at 658 - 779 nm. Images were acquired where by combinations of excitation wavelengths and emission filters for specific dyes are applied sequentially.

#### **5.3.4.2 Autophagic detection with LC3.**

SKOV-3 cells were seeded as previously described. Samples were fixed with 4% PFA (30 min, room temperature), permeabilised with 0.25% Triton X-100 (30 mins, 4°C) and blocked with 2% BSA (30 min, room temperature). Cells were incubated with primary antibody (1:500) was prepared in blocking solution (overnight, 4°C), secondary antibody (1:1000) goat anti-rabbit Alexa Fluor 647 (1 h, room temperature) and DAPI (4:10,000 min at room temperature) and mounted with ProLong Gold. Images were acquired on STED-Leica DMI8 confocal microscope with 100X lens. Alex Fluor 647 was excited with 653 nm laser and emission captured between 658-783 nm, while DAPI was excited with 405 nm picoquant laser unit and emission captured between 435-560 nm.

#### **5.3.4.3 Autophagic detection with MDC.**

Cells were seeded in glass bottom petri dishes as previously described. Following drug exposure, samples were incubated with monodansylcadervine (MDC) (50 µM, 37°C, 10 min), washed with PBS and confocal images were immediately acquired on STED-Leica DMI8 confocal microscope equipped with 100X objective. Samples were excited with 405 nm picoquant laser unit and emission captured 470-560 nm. Intensity profiles were analysed using Image J V2.0 on raw images in 8-bit format without further modification. MDC coloured images were enhanced in Adobe Photoshop for printing purposes only.

#### **5.4.5 Statistical Analysis.**

All ex vivo data is presented as mean  $\pm$  standard deviation where  $n = 3$ . Unpaired t-tests with Holm-Sidak method were applied to evaluate statistical analysis in GraphPad Prism V6 where  $p \leq 0.05$  were considered significant.

## 5.4 Results and discussion

### 5.4.1 Preparation of Mn-Oda

The complex  $[\text{Mn}_2(\eta^1\eta^1\mu^2\text{-oda})(\text{phen})_4(\text{H}_2\text{O})_2][\text{Mn}_2(\eta^1\eta^1\mu^2\text{-oda})(\text{phen})_4(\eta^1\text{-oda})_2]\cdot 4\text{H}_2\text{O}$  was prepared according to the method reported by Casey *et al.*<sup>27</sup> and contains  $[\text{Mn}_2(\eta^1\eta^1\mu^2\text{-oda})(\text{phen})_4(\text{H}_2\text{O})_2]^{2+}$  cations and  $[\text{Mn}_2(\eta^1\eta^1\mu^2\text{-oda})(\text{phen})_4(\eta^1\text{-oda})_2]^{2-}$  anions (both of which are centrosymmetric) along with four solvate water molecules. All of the manganese centers are 6-coordinate with two bidentate phen ligands and two oxygen donors in the *cis* positions. In both complex ions two manganese centers are linked by an oda<sup>2-</sup> ligand; the sixth site is occupied by water in the cation and by further oda<sup>2-</sup> groups in the anion (Figure 1A and B). Hydrogen bonding between the coordinated water molecule and the uncoordinated carboxylate groups of the anion link the complex ions into zig-zag chains and the chains are linked together by further hydrogen bonding involving the uncoordinated water molecules, generating a 3D network (Figure 1C).

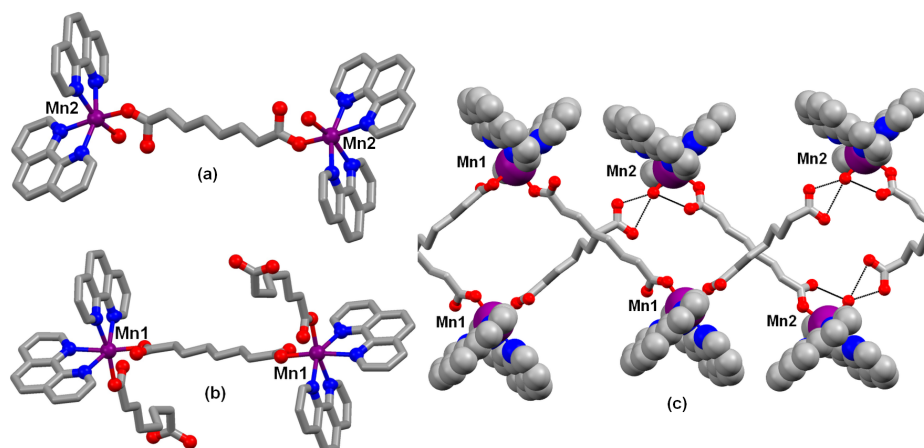


**Figure 5. 1A.** The cation  $[\text{Mn}_2(\eta^1\eta^1\mu^2\text{-oda})(\text{phen})_4(\text{H}_2\text{O})_2]^{2+}$ , **B.** Anion  $[\text{Mn}_2(\eta^1\eta^1\mu^2\text{-oda})(\text{phen})_4(\eta^1\text{-oda})_2]^{2-}$ , and **C.** Hydrogen bonded chains. Hydrogen atoms omitted for clarity, hydrogen bonds indicated by black dashed lines. Redrawn from coordinates taken from reference.<sup>27</sup> Colour key: C (grey), O (red), N (blue) and Mn (purple).

### 5.4.2 *In vitro* Drug-DNA interactions reveal intercalation at the minor groove

#### 5.4.2.1 Topoisomerase I mediated relaxation

Topoisomerases (Topo) are a specialised class of nuclear enzymes that catalyse the transient cleavage, passage and resealing of either a single strand (topo I) or double strands (topo II) of DNA in order to relax chain intertwinement, release superhelical tension and permit change in topology during replication, transcription and recombination.<sup>28,29</sup> Topo I, isolated from *E. coli*, specifically relaxes negatively coiled superhelical plasmid DNA (scDNA),<sup>30</sup> such as the pUC19 substrate used in this study. Topo I mediated relaxation of pUC19 was identified with increasing **Mn-Oda** (Figure 2A). The complex was found to completely relax scDNA at 20  $\mu\text{M}$  with positively wound

topology of intact scDNA being observed thereafter. This profile is comparable to that of classical intercalating molecules such as ethidium bromide (Figure S1) which unwinds DNA by 26° yielding similar topoisomeric patterns.<sup>31</sup> Doxorubicin (Dox), a clinically used Topo II poison,<sup>32</sup> exhibits enzymatic inhibitory effects on the Topo I with DNA relaxation occurring at 1 μM (Figure 2B). Samples treated with Dox extending this concentration render DNA degradation and shearing most likely through ROS generation consequent to redox cycling of the quinone moiety,<sup>33-35</sup> and these results in agreement with those described elsewhere.<sup>36</sup> Thus, the **Mn-Oda** complex is capable of unwinding dsDNA *via* intercalation but does not induce DNA damage or poison topoisomerase I during this process.

#### 5.4.2.2 Circular Dichroism studies

Circular dichroism (CD) spectroscopy is a powerful biophysical technique used to monitor conformational changes, drug-DNA binding interactions and structural dynamics of nucleic acids. The CD profile of classical right handed B-DNA exhibits two positive (220 nm and 268 nm) and two negative (210 nm and 246 nm) elliptical signals, while slight variations in this profile arise when the %A-T content of DNA is varied.<sup>37</sup> Conformations of salmon testes DNA (stDNA) and synthetic alternating copolymers poly[d(A-T)<sub>2</sub>] and poly[d(G-C)<sub>2</sub>] were studied with increasing *r* ([drug]/[DNA]) values, where *r* = 0.010 – 0.025 (experiments containing > 0.025 **Mn-Oda** were found to induce noise in the resulting spectra). **Mn-Oda** exhibits a concentration-dependent enhancement of the elliptical signals that can be attributed to hydrogen bonding and stacking interactions between nitrogenous bases and the right-handedness of DNA, irrespective of A-T content (Figure 2C). In the case of stDNA and poly[d(G-C)<sub>2</sub>], an increase in ellipticity associated with β-N-glycosidic linkages were also noted. **Mn-Oda**-DNA profiles were compared to that of classical non-covalent intercalating and groove binding molecules (data not shown) with structural perturbations induced by **Mn-Oda** suggesting an intercalative binding mode (268 nm), particularly at the minor groove, similar to that of EtBr since elliptical signals show an increasing trend at 210, 220 and 268 nm.<sup>38</sup> Additional viscosity analysis further corroborated an intercalating binding motif by **Mn-Oda** on stDNA (Figure S2).

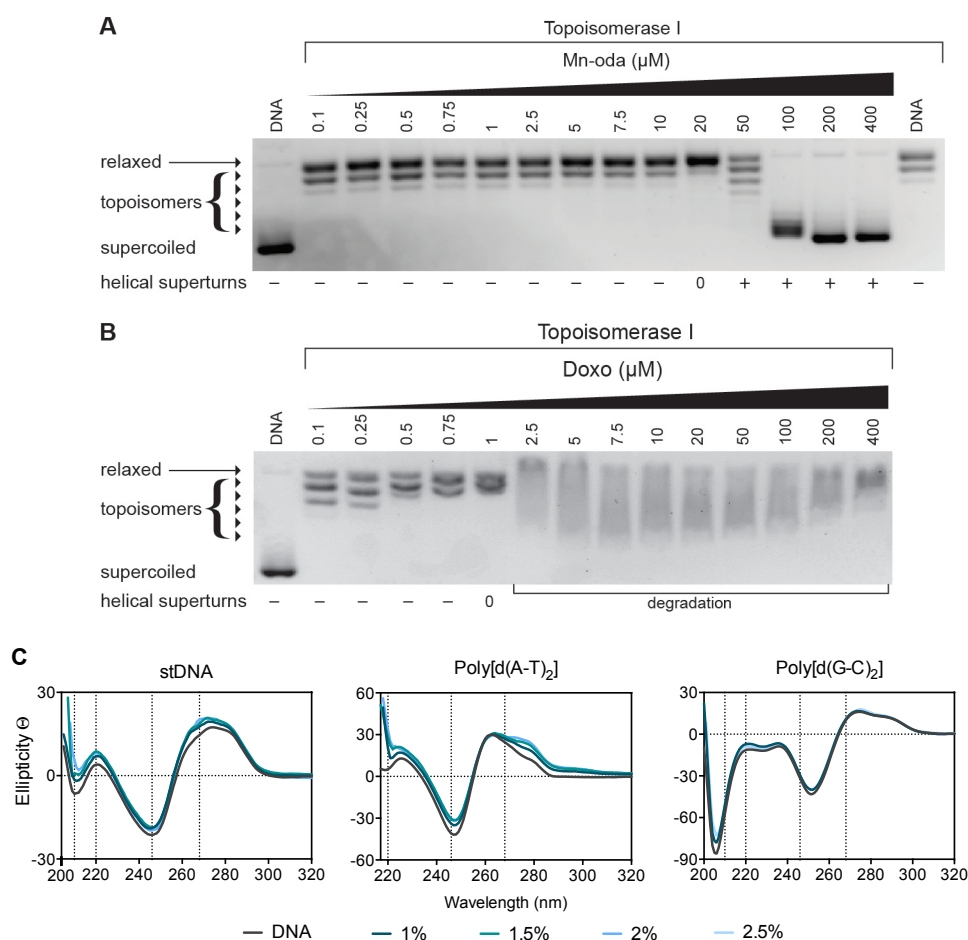


**Figure 5.2 A.** Release of topological tension of supercoiled plasmid DNA by **Mn-Oda** and **B.** Dox. **C.** CD profile of Mn-Oda with stDNA and alternating co-polymers poly[d(A-T)<sub>2</sub>] and poly[d(G-C)<sub>2</sub>] under drug loadings of 1.0 – 2.5% (respective *r* values of 0.010 – 0.025).

### 5.4.3 Genotoxicity studies imply indirect DNA damage

#### 5.4.3.1 COMET analysis

Single cell gel electrophoresis, otherwise known as the COMET assay, was employed to determine intracellular DNA damaging properties of the metal complex. Prior to analysis, viability profiles of **Mn-Oda** and Dox were identified over 24 h of exposure within the SKOV3 cell line using flow cytometry (Figure S3). SKOV3 cells were then exposed to 1.0 μM concentrations of both agents, embedded onto agarose coated glass slides and lysed of cellular structure and nucleosome resulting in the nucleoid scaffold that allows DNA migration based on integrity, when subjected to alkaline gel electrophoresis. Single strand breaks (SSB) and double strand breaks (DSBs) were visualised through fluorescence microscopy (Figure 3B). We selected the clinical anti-tumour antibiotic Dox as a positive control due to its DNA intercalating capacity, ROS generation and topoisomerase poisoning effects. The frequency distribution of the COMET tail moment induced by **Mn-Oda** (Figure 3A) showed a departure from the control profile, with a higher number of events occurring between tail moments of 40 and 20 (A.U.). Dox, however, exhibited a dispersed array of tail

moments with values reaching 240 a.u. and an elongated tail, extending residual DNA damage and reduced fluorescence intensity of the comet head. These results are in agreement with Manjanatha *et al.* who reported Dox-induced ROS could generate both direct and indirect DNA damage as indicated by the COMET assay.<sup>39</sup>

#### 5.4.3.2 Cell Cycle Analysis

In order to investigate the toxicity mechanism of the *di*-Mn<sup>2+</sup> complex, the effects on SKOV3 cell cycle phase distribution was examined. All cells have an innate growth and replication cycle, the revolution of which yields cell growth (G0/G1), replication of chromosomes (S) and production of daughter cells (G2/M).<sup>40</sup> As shown in Figure 3C and 3D, **Mn-Oda** induces a decrease (14.3%) in the G2/M phase and enrichment within the S (synthesis) phase (7.4%) when compared to the untreated control. A contraction of G2/M phase was also evident in Dox treated samples (10.4%) with escalation of S phase (13.3%) identified. Taken together, data here indicates that at 1.0  $\mu$ M exposure over 24 h, both tested agents induce cell cycle arrest within SKOV3 in the DNA synthesis phase.

#### 5.4.3.3 Immunodetection of $\gamma$ H2AX

A primary response to dsDNA damage is the site selective phosphorylation of histone H2AX that is indiscriminately incorporated during chromatin formation.<sup>41,42</sup> H2AX differs from other H2A histones through a carboxyl tail containing a 139-serine residue that becomes phosphorylated in the presence of DNA damage and denoted as  $\gamma$ H2AX.<sup>43</sup> Phosphorylated H2AX accumulate in the chromatin surrounding the site of damage, thus creating a focus for subsequent recruitment of DNA repair mechanisms. A proportional correlation is observed between the extent of DNA damage and formation of  $\gamma$ H2AX foci thus rendering it as a pertinent method for dsDNA damage detection. Following the advent of phosphorylation, the use of recognition antibodies for  $\gamma$ H2AX can visualise and quantify this process through fluorogenic conjugation. Immunodetection of  $\gamma$ H2AX within SKOV3 cells was quantified using flow cytometry after 24 h of exposure to **Mn-Oda** and Dox (1.0  $\mu$ M) (Figure 3E). **Mn-Oda** was found to induce remarkably high levels of DSBs (69.4%) in the cellular population. The control agent Dox was also efficient in DSB generation within SKOV3, but results here were notably lower (39.4%).

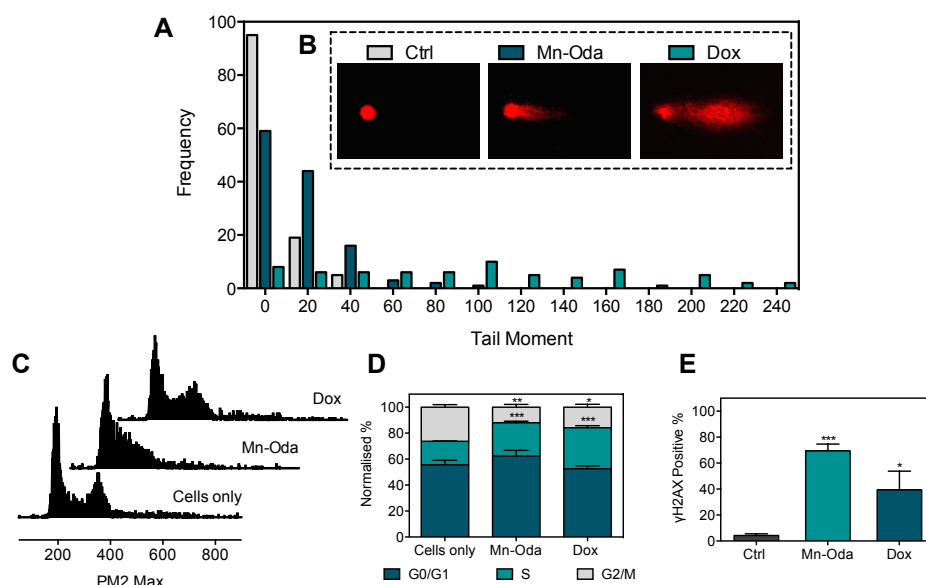


**Figure 5.3** SKOV3 cells were treated with 1.0  $\mu$ M Mn-Oda and Dox for 24 h and subsequently studied in the following assays. **A.** Comet assay analysis where the frequency of tail moment (A.U.). **B.** Examples of typical COMET shapes are represented below respective legends. **C.** Cell cycle histograms and, **D.** Cell cycle phase (G0/G1, S and G2/M) distributions. **E.** Immunodetection of  $\gamma$ H2AX positive cells. Not significant  $p > 0.05$ , \*  $p \leq 0.05$ , \*\*  $p \leq 0.01$ , \*\*\*  $p \leq 0.001$ .

#### 5.4.4 Mn-Oda stimulates mild caspase 9 release but does not trigger early or late-stage apoptosis in SKOV3 cells

##### 5.4.4.1 Annexin V

In order to confirm **Mn-Oda** cytotoxicity is provoked through a non-apoptotic cytotoxic pathway, a range of essential components in the form of caspases that contribute to the initiation and execution within this process, were investigated (Figure 4C-F). Stimulation of the intrinsic apoptotic pathway results in cytosolic release of cytochrome *c* and thus activation of caspase 9 within the apoptosome.<sup>46,47</sup> An alternative route of origin also exists through extracellular death factors that stimulate the activation of caspase 8.<sup>48,49</sup> Both caspase 8 and 9 result in the consequential activation of executioner caspases such as 3 and 7 that commence an irreversible cascade of proteolytic degradation and membrane collapse, precipitating in cell suicide.<sup>46,47</sup> **Mn-Oda** treated cells did not promote sufficient production of initiator caspase 8 (Figure 4E) but did activate caspase 9 by 13.2% (Figure 4F). However, a marginal increase only (4.4%) was observed in early apoptotic detection of executioner caspases 3/7 (Figure 4C), but not in the latter stages (Figure 4D). As expected, Dox had a significant effect on the activation of caspase 3/7 (Figure 4C and D) with activation, and subsequent apoptosis (Figure 4A and B) originating *via* the intrinsic pathway (Figure 4F).



#### 5.4.4.2 Caspase activation

In order to confirm a non-apoptotic cytotoxic pathway for **Mn-Oda**, a range of key components in the form of caspases—essential for the activation and execution of this process were investigated (**Figure 4.4E-H**); Caspase 9 is released from an intrinsic apoptotic proteins that ultimately results in cytosolic release of cytochrome *c* and thus activation of caspase 9 within the apoptosome.<sup>33,34</sup> An alternative apoptotic route also exists through extracellular death factors that stimulate the activation of caspase 8.<sup>35,36</sup> Both caspase 8 and 9 result in the consequential activation of executioner caspases such as 3 and 7 that initiate an irreversible cascade of proteolytic degradation and membrane collapse, precipitating cell suicide.<sup>33,34</sup> **Mn-Oda** treated cells did not promote sufficient production of initiator (8 and 9, **Figure 4.4G and H**) and executioner caspases (3/7, **Figure 4.4E and F**). As expected, Dox had a significant effect on the activation of caspase 3/7 (**Figure 4.4E**) with activation, and subsequent apoptosis (**Figure 4.4C and D**) originating via the intrinsic pathway (**Figure 4.4H**).

#### 5.4.4.3 Mitochondrial depolarisation

Due to the ability of **Mn-Oda** to generate intracellular ROS,<sup>4</sup> changes in mitochondrial transmembrane potential ( $\Delta\Psi_m$ ) were investigated; reduction of the redox potential across inner and outer mitochondrial membranes is also a characteristic of apoptotic induction. Depolarisation measurements were obtained using fluorogenic dye JC-1. The protonophore, and known uncoupler of  $\Delta\Psi_m$ , carbonyl cyanide *m*-chlorophenyl hydrazine (CCCP),<sup>29,30</sup> was employed as a positive control and found to depolarise 55.3% of the sample population while **Mn-Oda** induced 11.7% depolarisation—a marginal increase in comparison to Dox-treated and non-drug treated cells (6.0% and 4.6% respectively) (**Figure 4G**). Rather than **Mn-Oda** directly influencing deterioration of transmembrane potential, the extent of depolarisation is most likely due to the stimulation of intrinsic apoptosis. Fluorescent quantification of these apoptotic biomarkers, in combination with cytosolic caspases and Annexin V, suggests that **Mn-Oda** does not directly activate apoptosis as the primary mechanism of cell death to account for the 46% decrease in cellular viability (**Figure S3**).

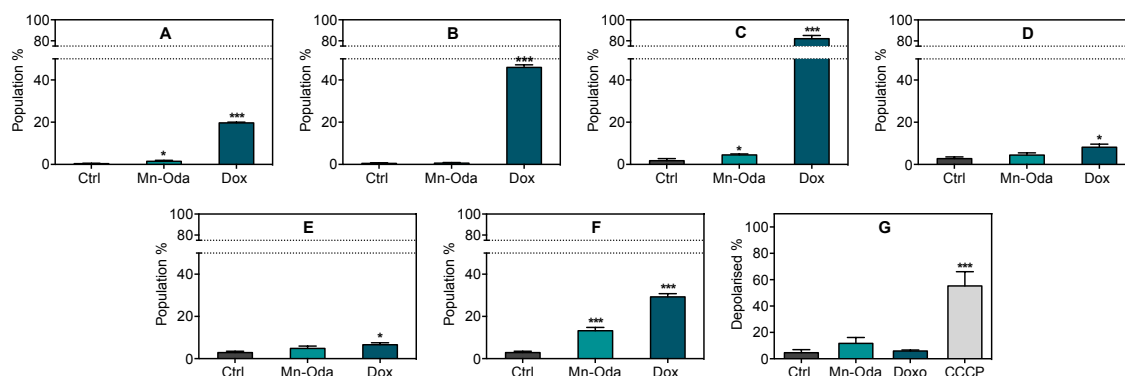


**Figure 5.4** Apoptotic investigation of Mn-Oda. **A.** Early and **B.** late apoptosis measured with the translocation of Annexin V substrate. **C.** Detection of caspase 3/7 in mid and **D.** late populations. **E.** Activation of initiator caspase 8 and **F.** caspase 9. **G.** Extent of mitochondrial depolarisation detected through bathochromic shift of JC-1 emission upon formation of J-aggregates. Not significant  $p > 0.05$ , \*  $p \leq 0.05$ , \*\* $p \leq 0.01$ , \*\*\* $p \leq 0.001$ .

#### 5.4.5 Mn-Oda stimulates autophagy prior to apoptosis

Owing to low levels of caspase 9, the extent of mitochondrial depolarisation and lack of Annexin V and caspase 3/7 detection, there is limited evidence here to suggest that **Mn-Oda** directly induces cell death *via* apoptosis. It is likely, therefore, that apoptotic initiation is a downstream effect mediated by an alternative mechanism and this prompted us to investigate the activation of autophagy triggered by **Mn-Oda**. The autophagy pathway is a lysosomal degradation process, monitoring the homeostasis, longevity, turnover of biomolecules and organelles, while replenishing the nutrient pool particularly under starvation conditions.<sup>50</sup> This complex pathway consists of sequential stages from initiation, nucleation, elongation and finally maturation through the activation and post-transcriptional modification of autophagy related proteins (ATG) (Figure 6A).<sup>15,20,50</sup> In order to evaluate the mechanistic pathway for **Mn-Oda** induced toxicity, fluorescent staining with monodansylcadaverine (MDC) was primarily monitored. MDC contains a fluorogenic dansyl moiety conjugated to a terminal amine that facilitates accumulation and ion trapping in low pH environments such as those found within autophagolysosomes.<sup>51</sup> Autophagy inducers employed in this study were: *i.*) rapamycin (Rapa), which inhibits mammalian target of rapamycin (mTOR) complex 1,<sup>52,53</sup> a downstream protein involved in the PI3K-AKT-mTOR regulation pathway, and *ii.*) suberoyanilide hydroxamic acid (SAHA), an inhibitor of histone deacetylase (HDAC) that induces transcriptional expression of LC3 and mTOR activation,<sup>54</sup> independent to apoptosis (Figure 6A). Non-treated cells demonstrate minimal fluorescence emission of MDC from innately present lysosomes (Figure 5A). Accumulation of MDC in spherical structures was observed upon **Mn-Oda** and Rapa treatment with localization observed in the perinuclear region. Upon complex treatment, quantification of fluorescent intensities (Figure 6B) revealed enhanced emission profiles due to accumulation of MDC in autophagolysosome when compared to non-treated SKOV3 cells, indicating the induction of **Mn-Oda**-mediated autophagy. Given that MDC specificity for selective

accumulation in autophagic vacuoles has been debated,<sup>55</sup> further evidence of **Mn-Oda** triggered autophagy was identified through aggregation of the autophagic marker LC3. Cytosolic LC3 (LC3-I) is proteolytically cleaved by Atg4, converted to its lipidated form (LC3-II) upon phosphatidylethanolamine (PE) binding,<sup>56</sup> and incorporated into the autophagosomal membrane.<sup>15</sup> Non-discriminate immunodetection of LC-3 showed dispersion within the cytosol in the non-treated control (Figure 5B). Autophagosome and consecutive autophagic vacuole formation is evident in Rapa and **Mn-Oda** treatments with the identification of LC3-II punta, supporting that the cytotoxic mechanism of **Mn-Oda** is attributed to autophagy activation.

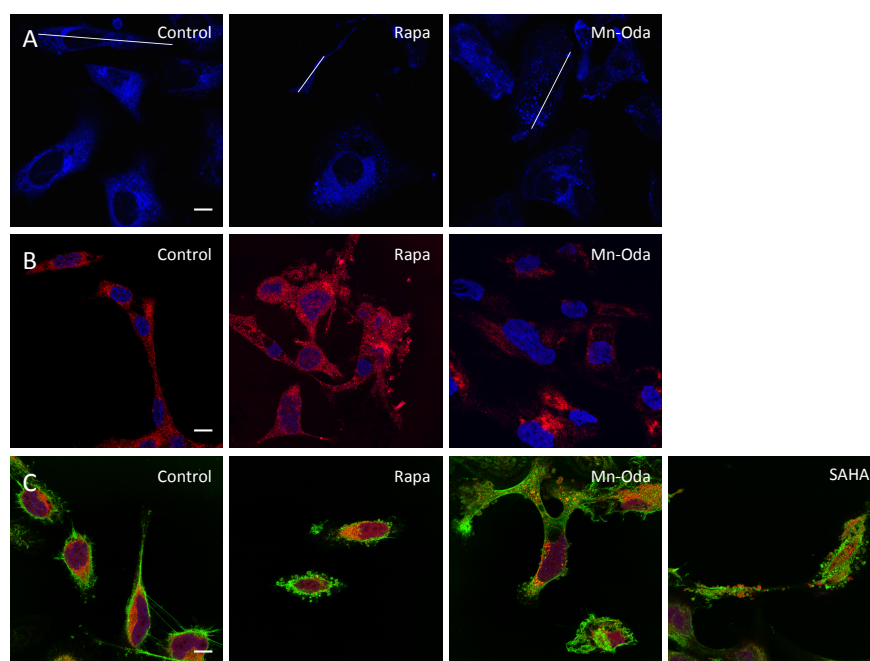


**Figure 5.** 5 Confocal images of SKOV3 100X treated with Mn-Oda, Rapa or SAHA to examine, **A.** MDC staining of acidic vacuoles (blue). White lines indicate cross sections for fluorescence quantification profiles (see figure 6B). **B.** Immunofluorescent staining of LC3 (red) and DAPI (blue) control. **C.** Morphological changes in cellular structure. Nuclei were stained with DAPI (blue), F-actin with Alexa Fluor 488 conjugated to phalloidin (green) and mitochondrial with MitoTracker deep red (red). All scale bars (control, bottom right) are 10  $\mu$ m.

#### 5.4.6 Cell morphology reveals Mn-Oda-promoted apoptosis

Confocal microscopy experiments were undertaken to further identify the cytotoxic effects of **Mn-Oda** within SKOV3 cells through the use of location-specific fluorogenic stains to visualise the nucleus, actin cytoskeleton and mitochondria (Figure 5C). Untreated SKOV3 cells exhibited adherent epithelial morphology with an elongated dome shape. Distinct changes in cellular structure were observed in rapamycin treated cells such as adherence contraction, enhanced elongation and cytoskeletal actin encapsulation absent of nuclear or mitochondrial debris. Cells exposed to SAHA exhibit similar contraction and elongation, with clear evidence of apoptotic bodies. **Mn-Oda** treatment, however, presents alterations in cell morphology and characteristic indicators of apoptosis, particularly with enlargement and fragmentation of the nucleus, organelle

contraction, dynamic membrane blebbing and formation of apoptotic bodies.<sup>57</sup> In conjunction with the flow-cytometric detection of caspase 9 and the loss mitochondrial transmembrane potential, evidence here suggests **Mn-Oda** induces intrinsic apoptosis as the concluding mechanism of cell death, which is preceded by the activation of autophagy.

#### 5.4.7 Initiation of autophagy is superoxide-dependent

To investigate the role of **Mn-Oda** in the activation of autophagy, we further probed cellular viability in the presence of antioxidants and autophagy inhibitors (Figure 6C). Inhibitors of autophagy are 3-methyladenine (3-MA), which competitively binds to class III phosphatidylinositol 3-kinase (PI3K),<sup>58,59</sup> and antimalarial agent chloroquine (CQ) which inhibits lysosomal protease degradation through accumulation of the weak base within acidic vacuoles, thus inhibiting autophagolysosome formation (Figure 6A).<sup>60,61</sup> Under physiological conditions ammonium chloride (NH<sub>4</sub>Cl) becomes protonated, acting as a lysosomotropic agent with similar neutralisation capacity to chloroquine, and causes an increase in local pH.<sup>62</sup> Due to the ROS generation properties of **Mn-Oda**,<sup>4</sup> antioxidants employed in this study consist of a variety of radical-specific trapping agents; tiron for superoxide (O<sub>2</sub><sup>•-</sup>),<sup>63</sup> mannitol for hydroxyl radical (•OH),<sup>64</sup> histidine for singlet oxygen (<sup>1</sup>O<sub>2</sub>),<sup>65,66</sup> and sodium pyruvate for hydrogen peroxide (H<sub>2</sub>O<sub>2</sub>).<sup>67</sup> Upon co-treatment with **Mn-Oda**, all autophagy inhibitors increased cellular viability with 3-MA and tiron at the highest extent (6.1 and 6.6% respectively). These results in conjunction with fluorescent detection of autophagic vacuoles, suggests that **Mn-Oda** promotes superoxide-mediated autophagy as hypothesised in Figure 6A. The combination of SAHA with CQ, NH<sub>4</sub>Cl and 3-MA significantly increased cell survival by 10.1, 8.3 and 10.4%, respectively. Interestingly, the most substantial increase was noted for O<sub>2</sub><sup>•-</sup> scavenging agent tiron (15.4%) as SAHA has previously demonstrated significant ROS generation properties,<sup>68,69</sup> which can be attributed to down-regulation of thioredoxin (TRX) a dithiol-reducing redox protein,<sup>70,71</sup> a key response to oxidative stress. The presence of autophagy inhibitors had minimal effect on Rapa viability, which could be due to the limited exposure period of 24 h; rapamycin typically exerts toxic effects within longer time-frames with IC<sub>50</sub> concentrations of 25.3 μM in PEO1 ovarian cancer cells after 72 hours.<sup>72</sup> Sequestering the basal levels of O<sub>2</sub><sup>•-</sup> enhanced live cell populations by 4.4%, most likely as O<sub>2</sub><sup>•-</sup> is known to inhibit the binding of TORC1 to Rapa:FKBP12 in yeast.<sup>73</sup> Furthermore, although rapamycin can innately generate significant levels of ROS, synergistic co-treated with a ROS liberating co-factor, such as curcumin analogue (EF24), can lead to excessive production and enhanced cell death.<sup>74</sup>

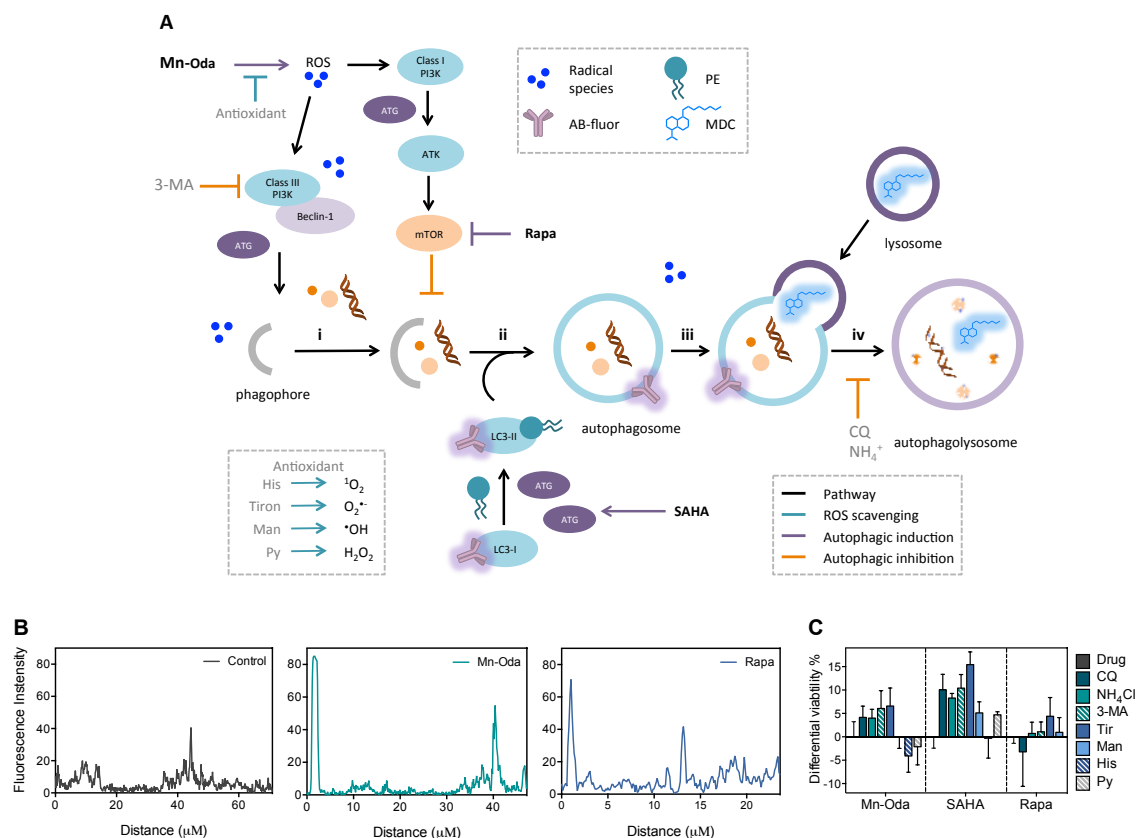


**Figure 5.6 A.** Schematic of autophagy pathway.<sup>15,20,50</sup> Due to the number of autophagy-related genes (ATGs) and the complexity of their role in the autophagy pathway, the family is represented by ‘ATG’ (purple) for simplicity, **i.** Initiation begins with the formation of isolation membrane known as a phagophore, engulfing cytoplasmic material, **ii.** Cytosolic LC3-I is converted to the membrane-associated form LC3-II, through phosphatylethanolamine (PE) lipidation and incorporated into autophagosomal double-membrane, **iii.** Docking and fusion of lysosome or late endosomes results in the formation of **iv.** autophagolysosome. Maturation and catabolic degradation results in recycling and restoration of nutrient stores. Autophagic inducers employed are Rapa and SAHA (purple pathway). Autophagic inhibitors are 3-methyladenine (3-MA), NH<sub>4</sub>Cl and chloroquine (CQ) (orange pathway) while antioxidants utilised are tiron, mannitol (man), histidine (his) and sodium pyruvate (Py) (teal pathway). Induction was probed through immunodetection of LC3 with fluoregenically conjugated secondary antibody and monodansylcadaverine (MDC), **B.** Intensity profiles (indicated in **Figure 5C**) were analysed using Image J on raw images in 8-bit format with no further modification. **C.** Differential viability percentages in the presence of radical scavengers and autophagy inhibitors pre-treated at 1 mM (with the exception of CQ, 10 μM) 2 h prior to drug addition. **Mn-Oda**, SAHA and Rapa were treated at respective concentrations, 1 μM, 100 μM and 50 μM, over 24 h.

## 5.5 Conclusions

Reactive oxygen species (ROS) play an integral role in the regulation and stimulation of autophagy.<sup>75,76</sup> Previous work by the Gibson group highlighted the fundamental requirement for ROS-mediated autophagic induction under specific starvation conditions leading to the activation of superoxide ( $O_2^{\cdot-}$ ) production, either alone or in combination with hydrogen peroxide ( $H_2O_2$ ).<sup>77</sup> Furthermore, the same study revealed over-expression of the antioxidant enzyme superoxide dismutase could inhibit the activation of this pathway, resulting in catalytic depletion of  $O_2^{\cdot-}$  to  $H_2O_2$ . The findings of the current study demonstrate clearly that **Mn-Oda** can intercalate dsDNA at the minor groove, however, unlike doxorubicin or  $Cu^{2+}$ -phenanthroline derivatives,<sup>4</sup> direct oxidative damage of nucleic acids is abrogated. Instead, there is strong evidence to suggest that DSBs, identified by immunodetection of  $\gamma$ H2AX, coupled with nuclear fragmentation observed in the COMET assay, are due to autophagic degradation initiated by complex-mediated intracellular ROS production. Combination of the *di*- $Mn^{2+}$  complex along with mediators that hinder radical generation and autophagy, indicate cell death promoted by  $O_2^{\cdot-}$  production. Metal-catalysed radical production does not directly influence nucleic acid degradation (evident from the absence of DNA shearing in topoisomerase relaxation), but rather functions as a signalling agent in the activation of autophagy, detected *via* MDC and immunofluorescence of LC3. Consequentially, intracellular ROS insult by **Mn-Oda** promotes autophagy, exceeding a critical threshold of adverse conditions, and activates apoptosis *via* the intrinsic, mitochondrial pathway (caspase 9 and mitochondrial depolarisation) as the lethal effector of cellular death. Further sensitivity may arise from the mutational status of p53 whereby depletion or point mutations can induce autophagy; in the cytosolic setting, baseline levels of p53 can inhibit autophagy under various stress factors such as therapeutic, nutrient or endoplasmic reticulum strains.<sup>78</sup> With this in mind, cancers that express mutant or null p53—such as SKOV3<sup>79</sup>—are more susceptible to autophagy. To our knowledge, **Mn-Oda** belongs to one of the few transition metal complexes to activate cell death in this sequential manner, where apoptosis is activated only in the final stages of cytotoxicity. In the wider context of metallodrug development and targeting, this complex may serve as a significant milestone in the construction of small molecule therapeutic leads that promote an alternative cytotoxic mechanism that are not dependent on traditional apoptotic initiation.

## 5.6 Supporting Material

Supplementary data associated with this chapter can be found in Appendix D/

## 5.7 References

- (1) Finney, L. A.; O'Halloran, T. V. Transition Metal Speciation in the Cell: Insights From the Chemistry of Metal Ion Receptors. *Science* **2003**, *300* (5621), 931–936.
- (2) Sarkar, B. Treatment of Wilson and Menkes Diseases. *Chem. Rev.* **1999**, *99* (9), 2535–2544.
- (3) Molphy, Z.; Prisecaru, A.; Slator, C.; Barron, N.; McCann, M.; Colleran, J.; Chandran, D.; Gathergood, N.; Kellett, A. Copper Phenanthrene Oxidative Chemical Nucleases. *Inorg. Chem.* **2014**, *53* (10), 5392–5404.
- (4) Kellett, A.; O'Connor, M.; McCann, M.; Howe, O.; Casey, A.; McCarron, P.; Kavanagh, K.; McNamara, M.; Kennedy, S.; May, D. D.; Skell, P. S.; O'Shea, D.; Devereux, M. Water-Soluble Bis(1,10-Phenanthroline) Octanedioate  $\text{Cu}^{2+}$  And  $\text{Mn}^{2+}$  Complexes with Unprecedented Nano and Picomolar *In Vitro* Cytotoxicity: Promising Leads for Chemotherapeutic Drug Development. *Med. Chem. Commun.* **2011**, *2* (7), 579–584.
- (5) Kellett, A.; O'Connor, M.; McCann, M.; McNamara, M.; Lynch, P.; Rosair, G.; McKee, V.; Creaven, B.; Walsh, M.; McClean, S.; Foltyn, A.; O'Shea, D.; Howe, O.; Devereux, M. Bis-Phenanthroline Copper(II) Phthalate Complexes Are Potent *In Vitro* Antitumour Agents with “Self-Activating” Metallo-Nuclease and DNA Binding Properties. *Dalton Trans.* **2011**, *40* (5), 1024–1027.
- (6) Slator, C.; Barron, N.; Howe, O.; Kellett, A.  $[\text{Cu}(\text{O-Phthalate})(\text{Phenanthroline})]$  Exhibits Unique Superoxide-Mediated NCI-60 Chemotherapeutic Action Through Genomic DNA Damage and Mitochondrial Dysfunction. *ACS Chem. Biol.* **2016**, *11* (1), 159–171.
- (7) a) Farrell, N. *Metal Complexes as Drugs and Chemotherapeutic Agents*; Comprehensive Coordination Chemistry II, 2003; Vol. 9, pp 809–840. b) Zhang, C. X.; Lippard, S. J. New Metal Complexes as Potential Therapeutics. *Curr. Opin. Chem. Biol.* **2003**. c) Tan, C.-P.; Lu, Y.-Y.; Ji, L.-N.; Mao, Z.-W. Metallomics Insights Into the Programmed Cell Death Induced by Metal-Based Anticancer Compounds. *Metallomics* **2014**, *6* (5), 978–995. d) van Rijt, S. H.; Sadler, P. J. Current Applications and Future Potential for Bioinorganic Chemistry in the Development of Anticancer Drugs. *Drug Discov. Today* **2009**, *14* (23-24), 1089–1097. e) Santini, C.; Pellei, M.; Gandin, V.; Porchia, M.; Tisato, F.; Marzano, C. Advances in Copper Complexes as Anticancer Agents. *Chem. Rev.* **2014**, *114* (1), 815–862.
- (8) a) Shingu, T.; Chumbalkar, V. C.; Gwak, H.-S.; Fujiwara, K.; Kondo, S.; Kelland, L. R.; Bogler, O. The Polynuclear Platinum BBR3610 Induces G2/M Arrest and Autophagy Early and Apoptosis Late in Glioma Cells. *Neuro-oncology* **2010**, *12* (12), 1269–1277. b) Guo, W.-J.; Zhang, Y.-M.; Zhang, L.; Huang, B.; Tao, F.-F.; Chen, W.; Guo, Z.-J.; Xu, Q.; Sun, Y. Novel Monofunctional Platinum (II) Complex Mono-Pt Induces Apoptosis-Independent Autophagic Cell Death in Human Ovarian Carcinoma Cells, Distinct From Cisplatin. *Autophagy* **2013**, *9* (7), 996–1008. c) Trejo-Solís, C.; Jimenez-Farfan, D.; Rodriguez-Enríquez, S.; Fernandez-Valverde, F.; Cruz-Salgado, A.; Ruiz-Azuara, L.; Sotelo, J. Copper Compound Induces Autophagy and Apoptosis of Glioma Cells by Reactive Oxygen Species and Jnk Activation. *BMC Cancer* **2012**, *12* (1), 156. d) Tan, C.; Lai, S.; Wu, S.; Hu, S.; Zhou, L.; Chen, Y.; Wang, M.; Zhu, Y.; Lian, W.; Peng, W.; Ji, L.; Xu, A. Nuclear Permeable Ruthenium(II) B-Carboline Complexes Induce Autophagy to Antagonize Mitochondrial-Mediated Apoptosis. *J. Med. Chem.* **2010**, *53* (21), 7613–7624. e) Guo, W.-J.; Ye, S.-S.; Cao, N.; Huang, J.; Gao, J.; Chen, Q.-Y. ROS-Mediated Autophagy Was Involved in Cancer Cell Death Induced by Novel Copper(II) Complex. *Exp. Toxicol. Pathol.*

- 2010**, 62 (5), 577–582. f) Paris, I.; Perez-Pastene, C.; Couve, E.; Caviedes, P.; Ledoux, S.; Segura-Aguilar, J. Copper Dopamine Complex Induces Mitochondrial Autophagy Preceding Caspase-Independent Apoptotic Cell Death. *J. Biol. Chem.* **2009**, 284 (20), 13306–13315. g) Gorojod, R. M.; Alaimo, A.; Porte Alcon, S.; Pomilio, C.; Saravia, F.; Kotler, M. L. The Autophagic-Lysosomal Pathway Determines the Fate of Glial Cells Under Manganese- Induced Oxidative Stress Conditions. *Free Radic. Biol. Med.* **2015**, 87, 237–251. h) Li, X.; Zhao, K.; Guo, W.; Liu, X.; Liu, J.; Gao, J.; Chen, Q.; Bai, Y. A Novel Manganese Complex LMnAc Selectively Kills Cancer Cells by Induction of ROS-Triggered and Mitochondrial-Mediated Cell Death. *Sci. China Life Sci.* **2014**, 57 (10), 998–1010. i) Liu, J.; Guo, W.; Li, J.; Li, X.; Geng, J.; Chen, Q.; Gao, J. Tumor-Targeting Novel Manganese Complex Induces ROS-Mediated Apoptotic and Autophagic Cancer Cell Death. *Int J Mol Med* **2015**, 35 (3), 607–616.
- (9) Takeshige, K.; Baba, M.; Tsuboi, S.; Noda, T.; Ohsumi, Y. Autophagy in Yeast Demonstrated with Proteinase-Deficient Mutants and Conditions for Its Induction. *J. Cell Biol.* **1992**, 119 (2), 301–311.
- (10) Tsukada, M.; Ohsumi, Y. Isolation and Characterization of Autophagy-Defective Mutants of *Saccharomyces Cerevisiae*. *FEBS Letters* **1993**, 333 (1-2), 169–174.
- (11) Mizushima, N.; Noda, T.; Yoshimori, T.; Tanaka, Y.; Ishii, T.; George, M. D.; Klionsky, D. J.; Ohsumi, M.; Ohsumi, Y. A Protein Conjugation System Essential for Autophagy. *Nature* **1998**, 395 (6700), 395–398.
- (12) Ichimura, Y.; Kirisako, T.; Takao, T.; Satomi, Y.; Shimonishi, Y.; Ishihara, N.; Mizushima, N.; Tanida, I.; Kominami, E.; Ohsumi, M.; Noda, T.; Ohsumi, Y. A Ubiquitin-Like System Mediates Protein Lipidation. *Nature* **2000**, 408 (6811), 488–492.
- (13) Klionsky, D. J. *et al.* Guidelines for the Use and Interpretation of Assays for Monitoring Autophagy. *Autophagy* **2014**, 8 (4), 445–544.
- (14) Shintani, T.; Klionsky, D. J. Autophagy in Health and Disease: a Double-Edged Sword. *Science* **2004**, 306 (5698), 990–995.
- (15) Li, L.; Ishdorj, G.; Gibson, S. B. Reactive Oxygen Species Regulation of Autophagy in Cancer: Implications for Cancer Treatment. *Free Radic. Biol. Med.* **2012**, 53 (7), 1399–1410.
- (16) Gibson, S. B. Investigating the Role of Reactive Oxygen Species in Regulating Autophagy. *Meth. Enzymol.* **2013**, 528, 217–235.
- (17) Giordano, S.; Darley-USmar, V.; Zhang, J. Autophagy as an Essential Cellular Antioxidant Pathway in Neurodegenerative Disease. *Redox Biol.* **2014**, 2, 82–90.
- (18) Hwang, J. J.; Kim, H. N.; Kim, J.; Cho, D.-H.; Kim, M. J.; Kim, Y.-S.; Kim, Y.; Park, S.-J.; Koh, J.-Y. Zinc(II) Ion Mediates Tamoxifen-Induced Autophagy and Cell Death in MCF-7 Breast Cancer Cell Line. *Biometals* **2010**, 23 (6), 997–1013.
- (19) Gozuacik, D.; Kimchi, A. Autophagy as a Cell Death and Tumor Suppressor Mechanism. *Oncogene* **2004**, 23 (16), 2891–2906.
- (20) Poillet-Perez, L.; Despouy, G.; Delage-Mourroux, R.; Boyer-Guittaut, M. Interplay Between ROS and Autophagy in Cancer Cells, From Tumor Initiation to Cancer Therapy. *Redox Biol.* **2015**, 4 (C), 184–192.
- (21) Mazure, N. M.; Pouyssegur, J. Hypoxia-Induced Autophagy: Cell Death or Cell Survival? *Curr. Opin. Chem. Biol.* **2010**, 22 (2), 177–180.
- (22) Kondo, Y.; Kanzawa, T.; Sawaya, R.; Kondo, S. The Role of Autophagy in Cancer Development and Response to Therapy. *Nat. Rev. Cancer* **2005**, 5 (9), 726–734.
- (23) McCann, M.; McGinley, J.; Ni, K.; O'Connor, M.; Kavanagh, K.; McKee, V.; Colleran, J.; Devereux, M.; Gathergood, N.; Barron, N.; Prisecaru, A.; Kellett, A. A New Phenanthroline-Oxazine Ligand: Synthesis, Coordination Chemistry and Atypical DNA Binding Interaction. *Chem. Commun.* **2013**, 49 (23), 2341–2343.



- (24) Peixoto, P.; Bailly, C.; David-Cordonnier, M.-H. Topoisomerase I-Mediated DNA Relaxation as a Tool to Study Intercalation of Small Molecules Into Supercoiled DNA. *Methods Mol. Biol.* **2010**, *613* (Chapter 15), 235–256.
- (25) Pozarowski, P.; Darzynkiewicz, Z. Analysis of Cell Cycle by Flow Cytometry. In *Methods in Molecular Biology*; 2004; Vol. 281, pp 301–311.
- (26) Brzozowska, K.; Pinkawa, M.; Eble, M. J.; Müller, W.-U.; Wojcik, A.; Kriehuber, R.; Schmitz, S. In Vivo Versus in Vitro Individual Radiosensitivity Analysed in Healthy Donors and in Prostate Cancer Patients with and Without Severe Side Effects After Radiotherapy. *Int. J. Radiat. Biol.* **2012**, *88* (5), 405–413.
- (27) Casey, M. T.; McCann, M.; Devereux, M.; Curran, M.; Cardin, C.; Convery, M.; Quillet, V.; Harding, C. Synthesis and Structure of the  $Mn^{II,II}$  Complex Salt  $[Mn_2(H^1H^1M_2-Oda)(Phen)_4(H_2O)_2][Mn_2(H^1H^1M_2-Oda)(Phen)_4(H^1-Oda)_2] \cdot 4H_2O$  (odaH<sub>2</sub>= Octanedioic Acid): a Catalyst for H<sub>2</sub>O<sub>2</sub> Disproportionation. *J. Chem. Soc., Chem. Commun.* **1994**, No. 22, 2643–2645.
- (28) Dekker, N. H.; Rybenkov, V. V.; Duguet, M.; Crisona, N. J.; Cozzarelli, N. R.; Bensimon, D.; Croquette, V. The Mechanism of Type IA Topoisomerases. *Proc. Natl. Acad. Sci. U.S.A.* **2002**, *99* (19), 12126–12131.
- (29) Khadka, D. B.; Cho, W.-J. Topoisomerase Inhibitors as Anticancer Agents: a Patent Update. *Expert Opin. Ther. Pat.* **2013**, *23* (8), 1033–1056.
- (30) Wang, J. C. DNA Topoisomerases. *Annu. Rev. Biochem.* **1996**, *65* (1), 635–692.
- (31) Wang, J. G. The Degree of Unwinding of the DNA Helix by Ethidium: I. Titration of Twisted PM2 DNA Molecules in Alkaline Cesium Chloride Density Gradients. *J. Mol. Biol.* **1974**, *89* (4), 783–801.
- (32) Capranico, G.; Kohn, K. W.; Pommier, Y. Local Sequence Requirements for DNA Cleavage by Mammalian Topoisomerase II in the Presence of Doxorubicin. *Nucleic Acids Res.* **1990**, *18* (22), 6611–6619.
- (33) Bachur, N. R.; Gordon, S. L.; Gee, M. V. Anthracycline Antibiotic Augmentation of Microsomal Electron Transport and Free Radical Formation. *Mol. Pharmacol.* **1977**, *13* (5), 901–910.
- (34) Gutteridge, J. M.; Quinlan, G. J. Free Radical Damage to Deoxyribose by Anthracycline, Aureolic Acid and Aminoquinone Antitumour Antibiotics. *Biochem. Pharmacol.* **1985**, *34* (23), 4099–4103.
- (35) Gewirtz, D. A Critical Evaluation of the Mechanisms of Action Proposed for the Antitumor Effects of the Anthracycline Antibiotics Adriamycin and Daunorubicin. *Biochem. Pharmacol.* **1999**, *57* (7), 727–741.
- (36) Foglesong, D. P.; Reckord, C.; Swink, S. Doxorubicin Inhibits Human DNA Topoisomerase I. *Cancer Chemother. Pharmacol.* **1992**, *30* (2), 123–125.
- (37) Chang, Y.-M.; Chen, C. K. M.; Hou, M.-H. Conformational Changes in DNA Upon Ligand Binding Monitored by Circular Dichroism. *Int. J. Mol. Sci.* **2012**, *13* (12), 3394–3413.
- (38) Wu, P. K.; Kharatishvili, M.; Qu, Y.; Farrell, N. A Circular Dichroism Study of Ethidium Bromide Binding to Z-DNA Induced by Dinuclear Platinum Complexes. *J. Inorg. Biochem.* **1996**, *63* (1), 9–18.
- (39) Manjanatha, M. G.; Bishop, M. E.; Pearce, M. G. Genotoxicity of Doxorubicin in F344 Rats by Combining the Comet Assay, Flow-Cytometric Peripheral Blood Micronucleus Test, and Pathway-Focused Gene Expression .... *Environ. Mol. Mutagen.* **2014**, *55*, 24–34.
- (40) Bertoli, C.; Skotheim, J. M.; de Bruin, R. A. M. Control of Cell Cycle Transcription During G1 and S Phases. *Nat. Rev. Mol Cell Biol.* **2013**, *14* (8), 518–528.
- (41) Bonner, W. M.; Redon, C. E.; Dickey, J. S.; Nakamura, A. J.; Sedelnikova, O. A.; Solier, S.;

- Pommier, Y.  $\gamma$ H2AX and Cancer. *Nat. Rev. Cancer* **2008**, 8 (12), 957–967.
- (42) Paull, T. T.; Rogakou, E. P.; Yamazaki, V.; Kirchgessner, C. U.; Gellert, M.; Bonner, W. M. A Critical Role for Histone H2AX in Recruitment of Repair Factors to Nuclear Foci After DNA Damage. *Curr. Biol.* **2000**, 10 (15), 886–895.
- (43) Rogakou, E. P.; Pilch, D. R.; Orr, A. H.; Ivanova, V. S.; Bonner, W. M. DNA Double-Stranded Breaks Induce Histone H2AX Phosphorylation on Serine 139. *J. Biol. Chem.* **1998**, 273 (10), 5858–5868.
- (44) Koopman, G.; Reutelingsperger, C. P.; Kuijten, G. A.; Keehnen, R. M.; Pals, S. T.; van Oers, M. H. Annexin v for Flow Cytometric Detection of Phosphatidylserine Expression on B Cells Undergoing Apoptosis. *Blood* **1994**, 84 (5), 1415–1420.
- (45) Verhoven, B.; Schlegel, R. A.; Williamson, P. Mechanisms of Phosphatidylserine Exposure, a Phagocyte Recognition Signal, on Apoptotic T Lymphocytes. *J. Exp. Med.* **1995**, 182 (5), 1597–1601.
- (46) Hengartner, M. O. The Biochemistry of Apoptosis. *Nature* **2000**, 407 (6805), 770–776.
- (47) Degtarev, A.; Boyd, M.; Yuan, J. A Decade of Caspases. *Oncogene* **2003**, 22 (53), 8543–8567.
- (48) Kruidering, M.; Evan, G. I. Caspase-8 in Apoptosis: the Beginning of "the End"? *IUBMB Life* **2000**, 50 (2), 85–90.
- (49) Cohen, G. M. Caspases: the Executioners of Apoptosis. *Biochem. J.* **1997**.
- (50) Kaur, J.; Debnath, J. Autophagy at the Crossroads of Catabolism and Anabolism. *Nat. Rev. Mol Cell Biol.* **2015**, 16 (8), 461–472.
- (51) Biederbick, A.; Kern, H. F.; Elsässer, H. P. Monodansylcadaverine (MDC) Is a Specific in Vivo Marker for Autophagic Vacuoles. *Eur. J. Cell Biol.* **1995**, 66 (1), 3–14.
- (52) Benjamin, D.; Colombi, M.; Moroni, C.; Hall, M. N. Rapamycin Passes the Torch: a New Generation of mTOR Inhibitors. *Nat. Rev. Drug. Discov.* **2011**, 10 (11), 868–880.
- (53) Chiarini, F.; Evangelisti, C.; McCubrey, J. A.; Martelli, A. M. Current Treatment Strategies for Inhibiting mTOR in Cancer. *Trends Pharmacol. Sci.* **2015**, 36 (2), 124–135.
- (54) Gammoh, N.; Lam, D.; Puente, C. Role of Autophagy in Histone Deacetylase Inhibitor-Induced Apoptotic and Nonapoptotic Cell Death. *Proc. Natl. Acad. Sci. U.S.A.* **2012**, 109, 6561–6565.
- (55) Niemann, A.; Baltes, J.; Elsässer, H. P. Fluorescence Properties and Staining Behavior of Monodansylpentane, a Structural Homologue of the Lysosomotropic Agent Monodansylcadaverine. *J. Histochem. Cytochem.* **2001**, 49 (2), 177–185.
- (56) Scherz-Shouval, R.; Shvets, E.; Fass, E.; Shorer, H.; Gil, L.; Elazar, Z. Reactive Oxygen Species Are Essential for Autophagy and Specifically Regulate the Activity of Atg4. *The EMBO Journal* **2007**, 26 (7), 1749–1760.
- (57) Kerr, J. F.; Wyllie, A. H.; Currie, A. R. Apoptosis: a Basic Biological Phenomenon with Wide-Ranging Implications in Tissue Kinetics. *Br. J. Cancer* **1972**, 26 (4), 239–257.
- (58) Petiot, A.; Ogier-Denis, E.; Blommaert, E. F.; Meijer, A. J.; Codogno, P. Distinct Classes of Phosphatidylinositol 3'-Kinases Are Involved in Signaling Pathways That Control Macroautophagy in HT-29 Cells. *J. Biol. Chem.* **2000**, 275 (2), 992–998.
- (59) Blommaert, E. F. C.; Schellens, J. P. M.; Vreeling Sindelárová, H.; Meijer, A. J.; Krause, U. The Phosphatidylinositol 3-Kinase Inhibitors Wortmannin and LY294002 Inhibit Autophagy in Isolated Rat Hepatocytes. *Eur. J Biochem.* **1997**, 243 (1-2), 240–246.
- (60) Poole, B.; Ohkuma, S. Effect of Weak Bases on the Intralysosomal pH in Mouse Peritoneal Macrophages. *J. Cell Biol.* **1981**, 90 (3), 665–669.
- (61) Glaumann, H.; Ahlberg, J. Comparison of Different Autophagic Vacuoles with Regard to Ultrastructure, Enzymatic Composition, and Degradation Capacity--Formation of Crinosomes. *Exp. Mol. Pathol.* **1987**, 47 (3), 346–362.

- (62) Kawai, A.; Uchiyama, H.; Takano, S.; Nakamura, N.; Ohkuma, S. Autophagosome-Lysosome Fusion Depends on the pH in Acidic Compartments in CHO Cells. *Autophagy* **2007**, *3* (2), 154–157.
- (63) Taiwo, F. A. Mechanism of Tiron as Scavenger of Superoxide Ions and Free Electrons. *J. Spectrosc.* **2008**, *22* (6), 491–498.
- (64) Goldstein, S.; Czapski, G. Mannitol as an OH. Scavenger in Aqueous Solutions and in Biological Systems. *Int. J. Radiat. Biol.* **1984**, *46* (6), 725–729.
- (65) Matheson, I. B. C.; Lee, J. Chemical Reaction Rates of Amino Acids with Singlet Oxygen. *Photochem. Photobiol.* **1979**, *29* (5), 879–881.
- (66) Foote, C. S.; Clennan, E. L. Properties and Reactions of Singlet Dioxygen. In *Active Oxygen in Chemistry*; Active Oxygen in Chemistry; Springer Netherlands: Dordrecht, 1996; pp 105–140.
- (67) Giandomenico, A. R.; Cerniglia, G. E.; Biaglow, J. E.; Stevens, C. W.; Koch, C. J. The Importance of Sodium Pyruvate in Assessing Damage Produced by Hydrogen Peroxide. *Free Radic. Biol. Med.* **1997**, *23* (3), 426–434.
- (68) Ruefli, A. A.; Ausserlechner, M. J.; Bernhard, D.; Sutton, V. R.; Tainton, K. M.; Kofler, R.; Smyth, M. J.; Johnstone, R. W. The Histone Deacetylase Inhibitor and Chemotherapeutic Agent Suberoylanilide Hydroxamic Acid (SAHA) Induces a Cell-Death Pathway Characterized by Cleavage of Bid and Production of Reactive Oxygen Species. *Proc. Natl. Acad. Sci. U.S.A.* **2001**, *98* (19), 10833–10838.
- (69) Petrucci, L. A.; Dupéré-Richer, D.; Pettersson, F.; Retrouvey, H.; Skoulikas, S.; Miller, W. H. Vorinostat Induces Reactive Oxygen Species and DNA Damage in Acute Myeloid Leukemia Cells. *PLoS ONE* **2011**, *6* (6), e20987.
- (70) Butler, L. M.; Zhou, X.; Xu, W.-S.; Scher, H. I.; Rifkind, R. A.; Marks, P. A.; Richon, V. M. The Histone Deacetylase Inhibitor SAHA Arrests Cancer Cell Growth, Up-Regulates Thioredoxin-Binding Protein-2, and Down-Regulates Thioredoxin. *Proc. Natl. Acad. Sci. U.S.A.* **2002**, *99* (18), 11700–11705.
- (71) Ungerstedt, J. S.; Sowa, Y.; Xu, W.-S.; Shao, Y.; Dokmanovic, M.; Perez, G.; Ngo, L.; Holmgren, A.; Jiang, X.; Marks, P. A. Role of Thioredoxin in the Response of Normal and Transformed Cells to Histone Deacetylase Inhibitors. *Proc. Natl. Acad. Sci. U.S.A.* **2005**, *102* (3), 673–678.
- (72) Foster, H.; Coley, H. M.; Goumenou, A.; Pados, G.; Harvey, A.; Karteris, E. Differential Expression of mTOR Signalling Components in Drug Resistance in Ovarian Cancer. *Anticancer Res.* **2010**, *30* (9), 3529–3534.
- (73) Neklesa, T. K.; Davis, R. W. Superoxide Anions Regulate TORC1 and Its Ability to Bind Fpr1:Rapamycin Complex. *Proc. Natl. Acad. Sci. U.S.A.* **2008**, *105* (39), 15166–15171.
- (74) Chen, W.; Zou, P.; Zhao, Z.; Chen, X.; Fan, X.; Vinothkumar, R.; Cui, R.; Wu, F.; Zhang, Q.; Liang, G.; Ji, J. Synergistic Antitumor Activity of Rapamycin and EF24 via Increasing ROS for the Treatment of Gastric Cancer. *Redox Biol.* **2016**, *10*, 78–89.
- (75) Wen, X.; Wu, J.; Wang, F.; Liu, B.; Huang, C.; Wei, Y. Deconvoluting the Role of Reactive Oxygen Species and Autophagy in Human Diseases. *Free Radic. Biol. Med.* **2013**, *65*, 402–410.
- (76) Chen, Y.; Gibson, S. B. Is Mitochondrial Generation of Reactive Oxygen Species a Trigger for Autophagy? *Autophagy* **2014**, *4* (2), 246–248.
- (77) Chen, Y.; Azad, M. B.; Gibson, S. B. Superoxide Is the Major Reactive Oxygen Species Regulating Autophagy. *Cell Death Differ.* **2009**, *16* (7), 1040–1052.
- (78) Tasdemir, E.; Maiuri, M. C.; Galluzzi, L.; Vitale, I.; Djavaheri-Mergny, M.; D'Amelio, M.; Criollo, A.; Morselli, E.; Zhu, C.; Harper, F.; Nannmark, U.; Samara, C.; Pinton, P.; Vicencio, J. M.; Carnuccio, R.; Moll, U. M.; Madeo, F.; Paterlini-Brechot, P.; Rizzuto, R.; Szabadkai, G.; Pierron, G.; Blomgren, K.; Tavernarakis, N.; Codogno, P.; Cecconi, F.; Kroemer, G. Regulation of

Autophagy by Cytoplasmic P53. *Nat. Cell Biol.* **2008**, *10* (6), 676–687.

(79) Yaginuma, Y.; Westphal, H. Abnormal Structure and Expression of the P53 Gene in Human Ovarian Carcinoma Cell Lines. *Cancer Res.* **1992**, *52* (15), 4196–4199.

## Conclusion and Future Perspectives

In summary, this work has shown the incorporation of *N,N'* or *O,O'* ligands in *mono*- or *di*-nuclear copper systems can fine-tune redox activity and the mechanism of cytotoxic action within transformed cells. Furthermore, substitution of the metal centre from  $\text{Cu}^{2+}$  to  $\text{Mn}^{2+}$  significantly alters the mode of intracellular death by inducing autophagy instead of apoptosis. The *bis*- $\text{Cu}^{2+}$  chemo-type demonstrates low micromolar and nanomolar sensitivity across the panel of NCI-60 cells lines with no comparative activity to clinically established cytotoxins, inclusive of metal-based agents. Particularly, the more rigid framework mediated by terephthalate linker, mediates high levels of intracellular reactive oxygen species, culminating in the dissipation of mitochondrial bioenergetics and genomic DNA integrity. As such, this particular complex will serve as a lead candidate for further development towards pre-clinical progression.

In order to fulfill this objective, further studies should be conducted to elucidate the innate and intricate mechanism involved in its apparent multi-modal targeting properties. As such, those who wish to continue this work may determine the lipophilicity of the complexes to justify mitochondrial transportation into the inner membrane and matrix. Specifically, predominant localization and accumulation of the series should be examined in subcellular fractionations *via* ICP-MS. DTF calculations can also determine isomerisation, geometric orientation and so the molecular orbitals which most likely facilitate the specific production of reactive oxygen species from molecular oxygen in the vicinity of the reduced form of *di*- $\text{Cu}^+$  agents. Cytotoxicity should also be conducted in 3D model assays and non-transformed human primary cells lines, while also investigating the inhibitory effects on metastatic and invasive cancer cells to advocate progression towards animal studies. Time-course analysis of differential expression of a wide panel of genes can be examined, such as enzymatic antioxidants and those associated with oxidative stress, in combination with key regulatory genes in response to genomic DNA damage and cell death mechanisms. Furthermore, any subsequent studies should also include leading members of the Casiopeina family as positive controls.

Alternatively, the substitution of the phenantroline ligand to designer phenazines can potentially enhance DNA intercalation and recognition properties within *di*-nuclear systems. Similarly, functionalization of *N,N'* ligands with DNA recognition sequences and/or specific targeting moieties could also be exploited within a multi-phen complex framework.

## **Appendices A-D**

## Appendix A

Supporting information associated with Chapter 2.

### S2.1 Corresponding nuclease activity for 8-oxo-dG conditions

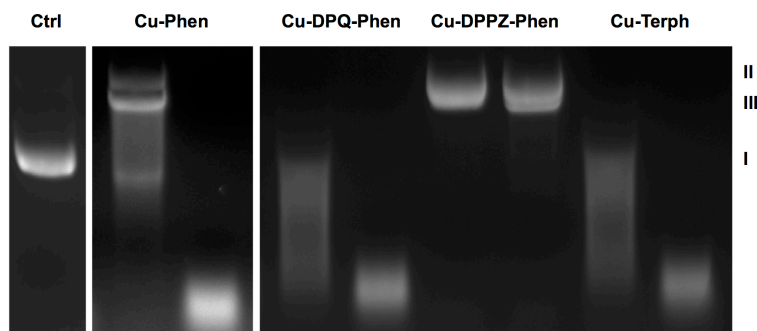


**Figure S2. 1** DNA cleavage reactions with 10 and 20  $\mu\text{M}$  test complex, 3000 ng superhelical pUC19 and 1 mM added Na-L-Ascorbate incubated at 37  $^{\circ}\text{C}$  for 30 minutes. Lane 1: pUC19 only, lane 2,3: 10 and 20  $\mu\text{M}$  Bis-Phen, lane 4,5: 10 and 20  $\mu\text{M}$  Cu-DPQ-Phen, lane 6,7: 10 and 20  $\mu\text{M}$  Cu-DPPZ-Phen, lane 8-9: 10 and 20  $\mu\text{M}$  Cu-Terph.

### S2.2 DNA cleavage optimisation (high concentration range with added reductant) for PCR amplification studies

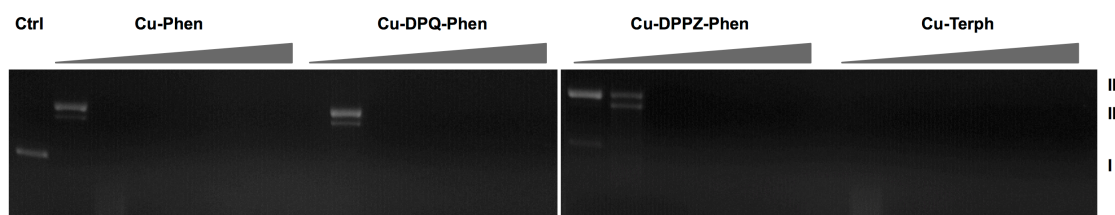


**Figure S2. 2** DNA cleavage reactions with 2.5, 5, 10, 20, 30, 40 and 50  $\mu\text{M}$  test complex, 400 ng superhelical pUC19 and 1 mM added Na-L-Ascorbate incubated at 37  $^{\circ}\text{C}$  for 30 minutes. Lane 1: pUC19 only, lane 2-8: Bis-Phen and lane 9-15: Cu-DPQ-Phen, lane 16-22: Cu-DPPZ-Phen and lane 23-29: Cu-Terph.

### S2.3 DNA cleavage optimisation (high concentration range without added reductant) for PCR amplification studies

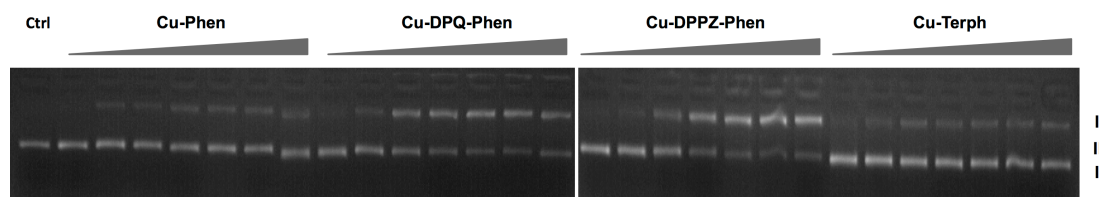


**Figure S2. 3** DNA cleavage reactions with 2.5, 5, 10, 20, 30, 40 and 50  $\mu$ M test complex, 400 ng superhelical pUC19 without added Na-L-Ascorbate incubated at 37 °C for 30 minutes. Lane 1: pUC19 only, lane 2-8: Bis-Phen and lane 9-15: Cu-DPQ-Phen, lane 16-22: Cu-DPPZ-Phen and lane 23-29: Cu-Terph.

### S2.4 PCR Primer Design

The pUC19 vector (2686 bp) was studied in detail and 3 sets of primers were designed such that it was possible to generate 120 bp long sequences of varying G-C content (35%, 50% and 63%). The lengths of the short nucleotide sequences were verified by carrying out PCR reactions (35 cycles) with 1 ng pUC19 plasmid using 2 $\times$  MyTaq Red Mix (Bioline) at suitable annealing temperatures for respective primer pairs and comparing the band generated by gel electrophoresis to a 50 bp DNA ladder (Fermentas).

35% forward: 5'-gatcttttctacggggtctg-3'

35% reverse: 5'-gatttaaaacttcattttta-3'

50% forward: 5'-ttatgccactggcagcagc-3'

50% reverse: 5'-accaaatactgttcttctag-3'

63% forward: 5'-tcgcgcgtttcggatgacg-3'

63% reverse: 5'-caccgctgacgcgccctgacg-3'



## S2.5 PCR amplification studies without reductant (high concentration range)

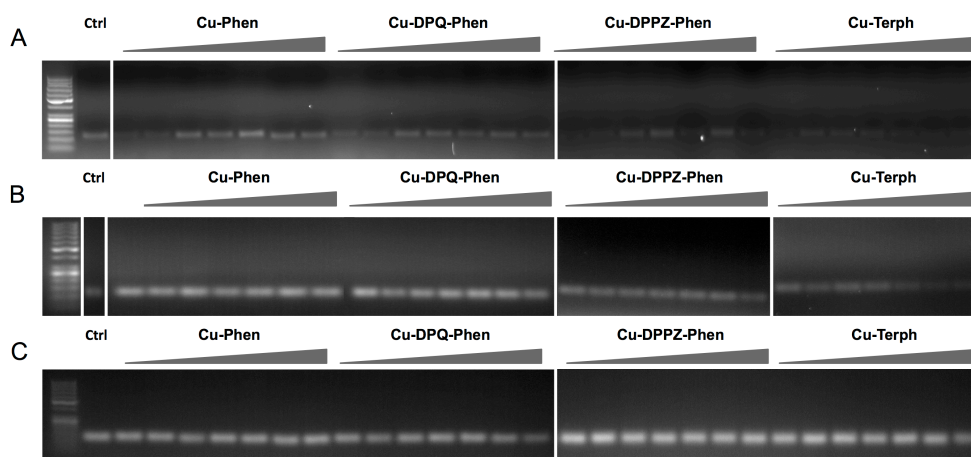


**Figure S2. 4** 400 ng pUC19 DNA was initially exposed to 2.5, 5, 10, 20, 30, 40 and 50  $\mu$ M of each test complex in the absence of added reductant at 37  $^{\circ}$ C for 30 minutes. 20 ng of complex exposed DNA template was removed from the reaction and PCR reaction was carried out as previously described with each varying G·C content primer set at optimum annealing temperatures and analysed using gel electrophoresis. Fig. A Lane 1: 35% G·C control, lane 2-8 35% G·C + Cu-Phen, lane 9-15: 35% G·C + Cu-DPQ-Phen and lane 16-22: 35% G·C + Cu-Terph. (B) 50% G·C and (C) 63% G·C respectively. All sequences generated were 120 base pairs.

## S2.6 PCR amplification studies with reductant (low concentration range)

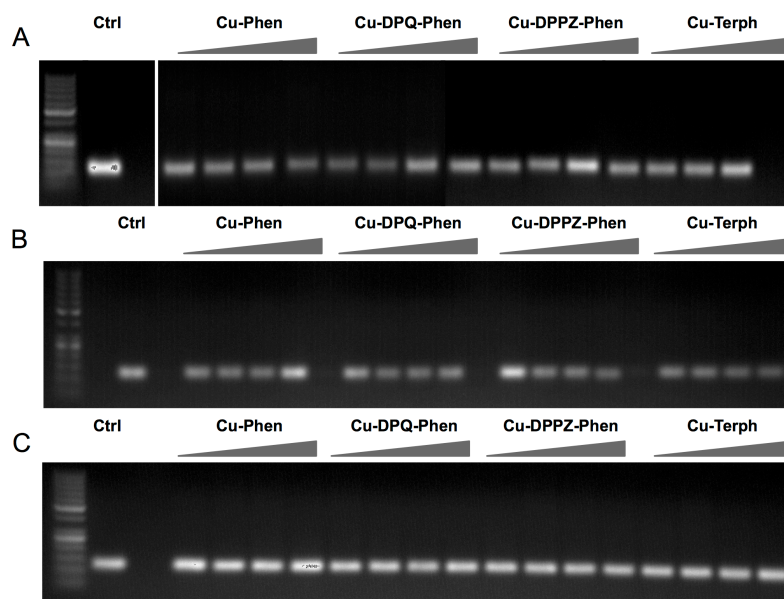


**Figure S2. 5** 400 ng pUC19 DNA was initially exposed to 250 nM, 500 nM, 1  $\mu$ M and 2.5  $\mu$ M of each test complex in the presence of 1 mM added reductant at 37  $^{\circ}$ C for 30 minutes. 20 ng of complex exposed DNA template was removed from the reaction and PCR reaction was carried out as previously described with each varying G·C content primer set at optimum annealing temperatures and analysed using gel electrophoresis. Fig. A Lane 1: 35% G·C control, lane 2-5 35% G·C + Cu-Phen, lane 6-9 35% G·C + Cu-DPQ-Phen and lane 10-13: 35% G·C + Cu-Terph. (B) 50% G·C and (C) 63% G·C respectively. All sequences generated were 120 base pairs.

## Appendix B

Supporting information associated with Chapter 3.

### S3.1 NCI-60 numerical values for GI<sub>50</sub>, TGI, LC<sub>50</sub>

**Table S3. 1** NCI-60 results. Concentrations required for 50 % growth inhibition (GI<sub>50</sub>), total growth inhibition (TGI) and 50 % lethal concentrations (LC<sub>50</sub>) were extracted from concentration-response curves by linear interpolation for the following cancers types:<sup>38</sup> leukemia (Leuk), non-Small Cell Lung (NSCL), colon, central nervous system, (CNS), melanoma (Mel), ovarian (Ov), prostate (Pros) and breast.

Cancer	Cell line	Units: $\mu$ M			Cancer	Cell line	Units: $\mu$ M		
		GI <sub>50</sub>	TGI	LC <sub>50</sub>			GI <sub>50</sub>	TGI	LC <sub>50</sub>
<b>Leuk</b>	CCRF-CEM	1.96	5.11	> 100		M14	1.58	3.18	6.40
	HL-60(TB)	2.35	6.01	77.4		MDA-MB-435	0.468	1.73	4.53
	K-562	2.2	5.55	> 100		SK-MEL-2	1.22	2.64	5.73
	MOLT-4	2.77	7.25	> 100		SK-MEL-28	1.21	2.49	5.16
	RPMI-8226	2.08	4.92	> 100		SK-MEL-5	0.215	0.487	1.32
	SR	2.63	7.39	> 100		UACC-257	1.18	2.46	5.13
						UACC-62	1.16	2.48	5.31
<b>NSCL</b>	A549/ATCC	1.19	2.62	5.79	<b>Ovar</b>	IGROV1	1.36	2.85	6.00
	HOP-62	2.35	4.01	6.82		OVCAR-3	1.92	3.35	5.85
	HOP-92	1.56	3.11	6.22		OVCAR-4	1.25	2.63	5.52
	NCI-H226	1.93	5.29	25.6		OVCAR-5	1.84	3.33	6.01
	NCI-H23	2.31	4.94	12.9		OVCAR-8	1.85	3.73	7.50
	NCI-H322M	1.57	2.92	5.43		NCI/ADR-RES	1.71	4.13	9.95
	NCI-H460	1.63	3.81			SK-OV-3	1.37	2.65	5.15
<b>Colon</b>	NCI-H522	0.426	1.39	4.75					
	COLO 205	1.87	3.39	6.17	<b>Renal</b>	786-0	1.83	3.27	5.82
	HCC-2998	1.87	3.41	6.21		A498	0.16	0.694	2.74
	HCT-116	1.95	3.87	7.68		ACHN	1.59	4.11	11.8
	HCT-15	1.26	2.58	10.8		CAKI-1	1.1	2.37	5.12
	HT29	1.99	3.89	7.61		RXF 393	1.41	3.01	6.39
	KM12	1.28	2.92	6.63		SN12C	1.69	3.18	5.98
	SW-620	1.78	3.53	6.99		UO-31	1.11	3.08	8.54
<b>CNS</b>	SF-268	1.57	3.00	5.75	<b>Pros</b>	PC-3	1.4	2.69	6.24
	SF-295	1.39	2.77	5.5		DU-145	1.38	3.36	6.16
	SF-539	1.6	2.98	5.54	<b>Breast</b>	MCF7	1.68	3.33	6.59
	SNB-19	1.71	3.24	6.12		MDA-MB-231/ATCC	1.35	2.86	6.02
	SNB-75	1.53	2.87	5.39		BT-549	1.9	3.48	6.39
	U251	1.58	2.96	5.53		T-47D	2.22	4.84	> 100
						MDA-MB-468	1.73	3.45	6.90
<b>Mel</b>	LOX IMVI	2.17	4.78	12.7					
	MALME-3M	2.02	3.65	6.59					

## Appendix C

Supporting information associated with Chapter 4.

### S1. Molecular structures of Cu-Oda and Cu-Terph.

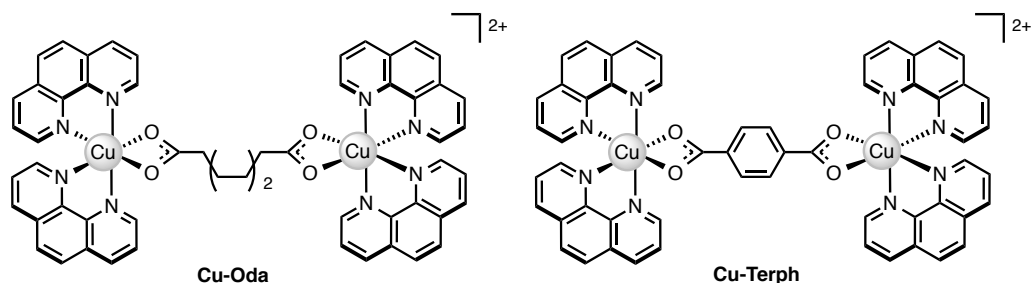


**Figure S4. 1** Molecular structure of  $[\{Cu(phen)_2\}_2(\mu-oda)]^{2+}$  (**Cu-Oda**, where oda = octanedioate) and  $[\{Cu(phen)_2\}_2(\mu-terph)]^{2+}$  (**Cu-Terph**, where terph = terephthalate).

### S2. NCI-60 human tumour drug screen

**Table S4. 1** NCI-60  $GI_{50}^a$ ,  $LC_{50}^b$  and  $TGI^c$  concentrations (molar, M)

Cancer	Cell line	Cu-Terph (M)			Cu-Oda (M)		
		$GI_{50}$	TGI	$LC_{50}$	$GI_{50}$	TGI	$LC_{50}$
Leukemia	CCRF-CEM	2.27E-07	5.31E-07	> 1.00E-4	4.19E-07	2.40E-06	4.97E-05
	HL-60(TB)	2.75E-07	9.27E-07	> 1.00E-4	4.42E-07	2.24E-06	>1.00E-04
	K-562	4.46E-07	> 1.00E-4	> 1.00E-4	1.25E-06	4.46E-06	>1.00E-04
	MOLT-4	2.90E-07	9.61E-07	> 1.00E-4	7.23E-07	3.64E-06	>1.00E-04
	RPMI-8226	2.73E-07	7.32E-07	> 1.00E-4	7.00E-07	3.21E-06	>1.00E-04
	SR	2.79E-07	1.00E-06	> 1.00E-4	1.43E-06	5.61E-06	>1.00E-04
NSCLC	A549/ATCC	2.12E-07	4.17E-07	8.17E-07	4.01E-07	1.62E-06	4.98E-06
	HOP-62	1.92E-07	3.41E-07	6.07E-07	1.32E-06	3.11E-06	7.31E-06
	HOP-92	2.27E-07	6.12E-07	2.48E-06	1.31E-06	2.66E-06	5.39E-06
	NCI-H226	2.78E-07	7.25E-07	2.67E-06	1.23E-06	3.08E-06	
	NCI-H23	2.57E-07	7.26E-07	4.66E-06	1.63E-06	3.50E-06	7.55E-06
	NCI-H322M	1.64E-07	3.03E-07	5.61E-07	6.80E-07	1.89E-06	4.38E-06
	NCI-H460	1.96E-07	3.87E-07		4.34E-07	2.26E-06	>1.00E-04
	NCI-H522	1.80E-07	3.70E-07	7.60E-07	2.47E-07	7.44E-07	3.40E-06
Colon	COLO 205	1.79E-07	3.24E-07	5.86E-07	6.80E-07	2.05E-06	5.68E-06
	HCC-2998	1.87E-07	3.62E-07	7.02E-07	1.01E-06	2.25E-06	5.50E-06
	HCT-116	3.09E-07	1.03E-06	4.52E-06	1.18E-06	2.70E-06	6.20E-06
	HCT-15	3.32E-07	1.32E-06	6.62E-06	3.95E-07	1.86E-06	6.99E-06
	HT29	2.02E-07	4.07E-07	8.22E-07	1.19E-06	3.05E-06	7.84E-06
	KM12	1.58E-07	3.08E-06	6.03E-07	3.29E-07	1.21E-06	4.93E-06
CNS	SW-620	2.04E-07	4.57E-07	1.18E-06	1.17E-06	3.18E-06	8.63E-06
	SF-268	1.69E-07	3.19E-07	6.04E-07	1.04E-06	2.45E-06	5.75E-06
	SF-295	1.79E-07	3.18E-07	5.64E-07	3.31E-07	1.41E-06	4.20E-06
	SF-539				4.24E-07	1.58E-06	4.10E-06

Melanoma	SNB-19	1.71E-07	3.08E-07	5.55E-07	1.28E-06	2.59E-06	5.27E-06
	SNB-75	1.53E-07	2.90E-07	5.48E-07	1.26E-06	2.51E-06	5.02E-06
	U251	1.77E-07	3.16E-07	5.65E-07	6.04E-07	1.92E-06	4.68E-06
	LOX IMVI	1.99E-07	4.06E-07	8.30E-07	1.49E-06	3.15E-06	6.65E-06
	MALME-3M	1.88E-07	3.61E-07	6.93E-07	1.75E-06	3.36E-06	6.46E-06
	M14	1.74E-07	3.46E-07	6.85E-07	4.09E-07	1.42E-06	4.41E-06
	MDA-MB-435	1.25E-07	2.50E-07	5.03E-07	2.00E-07	4.39E-07	9.62E-07
	SK-MEL-2	2.00E-07	4.24E-07	8.97E-07	3.22E-07	8.98E-07	3.21E-06
	SK-MEL-28	1.63E-07	3.06E-07	5.75E-07	3.33E-07	1.11E-06	3.41E-06
	SK-MEL-5	4.89E-08	1.66E-07	4.08E-07	1.62E-07	3.24E-07	6.49E-07
Ovarian	UACC-257	1.76E-07	3.49E-07	6.93E-07	6.20E-07	1.96E-06	4.54E-06
	UACC-62	1.76E-07	3.23E-07	5.84E-07	1.88E-07	4.07E-07	8.79E-07
	IGROV1	1.75E-07	3.65E-07	7.63E-07	2.59E-07	5.89E-07	2.03E-06
	OVCAR-3	1.87E-07	3.38E-07	6.14E-07	1.01E-06	2.21E-06	4.83E-06
	OVCAR-4	2.80E-07	7.74E-07	2.89E-06	3.31E-07	1.52E-06	4.04E-06
	OVCAR-5	1.91E-07	3.41E-07	6.08E-07	1.12E-06	2.42E-06	5.22E-06
	OVCAR-8	2.25E-07	4.64E-07	9.57E-07	6.61E-07	2.23E-06	6.12E-06
	NCI/ADR-RES	3.02E-07	1.13E-06	7.48E-06	4.39E-07	1.60E-06	5.22E-06
Renal	SK-OV-3	1.60E-07	2.94E-07	5.42E-07	1.00E-06	2.17E-06	4.69E-06
	786-0	1.88E-07	3.52E-07	6.58E-07	8.54E-07	2.08E-06	4.59E-06
	A498	1.59E-07	3.00E-07	5.67E-07	1.67E-07	3.72E-07	8.27E-07
	ACHN	4.24E-07	1.49E-06	4.04E-06	4.59E-07	1.60E-06	4.22E-06
	CAKI-1	1.78E-07	3.39E-07	6.48E-07	3.13E-07	1.16E-06	3.51E-06
	RXF 393	1.77E-07	3.28E-07	5.69E-07	9.84E-07	2.12E-06	4.90E-06
	SN12C	2.23E-07	4.82E-07	1.13E-06	1.06E-06	2.26E-06	4.81E-06
	TK-10	2.19E-07	5.03E-07	1.45E-06			
Prostate	UO-31	2.58E-07	1.25E-06	3.70E-06	3.38E-07	1.30E-06	3.71E-06
	PC-3	1.94E-07	4.56E-07	1.22E-06	4.85E-07	1.78E-06	4.35E-06
	DU-145	1.84E-07	3.46E-07	6.52E-07	9.36E-07	2.15E-06	4.73E-06
Breast	MCF7	1.93E-07	4.13E-07	9.62E-07	1.21E-06	2.88E-06	
	MDA-MB-231/ATCC	1.99E-07	3.94E-07	7.81E-07	3.10E-07	1.10E-06	3.44E-06
	HS 578T	3.15E-07	9.71E-07	>1.00E-04			
	BT-549	2.10E-07	4.40E-07	9.20E-07	8.94E-07	2.11E-06	4.66E-06
	T-47D	2.46E-07	6.16E-07	5.83E-06	1.72E-06	5.68E-06	>1.00E-04
	MDA-MB-468	1.77E-07	3.30E-07	6.17E-07	1.59E-06	3.19E-06	6.40E-06

<sup>a</sup> 50% growth inhibition, <sup>b</sup> 50% lethal concentration and <sup>c</sup> total growth inhibition

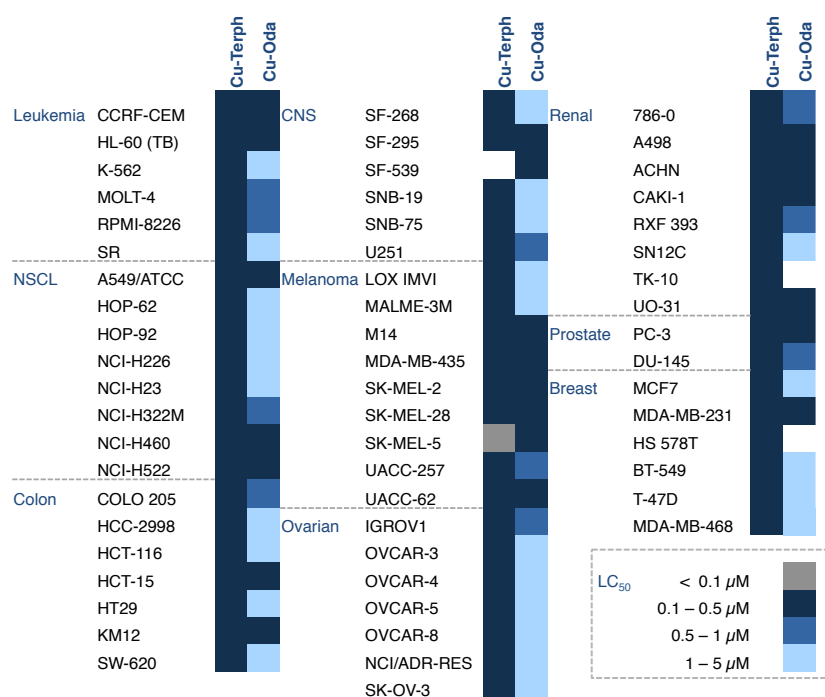


**Figure S4. 2** Heat map of  $GI_{50}$  concentration ranging from less than 0.1  $\mu M$  (grey) to 5  $\mu M$  (light blue) for **Cu-Terph** and **Cu-Oda**.

**Table S4. 2** Pearson correlation coefficients ( $r$ ) of  $GI_{50}$  concentrations generated from the NCI DTP COMPARE algorithm. Criteria threshold > 0.2 for **Cu-Oda** or **Cu-Terph**.

Drug	Mode of cytotoxicity <sup>1</sup>	NSC	Cu-Terph	Cu-Oda
chromomycin A3	DNA damaging	58514	0.467	
letrozole	Hormonal	719345	0.463	0.356
gallium nitrate	*	15200	0.400	0.261
didemnin B	*	325319	0.346	
maytansine	Tubulin-direacting	153858	0.345	
streptozotycin	DNA damaging	85998	0.339	
vinorelbine	Tubulin-direacting	608210	0.304	
cyanomorpholino-doxorubicin	DNA damaging	357704	0.235	0.317
procarbazine	DNA damaging	77213	0.232	0.303
anastrozole	Hormonal	719344		0.312
doxorubicin	Topoisomerase poison	123127		0.228

\*Non-FDA approved agents.

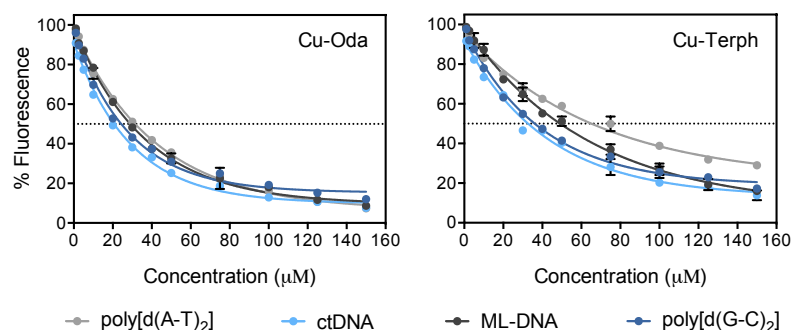
(1) FDA Approved Drugs [www.fda.gov](http://www.fda.gov).

### S3. Preferential DNA binding

**Table S4. 3** Apparent binding constants ( $K_{app}$ ) of dinuclear  $\text{Cu}^{2+}$  complexes, actinomycin D (Act D) and netropsin. Fluorescent profiles of **Cu-Oda** and **Cu-Terph** ethidium bromide displacement are shown in Figure S2.

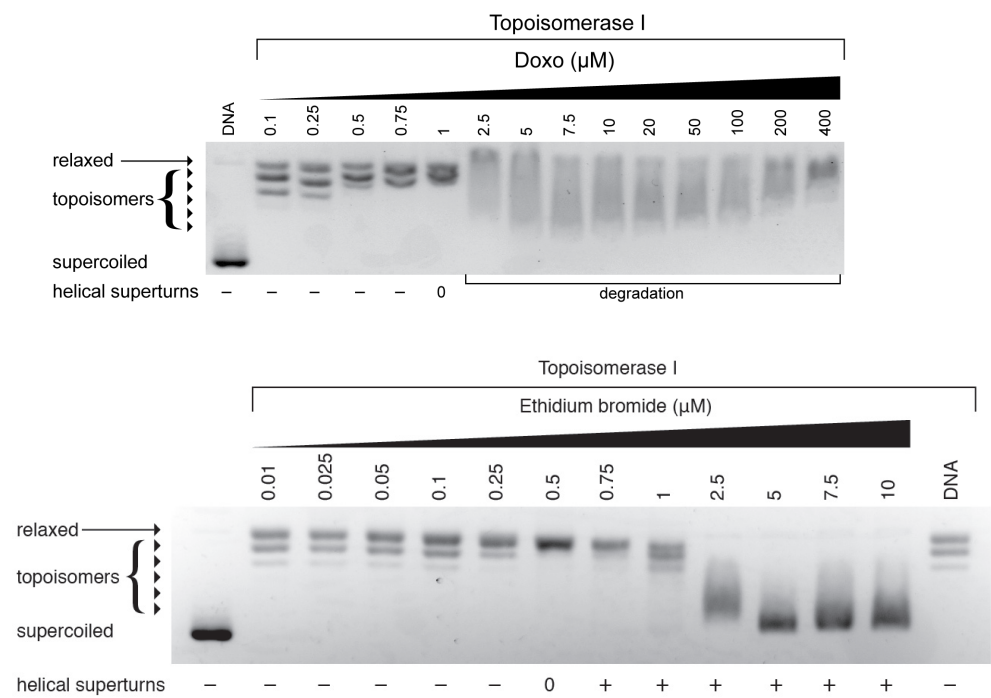
	$K_{app} \text{ M(bp)}^{-1}^a$			
	poly[d(A·T) <sub>2</sub> ] (100% AT)	ctDNA (58% AT)	ML-DNA (28% AT)	poly[d(G·C) <sub>2</sub> ] (0% AT)
Act D	N/A	$2.92 \times 10^7$	$3.03 \times 10^7$	$5.25 \times 10^7$
Netropsin	$5.75 \times 10^7$	$2.50 \times 10^7$	N/A	N/A
Cu-Oda	$3.79 \times 10^6$	$5.77 \times 10^6$	$4.12 \times 10^6$	$4.90 \times 10^6$
Cu-Terph	$1.84 \times 10^6$	$3.65 \times 10^6$	$2.44 \times 10^6$	$3.31 \times 10^6$

<sup>a</sup>  $K_{app} = K_e \times (12.6 / C_{50})$  where  $K_e = 9.5 \times 10^6 \text{ M(bp)}^{-1}$  and  $C_{50}$  = concentration that causes 50% reduction in EtBr fluorescence.



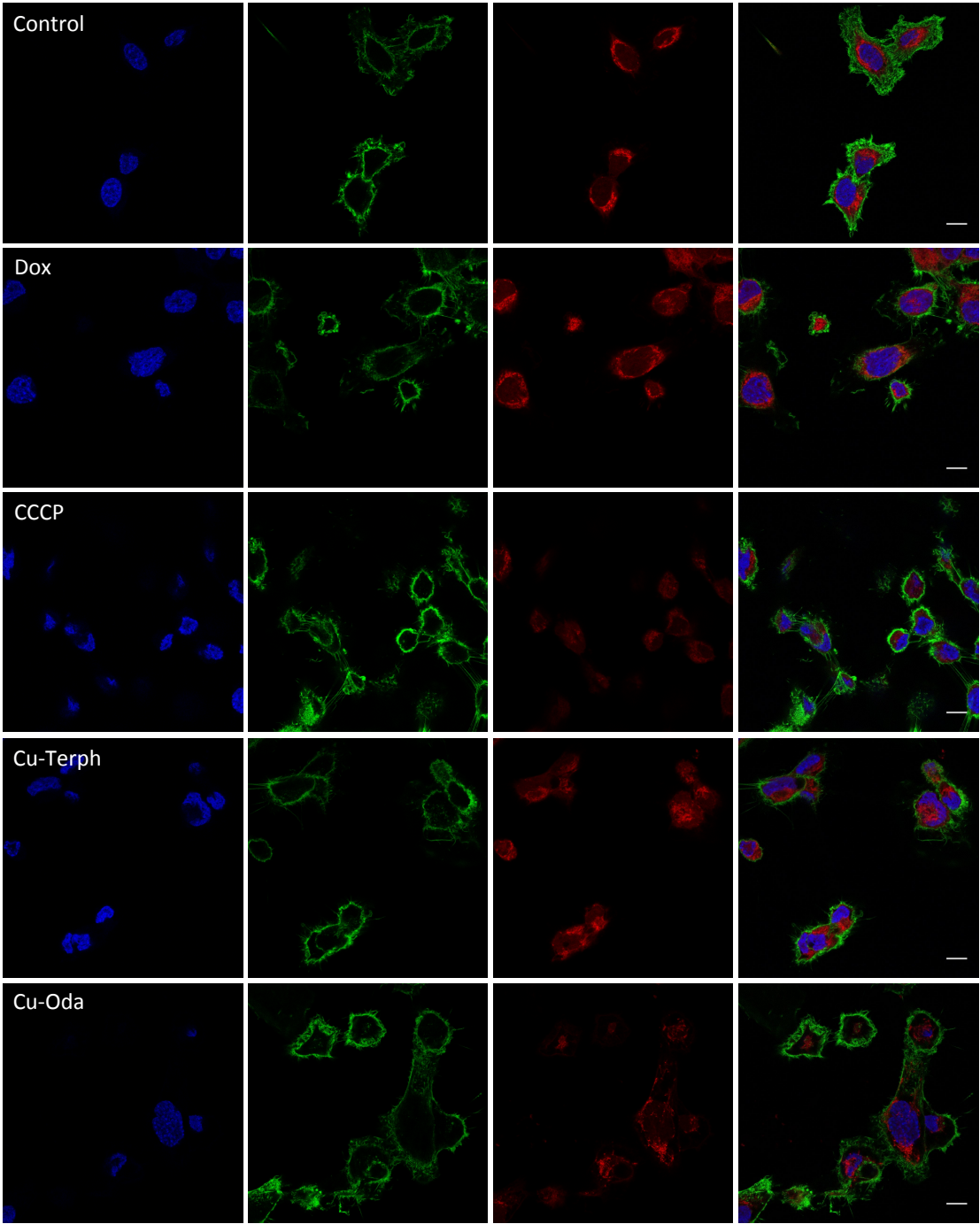
**Figure S4. 3** Competitive fluorescence binding of **Cu-Oda** and **Cu-Terph** to ethidium bromide (12.6  $\mu\text{M}$ ) saturated solutions of calf thymus DNA, *Micrococcus lysodeikticus* DNA (ML-DNA), poly[d(A·T)<sub>2</sub>], and poly[d(G·C)<sub>2</sub>] polynucleotides (10  $\mu\text{M}$ ) in 40 mM NaCl after 1 h incubation (final volume of 100  $\mu\text{l}$ ).

**S4. Topoisomerase I relaxation**



**Figure S4. 4** Topoisomerase I unwinding across concentration range 0.01 – 400  $\mu\text{M}$  for Dox and ethidium bromide.

**S5. Individual channel of confocal images**





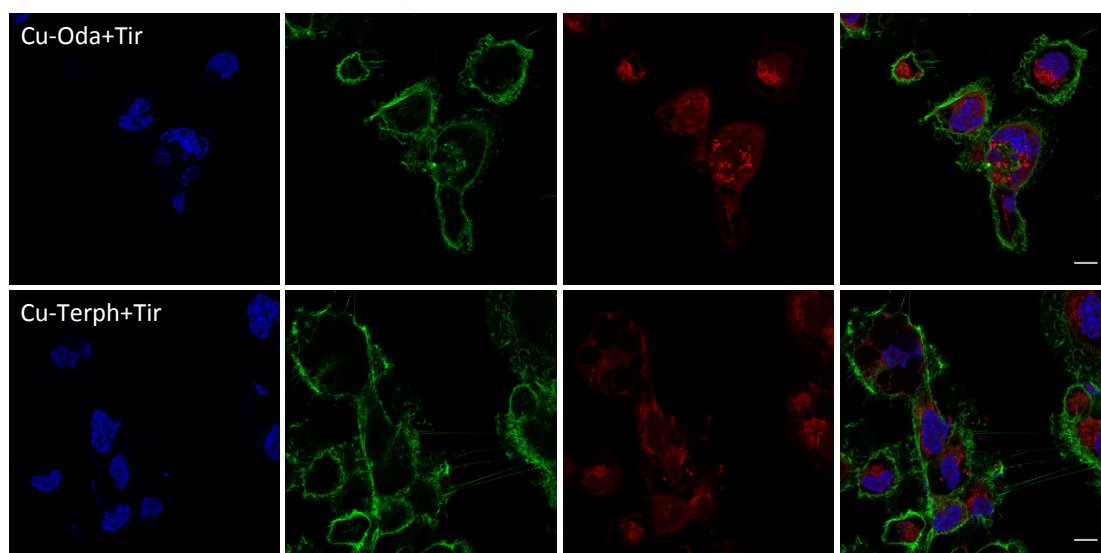


**Figure S4.5** 100 $\times$  confocal images of SKOV3 cells treated with **Cu-Oda** and **Cu-Terph** (1  $\mu$ M), CCCP (75  $\mu$ M) and Doxo (1  $\mu$ M). The nucleus is stained with DAPI (blue), cytoskeleton with Alexa Flour 488-Phalloidin and mitochondria with MitoTracker Deep Red.

#### S6. Mitochondrial depolarisation scatter plots

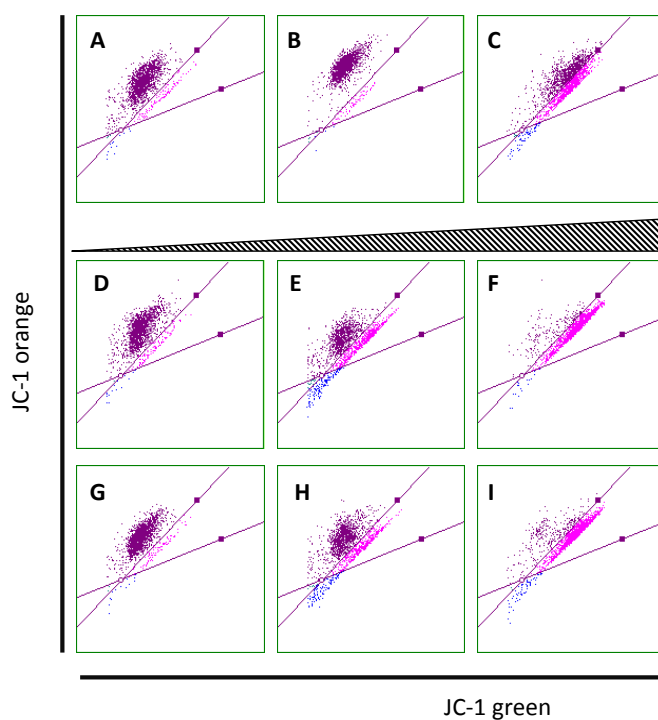


**Figure S4.6** Mitochondrial depolarisation scatter plots where polarised mitochondria are shown in purple, to depolarised mitochondria in pink and blue. **A)** cells only, **B)** 1.0  $\mu$ M Dox, **C)** 75  $\mu$ M CCCP, **D – F)** 0.5, 1.0, 2.0  $\mu$ M **Cu-Oda** and **G – I)** 0.5, 1.0, 2.0  $\mu$ M **Cu-Terph**.

## Appendix D

Supporting information associated with Chapter 5.

### S1. Topoisomerase I mediated relaxation of ethidium bromide.

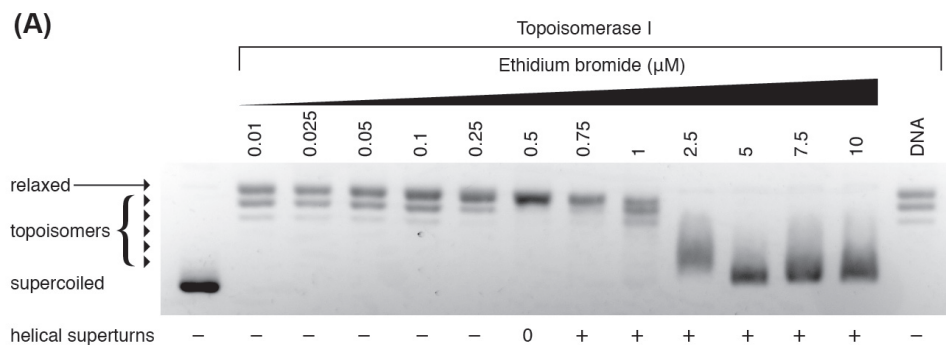


**Figure S5. 1** Topoisomerase I-induced DNA relaxation in the presence of ethidium bromide

### S2. Viscosity profile of Mn-Oda salmon testes DNA.

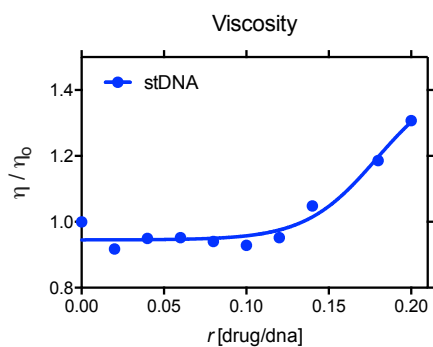


**Figure S5. 2** Viscosity properties ( $\eta / \eta_0$ ) of Mn-Oda at drug-DNA ratios ( $r$ ) 0.01 – 0.20.

### S3. Viability profiles of Mn-Oda and positive controls.

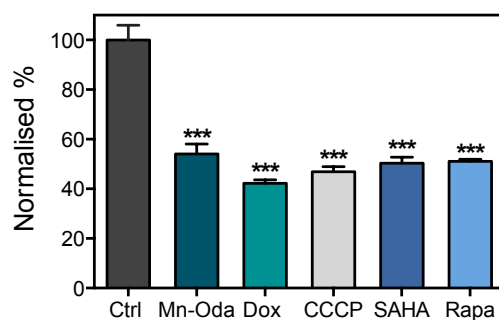


**Figure S5. 3** Viability profile after 24 h exposure to Mn-Oda (1  $\mu\text{M}$ ), Dox (1  $\mu\text{M}$ ), CCCP (75  $\mu\text{M}$ ), SAHA (100  $\mu\text{M}$ ) and Rapa (50  $\mu\text{M}$ ). Not significant  $p > 0.05$  and \*\*\* $p \leq 0.001$ .



